UNIVERSITY OF ROCHESTER
LABORATORY FOR LASER ENERGETICS

Volume 120
July–September 2009
DOE/NA/28302-910

LLE Review

Quarterly Report

About the Cover:

Top: This photo shows many of the 108 researchers from 29 universities and laboratories around the world, who attended the first OMEGA Users Group Workshop. The spirited workshop offered participants an opportunity to present and discuss, in an interactive but congenial atmosphere, their current work on OMEGA, their proposed experiments, and plans for taking experimental platforms developed on OMEGA to other facilities, such as the National Ignition Facility (NIF). In particular 31 outstanding presentations were made by 32 students and postdocs. The workshop poster sessions offered opportunities for students, professional scientists and engineers, postdocs, and academics to interact and discuss their research. Professor Roberto Mancini of the University of Nevada explains (bottom left) recent spectroscopic measurements obtained by his group to Prof. Michel Koenig of École Polytechnique, France. Through the National Laser Users' Facility Program, Dr. Mancini and his students are often frequent experimenters at the Omega Facility. Dr. Gilbert Collins of Lawrence Livermore National Laboratory describes (bottom right) how the inaccessible—the deep interiors of planets—becomes accessible through innovative experiments currently being conducted on OMEGA and, in the near future, the NIF.

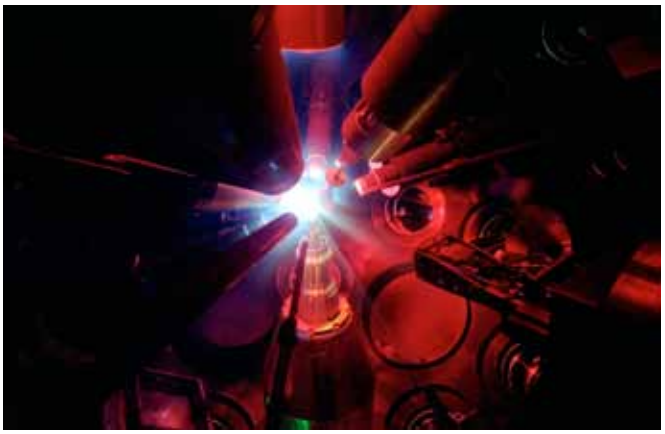

The OMEGA chamber during an experiment.

The focus of the 62 workshop presentations was often on the variety of OMEGA experiments (one of which is shown here and on the cover) that probe regimes of high-energy-density physics—a form of matter, radiation, and fields that can ordinarily be found only in the deep interior of stars and planets. For a few billionths of a second, these experiments are able to create unique stellar conditions—pressures of the order of 500 billion atmospheres (nearly twice that at Sun center); densities of about 300 g per cc (twice that of Sun center); temperatures of 100 million degrees C (seven times that of Sun center); and magnetic fields of 100 million gauss (the Earth's is about 0.3 gauss).

The work described in this volume includes current research at the Laboratory for Laser Energetics, which is supported by New York State Energy Research and Development Authority, the University of Rochester, the U.S. Department of Energy Office of Inertial Confinement Fusion under Cooperative Agreement No. DE-FC52-08NA28302, and other agencies.

Printed in the United States of America
Available from
National Technical Information Services
U.S. Department of Commerce
5285 Port Royal Road
Springfield, VA 22161
Price codes: Printed Copy A06
Microfiche A01

For questions or comments, contact Dana H. Edgell, Editor, Laboratory for Laser Energetics, 250 East River Road, Rochester, NY 14623-1299, (585) 275-0277.

Worldwide-Web Home Page: http://www.lle.rochester.edu/
(Color online)

UNIVERSITY OF ROCHESTER
LABORATORY FOR LASER ENERGETICS

Volume 120
July–September 2009
DOE/NA/28302-910

LLE Review

Quarterly Report

UR LLE

Contents

In Brief

This volume of the LLE Review, covering July–September 2009, features a summary and report on the first Omega Laser Facility Users Group (OLUG) Workshop organized by the Executive Committee: R. D. Petrasso (Plasma Science and Fusion Center, MIT), H. Baldis (University of California–Davis), J. Cobble (LANL), P. Drake (University of Michigan), J. Knauer (LLE), R. Mancini (University of Nevada–Reno), P. Norreys (Rutherford Appleton Laboratory), and M. Schneider (LLNL) (p. 161). More than 100 researchers from 29 universities and laboratories and 4 countries gathered at the Laboratory for Laser Energetics (LLE) from 29 April–1 May 2009 for the three-day workshop to facilitate communication and exchanges among individual Omega users and between users and LLE; to present ongoing and proposed research; to encourage research opportunities and collaborations that could be undertaken at the Omega Facility and in a complementary fashion at other facilities (such as LULI or the NIF); to provide an opportunity for students and postdoctoral fellows to present their research at the Omega Laser Facility in an interactive, yet congenial, atmosphere; and to provide feedback to LLE from the users about ways to improve the facility and future experimental campaigns. Invited talks on the Facility and science were given. The six overview science talks described the breadth and excitement of high-energy-density (HED) science undertaken on OMEGA, both present and future. The final overview talk concerned the role and importance of science to the National Nuclear Security Administration (NNSA) mission. Thirty-two students and postdoctoral fellows attended the workshop and presented 31 of the 48 contributed poster and oral presentations. The presentations ranged from target fabrication to simulating important aspects of supernovae. An important function of the workshop was to develop a set of recommendations and findings to guide future priorities for OMEGA. The original report and management's response are described beginning on p. 168. LLE management will use these recommendations as a guide for making decisions about OMEGA operations, priorities, and future capabilities. Another highlight of the workshop was the student/postdoctoral panel that discussed their experiences at the Omega Facility and their thoughts and recommendations on Facility improvements. Wide-ranging and engaging discussions resulted in the student/postdoctoral report contained in Findings and Recommendations of the Student/Postdoctoral Panel (p. 176).

Additional highlights of recent research presented in this issue include the following:

- T. R. Boehly, W. Seka, T. C. Sangster, D. D. Meyerhofer (LLE), R. E. Olson (Sandia National Laboratory), and P. M. Celliers, D. H. Munro, O. L. Landen, G. W. Collins, L. J. Suter (LLNL), describe the effect of condensates and inner coatings on the performance of vacuum hohlraum targets (p. 178). Experiments on the OMEGA Laser System using laser-driven vacuum hohlraum targets show distinct differences between cryogenic (<20 K) and warm targets. Warm hohlraum targets coated with 2 mm of CH replicate the behavior of cryogenic targets. This indicates that cryogenic hohlraums are affected by the condensation of background gases on the cold hohlraum surface. The introduction of low-Z material into the hohlraums significantly reduces the x-ray conversion efficiency, resulting in lower hohlraum radiation temperature. The coatings (both CH and condensates) produce long-scale-length, low-Z plasmas that reduce the absorption of laser light in the hohlraums. This causes higher reflectivity and produces hot electrons that generate hard x rays ($h\nu > 20$ keV), both of which are detrimental to the performance of hohlraum-driven inertial confinement fusion targets.

- S. N. Shafrir, H. J. Romanofsky, M. Skarlinski, M. Wang, C. Miao, S. Salzman, T. Chartier, J. Mici, R. Shen, S. D. Jacobs (LLE), J. C. Lambropoulos (Department of Mechanical Engineering, University of Rochester), and H. Yang (Department of Chemical Engineering, University of Rochester), report on magnetorheological finishing (MRF) spotting experiments performed on glasses and ceramics using a zirconia-coated-carbonyl-iron-particle–based magnetorheological (MR) fluid (p. 190). The coating layer was ~50 to 100 nm thick, faceted in surface structure, and well adhered. Coated particles showed long-term stability against aqueous corrosion. A viable MR fluid was prepared simply by adding water. Spot-polishing tests were performed on a variety of optical glasses and ceramics over a period of nearly three weeks with no signs of MR fluid degradation or corrosion. Stable material-removal rates and smooth surfaces inside spots were obtained.

- L. Sun and J. R. Marciante (LLE), and S. Jiang (AdValue Photonics, Inc.), demonstrate an all-fiber optical magnetic field sensor (p. 206). It consists of a fiber Faraday rotator and a fiber polarizer. The fiber Faraday rotator uses a 2-cm-long section of 56-wt%-terbium-oxide–doped silica fiber, and the fiber polarizer is a Corning SP1060 single-polarization fiber. The all-fiber optical magnetic field sensor has a sensitivity of 0.45 rad/T and can measure a magnetic field up to 3.5 T.

- J. Zhang and R. Sobolewski (Department of Electrical and Computer Engineering, University of Rochester and LLE), and A. Belousov, J. Karpinski, B. Batlogg (Laboratory for Solid State Physics, ETH Zurich), report their experimental studies on the time-resolved carrier dynamics in high-quality $Al_{0.86}Ga_{0.14}N$ single crystals, grown using a solution technique in a high-nitrogen-gas-pressure system (p. 210). Optical measurements were performed using two-color, femtosecond pump–probe spectroscopy. By studying the correlation signal amplitude's dependence on both the pump light's absorbed power and wavelength, they obtained a two-photon-absorption coefficient $\beta = 0.442 \pm 0.02$ cm/GW, as well as its spectral dependence, and confirmed that within the tuning range of the laser, the latter was in very good agreement with the Sheik–Bahae theory for wide, direct-bandgap semiconductors. The optical bandgap of the $Al_{0.86}Ga_{0.14}N$ crystal was determined to be 5.81 ± 0.01 eV.

- This volume concludes with a summary of LLE's Summer High School Research Program (p. 214), the FY09 Laser Facility Report (p. 216), and the National Laser Users' Facility and External Users' Programs (p. 218).

Dana H. Edgell
Editor

The Omega Laser Facility Users Group Workshop 29 April – 1 May 2009

Introduction

More than 100 researchers from 29 universities and laboratories and 4 countries gathered at the Laboratory for Laser Energetics (LLE) for the first Omega Laser Facility Users Group (OLUG) Workshop (see Fig. 120.1). The purpose of the three-day workshop was to facilitate communication and exchanges among individual Omega users and between users and LLE; to present ongoing and proposed research; to encourage research opportunities and collaborations that could be undertaken at the Omega Facility and in a complementary fashion at other facilities (such as LULI or the NIF); to provide an opportunity for students and postdoctoral fellows to present their research on OMEGA in an interactive, yet congenial, atmosphere; and to provide feedback to LLE from the users about ways to improve the facility and future experimental campaigns. Interactions at the workshop were spirited and lively, as can be seen in the photographs shown in this article. The names and affiliations of the 156 members of OLUG can be found at **www.lle.rochester.edu/pub/OLUG/OLUGMEMBERS.pdf**.

Invited talks on the facility and science were given during the first two mornings of the workshop. The facility talks were especially useful for those not intimately familiar with the complexities of performing experiments on OMEGA and OMEGA EP. The six overview science talks, given by leading world authorities, described the breadth and excitement of high-energy-density (HED) science undertaken on OMEGA, both present and future. The final overview talk concerned

U963JR

Figure 120.1

More than 100 researchers from around the world, from 29 universities and laboratories, attended this workshop. Workshop reports and nearly all 62 presentations can be found at **http://ouw.lle.rochester.edu**. Plans for the next OLUG Workshop to be held 28 April–1 May 2010 are well underway, with significant financial support from the National Nuclear Security Administration (NNSA) already allocated for student/postdoctoral travel expenses.

the role and importance of science to the National Nuclear Security Administration (NNSA) mission. The next section of this article contains a summary of the range of presentations; nearly all presentations can be found in their entirety at **http://ouw.lle.rochester.edu**.

Thirty-two students and postdoctoral fellows (Fig. 120.2), 27 of whom were supported by travel grants from NNSA, attended the workshop and presented 31 of the 48 contributed poster and oral presentations. The presentations ranged from target fabrication to simulating important aspects of supernovae. The presentations generated lively discussions, probing questions, and friendly suggestions. Seventeen excellent contributed presentations were made by professional scientists and academics.

U964JR

Figure 120.2
Students and postdoctoral fellows. Thirty-two students and postdoctoral fellows attended and presented 31 of the 48 contributed poster and oral presentations. Equally important, the student/postdoctoral panel wrote an outstanding report (p. 176) on how to improve the Omega Facility and on the opportunities and challenges young researchers face in implementing experiments at OMEGA and other HED facilities.

An important function of the workshop was to develop a set of recommendations and findings to guide future priorities for OMEGA. These findings were grouped into five areas: 60-beam OMEGA, OMEGA EP, General User Issues, Information Flow, and Broader Issues. These categories comprise a report provided to the Omega Laser Facility management. The original report and the management response are described in **Findings and Recommendations of the Executive Committee** (p. 168) and can be found at http://ouw.lle.rochester.edu. LLE management will use these recommendations as a guide for making decisions about OMEGA operations, priorities, and future capabilities. To cement this process, OLUG Executive Committee members and Omega management have been meeting on a bimonthly basis to assess progress toward achieving these objectives.

One highlight of the workshop was the student/postdoctoral panel that discussed their experiences at the Omega Facility and their thoughts and recommendations on facility improvements. Wide-ranging and engaging discussions resulted in the student/postdoctoral report contained in **Findings and Recommendations of the Student/Postdoctoral Panel** (p. 176) and at http://ouw.lle.rochester.edu.

The next OLUG Workshop will be held at LLE on 28 April–1 May 2010. Meetings of the Users Group and interested members of the HED community are formulating plans for this workshop and reviewing progress on implementing the **Findings and Recommendations** (p. 168) of the first workshop. These meetings were held at the IFSA Conference (8 September 2009) and are planned for the APS conference in Atlanta (3 November 2009).

The Presentations

Sixty-two talks and posters presented during the 2009 workshop focused on ongoing fast- and shock-ignition experiments; materials under extreme conditions on OMEGA and, in the near future, at the NIF; the critical role that simulations play in designing and interpreting experiments; the physics connections between the Omega Facility and the European ICF program; and present and future laboratory astrophysics experiments on OMEGA and the NIF.

The facility talks presented important details and developments on the status and performance of the Omega Facility from pulse shaping and duration to beam smoothing; the qualification process for interfacing new experiments; the existing, and soon-to-be-operating, diagnostics; and the critical role of targets, from design and procurement to full characterization, fielding, and finally shooting.

Forty-eight contributed posters and talks covered a wide spectrum of work on the Omega Facility, from target fabrication to fast-ignition experiments to basic and novel nuclear physics experiments (see http://ouw.lle.rochester.edu). Work on the opportunities for taking physics platforms developed on OMEGA to other facilities that are both larger (the NIF) and smaller (Jupiter, Trident, and LULI) was presented. The presentations, invited and contributed, formed much of the basis for discussions regarding the Findings and Recommendations and future capabilities, found in the next section (p. 168).

The following photographs (Figs. 120.3–120.21) provide a representative sampling of the workshop's talks, interactions, and spirited ambiance. A much larger collection of photographs can be found at http://ouw.lle.rochester.edu.

U965JR

Figure 120.3
Postdoctoral fellow Dr. Angelo Schiavi (Roma University) discussed, on behalf of his European colleagues, the latest theoretical developments in fast ignition. Dr. Schiavi delighted workshop attendees, not only with the clarity and depth of his presentation, but with his humorous and entertaining remarks!

U966JR

Figure 120.4
Dr. Ryan Rygg, an LLNL postdoctoral fellow, was chair of the student/postdoctoral panel (see their report herein and on http://ouw.lle.rochester.edu). Dr. Rygg is a frequent experimenter at the Omega and Jupiter facilities and is collaborating with MIT researchers on nuclear diagnostics currently being implemented at the National Ignition Facility. He is a member of Dr. Rip Collins's Shock/Materials Group (see Fig. 120.5) at LLNL.

U967JR

Figure 120.5
Probing the interiors of the planets through materials experiments on OMEGA, and soon at the NIF, was the focus of LLNL's Dr. Rip Collins's presentation. Here he describes how the inaccessible (planet interiors) becomes accessible through such laboratory experiments. Dr. Collins's gave an animated description of the challenges of compressing a tofu-like material to densities of ~100 g/cm^3 (five times the density of gold).

U968JR

Figure 120.6
Professor Peter Norreys of Rutherford-Appleton Laboratory discussed the reasons that the testing and development of fast-ignition concepts on OMEGA are so critical in preparing for and guiding the European consortium's fast-ignition experiments. Dr. Norreys is a member of the OLUG Executive Committee.


U969JR

Figure 120.7
Postdoctoral fellow Dr. Carolyn Kurantz (University of Michigan) makes decisive and unequivocal points about the subtleties and challenges of laboratory astrophysics experiments that she and colleagues have been implementing on OMEGA as part of their NLUF program, an effort led by Prof. Paul Drake. Dr. Kurantz is a member of the student/postdoctoral panel, and Prof. Drake is a member of the Executive Committee.


U970JR

Figure 120.8
During a coffee break, LLE Ph.D. student Maria Barrios (right) discusses her work and presentation on shock-compressed materials with her former professor Dr. Sharon Stephenson (Gettysburg College).


U971JR

Figure 120.9
Postdoctoral fellow Dr. Louise Willingale (University of Michigan) contemplates her response to a workshop attendee's query about aspects of her OMEGA EP experiment involving proton emissions from OMEGA EP's short-pulse beam interacting with a flat target. Dr. Willingale is a member of the student/postdoctoral panel.


U972JR

Figure 120.10
Keith Thorp, the Omega Facility Manager, presented an overview of the planning, processes, and coordination needed to conduct a successful experiment on OMEGA. Such talks gave attendees the opportunity to meet with, and hear from, some of the key individuals responsible for operating and improving the facility. Mr. Thorp is one of the many dedicated staff members involved in, and orchestrating, the day-to-day facility operations.

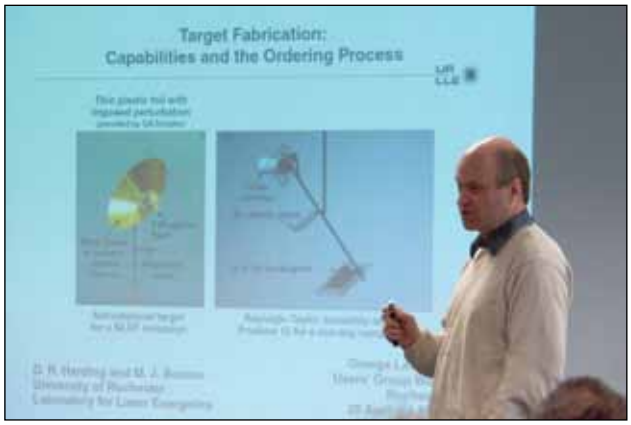

U973JR

Figure 120.11
Targets are a critical part of any experiment. Here, LLE's Dr. David Harding describes the range and complexity of targets that are designed and then meticulously assembled and characterized prior to their fielding. Each step in the process requires demanding attention to detail and design, often requiring many interactions between the experimenter and the target-manufacturing team. Most targets are manufactured at General Atomics (GA); the scope of GA's work was presented by Brian Vermillion. As the saying goes, "the targets are just as important as the laser"—a perspective that we are sure is shared by Dr. Harding.

U974JR

Figure 120.12
The crucial role that basic science, and OMEGA in particular, plays in NNSA's program was described by Dr. Chris Deeney, who heads the ICF branch of NNSA. NNSA was responsible for providing vital financial aid to 27 students and postdocs who attended the workshop.

U975JR

Figure 120.13
Spirited and lively discussions often ensued in poster and workshop breakout sessions, with the results of these discussions contained in the Reports of **Findings and Recommendations** [herein (p. 168) and at http://ouw.lle.rochester.edu]. Many of these "findings" are currently being implemented by OMEGA management, and discussions between management and the OLUG Executive Committee continue on a bimonthly basis.

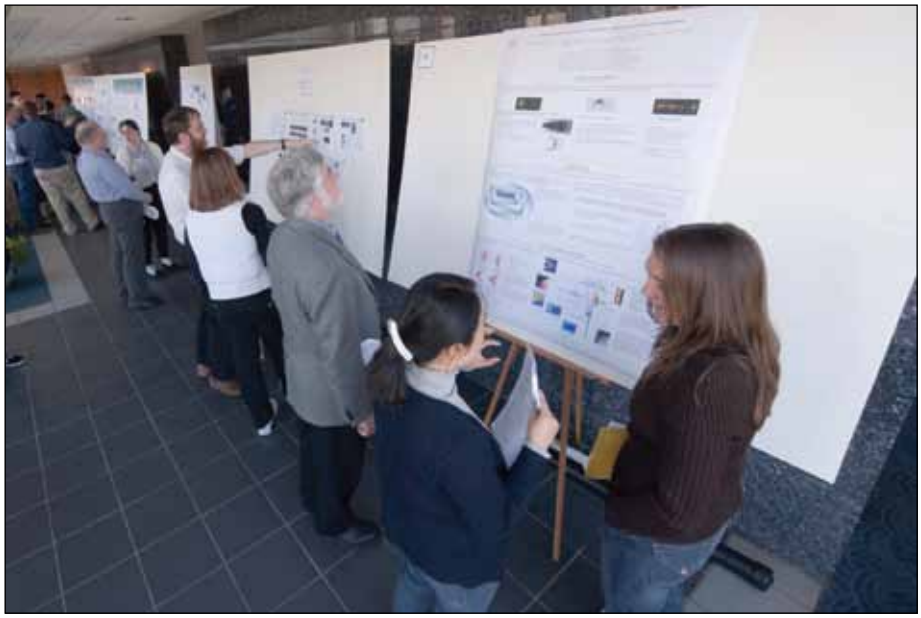
U976JR

Figure 120.14
The 62 workshop presentations, some of which are shown here during the poster session, covered a wide spectrum of cutting-edge, high-energy-density science relevant to OMEGA, the NIF, and other HED facilities.


U977JR

Figure 120.15
Here, Ph.D. student Teresa Bartel of the University of California–San Diego discusses her OMEGA EP experiments with Dr. Steve Craxton, one of LLE's theoretical physicists. Ms. Bartel's poster focused on proton beams relevant to fast ignition, one aspect of which was the exploration of proton-conversion efficiency achievable on OMEGA EP. A too-low proton-conversion efficiency would preclude this impulsive heating scheme for fast ignition. Ms. Bartel is a member of Prof. Farhat Beg's group.

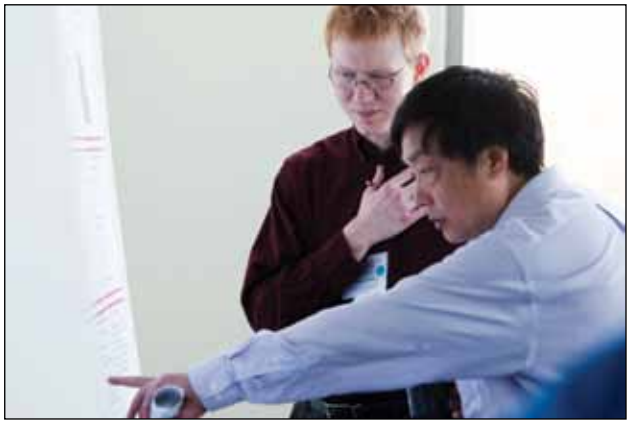
U978JR

Figure 120.16
Theoretical Ph.D. student Matt Terry of the University of Wisconsin–Madison listens intently to the query of experimentalist Dr. Chikang Li of MIT, regarding Matt's work on the stopping power of energetic particles in dense, hot plasmas. Such problems, while of basic interest to HED physics, are of special relevance to ICF where, for example, the stopping and energy deposition of alphas are crucial to the ignition instability. Matt discussed several theoretical stopping models and the differences between them. Could such differences, sometimes small, have subtle but nontrivial consequences on ignition criteria, making it either easier or more difficult to achieve ignition at the National Ignition Facility?


U979JR

Figure 120.17
At his poster about the measurements of fields associated with Rayleigh–Taylor (RT) instabilities, MIT Ph.D. student Mario Manuel talks with theoretical physicist Dr. Serge Bouget of CEA, France. Mr. Manuel's experimental investigation, conducted as part of MIT's NLUF program, utilizes monoenergetic 15- and 3-MeV protons to probe, via the Lorentz force, magnetic fields in RT experiments. Such posters, informal working groups, and frequent coffee breaks led to many opportunities for young researchers to interact and discuss their research with workers from a broad range of fields and experience within the world-wide high-energy-density physics community.


U980JR

Figure 120.18
The Omega Users Executive and Student/Postdoctoral Committees discuss details and assignments for writing the findings and recommendations of the workshop. The two committee reports and the initial management response can be found at http://ouw.lle.rochester.edu and in this document. The process of improving the Omega Laser Facility is an ongoing activity involving bimonthly meetings between the Executive Committee members and Omega management. Progress on the recommendations will be given in a satellite session at the Atlanta APS meeting (3 November 2009) and at the next OLUG Workshop (28 April–1 May 2010). An important finding of both committees was the excellence with which the Omega Laser Facility is run, offering exciting opportunities to users to perform world-class experiments.


U981JR

Figure 120.19
The French came in full force to the workshop, bringing a dashing but friendly contingent with exciting ideas and zest! Vive La France!


U982JR

Figure 120.20
A workshop banquet at the University of Rochester's Faculty Club offered an enjoyable evening for all workshop attendees.


U983JR

Figure 120.21
Our European colleagues share a light moment at the workshop banquet.

Findings and Recommendations of the Executive Committee

Executive Committee:

Richard Petrasso, Committee Chair, Massachusetts Institute of Technology
Hector Baldis, University of California–Davis
James Cobble, Los Alamos National Laboratory
Paul Drake, University of Michigan
James Knauer, LLE, University of Rochester (designated)
Roberto Mancini, University of Nevada–Reno
Peter Norreys, Rutherford Appleton Laboratory
Marilyn Schneider, Lawrence Livermore National Laboratory

1. Introduction

Extensive formal and informal discussions occurred during the workshop regarding (1) ways in which the Omega Facility could be more effective in using existing resources and (2) new capabilities or technologies that would be highly desirable. It is important to stress that there was a resounding response by the workshop attendees that the Omega Laser Facility is extremely well run and that the team operating it is both highly dedicated and very skilled.

Two workshop reports were written. The first, by the OLUG Executive Committee, was a summary of the views of the workshop attendees (108 professional scientists and engineers, academics, students, and postdocs from four countries). Its findings were grouped into five areas: 60-beam OMEGA, OMEGA EP, general user issues, information flow, and broader issues. The second report was written by the student/postdoctoral panel.

These two reports have many common issues, especially those relating to information flow and to the process of preparing for and executing campaigns in the OMEGA environment. This commonality is, in part, due to the challenging complexity, especially for new users, of the facility and its operations, even though there are myriad tools at the Omega Facility to navigate through this process. As will be obvious in the different sections of the Executive Committee report, these themes were often repeated. The management response was written to address the issues that were raised on the last day of the workshop (1 May 2009), and because sections of the Executive Report, as well as the management response, were written several days after the workshop, there is a slight mismatch between the issues of the formal Executive Report (contained herein in Secs. 2–6, pp. 168–172) and the Management Response. Because of the complexity of the issues involved and the need to iterate from recommendations to what is actually achievable from the management point of view, this report must be considered a work in progress. To that end, OLUG meets bimonthly with Omega management to discuss (1) what can be realistically achieved and (2) progress toward implementing the workshop findings and recommendations. Progress on the recommendations will be presented at the Atlanta APS meeting (3 November 2009) and at the next Omega Laser Facility Users Group Workshop (28 April–1 May 2010).

2. OMEGA (60 Beams)

The users developed a list of desired improvements to enhance the use of the 60-beam OMEGA Laser. The following information reflects both the degree of resonance across the users and the degree of importance to specific subgroups of users.

a. Delay and conflict information: A web page could be designed to provide the top 15 or so typical delays generated by decisions about how an experimental day is constructed. Examples would include the delays associated with repointing beams or moving a framing camera. This is of value to help users better develop their initial plans for shot days.

b. More options for driving the laser legs: The minimum functionality sought here is less than the ultimate one. The ultimate functionality would be the ability to drive any leg from any driver. We recognize that this is a tall order. The minimum functionality is the ability to use the smoothing by spectral dispersion (SSD) driver on one leg while using another driver on the other two legs. (This may include enabling the backlighter to drive on any two legs.) Having the capability to operate SSD and main drivers simultaneously could be quite important to x-ray Thomson-scattering experiments, an emerging area where much greater activity can be anticipated.

c. More static x-ray pinhole cameras: These diagnostics are rarely, if ever, critically important but are of value in assessing whether an experiment performed as intended. Their number has decreased in recent years and it would be helpful to see a few cameras re-activated.

d. More SG8 or similar phase plates: This would be particularly useful when users share shot days. Whether SG8's are the right choice or how this integrates with phase plates for OMEGA EP was not addressed. Most users agree that having some phase plates for OMEGA EP is far more important than having additional ones for the 60-beam OMEGA.

e. Spherical crystal imaging: This would be a very useful diagnostic if implemented and engineered to the point of being routinely available. The users understand that this would be an expensive prospect and do not rank it above other ways to spend the necessary funds. The users strongly encourage support for any effort by a major laboratory to implement this diagnostic.

3. OMEGA EP

a. Beam smoothing: Distributed phase plates (DPP's) significantly improve the spatial uniformity of irradiation in the focus of high-power laser beams. They reduce the growth of parametric instabilities, which have a number of deleterious effects, such as the generation of hot electrons (this causes preheat of the irradiated targets) and reduced coupling of laser energy to the plasma.

OLUG recommends the installation of 1-mm-spot-size DPP's on the long-pulse beamlines. This provision would benefit a number of users of the facility.

Temporal smoothing can be achieved with the implementation of smoothing by spectral dispersion (SSD). OLUG is aware that a preamplifier module (PAM) is being installed on the OMEGA laser to study two-dimensional SSD for direct-drive ICF at the National Ignition Facility (NIF).

OLUG urges facility management to make the necessary modifications to the NIF PAM so that it can be used as an alternate front end for OMEGA EP and allow for 2-D SSD studies to be implemented for the user community.

b. Pulse shaping: The NIF will be using long-pulse durations for some studies. Staging experiments from OMEGA EP to the NIF may need similar pulse shapes in the future.

OLUG recommends that options for implementing pulse shapes similar to the NIF's (100 ps to 30 ns) be explored by management so that an assessment of priorities can be made at the next OLUG meeting.

c. Intensity-contrast-ratio enhancement: The coupling of energy from the intense laser pulse to the fast-electron beam may be significantly affected by magnetic fields formed near the ablation front by the plasma generated by the prepulse. These fields have the effect of reducing the number of fast electrons entering the target. It may be necessary to improve the intensity contrast ratio to get better coupling.

OLUG recommends that options for enhancing the intensity contrast ratio be explored by management so that an assessment of priorities can be made at the next OLUG meeting.

d. Implementation of low-energy probe beams: Optical probes provide a range of powerful diagnostic tools that can be used to extract information from underdense laser-produced plasmas. Density gradients, for example, can be obtained from both shadowgraphy and Schlieren imaging, while density information can be extracted by unfolding interferograms and magnetic fields can be obtained with the simultaneous use of polarimetry. The working group is aware of the funded project to implement a 10-ps fourth-harmonic probe line for OMEGA EP by the end of this fiscal year.

OLUG urges management to make the completion and realization of this project a very high priority. These diagnostics will be of great assistance to a large number of users of the facility.

e. Addition of streaked optical pyrometry (SOP) with the active shock breakout (ASBO) diagnostic: The active shock breakout (ASBO) diagnostic has proved to be a valuable tool to study high-pressure equation of state of materials, as well as shock timing for inertial confinement fusion. The instrument has been used extensively by investigators based at a number of universities and national laboratories since the upgraded instrument was commissioned in 2006. A laser probe beam is used to illuminate the rear surface of the target. When the shock wave reaches the back surface of the witness plate, it rapidly heats the surface, resulting in a dramatic reduction in reflectivity of the probe beam. This makes it possible to measure shock-breakout times with high temporal and spatial resolution.

The provision of two "velocity interferometer for any reflector (VISAR)" channels is a unique feature of the upgraded instrument. These channels have different velocity sensitivities that make it possible to resolve any 2-D ambiguity that arises at velocity discontinuities. The working group agreed that the addition of passive streaked optical pyrometry (SOP) channels would be a valuable addition. These channels would make it possible to measure the lower radiation temperatures and shock pressures.

OLUG recommends the simultaneous provision of SOP with the ASBO diagnostic suite.

f. Spherical crystal imaging: Monochromatic x-ray imaging of high-photon-energy K_α radiation has proved to be a valuable tool in diagnosing energy transport in intense laser–plasma interactions. This has provided information in cone wire plasmas: for example, the energy coupling and the resistive electric field required to draw the return current. Many experiments will benefit from the provision of Ti, Cu, and higher-Z K_α imaging spectrometers.

OLUG recommends the provision of a spherical crystal imaging diagnostic on OMEGA EP.

g. Record of electromagnetic pulse (EMP) and radiological noise: High-intensity laser environments are harsh. Active diagnostics suffer considerable damage because of EMP, x-ray bremsstrahlung radiation, and (p,n)-induced activation of diagnostics placed close to the targets.

OLUG recommends that a record of instruments and detectors that have suffered from EMP and radiological noise damage be made available to facility users so that mitigation strategies can be undertaken when planning experiments.

h. Penalty and conflict information: It would be very useful when preparing experiments to have an appreciation of the time delays that are likely to occur as a result of changes to diagnostics, target alignment, and laser specifications during experimental campaigns.

OLUG recommends that a record of known delays be made available to facility users so that users are more aware of the costs of decisions.

4. General User Issues

A number of issues common to users of both OMEGA and OMEGA EP were discussed. These issues are based on operational details relevant to preparing and executing experiments, as well as the flow of information and communication between facility personnel and users, as well as among users themselves. The following points summarize these issues and *recommendations*:

(a) A number of users have indicated that it would be important to have available a larger volume of information and knowledge about facility operational details and the way in which they can impact the setup and execution of experiments. The information could include relationships between changes in laser-pulse energy, shaping, and smoothing options during a shot day, and their impact in shot delays, including a possible loss of shots. In general, the issue is, What is the optimal way to plan for these changes during a shot day (e.g., what is best to do first, second, etc.)? The idea is that what actually happens during the day (or half day) of shots is likely to be a compromise determined by practical facility operational details and considerations of science goals. How can changes and modification of diagnostic configurations during the shot day, relative to what was discussed in the initial plan, impact shot execution, and what conflicts or incompatibilities may arise?

The idea was proposed of having the option of starting the discussion process with relevant personnel in the facility several months ahead of time to detail the experimental proposal for the shots.

This is currently being done as the result of submitting the detailed experimental proposal two months ahead of the planned time. OMEGA and OMEGA EP users would like to have the option of starting this discussion process earlier or have alternative avenues available to them to address these issues.

(b) Another point of common concern is that of calibrating and characterizing diagnostics available on OMEGA and OMEGA EP. Flat fielding of streak and framing cameras is a typical example relevant to many users but certainly not the only one. The performance of streak and framing cameras has a broad impact on experiments since they are used in a variety of experimental campaigns, in different ways, to record valuable time-resolved data. Currently, users have to plan for characterizing and flat fielding these cameras as part of their own shot campaigns. The information they produce in this regard is potentially useful to many users. It would be more efficient and effective if this information could be made available to users on a standard basis and if it could be generated in such a way that it would not tax the shots dedicated to a given science campaign; i.e., it would not require dedicated shots allocated to a user that could have otherwise been used to address a science point. Two possible ways to address this issue were discussed. Characterization and flat fielding of streak and framing cameras could be done as a ride-along task; this would require planning and organization so that opportunities are not missed and sufficient and reliable information is recorded to achieve this goal. The facility could dedicate shots to perform this task or could include it as part of their regular facility maintenance.

Regardless of the way in which it is done, it was clear from discussions that there is a strong consensus among users

that characterizing and calibrating diagnostics available on OMEGA and OMEGA EP is an important point that affects many users and a critical issue that must be addressed.

(c) Evaluating and assessing the facility performance and the experimental campaign was an important topic of discussion since it provides an opportunity for users to convey feedback and comments to the facility management. Current procedures on OMEGA include an Effectiveness Assessment form that must be returned by the principal investigator (PI) to the Shot Director after each shot and an Experimental Critique sheet that is submitted during the week subsequent to the week of the shots. The sense among users was that, while there is value in the feedback provided in the Effectiveness Assessment form, this is done under pressure and too hurried. The quality of the feedback and comments provided in the Experimental Critique sheet is better the week after the shots. A thorough assessment of the experimental campaign, including the quality and quantity of the data recorded and how well the science goals were achieved, is something that often requires considerably more time.

OLUG recommends having the option to provide feedback on the experimental campaign, including facility performance, target fabrication, and level of accomplishment of science goals a few months after the shots. This feedback is likely to be the most accurate and realistic. The idea was also suggested to provide a place on the OMEGA web site accessible by users (via log-in and password) indicating the current status of OMEGA and OMEGA EP diagnostics.

(d) Better and more-complete information about the instruments and diagnostics available on OMEGA and OMEGA EP is needed.

This could be accomplished by establishing links in suitable web pages on the OMEGA web site, including (but not limited to) Shot Request Forms (SRF's), to internal reports and journal papers that document the details of instruments and diagnostics.

(e) The role that C. Sorce plays in LLNL experimental campaigns as a technical link between scientists (PI's) and facility engineers and technicians has been noted and praised by many users not involved in LLNL campaigns.

It was suggested that it would be useful to have a similar resource person to perform that task for all experimental campaigns.

(f) *OLUG recommends the continued use of Be in OMEGA and OMEGA EP shots.*

(g) *OLUG recommends additional office space be allocated for (outside) users when they are visiting and preparing for their shots.*

(h) *OLUG recommends that space be provided on the OMEGA web site to post information of common interest to many users as well as to establish web pages for areas of interest for groups of users, e.g., Thomson scattering, x-ray spectroscopy, particle measurements, etc.*

5. Information Flow

This topic involves better communication with Omega Facility users. In general, there is very good communication between LLE and users; however, the amount of information required for a successful campaign on OMEGA is very large. The suggestions represent the distilled recommendations of the Users Group to improve communication, *which is especially important for new users or those who have no LLE collaborators*.

a. Diagnostics: Just as the laser-pulse-shape "Help" page describes choices for laser pulses, a "Help" page for diagnostics would be of great benefit. This might be accomplished with an upgrade to the ***Diagnostic Status*** link on the OMEGA operations page. To the list of "Diagnostic Name" and "Lead Scientist," etc., the *upgrade* would add a brief description (a couple of sentences) of available SRF choices and links to published papers employing the diagnostic. For x-ray imagers, the page could list the date of the last flat fielding.

- If possible, a search-engine capability for diagnostics is attractive because it could enable would-be users to find out *who has recently used or is planning to use* specific diagnostics. The search could cover all SRF's within a +2/–1-month window with the idea of returning the names of PI's (who composed the SRF's) so that potential users of that diagnostic could contact them regarding how well it functioned and exchange details of actual/intended use. This should not violate accessibility/restriction of SRF's to users who may not be authorized to view an SRF in totality but is intended only to better communicate reasonable knowledge from one user to another. A corollary to this is an LLE-sponsored blog or "wiki" for areas of user interest, e.g., x-ray Thomson scattering or x-ray framing cameras.

- A new LLE notification procedure concerning *diagnostic status* would benefit users. Just like Laboratory staff are notified when credit for various training courses necessary for employment is about to expire, PI's could be notified if a primary diagnostic for their upcoming campaign becomes "unavailable." The implementation for this might involve automated email to all PI's for shots for the next ~2 months (a time period to be determined) when a diagnostic goes "off line." This may result in an increase of email to PI's who are not interested but could result in a reduction of surprises to PI's who are counting on using a particular diagnostic for future shots for which SRF's have not yet been created.

- Not all diagnostics are LLE diagnostics. Occasionally, it is desirable to test or flat field a user's diagnostic prior to the user's shot day. One means through which this might be accomplished is to provide an "empty-TIM" web page. Similar to the *Diagnostic Status* page, this page would list all empty TIM's for shots occurring during the next quarter. It could list the shot PI, the campaign, the target characteristics, and the laser energy on target. The intent is to make possible the *ride-along* testing of a user's diagnostic. Such multiplexing of experiments may increase the overall productivity of the facility. For example: the "neutron days" often conducted by V. Yu. Glebov attract a host of users with various TIM diagnostics that benefit from testing; the pointing shots conducted for LLE cryo shots can also be used in a similar way. If a user's imaging diagnostic or spectrometer can be fielded as a ride-along, or an x-ray flat fielding can be accomplished without costing a shot, this would increase productivity.

b. OMEGA EP Information: A high level of enthusiasm for OMEGA EP exists. Although it is recognized that OMEGA EP is a work in progress, the users' community is eager for status reports on OMEGA EP. OLUG recommends that, as soon as is practical, members of the users' group receive updates on OMEGA EP pulse-shaping capabilities, including

- minimum pulse length
- energy limits in relation to pulse width
- OMEGA EP contrast
- blast-shield status
- energy/power/focusability limits with blast shields

c. Miscellaneous: Similar updates are desirable for other OMEGA systems:

- phase-plate availability and numbers for both the 60-beam OMEGA and OMEGA EP
- DT-fill capability, especially with regard to changes in procedure that may affect LLE's ability to fill and field targets

6. Broader Issues

The Executive Committee, while recognizing that this issue is outside the scope of this report, expressed concern about the absence of direct support for diagnostic development at universities in general. This has an exacerbating effect on hands-on training in an era of increasingly formal facility operations. This issue is especially important to students and postdocs.

There is a general need for more small facilities as staging grounds for hands-on training, diagnostics, and experiment development. Again, students and postdocs are significantly impacted by this circumstance.

With regard to related research at other facilities, OLUG recommends that we proceed with the HIPER/US workshop to promote joint and complementary research on HEDP physics. In a similar vein, efforts should be made to coordinate and promote complementary physics research among Omega and other important HED laser facilities such as the NIF, LULI, RAL, Trident, and Texas PW. Through such coordinated activities and research, there are substantial opportunities to significantly advance the science of high-energy-density physics.

Initial Response of Omega Management to Findings and Recommendations

1. Introduction

LLE Management responded to the OLUG recommendations. Their response below was written on 1 May 2009. Since then, ongoing progress and updates have occurred and will be reported at the Atlanta APS Meeting (3 November 2009) and at the next Users Workshop. In addition, Omega management is meeting bimonthly with members of the OLUG Executive Committee to assess progress toward achieving these objectives.

2. OMEGA (60 beams)

(a) Penalty and conflict information would be helpful: e.g., pointing, framing-camera moves, phase plates, etc.

LLE Response: The LLE web site will be modified to make it easier to find this type of information.

(b) It would be desirable to be able to drive any legs from any driver, which has become a major problem for x-ray Thomson scattering.

LLE Response: Will submit a project in FY10 for evaluation. Cost and schedule are currently unknown. Significant resources are likely to be required.

(c) More static x-ray pinhole cameras would be helpful.

LLE Response: OMEGA H8 camera is now operational. LLE will evaluate target chamber (TC) port allocation for possible addition of fixed PHC's. It may be possible to deploy two or three decommissioned units.

(d) Spherical crystal imaging (diagnostic) would be a very useful diagnostic.

LLE Response: A crystal-imager project has been proposed by LLE for OMEGA EP but deferred until FY10. LLE is reviewing the requirements and benefits, but there are concerns that with the high energy of the OMEGA EP beams, significant target heating could shift the K-shell lines out of the imager-wavelength acceptance band. Any suggestions for system requirements are welcome from OLUG. There are currently no plans to provide a crystal imager for OMEGA.

3. OMEGA EP

(a) Phase plates with 1-mm spot size are essential to a number of users.

LLE Response: Two phase plates will be available starting in FY10. Four more substrates are on order and will be made into phase plates by FY11.

(b) SSD will also matter for a number of possible experiments.

LLE Response: SSD is not planned for OMEGA EP except on the NIF PAM (in mid-FY10), which will be able to feed Beam 3. Implementing SSD on additional beamlines would require significant resources.

(c) OLUG strongly endorses adding a simultaneous SOP to ASBO.

LLE Response: SOP cabinet location and beam path are part of the OMEGA EP ASBO design package. LLE believes that it has identified a streak camera for the SOP and, if available, will install it on OMEGA EP later in FY09 or early in FY10.

(d) Pulse-shaping equivalent to NIF capability will help a number of users (100 ps to 30 ns).

LLE Response: Current architecture does not support >10-ns operation. LLE is evaluating possible strategies to provide this capability as well as shorter pulses. Operating with individual beam-pulse durations greater than 10 ns will, however, require a significant redesign of the front end in addition to significant resources.

(e) Spherical crystal imaging would be very helpful.

LLE Response: A crystal-imager project has been proposed by LLE for OMEGA EP but has been deferred until FY10. LLE is reviewing the requirements and benefits, but there are concerns that with the high energy of the OMEGA EP beams, significant target heating could shift the K-shell lines out of the imager-wavelength acceptance band. Any suggestions for system requirements are welcome from OLUG. There are currently no plans to provide a crystal imager for OMEGA

(f) Low-energy probe beams would be helpful:

- 1ω chirped pulse via an air compressor to allow for adjustment;
- 2ω or 3ω would be better;
- up to 1 J would provide an x-ray option.

LLE Response: A fourth-harmonic probe is in development. It will provide a 10-ps (nonchirped) pulse of 20 mJ to 100 mJ at 263 nm. LLE's goal is to have the system installed in FY10, including light-collection optics that would allow for Schlieren imaging and grid refractometry. It will be on a fixed path in the plane, perpendicular to the backlighter direction, 60° from vertical.

(g) A record of experience with EMP versus the type of experiment, laser intensity, and diagnostics should be made available to users.

LLE Response: EMP signatures are currently collected on each short-pulse shot on OMEGA and OMEGA EP. Diagnostic EMI-related diagnostic failures are logged by the shot crew when encountered. We will organize and make this information available to users in the near future.

(h) Organized penalty and conflict information would be useful, e.g., blast shield.

LLE Response: LLE will organize and distribute this package shortly. It will also become available on the web site.

4. General User Issues

(a) Earlier assessment of conflicts or problems in the setup; e.g., it would be beneficial to have access to Scheduling Committee outputs six months in advance. Users also want to know what operational delays may be introduced by the initial plan.

LLE Response: Omega management staff are available for advance planning at the request of any user. Campaign proposals can be submitted at any time in advance of the two-month required date. Users can request an early evaluation of their proposal, although this will not include potential conflicts with other experiments the same week. Users should make this request to J. M. Soures.

(b) The need to establish a link to scientists/engineers/technicians as mentors (as C. Sorce does for LLNL).

LLE Response: LLE agrees with the need for this enhanced liaison function and will support to the limit of our resources. Specific requests are generally supported. Requests for links to LLE staff should be directed to J. M. Soures.

(c) Zero interframe timing for x-ray framing cameras would

- be a standard operating procedure each day
- be readily available on the web
- arrange calibration and testing as a dedicated instrument maintenance block of time

LLE Response: These operations currently occur as part of routine operations. We will make this information more readily available to the users in the near future through the web site. Calibration and testing where required for data analysis should be included in experiment planning.

(d) LLE should host wikis for areas of user interest, e.g., x-ray Thomson scattering, x-ray framing cameras, etc.

LLE Response: LLE could host a blog forum for users to discuss the status of operational diagnostics. Diagnostic status information is currently available on the web site. LLE will explore options that allow user dialogue.

(e) It is important to continue to use Be.

LLE Response: LLE expects to continue to support the use of Be at the Omega Facility. We are evaluating current regulations.

(f) Improved links to more information in SRF's and other material, especially for each diagnostic, including brief description, contact people, RSI or other reference, procedures, etc.

LLE Response: Improved documentation including an Equipment Qualification Package will be linked shortly via SRF web pages.

(g) Provide dedicated laboratory space for visiting groups:

- enable a user to make preparations without conflicts
- computer linkages in this laboratory or wherever preparations occur

LLE Response: Dedicated "side-lab" space is currently available in LLE rooms 175, 177, 182, and 6000 (OMEGA EP diagnostic workshop). Additional transient space is available upon request. Ethernet is available but must be pre-arranged. Note that space is limited.

(h) Comments on after-shot feedback process:

Quality is not entirely satisfying. The overall sense is that 20%, give or take, of the feedback is too hurried or pressured to be accurate. Issues like data quality are often not immediately clear.

- add "Shot Cycle Assessment" line to feedback form.

LLE Response:

- *The Experiment Effectiveness Assessment Form (EEAF) is used for tactical evaluation during shots by the shot crew. Best-effort feedback is the objective. Longer-term issues that take time to sort out should be included in the Experimental Critique one to two weeks after the campaign. If the information changes after the initial experimental critique is submitted, the user is encouraged to submit a revised critique.*

- *Users can review shot-cycle information, including cause and length of delays in real time on "OMEGA Availability" on the Operations web site. LLE is considering adding a "Comment" area for shot-cycle assessment to the EEAF.*

5. Information Flow

(a) Detailed information flow is a challenge, especially when strong internal connections are lacking, despite the fantastic job OMEGA is doing.

LLE Response: LLE is working on a presentation and table showing users how to use the database system to find specific shot-planning and analysis information.

(b) Put an "X-ray Framing Camera Status" and a "Streak Camera Status" page on the web for user access. Coordination and information flow for framing-camera flat fields and signal levels would also be very useful—to improve user planning (see wikis).

LLE Response: LLE could host a blog forum for users to discuss status of operational diagnostics. Diagnostic status information is currently available on the web site. LLE will explore options that allow user dialogue.

(c) Implement a search capability to enable all users to find out who has used or is planning to use specific diagnostics or other capabilities (including SRF's and PI's).

LLE Response: LLE will implement a "Recent Use" history database of each diagnostic that will be available to users.

(d) Implement automatic notification of diagnostic status during run up toward shots using this particular diagnostic.

LLE Response: Automated link to blog could be implemented. The best way to get this information, however, is for the users to read the Diagnostic Status page.

(e) There is a need for more information relating to changes in policy about DT fill, although, in general, users report good communication about policy changes.

LLE Response: Formal announcements of policy changes will be distributed via the Scheduling Committee. The committee meets biweekly (could the OLUG mailing list be used to distribute regular notices of changes in facility policy to users?).

(f) OMEGA EP information

- need focus, energy, and regular timing of update
- need to know, ASAP, focus ability versus energy through blast shields in OMEGA EP
- need to know, ASAP, contrast on OMEGA EP
- need to know status of TIM updates

LLE Response: LLE is actively developing the diagnostics to address these items. We want to make them available ASAP, subject to finite development time and resources. The LLE System Science staff believes that providing accurate information is extremely important and will release information only when they are confident that it is correct. They are actively working on these issues.

- Focus and energy operating envelope will be further explored in the coming months.
- Blast-shield use impact is being analyzed and will be disseminated when available.
- A high-contrast diagnostic is being deployed as a high priority.
- Initial capability is expected in FY09.
- TIM-10 and TIM-11 will be completed in Q4 FY09; TIM-15 is expected in Q1 FY10. Information will be posted on the Omega Laser Facility web page.

(g) Regular updates on phase-plate inventories and availability (both OMEGA and OMEGA EP) would be beneficial.

LLE Response: They will be selectable with far-field information on the SRF interface as soon as they are available. Much of this information already exists online in the DPP database.

6. Broader Issues

OLUG recommends consideration of the following issues:

(a) The absence of explicit support for diagnostic development in universities has an increasingly adverse effect on hands-on training in an area of increasingly formal facility operations.

(b) The availability of small facilities as staging grounds for hands-on training, diagnostics, and experiment development is a concern.

(c) OLUG encourages a HIPER/US workshop to promote joint and complementary research on HEDP physics.

LLE Response: These issues are beyond LLE's control, but LLE will work with NNSA to address them.

Findings and Recommendations of the Student/Postdoctoral Panel

OLUG Student/Postdoctoral Panel:

Ryan Rygg, Chair, Lawrence Livermore National Laboratory
Dan Casey, Massachusetts Institute of Technology
Carolyn Kuranz, University of Michigan
Hiroshi Sawada, University of California–San Diego
Louise Willingale, University of Michigan

A variety of topics were raised during the student/postdoctoral/new-user panel session at the OLUG meeting. Although the chance to perform experiments on OMEGA is a wonderful opportunity for students and postdocs, a number of issues are of particular concern for new users, especially those who are not members of groups with strong ties to LLE. In an effort to increase the effectiveness of experiments performed by students, postdocs, and other new users, the major areas of discussion are summarized below.

1. Information for New Users

Copious information about many aspects of OMEGA is available on the LLE web site. Navigating the web site to find relevant documents can be overwhelming for external users, however, partly because the information for external OMEGA users is intermingled with the much greater volume of information provided specifically for facility staff.

New users would benefit from a concise and easy-to-find overview of the location and purpose of relevant documents and resources. For example, the NLUF Users' Guide is a particularly useful resource, yet it is not well known by all external users and, in particular, would be hard to identify as a useful document for those new users not funded by NLUF.

Many also expressed a desire for readily accessible descriptions of available diagnostics. The current "Help" links from the SRF diagnostic pages are too cryptic to be very useful for inexperienced users, and the NLUF Users' Guide's diagnostics section is sometimes too far removed from the terse SRF labels to make it possible to evaluate which diagnostics are appropriate for a given experiment. It was proposed that a Diagnostic Summary page be provided (perhaps in parallel or perhaps merged with the Diagnostic Status page) that includes the diagnostic acronym, a two- to three-sentence description of its use and limitations, operational procedures, a link to relevant RSI papers, and examples of calibration or experimental data, if available. Links to this Diagnostic Description Summary page directly from the SRF form or SRF diagnostic Help page would also be useful.

In addition to a resource diagnostic summary, other information suggested as valuable on a *new users' summary page* includes concise (as compared to the 227-page NLUF Users' Guide) descriptions of the laser system's capabilities; tools to aid in experimental planning, such as delays incurred by laser or diagnostic-configuration changes; and a list of whom to contact with questions regarding various topics.

2. Engineering Liaison for External Users

One recommendation that was echoed in later sessions was to designate an engineering liaison for external users. OMEGA users are widely spread both nationally and internationally, and it is impractical for each group to have a representative at LLE for the weeks and months prior to a shot day to prepare and interface the experiment with the facility. These external users could share a designated representative who is familiar with the facility, knows of whom to ask which question, can perform some of the legwork in the weeks prior to shot day, and is up to date on the latest news/issues that may affect the experiment. The suggested archetype for this liaison is the role that C. Sorce currently performs for the national labs. In summary, students and postdocs would greatly benefit from contact with a designated junior technical staff member or liaison who could answer numerous questions.

3. Availability of Smaller Facilities

Finally, many expressed concerns regarding the continued availability of smaller-scale experimental facilities. Smaller-scale facilities provide a practical means of testing new diag-

nostics and experimental ideas prior to their implementation on OMEGA. In addition, they offer an opportunity for hands-on experience to students and postdocs in a relatively low stakes environment, where the cost of mistakes—an essential element of experience gain—is lessened.

Given OMEGA's limited experimental time and to help ascertain whether OMEGA is the proper facility, a list could be supplied of alternative smaller-scale experimental facilities for potential use for diagnostic and experimental development. Suggestions were also made to include the proposal process and deadlines, if any, for each facility in addition to the name, location, and description.

Conclusions and Future Workshops

This first OLUG workshop, with over 100 attendees, was the beginning of a process that will keep members of the inertial confinement fusion and high-energy-density physics communities involved in conversations and collaborations with each other and with the facility. OLUG Executive Committee members and facility management have been meeting on a bimonthly basis to assess progress, compatible with facility resources and impact, toward the implementation of the *Findings and Recommendations*. Progress will be reported on at a satellite meeting at the Atlanta APS Meeting (3 November 2009) and at the next OLUG Workshop.

The next Omega Lasers Users Group Workshop will be held at LLE on 28 April–1 May 2010. Significant financial support from NNSA has already been procured to help defray the cost of student and postdoc travel.

ACKNOWLEDGMENT

For capturing the ambiance and spirit of the workshop through his lens, we thank Eugene Kowaluk. We thank Irina Cashen, Sarah Frasier, Kathie Freson, Jenny Hamson, Karen Kiselycznyk, Katie Leyer, Jody Mayer, Lisa Stanzel, Jean Steve, and Jennifer Taylor for their gracious help and assistance. To NNSA, we gratefully acknowledge the financial assistance for student/postdoc travel expenses. We thank the University of Rochester's Fusion Science Center, which co-sponsors the OMEGA Users Group Workshops.

This updated review was compiled and edited by R. D. Petrasso (petrasso@psfc.mit.edu) of MIT's Plasma Science and Fusion Center with critical input and contributions by Workshop attendees, the Executive and Student/Postdoctoral Workshop Committees, and LLE management.

The Effect of Condensates and Inner Coatings on the Performance of Vacuum Hohlraum Targets

Introduction

Inertial confinement fusion (ICF) targets for the National Ignition Facility (NIF)[1] consist of a cryogenic capsule containing frozen deuterium–tritium (DT) fuel inside a gold or uranium hohlraum.[2] High-power laser beams enter the cylindrical hohlraum through a hole in each end cap, heating the interior to a temperature of ~300 eV (Ref. 3). This thermal radiation drives ablation of the capsule, causing it to implode and ignite the DT fuel. We report the results of experiments on the OMEGA laser[4] that support the national campaign to achieve ignition. These experiments used cryogenic hohlraums containing a sample of the ignition capsule ablator material and were driven to ~180 eV.

Although the primary purpose of these OMEGA experiments was to study the shock-timing technique for NIF ignition targets, we observed and identified the cause of an interesting discrepancy between the x-ray drive in cryogenic and identical room-temperature hohlraums. Namely, peak drive temperatures were 15% lower in cryogenic hohlraums than in identical warm hohlraums, and the temporal history of the drive was also changed. Furthermore, laser–plasma interaction processes produce hard x rays ($h\nu > 20$ keV) 100× more abundantly in cryogenic targets. Spatial nonuniformities in the x-ray emission were also observed within cryogenic hohlraums.

The reduced performance of the cryogenic targets resulted from the condensation of background gases on the inner walls of the cryogenic hohlraums. This was confirmed when hohlraum targets coated with thin (~2-μm) layers of CH reproduced the behavior of the cryogenic targets. The primary effect of low-Z coatings (CH and condensates) is the reduction of x-ray conversion efficiency within the hohlraum. They also produce longer plasma scale lengths that cause laser–plasma instabilities, which reduce the absorption of the drive laser and produce hot electrons and x rays. These finding are important to some non-ignition hohlraums that use low-Z liners[5–8] (or layers) on the inside hohlraum walls to tamp or resist the expansion of the laser-ablated wall material. In contrast, ignition hohlraums will be filled with a low-Z gas to keep the laser entrance hole open.[9,10] Windows are placed on the laser entrance holes to retain the gas; these windows also serve to protect the inside of the hohlraum from the deposition of condensates. Moreover, the NIF cryogenic targets are housed inside shrouds to minimize condensation until they open a few seconds before the shot. These OMEGA experiments confirm that eliminating condensation on cryogenic targets is crucial for optimal hohlraum performance.

Experimental Configuration

A series of experiments were performed on the OMEGA Laser System to demonstrate a technique to time the multiple shock waves in the ignition targets planned for the NIF.[11] This study used gold hohlraum targets with re-entrant cones to diagnose the shock-wave trajectories. The hohlraums were empty (also termed vacuum hohlraums): they contained no gas nor did they have windows on the laser entrance holes. Both warm and cryogenic targets were used in these experiments. (In the cryogenic targets, the liquid deuterium was confined to the re-entrant cones and did not enter the hohlraum.)

The hohlraums were made of 25-μm-thick Au, were 2.55 mm long and 1.6 mm in diameter, and contained 1.2-mm-diam laser entrance holes (LEH's). They were oriented along the P6–P7 axis of the OMEGA target chamber and driven with 38 OMEGA beams that had no beam smoothing (phase plates nor spectral dispersion) and were focused in three cones of beams (with different angles of incidence) in a standard configuration for hohlraums on OMEGA. The three cones of beams were five beams at 21°, five beams at 42°, and nine beams at 59° entering each end of the hohlraum (angles are relative to the hohlraum axis). These cones were each pointed along the hohlraum axis but outside the LEH by 0.725, 0.2, and 0 mm, respectively. They focused at 0.8, 0.5, and 0.0 mm (respectively) before these pointing positions. The drive pulse was a 2-ns temporally square pulse that produced spot intensities greater than 10^{14} W/cm^2 on the inner surface of the hohlraum. Figure 120.22 shows the hohlraum and drive-beam configuration with the x-ray and optical diagnostics used in the experiments.

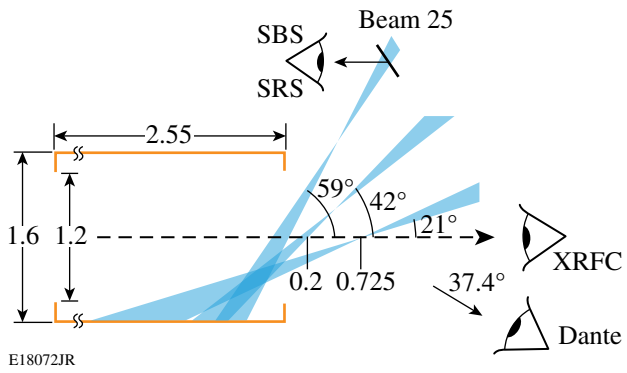

Figure 120.22
The experimental configuration where hohlraum targets are irradiated at each end by three cones of beams at 21°, 42°, and 59°. X-ray diagnostics viewed the hohlraum through the laser entrance hole and optical diagnostics detected light scattered back through Beam 25, a 59° beam.

These experiments employed a suite of diagnostics to monitor the performance of the hohlraums. The radiation temperature within the hohlraum was measured using the Dante diagnostic:[12–14] an array of 12 x-ray diode detectors filtered to provide the x-ray emission in various bands of x-ray energies. The responses of the detectors were absolutely calibrated (temporally and in x-ray energy) so the diode current could be converted into a temporal history of the x-ray flux in the energy band determined by the filtration. By fitting these multi-energy measurements to a blackbody distribution, one can determine the equivalent radiation temperature within the hohlraum as a function of time.[13,15] Another array of four x-ray photomultiplier tubes measured the integrated energy of hard x rays, i.e., those above cut-off energies of 20, 40, 60, and 80 keV (Ref. 16).

A framing x-ray pinhole camera[17] (XRFC) viewed the hohlraum along the hohlraum axis through the LEH. This device uses pinholes backed by both soft x-ray mirrors and x-ray filters to provide images of the hohlraum at x-ray energies of $h\nu$ = 0.5, 0.9, and 1.5 keV.

One of the drive-laser beams (Beam 25) has a diagnostic that records the temporal and spectral profiles of light reflected from the hohlraums back through the focus lens. This is done for two spectral regions: one near 351 nm (the drive-laser wavelength) and the other in the range 400 nm to 700 nm. These wavelength regions are used to diagnose the presence of stimulated Brillioun scattering (SBS) and stimulated Raman scattering (SRS), respectively. The total energy reflected back through the focus lens was measured with a calorimeter. These diagnostics were used to monitor the effects of nonlinear laser–plasma interaction processes that scatter the drive-laser light.

Radiation Temperature

In these experiments a distinct difference was observed in the behavior of warm (ambient temperature) and cryogenic ($T <$ 20 K) hohlraums. Figure 120.23 shows the radiation temperature (measured by Dante) in hohlraum targets as a function of laser drive energy. The upper red points are the measured peak radiation temperatures for warm hohlraums. The red curve is a $T_{rad} \alpha E^{0.25}$ power law fit to those data. All of these hohlraums had re-entrant diagnostic cones for the shock-timing experiments. In all but three, the tips of those cones were fitted with Be–Cu–Be sandwiches[11] that replicate the x-ray opacity of the ablator in an ignition capsule.[18] In Fig. 120.23, at ~12-kJ drive energy, three yellow squares show the radiation temperatures for identical hohlraum targets that had gold cone tips instead of

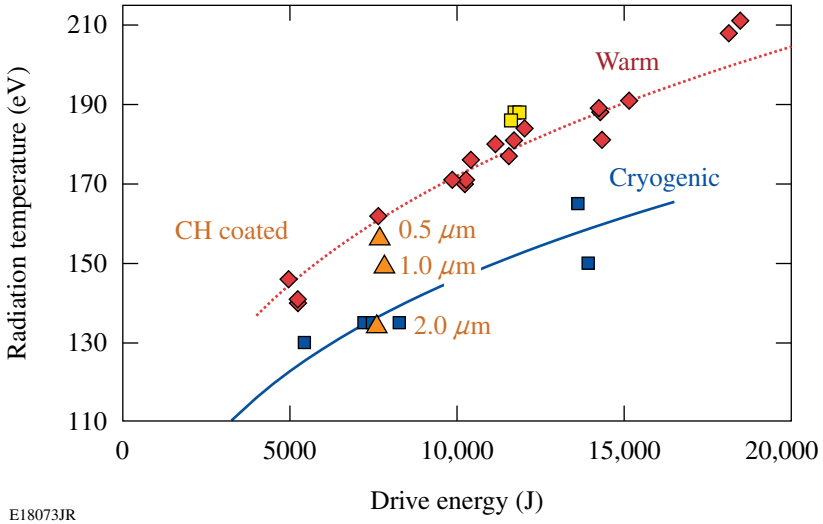

Figure 120.23
Hohlraum radiation temperature (as measured by Dante) as a function of drive-laser energy for warm hohlraums (red diamonds) and cryogenic hohlraums (blue squares). The red and blue curves are $T_{rad} \alpha E^{0.25}$ fit to the warm and cold data. The three yellow squares at 12 kJ are targets with cone tips made of gold instead of Be–Cu. The orange triangles are warm hohlraums coated with CH in the thicknesses shown.

the Be–Cu sandwiches. These gold-tipped targets show slightly higher radiation temperatures than the other warm targets, demonstrating the sensitivity of the radiation temperature to materials within the hohlraum. The Be–Cu sandwiches had a surface area that was ~10% of that of the hohlraum. The lower albedo of the Be surface reduces the x rays returned to the radiation field by that surface; therefore, when the Be sandwiches are replaced with gold, the radiation temperature rises.

The lower blue points and blue curve (again a $T_{rad} \alpha E^{0.25}$ fit) are the radiation temperatures for the cryogenic hohlraums. The hohlraums used for these data were identical to the ones discussed above: they were nominally empty and were fitted with the diagnostic cone. Liquid (cryogenic) deuterium filled the diagnostic cones but did not enter the hohlraum. The cryogenic targets show a 15% reduction in peak radiation temperature compared to identical warm ones.

Figure 120.24 shows the radiation temperature as a function of time for four experiments: two warm and two cryogenic. (The radiation temperatures plotted in Fig. 120.23 are the peak values of this type of data.) The upper bold and thin dotted lines are results for warm experiments performed at 14 kJ (shot 47240) and 7.5 kJ (shot 47241), respectively. These data exhibit the standard profile for radiation temperature produced by a 2-ns square pulse: an initial fast rise as hot, low-density plasma is created and the laser deposits energy into this plasma. This is followed by a slow rise as a thermal x-ray–driven Marshak wave[19] moves into the gold wall, producing a rise in the wall albedo. When the drive-laser pulse ends, the radiation temperature has peaked and the hohlraum begins to cool at a rate determined by its geometry and the total heated mass contained in the hohlraum. The warm experiments exhibit identical behavior, differing only in their magnitudes.

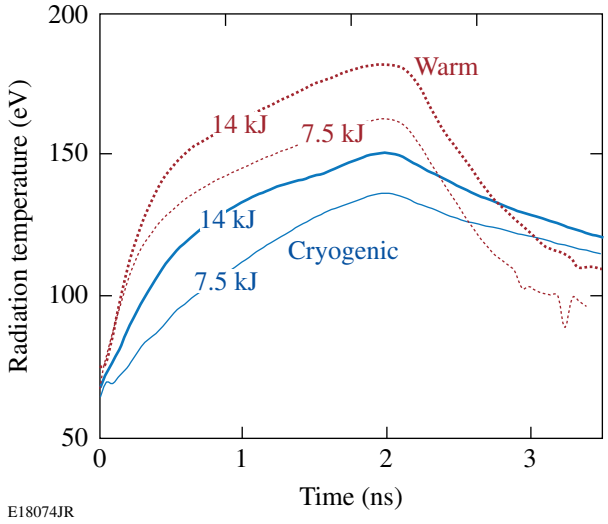

Figure 120.24
The temporal profile of the radiation temperature for four experiments: two warm targets (upper curves) at 14-kJ (bold dotted) and 7.5-kJ (thin dotted) drive energy and two cryogenic targets (lower curves) at 14-kJ (bold solid) and 7.5-kJ (thin solid) drive energy. The cryogenic targets show distinctly different behavior: lower rise times, lower peak temperatures, and decreased cooling rates.

The lower bold and thin solid curves are the radiation-temperature profiles for identical targets cooled to cryogenic temperatures and driven by similar energies [14 kJ (shot 48884) and 7.5 kJ (shot 48881)]. These shapes are distinctly different than the warm targets but are similar to each other. Their rate of rise is much slower, their peak temperatures are lower, and they cool at a significantly slower rate than the warm targets. The performance of the cryogenic hohlraums is reduced compared to warm ones: the peak temperatures are lower and the response time is slower.

Effect of CH Coatings

The differences between the warm and cryogenic targets appear to be the result of condensation layers that form on the inner walls of the cryogenic hohlraums. The cryogenic targets were mounted on the cold finger of a sizable cryogenic system[20] that connects to the OMEGA target chamber and has its own vacuum system. Targets were installed in the cryogenic system, which was evacuated (separately from the target chamber), and then the targets were cooled. As a result, the cryogenic hohlraum targets spent 20 to 50 min at temperatures below 70 K, where the pressure was $\geq 10^{-5}$ Torr. At these temperatures, background gases will condense on the cold surfaces. Residual gas analysis on the vacuum systems show that the background gases in these systems were comprised predominantly of water vapor, nitrogen, and oxygen.

In low-mass cryogenic targets, a protective shroud is frequently used to shield the target from thermal radiation. The cold surfaces of the shroud act as cryogenic pumps that produce lower pressure in the vicinity of the target. This reduces the level of background gas that can condense onto the cold target. The thermal mass of the cold finger for these hohlraums targets was sufficient to prevent heating by background radiation. For expediency the cryogenic hohlraum targets were fielded *without* a protective shroud. The targets easily maintained temperatures to produce liquid deuterium but were likely exposed to increased condensates. Simple estimates for condensation rates at the applicable pressures indicate that these targets could have had several microns of condensed material on them.

To test whether the behavior of the cryogenic targets resulted from condensation, hohlraums (identical to those described above) were lined with thin layers of parylene (CH) and irradiated in the same manner as the warm hohlraum targets. The results of three experiments with CH-lined targets are shown in Fig. 120.23 as orange triangles at ~7.8 kJ. Note that as the CH-coating thickness increases (0.5, 1.0, and 2.0 μm), the radiation temperature decreases, ultimately matching the cryogenic target results quite closely. This progression and the replication of the behavior of cryogenic targets are shown in Fig. 120.25 as another plot of radiation temperature as a function of time. The upper and lower curves are the thin curves from Fig. 120.24 for warm (red) and cryogenic (blue) targets. The data (orange) for the CH-lined target show that as the CH-coating thickness increases, the temporal profile better replicates the cryogenic target's behavior: The rate of rise decreases, the peak radiation temperature decreases, and the cooling time increases. The data for the 2-μm CH coating closely replicate the behavior of the cryogenic hohlraums, suggesting that the cryogenic targets have a condensation layer that is equivalent to ~2 μm of CH. [These CH-coated data are also consistent with previous results for hohlraums lined with 0.44 μm of CH (Ref. 21).]

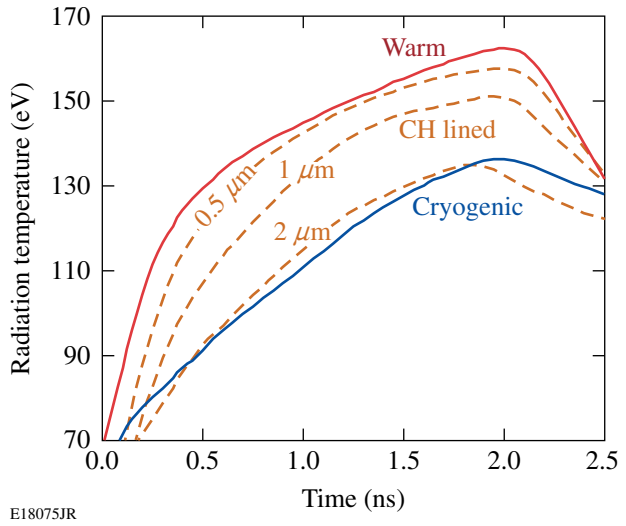

Figure 120.25
The effect of CH coatings on the temporal profiles of radiation temperatures. Profiles for warm and cryogenic hohlraums targets driven at 7.5 kJ are the red and blue curves (from Fig. 120.24). The orange curves depict the profiles for hohlraums with CH coatings of 0.5-, 1.0-, and 2.0-μm thicknesses.

X-Ray Emission

Figure 120.26 shows time-gated x-ray pinhole camera images of the targets, viewed through the LEH, for two shots: (a) a warm hohlraum driven by 14.2 kJ (shot 48879) and (b) a cryogenic hohlraum driven by 13.9 kJ (shot 48884). In both figures the left and right images were formed with 500-eV and 900-eV radiation, respectively. The center images were formed with radiation greater than 1.5 keV. For those lower-energy images, spectral discrimination was obtained with grazing-incidence mirrors; for the >1.5-keV image, a simple transmission filter was used. As a result, the left and right images are inverted (left for right) with respect to the center image. Note that the <1-keV x-ray images in both warm and cryogenic experiments are fairly uniform, as is the >1.5-keV x-ray image for the warm hohlraum. In contrast, the >1.5-keV x-ray image of the cryogenic hohlraum has significant structure.

The enlarged images are those at $h\nu > 1.5$ keV for (a) the warm and (b) the cryogenic experiments. The warm image has a fairly uniform emission profile within the hohlraum, and one can discern the outline of the lower-albedo Be cone tip. [For reference, Fig. 120.26(c) is an image of a hohlraum target through the LEH along the same direction as the framing camera that produced the images in Figs. 120.26(a) and 120.26(b).] The image of the cryogenic experiment exhibits strongly structured emission in radial spokes that are triangular in shape. This structure has a configuration similar to the pointing arrangement of a subset of the incident laser beams.

Three cones of laser beams enter the hohlraum through the LEH at angles of 21°, 42°, and 59° with respect to the hohlraum axis. The outer nine beams (at 59°) were pentagonally arranged with two beams on each edge (minus one beam not used in these experiments). Because of their steep angle of incidence, these beams are closest to the LEH and the x-ray emission from their spots is most visible from outside the hohlraum. Figure 120.26(d) is a simple drawing of the target and LEH showing the outer beams from their focal point (on the hohlraum axis) to the hohlraum wall. They are pointed at the center of the LEH but come to focus 0.8 mm before that point. The beams are diverging so the blowoff plasma flows into higher laser intensity as it expands off the hohlraum wall. Lastly, the low-Z material expanded more rapidly than the gold, therefore extending farther into the beam path.

The enlarged image in Fig. 120.26(b) shows the similarity to that beam configuration, with the dark areas representing the beam profiles where the x rays were created. Only eight beams appear in the image because one beam interacted obliquely with the diagnostic cone and had reduced x-ray brightness. X-ray images of the CH-lined targets exhibit spoke-like features similar to those in the cryogenic targets, as shown in Fig. 120.26(b).

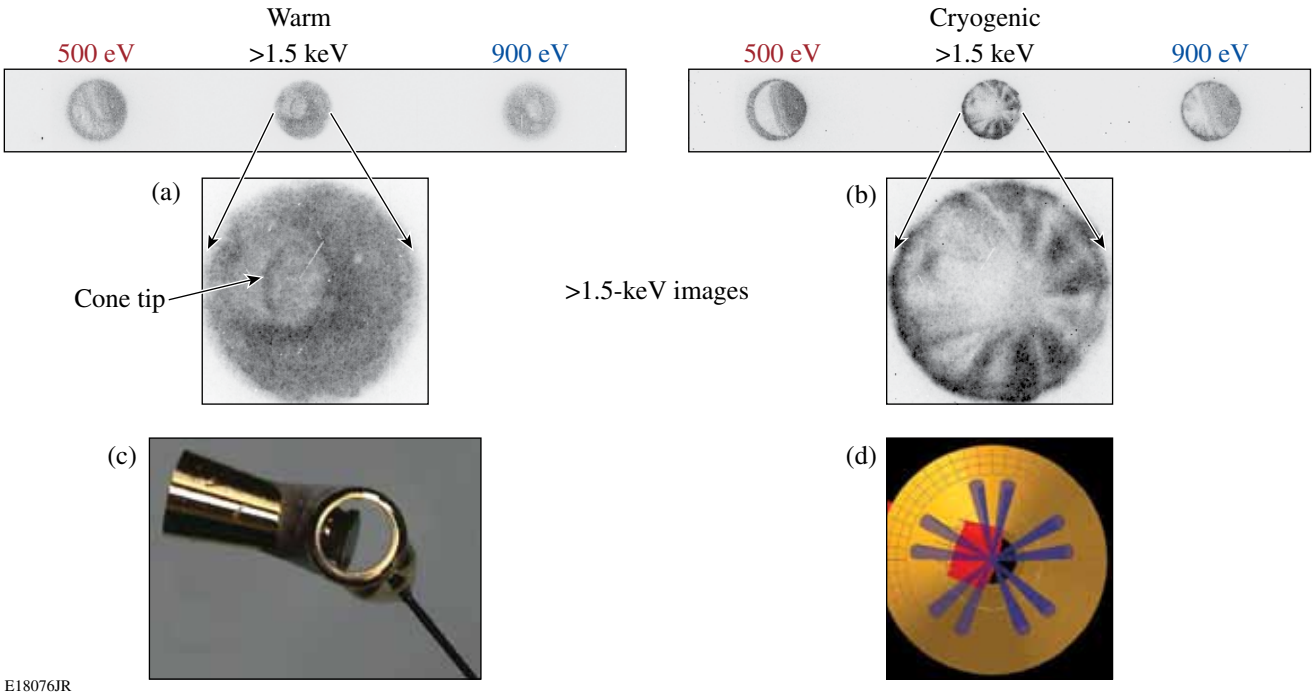

Figure 120.26
Framing x-ray pinhole camera images the hohlraum targets through the LEH and along the hohlraum axis for (a) a warm hohlraum target and (b) a cryogenic hohlraum target. The data for each comprise three images, each taken at 1.8 ns. The image on the left is 500-eV radiation and the right is 900-eV radiation. The center was radiated with $h\nu > 1.5$ keV. (The 1.5-keV images are expanded for clarity.) (c) Image of the hohlraum target through the LEH [at same view as that of Figs. 120.26(a) and 120.26(b)] showing the configuration of the hohlraum and VISAR cone. (d) Drawing of the LEH with the outlines of the outer cone of beams superposed. The x-ray emission in (b) has a similar structure.

Reflected Light and Hard X-Ray Measurements

The full-aperture backscatter diagnostics on Beam 25 (FABS25) resolve light scattered into the *f*/6 focusing optics temporally and spectrally in two wavelength bands, corresponding to stimulated Brillouin scattering (SBS, 351±2 nm) and stimulated Raman scattering (SRS, 400 nm to 700 nm). The temporal and spectral resolutions in these bands are typically ~40 ps and ~0.04 nm for the SBS channel and ~100 ps and ~15 nm for the SRS channel. All time-resolved spectra are shown in false-color images on logarithmic scales. The laser pulse shapes and the normalized, spectrally integrated scattered powers (Fig. 120.27) are superposed on the spectra in black and white, respectively. The SBS spectra also show a weak, narrow unshifted spectral component at 351 nm, caused by stray drive-laser light that misses the target.

Figure 120.27 shows SBS spectra for three hohlraum experiments: (a) a room-temperature hohlraum and (b) a cryogenic hohlraum, both driven at 14 kJ, and (c) a room-temperature hohlraum driven at 7.9 kJ. All hohlraum targets were gold and the hohlraum in Fig. 120.27(c) had a 2-μm layer of CH.

The corresponding SRS spectra are shown in Fig. 120.28. The intensity of Beam 25 at the LEH is estimated to be between 2 and 4×10^{15} W/cm^2. While a simple, uncoated gold hohlraum is not expected to have very much plasma near the LEH during most of the laser pulse, a hohlraum with low-Z layers (CH or condensates) may well have significant plasma near the LEH at early times. (This results from high-velocity blowoff from the hohlraum interior and from the edge of the LEH.) The highly blue shifted SBS signal early in Fig. 120.27(b) could result from a plasma that is rapidly expanding (highly supersonic) toward the laser. Alternatively, the incident light could be rapidly blue shifted as the result of a lateral influx of plasma into the beam.[22]

The broad bandwidth could be caused by strong coupling effects (high intensity near the LEH) but may also be associated with varying plasma conditions within the beam. The backscatter energies for both SBS and SRS for the three shots shown in Fig. 120.27 are given in Table 120.I, along with typical intensities at the LEH and at the hohlraum wall for Beam 25.

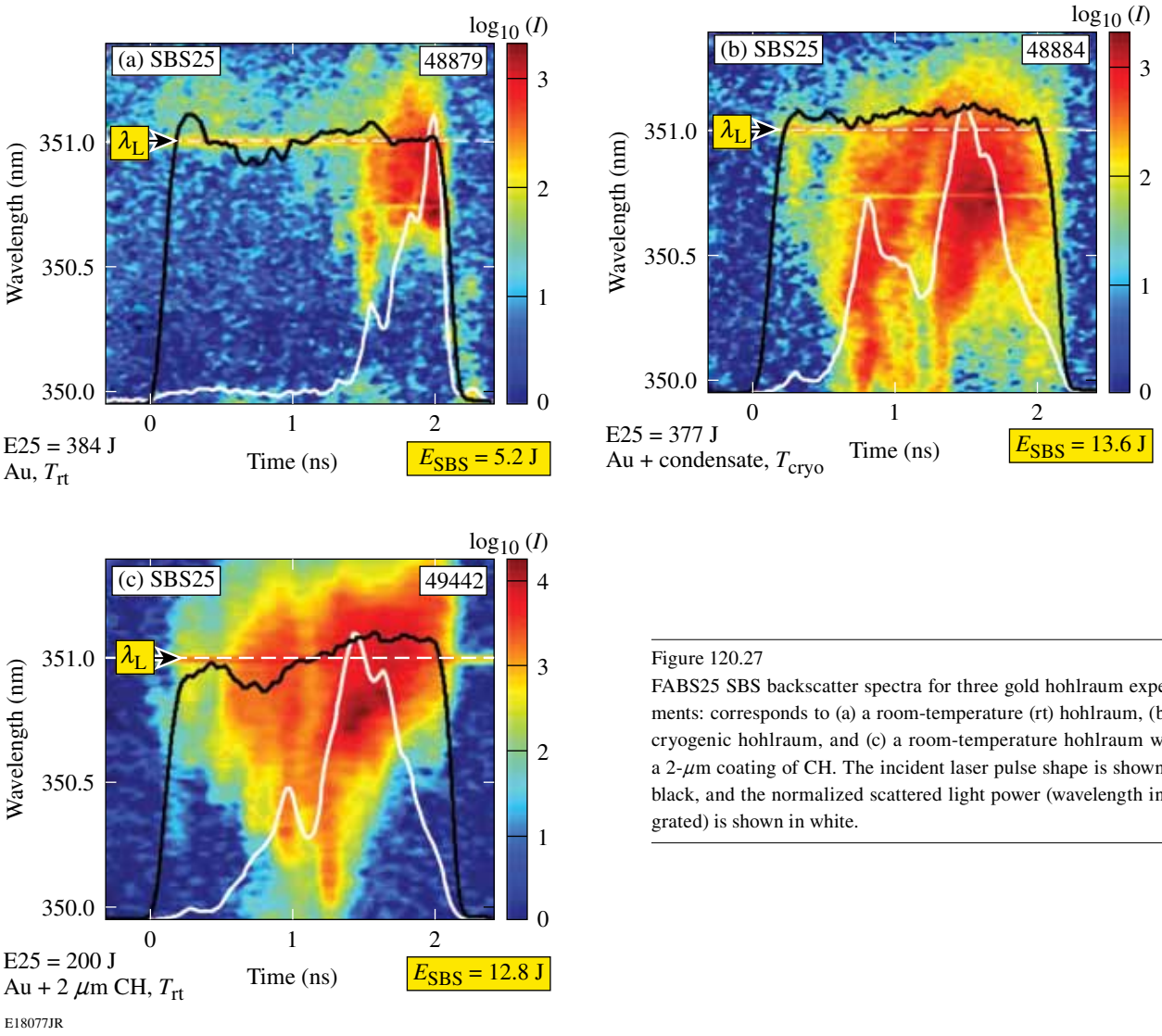

Figure 120.27
FABS25 SBS backscatter spectra for three gold hohlraum experiments: corresponds to (a) a room-temperature (rt) hohlraum, (b) a cryogenic hohlraum, and (c) a room-temperature hohlraum with a 2-μm coating of CH. The incident laser pulse shape is shown in black, and the normalized scattered light power (wavelength integrated) is shown in white.

Table 120.I: SBS and SRS backscatter energies and reflectivities.

Shot Number	I_{LEH}	I_{wall}	E_{SBS} (J)	E_{SRS} (J)
48879 (warm)	2 to 4 × 10^{15} W/cm^2	5 to 10 × 10^{14} W/cm^2	5 J (1.3%)	1.5 J (0.4%)
48884 (cryo)	2 to 4 × 10^{15} W/cm^2	5 to 10 × 10^{14} W/cm^2	13.6 J (3.6%)	19 J (5%)
49442 (CH-lined)	1 to 2 × 10^{15} W/cm^2	2 to 5 × 10^{14} W/cm^2	12.8 J (6.4%)	13 J (6.6%)

The SRS spectra indicate that the main part of this backscatter radiation emanates from density regions that are 12%–14% of n_c, where n_c is the critical density ($n_c = 10^{22}$ cm^{-3} for λ_L = 351 nm). [The wavelength scale shown in Fig. 120.28(a) was converted to a density scale in Fig. 120.28(c) based on the plasma-wave dispersion relation for $T_e = 2$ keV. The temperature correction is essentially negligible.] We conjecture that these relatively high densities are likely located close to the hohlraum wall inside the hohlraum and not at the LEH. There is extremely little SRS radiation for the room-temperature gold hohlraum, while significant SRS is observed for both the cryogenic gold hohlraum and the CH-coated room-temperature hohlraum.

Figure 120.29 shows the energy reflected back into Beam 25 as a function of incident beam energy. The warm, unlined hohlraums reflect 0.3%–1% of the beam energy, whereas the cryogenic and CH-lined hohlraums reflect 3%–7%. It is noteworthy that each of the CH thicknesses has the same high reflectivity as the cryogenic targets; no intermediate behavior for the thinner coatings is observed.

Figure 120.30 shows the total hard x-ray signal (in the $h\nu >$ 20-keV channel) as a function of total incident laser energy for the various targets. The hard x-ray signal increases dramatically (αE^7) above a threshold that depends on the type of target: For warm, unlined hohlraums, the hard x-ray signal does not reach 1 pC until the drive energy is ~7.6 kJ, whereas the cryogenic hohlraums reach that level at half that energy (3.8 kJ). For a given drive energy, the cryogenic hohlraums produce ~100× the hard x-ray flux of the warm, unlined hohlraums. The CH-lined targets show an increase in hard x-ray production as compared to the unlined hohlraums, with the thinnest CH

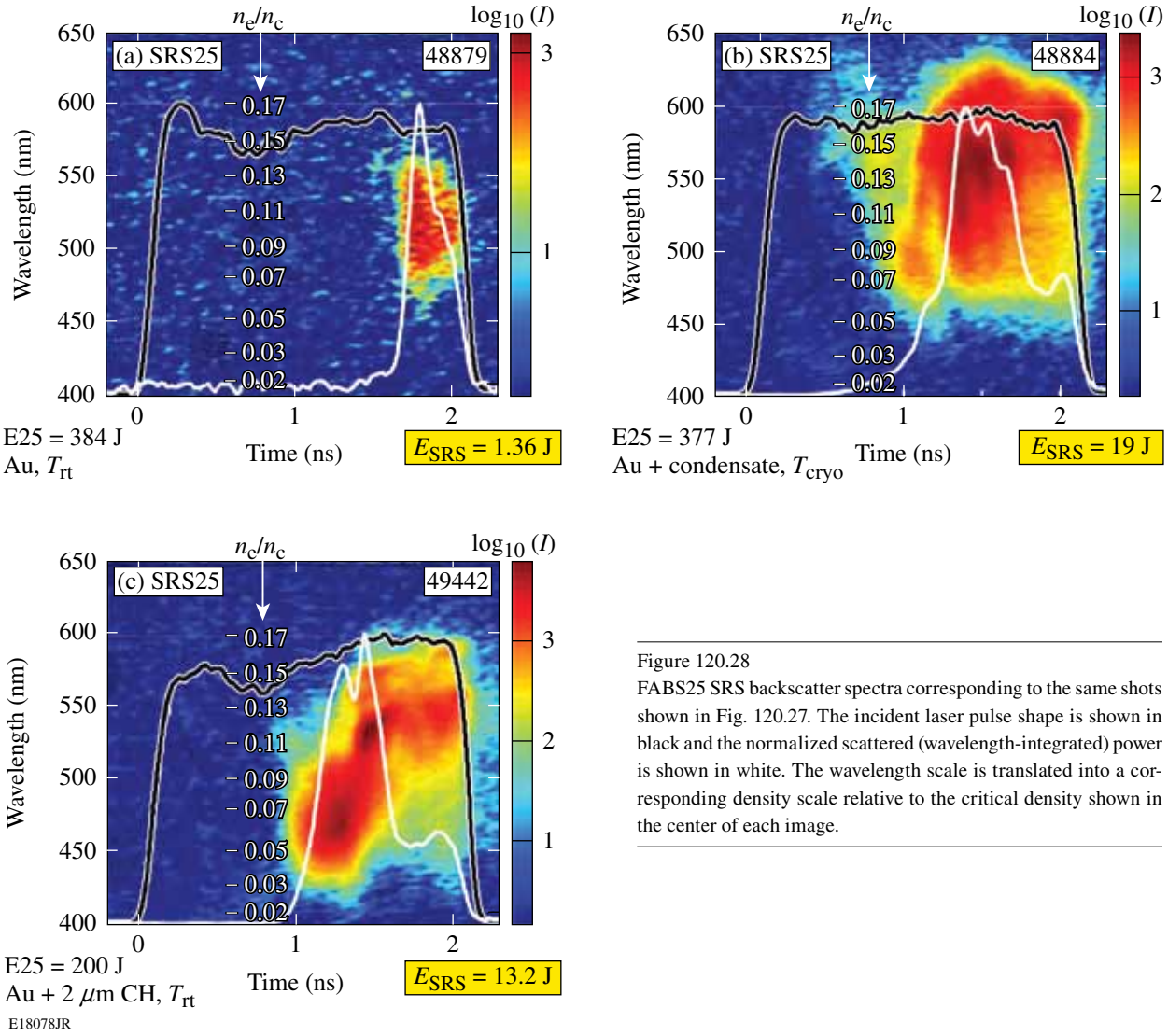

Figure 120.28
FABS25 SRS backscatter spectra corresponding to the same shots shown in Fig. 120.27. The incident laser pulse shape is shown in black and the normalized scattered (wavelength-integrated) power is shown in white. The wavelength scale is translated into a corresponding density scale relative to the critical density shown in the center of each image.

coating producing 10× that of the unlined targets. Increased CH thickness increases the hard x-ray production: the 2-μm case being 280× that of the uncoated warm target.

The radiation temperature results (Figs. 120.23 and 120.25) show that the CH-lined hohlraum replicates the behavior of the cryogenic hohlraums quite well. This effect is the result of the relatively low x-ray conversion efficiency of the low-Z materials (condensates and CH). Figures 120.29 and 120.30 show that there are some differences in the mechanisms by which condensates and CH coatings interact with the laser-scattered light and produce hard x rays. This is likely due to different materials (Z) of the two coatings affecting the plasma conditions and scale lengths. These laser–plasma coupling effects are small compared to that of the x-ray conversion but, nevertheless, can be important for the performance of hohlraum-driven targets because fast electrons and hard x rays are produced.

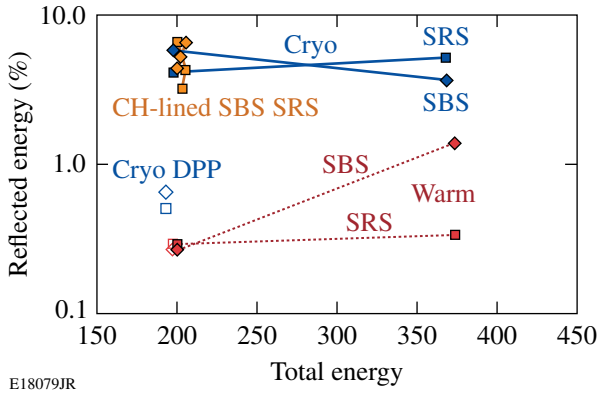

Figure 120.29
The reflected energy (% of incident) in Beam 25 as a function of energy and for various target types. The warm, unlined hohlraums reflect 0.3%–1% of the beam energy; the cryogenic and CH-lined hohlraums reflect 3%–7%.

Effect of Background Pressure

In one cryogenic experiment the target-cooling procedure was changed. Instead of cooling the target within the ancillary vacuum in the cryogenic system, the target was not cooled until it reached the center of the OMEGA target chamber, where the pressure was considerably lower. Figure 120.31 compares the radiation-temperature temporal profiles of a warm target (black), a cryogenic target cooled in the cart (blue), and a cryogenic target (shot 49453) cooled at the center of the target

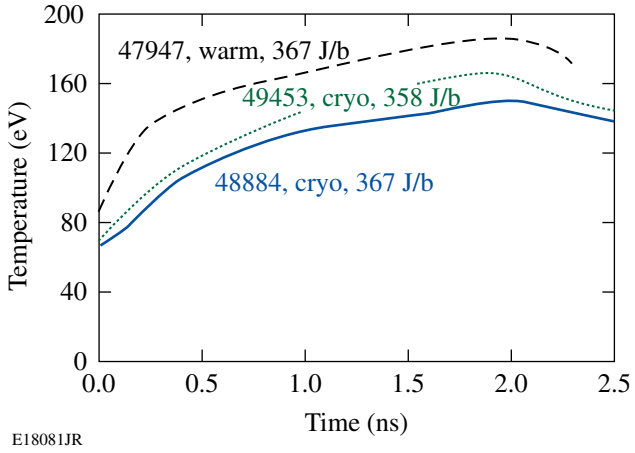

Figure 120.31
Radiation temperature temporal profiles for a warm target (black), a cryogenic target cooled in the cart (blue), and a cryogenic target cooled at the center of the target chamber (green). The cart has a higher background pressure than the target chamber and therefore a greater deposition rate for condensates.

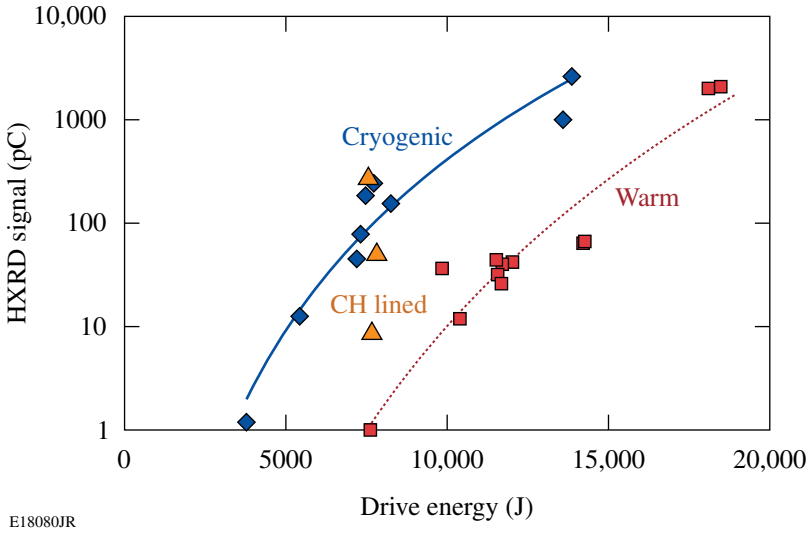

Figure 120.30
Hard x-ray signal (in the $h\nu > 20$-keV channel) as a function of total incident laser energy for the various targets. The cryogenic, CH-coated targets produce more hard x rays than the warm, uncoated targets. This is a result of the long-scale-length plasmas that are created when the low-Z coating is present.

chamber (green). The target cooled in the target chamber shows a higher peak radiation temperature, and its rate of rise and cooling rates are incrementally closer to the behavior of the warm target. The peak radiation temperatures for these two shots are the cryogenic target data at 14 kJ in Fig. 120.23. These data and the CH-coated–target data confirm that the reduced performance in the cryogenic targets results from the condensation of background gases inside the cryogenic hohlraums. In the case of shot 49453, the reduced background pressure reduced the deposition rate of condensate, producing a thinner layer within the hohlraum. This manifested itself as higher radiation temperature and a temporal profile that is closer to that of a warm hohlraum.

Effect of Focus Conditions

Laser-beam smoothing is used to enhance laser-target coupling and reduce laser–plasma instabilities. The results discussed above show that the reduced performance of cryogenic and coated hohlraum is due primarily to the presence of low-Z material and that laser–plasma coupling is less important. This is demonstrated by hohlraum experiments performed with different focal positions and with beams having distributed phase plates (DPP's)[23,24] in the drive-laser beams. In the former ("tight-focus case"), all of the targets were warm and all of the drive beams were pointed and focused at the center of the LEH. In the latter, the focus was the same as described above, but the beams were fitted with "elliptical" DPP's that produced circular spots at the LEH.[24] The results for these experiments are shown in Fig. 120.32, a repeat of Fig. 120.23 with green triangles depicting the tight-focus case and the open red (warm) and blue (cryogenic) points depicting data from experiments using the DPP's. Note that the tight-focus case exhibits a lower radiation temperature in the warm targets. This is likely due to increased scattered-light fractions associated with the high intensities produced at the LEH by this beam configuration. This conclusion is supported by the apparent scaling suggested by the points at higher drive energies, which have even lower radiation temperatures with respect to the standard-focus case. As the intensity (energy) increases, so do the effects of laser–plasma instabilities. For the DPP case, note that the open data points replicate the respective behaviors of warm and cryogenic targets. The radiation temperature is still lower for cryogenic targets. Refer back to Fig. 120.30 and note the open data points; they represent experiments with DPP's. Those data show that smoother beams (with DPP's) reduce the scattered-light fractions in cryogenic targets but do not alter the hard x-ray production. These data indicate that the scattered-light fraction plays a small role in the reduction in radiation temperature for cryogenic and CH-coated targets.

X-Ray Conversion Efficiency

The Dante diagnostic provides a direct measure of time-resolved x-ray power emitted from the hohlraum target. One of the most striking results of these experiments is that the x-ray energy radiated from the hohlraum lined with 2 μm of CH is a factor of 2 lower than that from an unlined hohlraum. This is observed in both the peak and the instantaneous fluxes (as in Figs. 120.23 and 120.25, respectively).

The data show that cryogenic targets reflect about 5%–7%, but this is insufficient to explain the 15% reduction in radiation temperature. The blackbody radiation temperature scales roughly as the one-fourth power of the energy absorbed by the hohlraum. To produce a 15% reduction in the radiation tem-

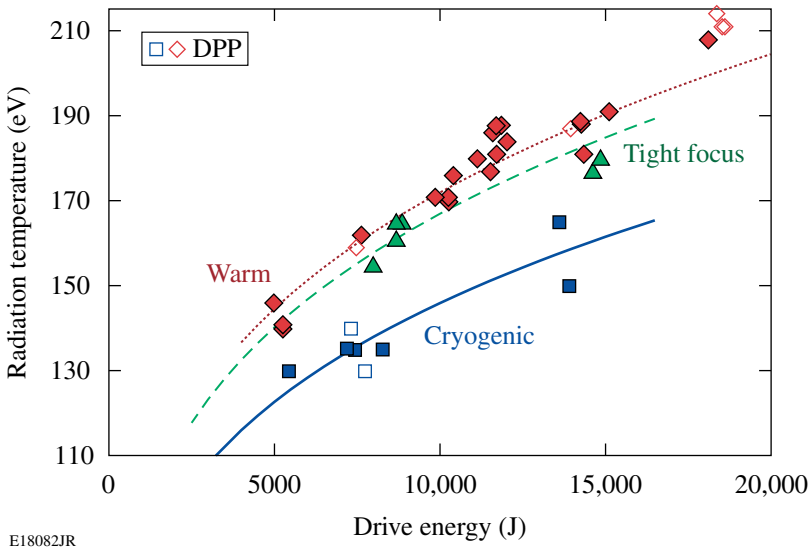

Figure 120.32
Radiation temperature versus drive energy (repeat of Fig. 120.23) with data for "tight-focus case" (green triangles) and for experiments using the DPP's with warm targets (red) and cryogenic targets (blue).

perature, the absorbed energy must be reduced to 50%. Instead, the reduction of radiation temperature is caused mainly by the addition of materials with low x-ray conversion efficiency. These materials interact with the laser and are heated but do not re-radiate x-ray energy as effectively as gold, so the radiation temperature is reduced.

Hohlraum targets have increased x-ray conversion efficiency[2,25] as compared to open (non-confined) targets, where the blowoff plasma is free to expand. In hohlraums, the plasma energy and mass accumulate within the hohlraum volume. Increased x-ray conversion efficiency results initially from the conversion of kinetic energy[26] but later is predominantly a result of emission from the accumulated material that is heated by the drive lasers. Experiments[27] show that the intensity of the x rays emitted from laser-irradiated plasmas in hohlraums is similar to that of open-geometry laser plasmas. The increase in hohlraum x-ray conversion efficiency, therefore, results from the confinement and heating of the gold blowoff plasma that creates larger regions of x-ray emission. When low-Z layers are added to hohlraums, they fill the hohlraum with a plasma that (a) does not emit x rays as efficiently as gold and (b) reduces the energy that ultimately reaches the gold wall. These significantly reduce the radiation temperature.

For the hohlraum radiation temperatures of interest in these experiments, the CH plasma (resulting from the 0.5- to 2.0-μm CH liners) provides little opacity to thermal x rays from the gold walls. The x-ray power invested in the heating of the gold hohlraum wall can be approximated by $(1-\alpha)\, A_w T^4$, where T is the hohlraum temperature, A_w is the wall area, and $(1-\alpha)$ is the absorbed x-ray fraction from the thermal-diffusion process [Eq. (2) of Ref. 28], based on the physics model for hohlraum energetics.[29] By implication, energy that is not radiated from the target, absorbed by the wall via penetration of the thermal wave, or directly backscattered from the target is therefore "lost" to the direct laser heating of the hot (>keV), low-density blowoff plasma. Figure 120.33 shows a plot comparing this lost energy for comparably driven hohlraums with bare Au walls and CH liner thicknesses of 0.5, 1.0, and 2.0 μm. In a hohlraum target, energy that directly heats the low-density, low-Z plasma constitutes inefficiency. A highly radiating plasma (e.g., gold) is advantageous, whereas a low-Z plasma tends to absorb the laser energy without significant re-radiation in the x-ray region. In Fig. 120.34, the measured radiation fluxes are recast into plots of x-ray conversion efficiency. It can be seen that the inferred x-ray conversion efficiencies reach levels as high as 85% in the unlined Au hohlraum but are reduced to as low as 50% in the hohlraum with the 2-μm CH liner.

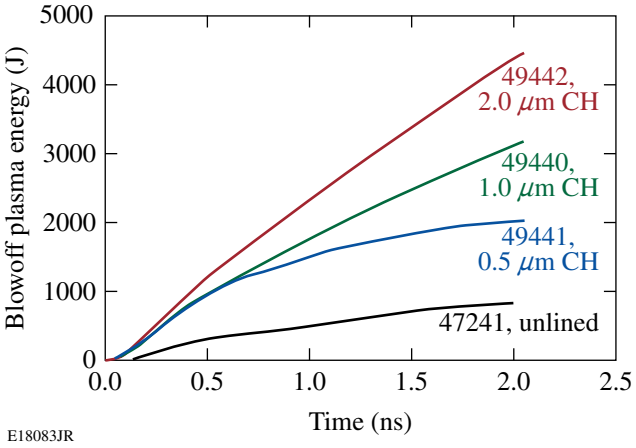

Figure 120.33
The plasma blow-off energy (or energy "lost") as a function of time for bare (black) and CH-coated (blue, green, and red) hohlraums.

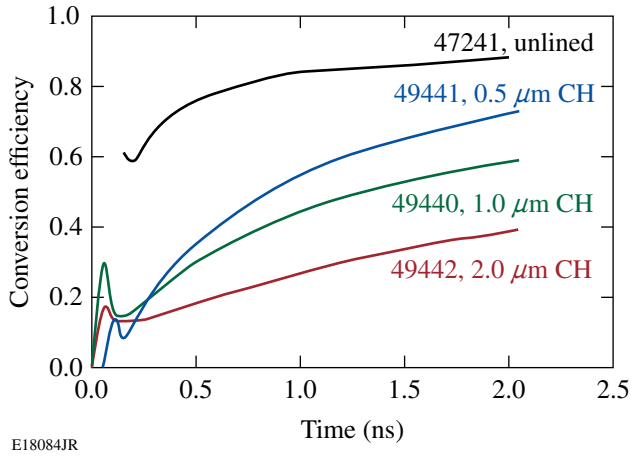

Figure 120.34
X-ray conversion efficiency as a function of time for bare (black) and CH-coated (blue, green, and red) hohlraums. Conversion efficiency is calculated from the x-ray flux (Dante) data.

Simulations

These experiments were simulated using the radiation–hydrodynamics code LASNEX.[30] Figure 120.35 shows the simulated radiation temperature as a function of time for four hohlraum experiments: (a) uncoated and [(b)–(d)] coated with 0.5, 1.0, and 2.0 μm of CH. The continuous curves are the simulations and the points (with error bars) are the Dante data. (These data are the warm and CH-lined data shown in Fig. 120.25 above.) The simulations model the radiation temperatures quite well. The magnitude and temporal behavior of each target are modeled as is the effect of CH coatings, where

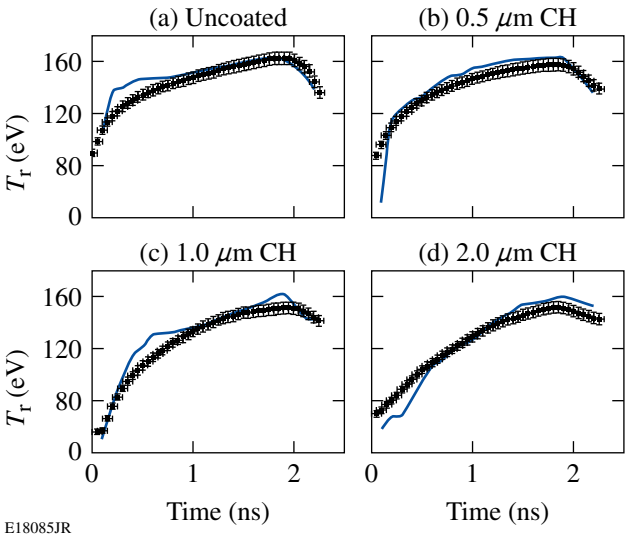

Figure 120.35
Simulation results for four warm hohlraum targets: (a) uncoated and coated with (b) 0.5, (c) 1.0, and (d) 2.0 μm of CH. Note that the behavior of these radiation temperature profiles is quite similar to the experiments depicted in Fig. 120.25.

the reduced rise time, lower peak radiation temperature, and slower temperature decrease are all replicated. The experimental scattered-light signals were input into the simulations, so the primary effect modeled here is the reduced x-ray conversion efficiency and the hydrodynamics of the liner material.

Summary

Experiments show that cryogenic vacuum hohlraums exhibit a significantly different behavior than identical warm hohlraums. The temporal profile of the radiation temperature for the cryogenic targets is changed with respect to the warm targets: early in the pulse the temperature rate of rise is lower, the peak temperature achieved is lower, and the cooling rate after the drive ceases is decreased. These observations are accompanied by significant changes in the x-ray emission structure within the hohlraum and by dramatic changes to the amount and character of the laser light that is reflected from the hohlraum.

For these experiments, the condensation of background gases onto the cold hohlraum surfaces is responsible for the degraded performance of the cryogenic hohlraums. This deposited material has lower x-ray conversion efficiency, which reduces the x-ray flux within the hohlraum. This affects the temporal rate of rise in the radiation temperature—its peak value. Experiments with identical warm hohlraum targets lined with 2 μm of CH replicated the behavior of the cryogenic hohlraum targets, confirming the effect of low-Z materials on the performance of hohlraum radiation temperature. The temporal profile of the radiation temperature in the lined targets was nearly identical to that of the cryogenic targets. This indicates that the cryogenic targets had a condensation layer equivalent to about 2 μm of CH, which is consistent with estimates for the background gas that were present in the cryogenic system.

In addition to these radiation effects, the absorption of the drive-laser energy is reduced as a result of increased scattering caused by SBS and SRS. These instabilities produce hot electrons and hard x rays that can be detrimental to the performance of ICF targets. The temporal and spectral features of reflected light in the CH-lined targets were similar to that of the cryogenic targets, again confirming that the cryogenic targets contained layers of low-Z condensation.

These results are useful because they demonstrate the effect that low-Z layers have on the performance of laser-driven hohlraums. These effects are important for vacuum hohlraums, i.e., those without LEH windows or fill gases within the hohlraum. Ignition hohlraums at the National Ignition Facility will have both and are expected to be immune to these effects because background gases will be unable to condense on the hohlraum's inner surfaces and the fill gas will be of low-enough density to have little effect on x-ray conversion.

ACKNOWLEDGMENT

This work was supported by the U.S. Department of Energy Office of Inertial Confinement Fusion under Cooperative Agreement No. DE-FC52-08NA28302, the University of Rochester, and the New York State Energy Research and Development Authority. The support of DOE does not constitute an endorsement by DOE of the views expressed in this article.

REFERENCES

1. J. A. Paisner, E. M. Campbell, and W. J. Hogan, Lawrence Livermore National Laboratory, Livermore, CA, Report UCRL-JC-117397, NTIS Order No. DE95010923 (1994). Copies may be obtained from the National Technical Information Service, Springfield, VA 22161.

2. J. D. Lindl *et al.*, Phys. Plasmas **11**, 339 (2004).

3. S. W. Haan *et al.*, Nucl. Fusion **44**, S171 (2004).

4. T. R. Boehly, D. L. Brown, R. S. Craxton, R. L. Keck, J. P. Knauer, J. H. Kelly, T. J. Kessler, S. A. Kumpan, S. J. Loucks, S. A. Letzring, F. J. Marshall, R. L. McCrory, S. F. B. Morse, W. Seka, J. M. Soures, and C. P. Verdon, Opt. Commun. **133**, 495 (1997).

5. J. D. Lindl, *Laser Program Annual Report 1978*, Lawrence Livermore National Laboratory, Livermore, CA, Report UCRL-50055-78, 2-77 (1978).

6. S. Pollaine, *Laser Program Annual Report 1988*, Lawrence Livermore National Laboratory, Livermore, CA, Report XDIV-90-0054, 246 (1988).

7. A. R. Thiessen, *Laser Program Annual Report 1988*, Lawrence Livermore National Laboratory, Livermore, CA, Report XDIV-90-0054 (1988).

8. S. Pollaine, *Laser Program Annual Report 1990/1991*, Lawrence Livermore National Laboratory, Livermore, CA, Report UCRL-LR-116901-90/91, 214 (1991).

9. S. W. Haan *et al.*, Phys. Plasmas **2**, 2480 (1995).

10. W. J. Krauser *et al.*, Phys. Plasmas **3**, 2084 (1996).

11. T. R. Boehly, D. H. Munro, P. M. Celliers, R. E. Olson, D. G. Hicks, V. N. Goncharov, G. W. Collins, H. F. Robey, S. X. Hu, J. A. Marozas, T. C. Sangster, O. L. Landen, and D. D. Meyerhofer, Phys. Plasmas **16**, 056302 (2009).

12. H. N. Kornblum, R. L. Kauffman, and J. A. Smith, Rev. Sci. Instrum. **57**, 2179 (1986).

13. C. Decker, R. E. Turner, O. L. Landen, L. J. Suter, H. N. Kornblum, B. A. Hammel, T. J. Murphy, J. Wallace, N. D. Delamater, P. Gobby, A. A. Hauer, G. R. Magelssen, J. A. Oertel, J. Knauer, F. J. Marshall, D. Bradley, W. Seka, and J. M. Soures, Phys. Rev. Lett. **79**, 1491 (1997).

14. C. Sorce *et al.*, Rev. Sci. Instrum. **77**, 10E518 (2006).

15. R. L. Kauffman *et al.*, Rev. Sci. Instrum. **66**, 678 (1995).

16. C. Stoeckl, V. Yu. Glebov, D. D. Meyerhofer, W. Seka, B. Yaakobi, R. P. J. Town, and J. D. Zuegel, Rev. Sci. Instrum. **72**, 1197 (2001).

17. D. K. Bradley *et al.*, Rev. Sci. Instrum. **66**, 716 (1995).

18. S. W. Haan *et al.*, Phys. Plasmas **12**, 056316 (2005).

19. R. E. Marshak, Phys. Fluids **1**, 24 (1958).

20. *LLE Review Quarterly Report* **103**, 128, Laboratory for Laser Energetics, University of Rochester, Rochester, NY, LLE Document No. DOE/SF/19460-626, NTIS Order No. PB2006-106675 (2005). Copies may be obtained from the National Technical Information Service, Springfield, VA 22161.

21. S. H. Batha and J. R. Fincke, Rev. Sci. Instrum. **75**, 3934 (2004).

22. T. Dewandre, J. R. Albritton, and E. A. Williams, Phys. Fluids **24**, 528 (1981).

23. Y. Lin, T. J. Kessler, and G. N. Lawrence, Opt. Lett. **20**, 764 (1995).

24. S. P. Regan, D. D. Meyerhofer, T. C. Sangster, R. Epstein, L. J. Suter, O. S. Jones, N. B. Meezan, M. D. Rosen, S. Dixit, C. Sorce, O. L. Landen, J. Schein, and E. L. Dewald, Bull. Am. Phys. Soc. **51**, 68 (2006).

25. L. J. Suter *et al.*, Phys. Plasmas **3**, 2057 (1996).

26. J. Massen, G. D. Tsakiris, and R. Sigel, Phys. Rev. E **48**, 2073 (1993).

27. F. Ze *et al.*, presented at the 1993 Topical Conference on Physics of Radiatively Driven ICF Targets, Monterey, CA (1993).

28. R. E. Olson *et al.*, Rev. Sci. Instrum. **74**, 2186 (2003).

29. M. D. Rosen, Phys. Plasmas **3**, 1803 (1996).

30. G. B. Zimmerman and W. L. Kruer, Comments Plasma Phys. Control. Fusion **2**, 51 (1975); J. A. Harte *et al.*, *ICF Quarterly Report: Special Issue: Computational Advances in ICF*, 150, Lawrence Livermore National Laboratory, Livermore, CA, Report UCRL-LR-105821-96-4 (1996).

Zirconia-Coated-Carbonyl-Iron-Particle–Based Magnetorheological Fluid for Polishing Optical Glasses and Ceramics

Introduction

Zirconia (ZrO_2) is a hard polishing abrasive used in conventional polishing of hard and soft glasses.[1] Monoclinic zirconia is the preferred crystalline form for glass polishing, although cubic zirconia is also used. Excellent removal rates and surface roughness values have been reported[2] for polymer [poly(arylene) ether] using 50 nm of zirconia in comparison to ceria (CeO_2), silicon oxide (SiO_2), and tin oxide (SnO_2). Fused silica (FS) polished with zirconia has been shown to leave surfaces that, upon laser damage testing in the UV and at 355 nm, exhibit superior damage resistance compared to surfaces polished with other abrasives.[3,4] Applications for such surfaces exist in UV/DUV/EUV lithography for the semiconductor wafer industry and in research laboratories that explore inertial confinement fusion. A polishing slurry consisting of a blend of zirconia and fumed silica was recently found to be optimal for chemical mechanical polishing (CMP) of a tetraethyl orthosilicate (TEOS) layer on a silicon wafer.[4,5] The advantages of using loose zirconia abrasives in conventional polishing are summarized by Menapace *et al.*[6]

Magnetorheological finishing (MRF) is a novel polishing technology that uses a magnetorheological (MR) fluid consisting of micron-sized magnetic carbonyl iron (CI) particles in an aqueous medium containing a nonmagnetic polishing abrasive like CeO_2 or nanodiamonds. MRF was commercialized in 1997 by QED Technologies[7,8] and is considered to be an excellent, deterministic process for finishing optics to high precision. A variety of computer numerically controlled (CNC) machines and MR fluids are used throughout the world on a regular basis.

In this article we report on a new development in MRF—a zirconia-coated magnetic CI powder. The coated CI particles are produced via a sol-gel synthesis process that has been scaled to kilogram (kg) quantities. The uniqueness of the MR fluid composition manufactured from this coated powder is twofold: first, free zirconia nanocrystalline abrasives are produced during the CI coating process, resulting (with the simple addition of water) in a self-polishing, abrasive-charged MR fluid for polishing; and second, the zirconia layer protects the CI particles from aqueous corrosion.

A zirconia-coated-CI–based MR fluid was designed, prepared, and circulated in an experimental MRF platform for a period of nearly three weeks with no signs of degradation or corrosion. A variety of optical glasses spanning a range of hardness values were tested, as well as several polycrystalline optical ceramics. In the following sections we briefly review MRF, MR fluids, and the issues of stability and corrosion. We then describe our zirconia-coated magnetic CI particle work and polishing experiments that validate the performance of this novel MR fluid.

Background

1. Magnetorheological (MR) Fluid

MR fluids are the key element of MRF technology.[9,10] In general, MR fluids consist of uniformly dispersed noncolloidal magnetic particles, e.g., CI, in a carrier fluid. Properties like plasticity, elasticity, and apparent viscosity change with the application of a magnetic field. A typical MR fluid for MRF applications[11] is compatible with most optical substrates, providing relatively high removal rates and acceptable smoothing for precision optics applications, without the risk of scratching the workpiece surface with oversized abrasive particles, as may happen with a solid lap. Material removal is accomplished primarily by nonmagnetic abrasive particles incorporated in the MR fluid. Two current commercial options are either cerium oxide (CeO_2) or nanodiamonds. "The choice of nonmagnetic abrasive material is dictated by the physical properties (e.g., hardness) and chemical properties (e.g., chemical durability) of the workpiece to be finished."[11]

2. MRF Technology

MRF is a subaperture polishing process. For a conventional MRF setup, the MR fluid is pumped through a delivery system and ejected through a nozzle in the form of a ribbon onto a rotating vertical wheel. The ribbon stiffens upon passing into a region with a high magnetic field in the vicinity of the

workpiece. The MRF removal function is characterized by a D-shaped polishing spot in the zone of contact between the ribbon and the workpiece,[12] and the material removal rate is determined by the time of contact (e.g., dwell time) as well as other process and workpiece parameters.[9,13] The temperature of the MR fluid is controlled by a chiller normally set to ~20°C.

Shorey *et al.*,[13] DeGroote *et al.*,[12] and, most recently, Miao *et al.*[14] have reported on experiments performed on an MRF platform designated as a spot-taking machine (STM) with characteristics similar to those of a conventional MRF machine. The STM is limited to partial motion up and down into the MR fluid ribbon, under computer control, but without workpiece rotation capabilities. This permits one to take only MRF spots on a part. The STM fluid delivery system uses peristaltic pumps to limit exposure of the MR fluid to mechanical parts. The pump flow rate is thus slower in comparison to the centrifugal pumps used in many commercial MRF machines, but this configuration allows one to test different types of fluid compositions without the risk of damaging the fluid delivery system. The STM was used for all of the work reported here.

3. Stability of MR Fluids

The MRF removal function is very sensitive to the stability of the MR fluid. Changes in MR fluid properties can reduce the determinism of MRF over time (the nominal life time of a standard MR fluid is ~2 weeks compared to 3 to 4 months with a polyurethane polishing pad[15]). Stabilizers such as glycerol may be added[11] to improve fluid stability (i.e., control viscosity and keep both magnetic and nonmagnetic particles in suspension). For glass polishing, however, an excess amount of glycerol inhibits the water hydration at the workpiece surface that is needed to soften the glass surface.[16]

Even though the MR fluid has only limited exposure to the atmosphere, it can still absorb carbon dioxide, which lowers the pH of the fluid and contributes to the oxidation of CI.[11] Corrosion may cause the MR fluid to change its compositional properties, which subsequently result in an unpredictable MRF removal function. Using deionized (DI) water as the carrier fluid provides only a limited solution to the problem. The use of buffers such as sodium carbonate (Na_2CO_3) increases the fluid pH to ~10, resulting in a more-stable fluid. Na_2CO_3 reduced the corrosion problem sufficiently to make possible the development of a commercial MR fluid for MRF.[11]

Schinhaerl *et al.*[17] studied the stability of a commercial CeO_2-based MR fluid over a period of 6 weeks in terms of the fluid density and pH. They found that the fluid density (~3.6 kg/liter) was essentially unchanged over the course of 6 weeks and therefore was not a good indication of fluid stability/viability. The fluid pH decreased from ~11 after preparing the fluid (i.e., mixing the solids and the liquids) to ~9.6 after 3 days of circulating in the MRF machine. The reduction in pH was attributed to exposure to air (i.e., on the wheel, where the MR fluid ribbon was formed). The fluid was continuously collected off the wheel and pumped back into the fluid reservoir with very little additional change in pH over 6 weeks of use (without replenishing the fluid during the experiment). Removal rates for an N-BK7 flat disk dropped by ~50% from ~4.9 μm/min to ~2.4 μm/min after 6 weeks, but the resulting surface roughness was unchanged.

In a more recent study, Schinhaerl *et al.*[18] compared five different commercial diamond- and CeO_2-based MR fluids. The removal rate was studied for soft, medium, and hard optical substrates (SF57, N-BK7, and quartz, respectively). As expected, the removal rate scaled inversely with material hardness. Per Ref. 18, "The harder the material, the lower the removal rate. Diamond fluids cause a higher material removal (than) cerium oxide–based fluids." Each fluid exhibited a different flow rate, which was associated with different CI particle dispersion characteristics and/or different concentrations of CI. This may have had an effect on the resulting material removal characteristics (e.g., smoothness and amount of material removed).

4. Purposefully Modified MR Fluids for Unique Materials

A water-based MR fluid is used for most optical finishing applications. The commercial MR fluids contain nonmagnetic abrasives such as CeO_2 (C10) and diamonds (D20, D10, and D11) to enhance material removal and to control final surface roughness for a wide range of optical materials.[7] The development of modified fluid compositions that are compatible with a wider range of optical materials is summarized in this section.

Water-soluble crystals have important applications in optics. One example is potassium dihydrogen phosphate (KDP/KH_2PO_4), whose solubility is ~21.7 g/100 g of water at room temperature.[19] KDP is the only nonlinear, single-crystal electro-optical material that can be grown in sizes large enough for use as a switch or as a frequency converter in solid-state lasers that investigate inertial fusion, such as the OMEGA and OMEGA EP lasers at the University of Rochester's Laboratory for Laser Energetics (LLE) and the National Ignition Facility (NIF) at Lawrence Livermore National Laboratory

(LLNL). Arrasmith *et al.*[20] showed that a nonaqueous MR fluid, composed of 40-vol % CI, 0.05-vol % nanodiamonds, and ~60-vol % dicarboxylic ester (DAE), when used as the carrier fluids could successfully polish a previously diamond turned KDP part to an rms surface roughness of ~2 nm, removing all diamond-turning marks.

Substituting the conventional nonmagnetic abrasives in an MR fluid (i.e., CeO_2 or nanodiamonds) with other commercial polishing abrasives may result in improved surface smoothing of relatively soft materials. DeGroote *et al.*[21] reported on the use of 200-nm–sized monoclinic zirconia powder for smoothing surfaces of the polymer PMMA.

Kozhinova *et al.*[22] showed that an MR fluid containing mechanically soft CI (~4-μm diameter)[13] and alumina abrasives could yield improved surface roughness for chemical vapor deposition (CVD) polycrystalline zinc sulfide (ZnS). This chemically altered MR fluid composition also showed no significant dependence on the initial surface preparation (single-point diamond turning, pitch polishing, or deterministic microgrinding).

Zirconia Coating of CI Powders

Many coating and surface treatments applied to CI particles for use as MR fluids in industrial applications (e.g., vibration dampers,[23] clutches,[23] and actuating modules[24]) have achieved the following benefits: improved sedimentation stability, improved dispersability, improved oxidation and corrosion resistance, and stability at higher solids concentrations. Coating media that have been explored include nonmagnetic metals, ceramics, high-performance thermoplastics, thermosetting polymers, polyvinyl butyral,[25] polystyrene nanospheres,[26] silicon,[27] phosphates,[28] metal oxides like silica and zirconia, and combinations of some of the above.[29] Enhancement of the particle surface with nitrogen has also been reported.[30] Of the many coating application methods employed, the sol-gel method has often been used because it is suited to a variety of materials and offers excellent process control.[31–33]

Here we report on zirconia coating of CI [$d_{50} \sim 1.1$ μm (Ref. 34)] for MRF via a sol-gel technique. The synthesis process was successfully demonstrated to produce a thin layer of zirconia on the CI particle surface. The zirconia sol (pH ~ 1) was prepared at room temperature using a zirconia butoxide precursor and nitric acid as discussed in detail by Shen *et al.*[35] for batches of CI up to 50 g. In this work a modified synthesis protocol made it possible to coat kilogram quantities of CI by minimizing the total volume of solvent used, i.e., coating the maximum amount of CI in as little water as possible. This approach allowed us to increase the amount of solids in a batch (~200 g per batch) and minimize the number of batches needed to produce >3 kg of coated particles in less than 10 days. The synthesis procedure is further detailed in Appendix A.

1. Characterization

Characterization of CI in terms of coated particle surface morphology, density, particle-size distribution, and corrosion resistance under accelerated acidic conditions is discussed in this section. A brief description of the instrumentation used for particle characterization is also provided.

a. Morphology, size, and surface properties. Scanning electron microscopy (SEM) was used to obtain morphological data for uncoated and coated CI particles. Measurements were made with a thermal field-emission–type SEM (resolution 1.3 to 2.1 nm at 15- to 1-kV acceleration voltage, respectively).[36] Two types of samples were observed: free particles (uncoated and coated) and cross-sectioned particles (uncoated and coated). The technique for preparing particle cross sections using MRF is described in Appendix B.

Figure 120.36(a) shows uncoated CI particles ranging in size from ~0.5 to 2 μm. This distribution of particle sizes was consistent with the manufacturer's CI powder particle size distribution data [$d_{10} = 0.5$, $d_{50} = 1.1$, and $d_{90} = 2.2$ μm (Ref. 34)]. The particles are spherical and their surfaces are relatively smooth. Figure 120.36(b) shows a cross-sectional SEM image of uncoated particles, identifying three particles with particle size ranging from ~1 to 1.3 μm. No surface layers are apparent.

A coated CI particle (size ~1.4 μm) is shown in Fig. 120.36(c). There is a thin, rough zirconia layer over the particle surface. The top of this layer consists of overlapping nanocrystallites of faceted zirconia, ~50 to 100 nm in size. The cross-sectional SEM image of a coated particle reveals the coating to be continuous, with a thickness of 5% to 15% of the uncoated particle diameter [see Fig. 120.36(d), where the particle size is ~1.1 μm and the coating thickness is ~100 nm]. We hypothesize from this preliminary observation that the coating process does not increase the overall particle size of the powder by more than 5% to 15%.

Figure 120.36(e) shows nanocrystalline zirconia crystals adjacent to a coated CI particle. These free zirconia crystals are co-generated out of the precursor used during the synthesis process (see Appendix A). The crystals are relatively uniform in size (nominal size 10 to 50 nm). The crystals appear to exist

as agglomerates in this image. We hypothesize that within the environment of the STM delivery system (i.e., under mixing and shear) these agglomerates rapidly break up, producing a nanocrystalline, free zirconia-charged MR fluid for polishing. Attempts were made to separate the dried zirconia-coated CI powder into magnetic and nonmagnetic fractions, but these attempts failed. Zirconia coating and free zirconia crystals were identified by Shen *et al.*[35] using energy-dispersive x-ray spectroscopy (EDX) techniques, which agree with other work[37] on zirconia synthesis at low temperatures. From this point onward the term "zirconia-coated CI" refers to both the coated CI particles and the co-generated free nanocrystalline zirconia abrasives as one unit.

The faceted coating texture of the coated CI particles may also explain why the initially grey, uncoated CI powder appears black after processing. Zirconia powders are known to be white to off-white in color.[38] Roughening via light trapping to enhance absorption of visible light has been reported for single-crystal silicon in solar energy applications.[39] The silicon wafer's surface turns from metallic grey to black in appearance. We believe that this absorption phenomenon is manifest for our coated CI particles.

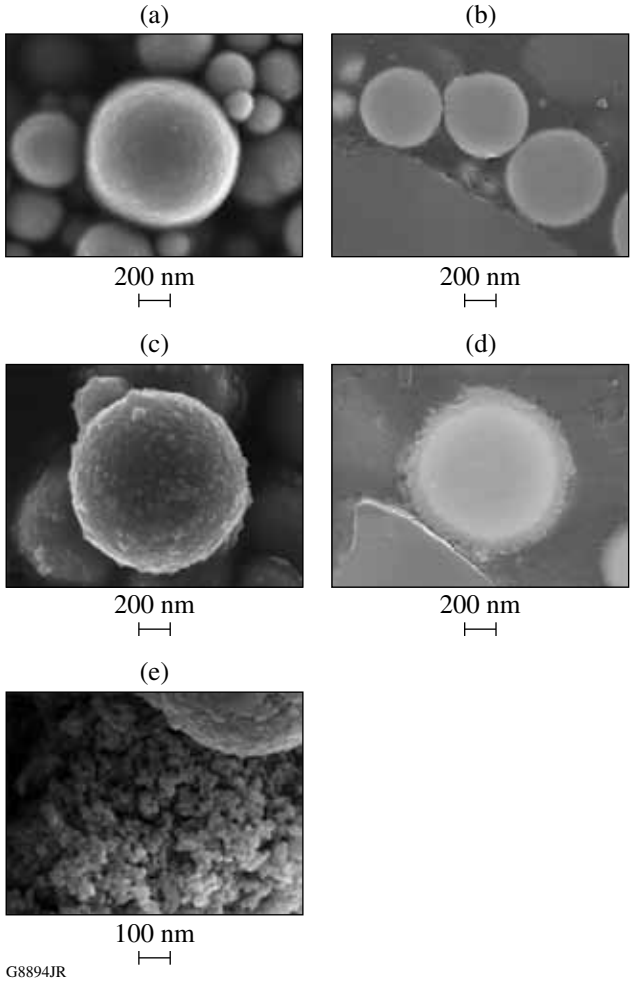

Figure 120.36
SEM images of uncoated CI (a) and zirconia-coated CI (c) and their cross sections [(b) and (d), respectively]; (e) free zirconia nanocrystals.

Contact angle testing was performed with a video microscope system[40] to investigate the affinity of the CI powder for water. Uncoated and coated CI powder samples were prepared as ~100-μm-thick dry films on glass microscope slides by a simple hand pressing/compacting process. A single drop of DI water (~4 μL) was placed on each film surface and viewed in the microscope. For both powder samples, the first drop was absorbed. However, when a second drop was deposited on the surface of the uncoated powder film at the same location, it resulted in a preserved drop whose contact angle was ~90°. Only with the deposition of four drops was it possible to measure a contact angle for the coated powder film, and the resulting contact angle was found to be ~12°. This test was repeated at several randomly chosen locations for each powder film with the same results. We conclude that the initially uncoated CI powder is hydrophobic and becomes hydrophilic after the sol-gel zirconia treatment process is applied.

b. Density. Density measurements were performed using a gas (helium) pycnometer at room temperature.[41] A sample of uncoated or coated CI powder was placed in a 1-cm^3 sample cup (stainless steel, provided by the manufacturer) and baked in vacuum (~432 mm Hg) at ~100°C for ~30 min. The sample was transferred to a desiccator and cooled down to room temperature before being measured. This minimized exposure to the atmosphere (~33% relative humidity). The density of uncoated CI was 7.68±0.04 g/cm^3 (average of 4 samples measured), a value consistent with that reported by the manufacturer (>7.5 g/cm^3 from Ref. 34). The density of the zirconia-coated CI was 6.72±0.07 cm^3 (average of 26 samples from eight 200-g batches). [The density of monoclinic zirconium oxide (ZrO_2) is ~5.7 g/cm^3].[42]

2. Accelerated Corrosion Resistance Test

Aqueous corrosion tests were conducted for uncoated and coated CI powders to provide a qualitative indication of coating coverage over the particle surface and to detect variations from batch to batch. Corrosion tests were conducted by preparing small batches of MR fluid, where each batch contained a mixture of 5 mL of an acetic acid–based aqueous solution (pH 4.4) and 1 g of CI particles (uncoated or coated). Each batch was stirred using a magnetic stirrer on a magnetic hot plate set

to 200 rpm and 30°C. While stirring, a 0.2-ml sample of the batch was extracted with a digital EDP rapid charger pipette (Rainin Instrument Co.) at intervals of 2, 5, 10, 20, 30 min, up to 1 h and then every several hours for up to 22 days. Extracted samples were deposited on a paper towel. The coloration of the towel provided a qualitative indication of the onset of corrosion.

Results are shown in Fig. 120.37(a) for the uncoated CI powder. A yellow/brownish-orange color was observed for the sample extracted from the acidic environment after 5 min. This coloration is consistent with that of goethite (FeOOH), a known product of corrosion.[43] Figure 120.37(b) shows the results obtained for samples taken from one batch of zirconia-coated CI. No corrosion products were observed, even after 530 h (22 days), at which time the test was terminated. Similar results were obtained for seven additional batches under the same testing conditions, suggesting that the coating completely covered the CI particles. Thermal gravimetric analysis in air at temperatures above 300°C (Ref. 35) showed improved resistance against oxidation for the zirconia-coated CI particles, supporting the qualitative results of this corrosion test.

(a)

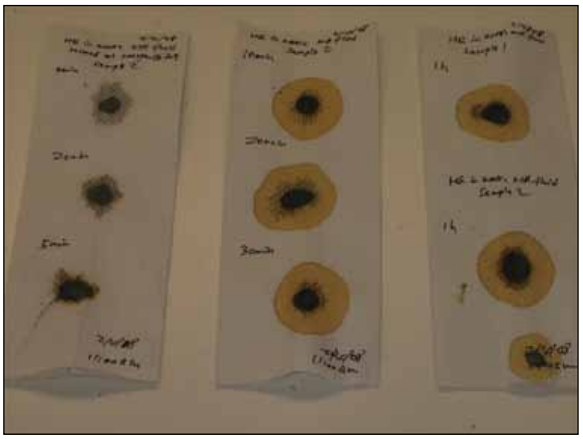

(b)

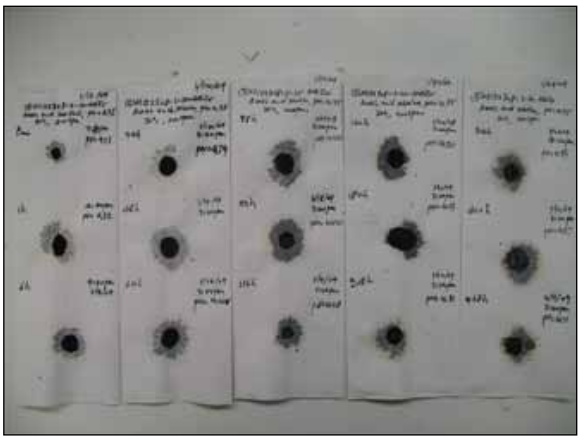

G8895JR

Figure 120.37
Images from a corrosion towel test: (a) uncoated CI up to ~1 h; (b) zirconia-coated CI up to ~530 h.

3. Design and Preparation of a Zirconia-Coated-CI-Particle–Based MR Fluid

Maximum removal rates are achieved for MR fluids whose magnetic CI particle concentrations are high. However, increasing the magnetic particle solids concentration also causes a rise in the out-of-field viscosity of the MR fluid. Off-line composition studies are required to determine how much CI can be incorporated into a carrier liquid without causing pump failure of the fluid delivery system. This section describes the development of high-solids-concentration, coated-CI-composition MR fluid using viscosity measurements and the techniques used to prepare a larger batch for experiments in the STM.

a. Viscosity. Off-line viscosity measurements were performed using a cone and plate–style viscometer, temperature stabilized at 25±0.5°C (Ref. 44). Several 15-ml batches of coated CI powder in DI water were prepared with solids concentrations of 35 vol % and 40 vol %. The coated powder was added to DI water in a series of small portions without any other dispersing agents. Hand shaking was performed for a portion, followed by high shear mixing at approximately 25,000 rpm for 5 min. This procedure was repeated in increments to elevate the solids concentration. Uniformly dispersed slurries were ultimately produced. Shortly after mixing, a 0.5-ml sample was extracted from a batch and injected into the viscometer for measurement. Viscosity as a function of shear rate from 50 s^{-1} to 1000 s^{-1} was recorded.

With this instrument it was not possible to measure the viscosity of a 40-vol %-coated-CI-particle MR fluid. Successful measurements were obtained at a 35-vol % solids concentration, where the fluid exhibited shear thinning behavior. Because the shear rate of the MR fluid leaving the nozzle of the STM was ~800 s^{-1}, attention was focused on the MR fluid viscosity at this shear rate. The 35-vol %–coated CI particle's viscosity at 800 s^{-1} was found to be 110±11 cP (average of three separate measurements). For comparison, 50-ml samples of commercial ceria–based and nanodiamond-based MR fluids were prepared and evaluated under identical conditions. Their viscosities at a shear rate of 800 s^{-1} were found to be 89±2 cP and 111±13 cP, respectively. It was concluded that a water–based, 35-vol %-solids-concentration, coated-CI-particle MR fluid could be successfully pumped and circulated in the STM.

b. MR fluid preparation. Using our synthesis process, we successfully produced >4 kg of zirconia-coated CI powder. However, only ~2.3 kg of powder was needed to prepare a sufficient volume of MR fluid (i.e., 1 liter) to begin tests on the STM. The composition that was prepared is given in Table 120.II.

Table 120.II: Composition of MR fluid based on zirconia-coated CI.

Component	Density (g/cm^3)	Mass (g)	Vol. (mL)	Vol %	Mass %
ZrO_2-coated CI	6.7	2345	350	35	78
DI water	1	650	650	65	22
Total		2995	1000	100	100

Incorporation of these hydrophilic particles into an aqueous suspension without the aid of a dispersing agent was difficult. To overcome this difficulty, the coated CI powder was slowly added to the water while mixing at ~1000 rpm (comparable to the mixing speeds used in the STM fluid reservoir) until a uniform slurry (as inspected by eye) was achieved. Then the fluid was transferred into the STM reservoir for continuous mixing while circulating in the STM delivery system in bypass mode for ~30 min before directing the fluid over the STM wheel to form a ribbon. Machine settings while in bypass mode were ~70 rpm for the pump and ~1000 rpm for the mixer, whereas after the fluid was directed over the wheel, the pump speed was increased to ~115 rpm, the mixer speed was unchanged, the wheel was set to rotate at ~200 rpm, and the electric current to the magnet was set at ~15 A (resulting in an ~2-kG fringing field strength). The resulting ribbon height was ~1.5 mm, which was kept constant by adjusting the pump speed as needed. Throughout the spotting experiment described on p. 199, constant part immersion at a depth of ~0.3 mm was used for all tested materials. Unless specified, all machine operating conditions were kept constant throughout the experiment.

Spotting Experiment

In this section we introduce the materials used for spotting experiments and the metrology used to characterize these samples [the MRF platform was discussed in **MRF Technology** (p. 190)]. Most samples were prepared from commercial materials.

1. Substrate Materials

A wide range of optical glasses and hard ceramics were chosen for this study. Table 120.III lists these materials in order of increasing hardness, separated by type (i.e., glasses and ceramics). The optical glasses represent a wide range of glasses spread over the entire glass table. The polycrystalline ceramics are of interest in military[48] applications such as windows and domes as well as in other commercial applications.

Samples were prepared by LLE's Optical Fabrication Shop. Glass substrates were first ground with 40, 20, and 9 μm of Al_2O_3 (Ref. 49) on a cast iron backing plate and then polished with CeO_2 (Ref. 50) on a pitch[51] lap. Ceramic substrates were ground with diamonds (6 μm)[52] on a glass backing plate. The glass plate had grooves to promote diamond distribution and to reduce scratches. The ceramic substrates were polished with diamonds (0.5 μm)[53] on pitch.[51] ZnS was ground with 40, 20, and 9 μm of Al_2O_3 (Ref. 49) on a glass tool. The ZnS was polished on a tool made of 10% beeswax and 90% #73 Gugolz with a mixture of 50% Praxair A (0.3 μm) Al_2O_3 and 50% Syton HT-50 colloidal silica (from Ref. 22). Initial surface roughness data for all polished parts are tabulated in Table 120.III.

2. Metrology

The sample surface figure and spot shape after MRF processing were examined using a laser interferometer.[54] Valid data for spots required spot depths less than ~0.2 μm; otherwise, dropout occurred and no data could be collected. Alternatively, we used a white-light interferometer[55] equipped with 1× objective for spots deeper than 0.2 μm. The field of view for this instrument and objective was 14.7 mm by 10.7 mm.

A white-light interferometer[46] equipped with a 50× Mirau objective, which provided a 350 × 350-μm measurement area, was used to measure surface roughness. The areal rms surface roughness values reported in Tables 120.IV–120.VI represent an average over five measurement sites on the surface of the initially polished samples or within the depth of deepest penetration (ddp) for each spot. The lineout rms surface roughness values reported in these tables represent an average of 500 profiles (100 per areal measurement automatically distributed by the software) within the area of measurement. Within spots, lineouts are taken parallel to the direction of ribbon motion over the part surface to better evaluate smoothing by MRF on a nonrotating part (see Ref. 47 for further discussion).

Results and Discussion

Three silicate glasses—S-BSL-7, BK-7, and FS—were used as baseline materials for the experiment. Removal rates and roughness values were recorded for these glasses over time as out-of-field MR fluid viscosity was purposefully altered. All results are presented in a table and selected data are plotted. Spot-polishing results at a fixed viscosity for all glasses and the ceramics are then tabulated and examined as a function of material hardness. Finally, we comment on the evolution of

Table 120.III: Substrate materials used for the experiment, in order of increasing hardness and separated by type (i.e., glasses and ceramics)[a].

Material ID	Source	Dimensions ∅ × h (mm)	ρ (g/cm^3)	Tg (°C)	E (GPa)	Poisson's ratio v	Vickers hardness at 200 gf (GPa)[b]	Fracture toughness K_c (MPa m$^{1/2}$)[b]	Initial areal rms (nm)[c]	Initial line rms (nm)[d]
Glasses										
S-FPL 53	OHARA (FCD 100 HOYA Equiv.)	47.3 × 7.7	3.63	436	69.4	0.302	3.75	0.52	1.13±0.03	0.28±0.02
KzFS N4	SCHOTT	48.9 × 7.8	3.2	492	60	0.29	3.8	--	1.26±0.04	0.29±0.02
LHG 8	HOYA	38.8 × 11.1	2.83	485	62	0.26	4.01	0.5	0.89±0.08	0.22±0.02
S-PHM 52	OHARA (PCD 4 HOYA Equiv.)	50.3 × 9.3	3.67	587	71.5	0.292	4.4	0.49	0.80±0.05	0.20±0.01
PBM 2Y	OHARA	50.2 × 7.7	3.61	436	57.1	0.223	4.6	0.66	2.12±0.44	0.48±0.07
S-NPH 2	OHARA	50.3 × 7.8	3.58	650	99.1	0.249	5.1	0.58	2.19±0.15	0.37±0.10
S-FSL 5	OHARA (FK 5 SCHOTT Equiv./ FC 5 HOYA Equiv.)	50.3 × 9.5	2.46	500	62.3	0.227	5	0.63	4.11±1.50	0.74±0.90
S-LAL 10	OHARA (LaK 10 SCHOTT Equiv./LaC 10 HOYA Equiv.)	50.2 × 7.8	3.98	674	103.9	0.288	5.5	0.8	0.74±0.04	0.18±0.01
S-NBM 51	OHARA	50.3 × 7.9	2.93	554	81.7	0.243	6.25	0.84	1.13±0.07	0.25±0.02
S-TIH 6	OHARA (SF L6 SCHOTT Equiv./ FD 60 HOYA Equiv.)	50.2 × 7.8	3.37	604	93.1	0.261	6.3	0.63	1.53±0.22	0.31±0.40
S-BAL 35	OHARA (SK 5 SCHOTT Equiv./ BaCD 5 HOYA Equiv.)	49.9 × 7.9	3.31	669	83.2	0.25	6.7	0.86	1.14±0.06	0.25±0.03
S-BSL 7	OHARA (BK 7 SCHOTT Equiv./ BSC 7 HOYA Equiv.)	60.1 × 11.8 (50.2 × 7.9)	2.52	576	80	0.205	6.9	0.86	0.79±0.01	0.21±0.01
S-LAH 64	OHARA (LaF N 21 SCHOTT Equiv./TaF 4 HOYA Equiv.)	50.3 × 9.6	4.3	685	122.4	0.294	8.5	1.08	0.68±0.06	0.44±0.02
BK 7	SCHOTT	39.9 × 19.6	2.51	559	81	0.208	8.58	0.8	1.05±0.04	0.25±0.01
FS	CORNING	50.0 × 9.6	2.201	1090	72.7	0.16	9.45	0.7	0.74±0.02	0.21±0.00
TAFD 5	HOYA	52.2 × 11.1	4.92	670	125.9	0.3	11.27	1.54	0.62±0.08	0.15±0.00
Polycrystalline Ceramics										
Material ID	Source	Dimensions ∅ × h (mm)	ρ (g/cm^3)	Grain size (μm)	E (GPa)	Poisson's ratio v	Vickers hardness at 500 gf (GPa)	Fracture toughness K_c (MPa m$^{1/2}$)	Areal rms (nm)	Line rms (nm)
CVD ZnS[f]	NA	40.4 × 6.5	4.09	~3–8	96.5	0.41	3.47	0.8	1.22±0.12	0.26±0.03
Spinel	TA&T Optical Ceramics Div.	35.1 × 2.1	3.58	100–200	273	0.26	13.63	2.07	1.78±0.67	0.22±0.03
ALON	SURMET	46.1 × 10	3.681[e]	150–250[e]	334	0.24	15.77[e]	2.837[e]	2.83±0.48	0.39±0.06
PCA[g]	CERANOVA	38.0 × 2.1	3.99[e]	~0.3[e]	400	--	21.84[e]	3.3[e]	2.90±0.10	0.65±0.05
CVC SiC[h]	Trex	39.7 × 40.8 × 12.7	~3.2	5–15	456	0.21	27.9585	3.39	2.88±0.13	0.49±0.04

[a]Literature values (unless otherwise specified).
[b]Data from Lambropoulos *et al.*[45]
[c]Areal roughness was measured using a white-light interferometer[46] equipped with a 50× Mirau objective, which provided a 350- × 350-μm measurement area. The areal rms surface roughness represents an average of five measurement sites on the surface of the prepolished samples or within the depth of deepest penetration (ddp) for each spot.
[d]Lineout rms surface roughness represents an average of 500 profiles (100 per areal measurement automatically distributed by the software) within areal measurements.
[e]Data from Shafrir *et al.*[47] (unless otherwise specified).
[f]Zinc sulfide (ZnS) standard grade (see Table 5.3 in Ref. 48).
[g]CeraLumina™ polycrystalline alumina (PCA) disks were provided by CeraNova Corporation. Development of this material by CeraNova is funded by NAVAIR through the U.S. Government SBIR program; SBIR data rights apply.
[h]Rectangular part.

Table 120.IV: Results for spotting experiment on baseline glasses S-BSL-7, BK-7, and FS obtained over 18 days with a zirconia-coated-CI-particle–based MR fluid (for measurement conditions, see **Metrology**, p. 195).

	Material ID	Fluid pH	Viscosity (cP)	MRR (μm/min)	Areal rms (nm)	Line rms (nm)	Number of spots
Day 1	S-BSL 7	7.3	97	1.95	1.06±0.10	0.25±0.02	1
	S-BSL 7	7.3	87	1.845	1.17±0.12	0.25±0.01	1
	S-BSL 7	7.2	72	1.59±0.04	1.15±0.09	0.26±0.03	4
	FS	7.2	72	0.73±0.03	0.97±0.08	0.25±0.01	2
Day 2	S-BSL 7	7.2	53	1.62±0.05	1.40±0.37	0.26±0.02	4
	FS	7.2	53	0.765	0.90±0.06	0.23±0.01	1
Day 3	BSL7	8.3	51	2.06±0.04	2.21±1.38	0.37±0.29	2
Day 4	BSL7	8.4	51	2.06±0.11	1.71±0.86	0.28±0.03	2
Day 9	S-BSL7	8.3	51	1.965	1.35±0.22	0.25±0.02	1
	BK 7		51	2.22	1.95±0.52	0.27±0.03	1
	BK 7		70	2.835	2.54±0.58	0.77±0.50	1
	FS		70	1.365	1.47±0.17	0.35±0.02	1
Day 10[(a)]	S-BSL7	8.4	51	2.1	1.67±0.94	0.37±0.23	1
	BK 7		51	2.445	1.11±0.09	0.25±0.02	1
	S-BSL7		70	2.61	1.23±0.31	0.23±0.01	1
	BK 7		70	2.88±0.17	MISSING	MISSING	2
	FS		70	1.275	1.04±0.14	0.30±0.06	1
Day 11	S-BSL7		70	2.89±0.16	1.11±0.06	0.42±0.35	2
	S-BK7		70	2.96	1.40±0.24	0.24±0.01	1
	FS		70	1.47	1.06±0.11	0.25±0.03	1
Day 16	S-BSL7	8.3	70	3.20	1.30±0.21	0.25±0.01	1
	S-BSL7		90	3.96	1.11±0.04	0.26±0.02	1
Day 17[(b)]	S-BSL7	8.3	90	4.10±0.10	1.21±0.22	0.26±0.03	5
	FS		90	1.92±0.06	1.07±0.21	0.24±0.02	5
Day 18	S-BSL7	8.2	90	3.75	1.04±0.07	0.24±0.01	1
	FS		90	1.95	0.88±0.04	0.24±0.02	1
	S-BSL7		70	3.36	1.09±0.13	0.24±0.01	1
	FS		70	1.68	0.86±0.04	0.23±0.03	1
	S-BSL7		50	2.72	1.08±0.26	0.22±0.00	1
	FS		50	1.28	0.88±0.04	0.24±0.01	1

[(a)]At the end of day 9, 250 mL of zirconia-coated-CI-particle–based MR fluid (40-vol % solid content with DI water) were added to the fluid vessel.

[(b)]A total of 3.3 g of nanodiamonds were added to the fluid (increments of 0.8 g).

Table 120.V: Results for spotting experiment on optical glasses obtained over 2 days with a zirconia-coated-CI-particle–based MR fluid (for measurement conditions, see **Metrology**, p. 195).

	Day 1: Viscosity ∼ 72 cP, pH ∼ 7.3				Day 2: Viscosity ∼ 53 cP, pH ∼ 7.4			
Material ID	MRR (μm/min)	Areal rms (nm)	Line rms (nm)	Number of spots	MRR (μm/min)	Areal rms (nm)	Line rms (nm)	Number of spots
S-FPL 53	12.84	1.87±0.53	0.26±0.01	1	13.44±1.19	1.70±0.48	0.27±0.00	2
KzFS N4	6.24	1.86±0.08	0.36±0.07	1	5.73	1.73±0.24	0.29±0.02	1
LHG8	3.012	1.69±0.34	0.21±0.05	1	3.9	1.21±0.40	0.21±0.02	1
S-PHM 52	7.68	1.14±0.06	0.20±0.01	1	6.48	1.06±0.21	0.20±0.01	1
PBM 2Y	2.976	1.94±0.22	0.33±0.04	1	2.85	2.43±1.23	0.32±0.03	1
S-FSL 5	2.112	1.18±0.07	0.26±0.02	1	1.92	1.36±0.40	0.27±0.02	1
S-NPH 2	7.68	1.71±0.06	0.25±0.01	1	6.87	2.95±1.00	0.33±0.04	1
S-LAL10	4.272	1.98±0.14	0.37±0.06	1	3.795	1.33±0.08	0.33±0.08	1
S-NBM 51	2.82	1.63±0.12	0.29±0.02	1	2.715	1.33±0.08	0.26±0.02	1
S-TiH 6	3.276	1.77±0.12	0.32±0.03	1	3.27	1.60±0.06	0.32±0.05	1
BAL 35	3.072	1.45±0.13	0.31±0.04	1	3.015	1.26±0.23	0.26±0.04	1
S-LAH 64	3.024	1.36±0.18	0.26±0.04	1	2.715	0.99±0.04	0.20±0.03	1
TAFD5	2.832	1.58±0.07	0.29±0.06	1	2.52	0.92±0.10	0.19±0.01	1

Table 120.VI: Results for spotting experiment on polycrystalline ceramics obtained on days 11, 17, and 18 of the experiment with a zirconia-coated-CI-particle–based MR fluid (for measurement conditions, see **Metrology**, p. 195).

	Material ID	Fluid pH	Viscosity (cP)	MRR (μm/min)	Areal rms (nm)	Line rms (nm)	Number of spots
Day 11	ZnS	8.4	70	0.10±0.01	4.50±0.38	3.55±1.09	2
	Spinel			0.02±0.00	56.74±20.89	5.18±2.97	2
	ALON			0.03±0.00	19.05±4.29	2.56±0.52	2
Day 17[(a)]	Spinel	8.3	90	0.65±0.21	105.27±19.08	5.36±3.14	4
	ALON			0.62±0.09	488.3±189.8	20.34±13.14	2
Day 18	Spinel	8.2	90	0.62	18.68±4.19	1.11±0.41	1
	ALON			0.71±0.03	16.09±3.11	1.31±0.39	2
	PCA			0.25	3.87±0.08	0.95±0.07	1
	CVC SiC			0.12	12.94±1.55	2.22±0.34	1
	Spinel	8.2	70	0.68	26.44±9.44	1.84±0.86	1
	ALON			0.56	28.96±9.28	2.29±0.58	1
	PCA			0.21	5.08±0.11	1.18±0.19	1
	CVC SiC			0.09	13.70±0.53	2.19±0.46	1
	Spinel	8.2	50	0.39	20.32±4.58	1.50±0.86	1
	ALON			0.45	22.80±2.96	1.84±0.63	1
	PCA			0.14	5.04±0.18	0.98±0.09	1
	CVC SiC			0.06	11.96±0.70	1.93±0.47	1

[(a)]After a total addition of ∼3.3 g of nanodiamonds to the MR fluid reservoir.

the texture of the zirconia-coated CI particle surface over the life of the experiment.

1. MRF Spotting Results for Baseline Optical Glasses

Peak material removal rates and in-spot rms roughness (areal and lineout) are given in Table 120.IV for spots taken on S-BSL-7, BK-7, and FS over 18 days. Included in this table are the time evolution of MR fluid pH (measured periodically by inserting a probe[56] into the STM fluid reservoir) and out-of field viscosity (reported from flow and pressure sensors present in the STM fluid delivery system) at a shear rate of ~800 s^{-1}.

For ease of discussion, the removal rate data for S-BSL-7 and BK-7 are extracted from Table 120.IV and plotted in Fig. 120.38. The horizontal axis is arranged to track the number of the spot taken, annotated by the elapsed time in terms of the day of the experiment. Measurements of fluid pH and viscosity recorded at the time of spotting are also plotted.

The initial fluid pH after being loaded into the STM was ~7. It rose to pH ~ 8 after 3 days, remaining stable in time until day 18. Within hours on day 1 the initial fluid viscosity dropped from 100 cP to 72 cP, presumably caused by additional mixing. Thereafter, viscosity was easily controlled by the automated dripper on the STM. Viscosity was purposefully adjusted during the course of the experiment to 50 cP on day 2, back to 70 cP on day 10 (by turning off the automated STM dripper), and up to 90 cP at the end of day 16.

Peak material removal rates for S-BSL7 were stable at ~2 μm/min for the first 9 days. A typical 4-s–duration MRF polishing spot taken on day 1 is shown interferometrically in Fig. 120.39. The spot is symmetric in all aspects, with good edge definition along the leading and trailing edges. The lineout through the center of the spot shows a smoothly varying profile. Because MR fluid was lost from going into bypass operation each night, an additional charge of 250 mL (at 40 vol %) was added at the end of day 9. The removal rate followed the increase in viscosity caused by this addition of fluid. The peak removal rate climbed to nearly 3 μm/min at 70 cP from day 10 to day 16, with a further increase on day 16 to 4 μm/min at 90 cP. No additional increase in removal rate for this borosilicate glass was observed with the addition of 3.3 g of loose nanodiamond abrasives on day 17. We hypothesize that since the nanozirconia abrasives are hard compared to this borosilicate glass, the addition of even-harder nanodiamonds has no additional effect on removal. Saturation of the MRF peak removal rate for FS as a function of increasing nanodia-

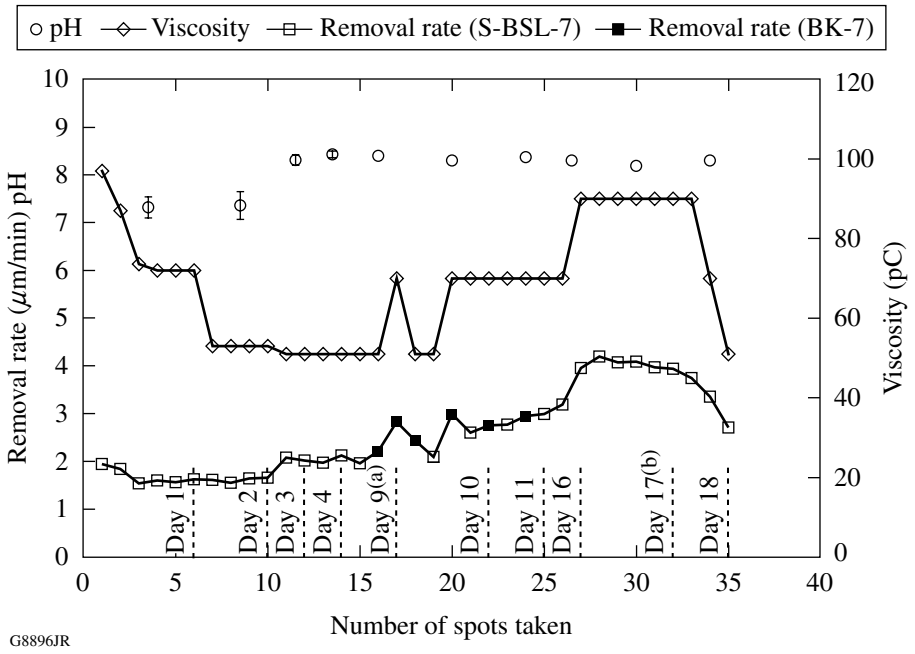

Figure 120.38
Evaluation of coated-CI MR fluid properties (pH and viscosity) and peak removal rates for glasses S-BSL-7 and BK-7 during the spotting experiment. Results are plotted against spot number and elapsed time (days of fluid circulation in the STM). (a) End of day 9: replenishing the fluid with an additional 250 mL (at 40 vol % CI). (b) Day 17: 3.3-g addition of nanodiamonds.

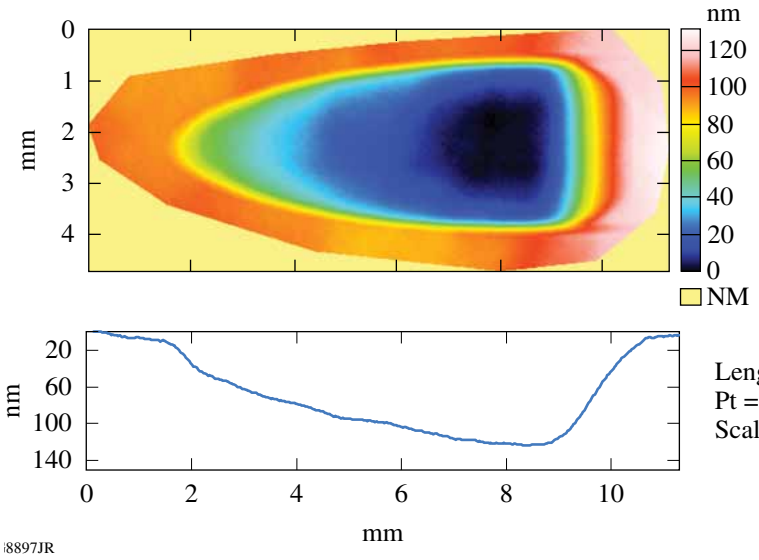

Figure 120.39
A 4-s–duration polishing spot taken on an S-BSL-7 part on day 1, using the coated-CI-particle MR fluid. The 3-D pseudo color image was measured on a white-light interferometer[55] with a 1× objective, giving a field of view of 14.7 mm by 10.7 mm. The lineout taken through the center of the part shows the spot depth to be ~124 nm.

mond abrasive concentration up to ~0.1 vol % was previously reported by Shorey *et al.*[13]

We hypothesize that the free nanozirconia abrasives in the MR fluid play the major role in promoting polishing the part. We are working on devising a method for separating out the nanozirconia particles from the zirconia-coated-CI powder. Such a separation procedure is required to evaluate the polishing behavior of the coated CI particles themselves.

Roughness values measured inside of MRF spots in the region of deepest penetration are given in Table 120.IV. The areal rms roughness data for all three glasses varied between 1.0 and ~1.5 nm throughout the experiment. The lineout rms data varied from 0.2 nm to 0.4 nm. These results are similar to the roughness value given in Table 120.III for the initially pitch polished surfaces, demonstrating the excellent smoothing capability for this zirconia-coated-CI MR fluid.

2. Optical Glass Survey

Additional spots were taken during days 1 and 2 on a variety of glasses with a range of mechanical, thermal, and optical properties. Results are summarized in Table 120.V at fluid viscosities of 53 cP and 72 cP. Areal roughness values were between 1-nm and 2-nm rms, not unlike the initial surface values given in Table 120.III. Again, lineout rms data inside spots were between 0.2 and 0.4 nm, demonstrating good smoothing.

Peak material removal rates are plotted as a function of glass hardness at three viscosities in Fig. 120.40. Soft glasses (H_V < 4 GPa) exhibited removal rates from ~4 μm/min to ~13 μm/min. Glasses increasingly harder than 5 GPa are polished with removal rates from 3 μm/min down to 2 μm/min, even for the hardest glass at 11.5 GPa (TaFD5). The range of glass removal rates given in Table 120.V are commensurate with values reported in the literature for commercial MR fluids used on commercial MRF machines,[57] and for experimental fluids used on the STM (see Refs. 12–13). We observe that our zirconia-coated-CI-particle MR fluid polished glasses over a broad range of hardness values with equal efficiency. In classical polyurethane pad-polishing experiments, Cumbo *et al.*[1] observed that, in comparison to ceria and alumina slurries, monoclinic zirconia was least sensitive to glass type (BK7, SF6, and FS) or slurry fluid chemistry. Our results are consistent with his observations.

3. Spotting Results for Polycrystalline Ceramics

Polycrystalline ceramics were spotted before and after the addition of nanodiamond abrasives. Table 120.VI summarizes the experimental conditions (pH and viscosity), peak material removal rate, surface roughness, and number of spots taken. For soft ZnS, material removal rates were relatively low in comparison to that observed for the glasses at a viscosity of ~70 cP. Inspection of the spots taken on the surface of ZnS indicated that the spot topography was irregular and textured. We conclude that, at pH 8, this zirconia-coated-CI-particle–based slurry is not suitable for polishing CVD polycrystalline ZnS.

Removal rates for hard ceramics ALON and Spinel were negligible at a viscosity of ~70 cP, and therefore other hard polycrystalline materials were not tested at this viscosity. On day 17 we increased the fluid viscosity to ~90 and added 3.3 g

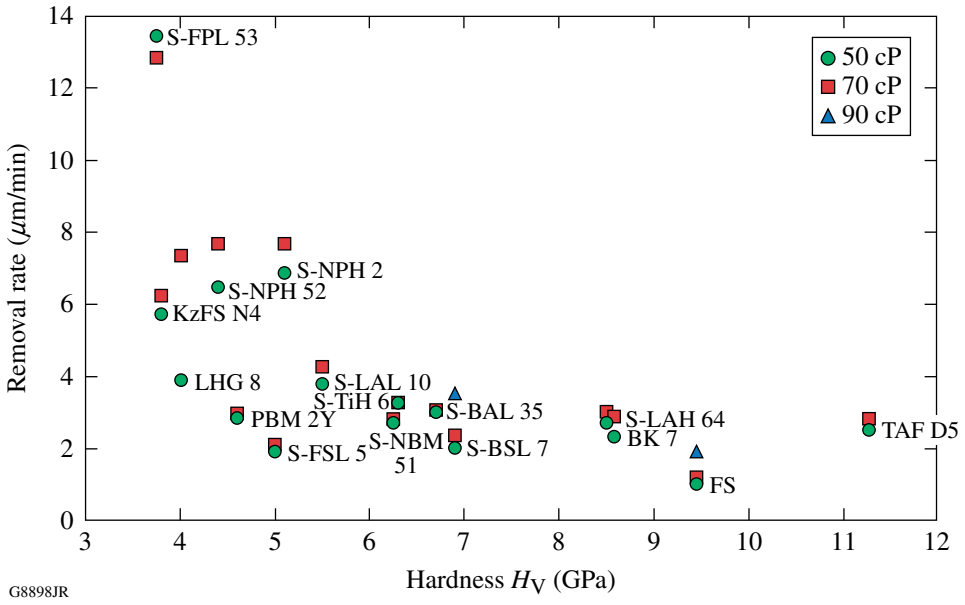

Figure 120.40
Peak removal rates for optical glasses as a function of Vickers hardness for three coated-CI-particle–based MR fluid viscosities. The MR fluid consisted of coated particles and water only.

of nanodiamonds. Material removal rates increased by a factor of ~30 for both materials. A further increase of ~15% in the removal rate for ALON was observed at the beginning of day 18 at 90 cP. Thereafter, fluid viscosity was purposefully reduced from 90 to 70 and finally to 50 cP. Spots were taken on samples of PCA and SiC. Figure 120.41 shows the relationship between removal rate and Vickers hardness at the three viscosities. The intermediate hardness ceramics (i.e., Spinel and ALON) appear to be more sensitive to changes in fluid viscosity than harder ceramics. We have no explanation for this, other than to note the differences in grain size [and possibly grain-size distribution for these materials (see Table 120.III)].

Roughness values measured inside the MRF spots in the region of deepest penetration are given in Table 120.VI. Significant roughening of Spinel and ALON immediately after the addition of 3.3 g of nanodiamonds shown on day 17 improved considerably after the nanodiamonds circulated in the STM delivery system over night (i.e., day 18). On day 18, areal rms surface roughness varied from ~5 nm for PCA to ~22 nm for the intermediate hardness ceramics (i.e., Spinel and ALON). The lineout rms data varied from ~0.9 nm (PCA) to ~2.3 nm (ALON).

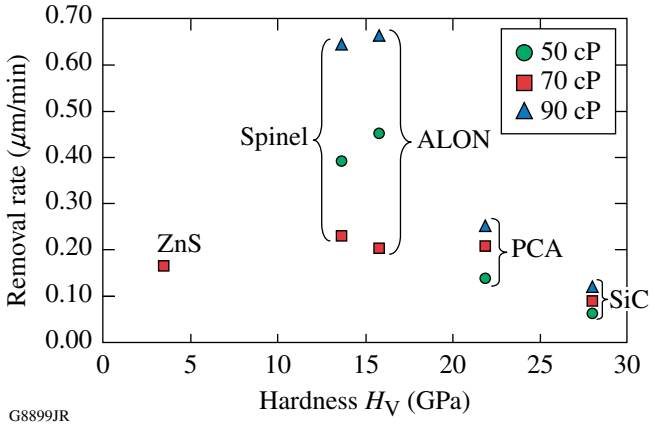

Figure 120.41
Peak removal rates for polycrystalline ceramics as a function of Vickers hardness for three coated-CI-particle–based MR fluid viscosities. The MR fluid consisted of coated particles, loose nanodiamond abrasives, and water.

4. Evolution of Coated-CI Topography Throughout the Experiment

The evolution of coated-CI surface topography throughout the experiment was studied via SEM. Figure 120.42 shows SEM images of zirconia-coated CI particles after different durations of use in the STM delivery system, from 3 to 22 days.

The images indicate that the spherical particles maintain their coated, faceted nanocrystalline zirconia texture even after 22 days of circulation and use. The low magnification images of the particles after 3 days of circulation show that the distribution of particle sizes is between ~0.5 to ~2 μm, a range that is comparable to the published data of uncoated CI used in the synthesis process. This provides additional support to our statement (see **Morphology, Size, and Surface Properties**, p. 192) that the zirconia layer is thin relative to the size of the CI particle and therefore does not change the initial powder-size distribution in a significant way. High-magnification images of the coated particles after use in the STM for 10 and 22 days confirm that the zirconia-coating layer is unabraded and well adhered to the particles.

The persistence of a thin layer of zirconia is further established in Fig. 120.43, which shows several coated-particle cross sections after 22 days of circulation in the STM system. Visual examination of fluid samples extracted from the fluid reservoir were deposited on a paper towel. The coloration of the towel provided a qualitative indication of the onset of corrosion (not shown here). This test showed no evidence of corrosion, suggesting that our sol-gel process effectively coated the CI particles with zirconia and that the coating did not wear under the experiment conditions.

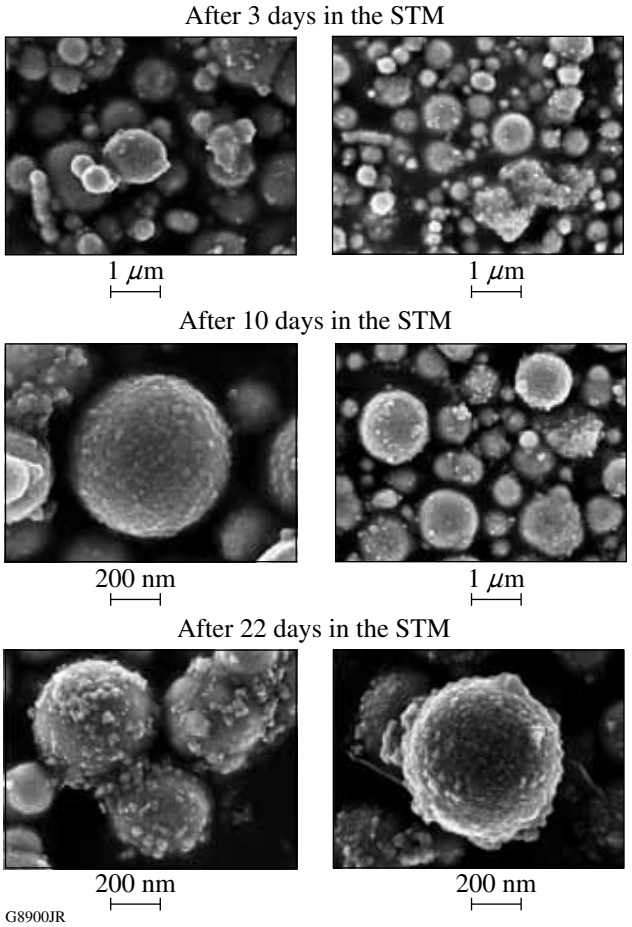

Figure 120.42
SEM images of zirconia-coated CI after being circulated in the STM delivery system for 3, 10, and 22 days, respectively.

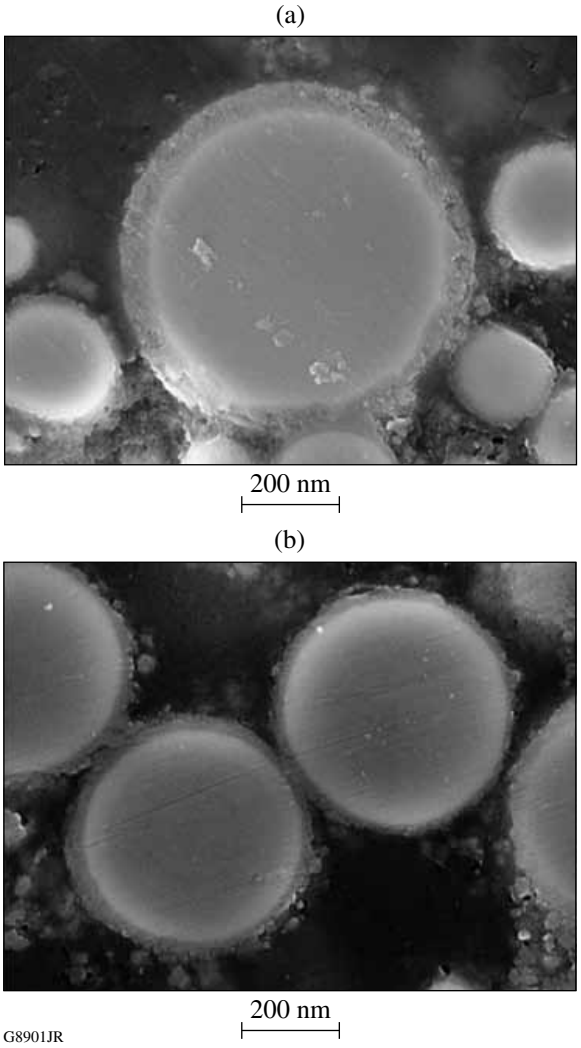

Figure 120.43
SEM cross-sectional images of zirconia-coated CI after being circulated in the STM delivery system for 22 days.

Summary

Here we have reported on a new development in MR fluids for MRF applications. A zirconia-coated-CI-particle–based MR fluid was designed, prepared in kilogram quantities, and circulated using an experimental MRF setup for three weeks with no signs of MR fluid degradation or corrosion. The fluid

composition contained free nanozirconia polishing abrasives generated in the coating process. When mixed with only water, the resulting MR fluid was stable at pH 8 for 18 days. This zirconia-coated-CI-particle–based fluid exhibited stable material removal rates and smooth surfaces inside spots for a variety of optical glasses and polycrystalline ceramics.

ACKNOWLEDGMENT

The authors thank Alex Maltsev and Mike Kaplun from the Laboratory for Laser Energetics (LLE) at the University of Rochester for sample preparation and acknowledge LLE for continuing support. Two of the coauthors (C. Miao and R. Shen) are LLE Horton Fellows. Research was sponsored by the U.S. Army Armament, Research, Development, and Engineering Center (ARDEC) and was accomplished under Cooperative Agreement Number W15QKN-06-2-0104 and the U.S. Department of Energy Office of Inertial Confinement Fusion under Cooperative Agreement No. DE-FC52-08NA28302, the University of Rochester, and the New York State Energy Research and Development Authority. The views and conclusions contained in this document are those of the authors and should not be interpreted as representing the official policies, either expressed or implied, of U.S. Army ARDEC or the U.S. Government. The support of DOE does not constitute an endorsement by DOE of the views expressed in this article. The U.S. Government is authorized to reproduce and distribute reprints for Government purposes notwithstanding any copyright notation hereon.

Appendix A: Synthesis Procedure of Zirconia-Coated CI Using the Sol-Gel Technique

This appendix describes the sol-gel synthesis procedure for coating CI powder. The first step was the preparation of zirconia sol-gel. Zirconia sol was prepared by mixing 1000 mL of DI water [H_2O], 73 mL of zirconium (IV) butoxide [$Zr(OC_4H_9)_4$], and 30 mL of nitric acid [HNO_3] at room temperature to produce ~1100 mL of sol. The mixing process is completed when the solution is clear (pH ~ 1).

Second, the following procedure was followed to prepare a 200-g batch of zirconia-coated CI at 10-vol % zirconia sol:

- CI powder (200 g) was dispersed in DI water (600 mL) in a 2-liter flask.
- The mixture/flask was placed in an ultrasonic bath for 30 min at room temperature.
- The flask was then placed in a water bath on top of a hot plate, and the mixture was agitated using a mechanical stirrer (~60 rpm).
- Zirconia sol (400 mL) was added to the flask containing the CI and water. The amount of sol determined the thickness of the zirconia coating and the amount of free zirconia nanocrystals formed.
- The water bath temperature was set to 70°C and was left to stir for 4 h after which the hot plate was turned off and the mixture continued to stir overnight.
- Finally, the zirconia-coated CI particles were separated out from the liquid mixture (~10 pH) using a magnet and washed three times with ~2 liters of DI water and ethanol. The particles were dried in an aluminum foil pan in a fume hood for 2 to 3 days to a moisture level of less than 2 wt%.[58]
- The dried particles were then milled by hand with a mortar and pestle to form a uniform powder.

Appendix B: Sample Preparation Procedure for SEM

This appendix describes the preparation of samples for SEM imaging. Two types of samples were prepared: loose particles and imbedded particles for cross sectioning. Loose particles of both uncoated and zirconia-coated CI powder (<1 g) were spread over an SEM-designated stub covered with a double-sided carbon tape. No conductive layer was required for uncoated CI, but a conductive layer of gold/palladium alloy was used for the zirconia-coated CI particles to minimize the effect of electric charge accumulation on the specimen during electron irradiation to yield good image quality. In general, for both sample types, a low electron beam voltage was used (~3 to 5 kV) with a relatively short SEM working distance (~2 to 5 mm).

The following procedure was taken to prepare samples of imbedded particles for cross sectioning:

- 3 g of CI particles (uncoated or coated) were milled by hand with a mortar and pestle, subsequently mixed with 3 g of conductive molding compound.[59]
- A sample press[60] was preheated to ~200°C, filled with 10 g of pure conductive molding compound, and then covered with the mixture of CI and molding compound on top.
- A pressure of 4500 psi was applied for ~10 min and the sample was allowed to cool down at room temperature for ~20 min.
- The final puck dimension was ~30 mm in diameter by ~15 mm high.

- Samples were spotted on our spot-taking machine (STM, discussed in **MRF Technology**, p. 190) using a standard MR fluid with nanodiamonds. A spotting time of ~30 min produced a visible spot. This "spotting" procedure provides a new deterministic polishing technique for cross sectioning encapsulated particles for SEM.

REFERENCES

1. M. J. Cumbo, D. Fairhurst, S. D. Jacobs, and B. E. Puchebner, Appl. Opt. **34**, 3743 (1995).
2. D. Towery and M. A. Fury, J. Electron. Mater. **27**, 1088 (1998).
3. D. W. Camp *et al.*, in *Laser-Induced Damage in Optical Materials: 1997*, edited by G. J. Exarhos *et al.* (SPIE, Bellingham, WA, 1998), Vol. 3244, pp. 356–364.
4. M. A. Nichols *et al.*, U.S. Patent No. 6,099,389 (8 August 2000).
5. S.-W. Park, Y.-J. Seo, and W.-S. Lee, Microelectron. Eng. **85**, 682 (2008).
6. J. A. Menapace *et al.*, U.S. Patent No. 6,920,765 (26 July 2005).
7. QED Technologies, LLC, Rochester, NY 14607.
8. J. D. T. Kruschwitz, Opt. Photonics News **17**, 10 (2006).
9. V. W. Kordonski and D. Golini, in *Proceedings of the Sixth International Conference on Electro-Rheological Fluids, Magneto-Rheological Suspensions and Their Applications*, edited by M. Nakano and K. Koyama (World Scientific, Singapore, 1998), pp. 837–844.
10. V. W. Kordonski, D. Golini, P. Dumas, S. J. Hogan, and S. D. Jacobs, in *Smart Structures and Materials 1998: Industrial and Commercial Applications of Smart Structures Technologies*, edited by J. M. Sater (SPIE, Bellingham, WA, 1998), Vol. 3326, pp. 527–535.
11. S. D. Jacobs, W. Kordonski, I. V. Prokhorov, D. Golini, G. R. Gorodkin, and T. D. Strafford, U.S. Patent No. 5,804,095 (8 September 1998).
12. J. E. DeGroote, A. E. Marino, J. P. Wilson, A. L. Bishop, J. C. Lambropoulos, and S. D. Jacobs, Appl. Opt. **46**, 7927 (2007).
13. A. B. Shorey, S. D. Jacobs, W. I. Kordonski, and R. F. Gans, Appl. Opt. **40**, 20 (2001).
14. C. Miao, S. N. Shafrir, J. C. Lambropoulos, J. Mici, and S. D. Jacobs, Appl. Opt. **48**, 2585 (2009).
15. For a medium-hardness polyurethane polishing pad (SUBA X pads) on a double-sided polishing machine, the useful lifetime is within the range of 100 to 110 h. Pads on a single-sided polishing machine last considerably longer, approximately three to four months. From personal communication with Mr. Mike Naselaris, Sydor Optics, Rochester, NY (2009).
16. T. S. Izumitani, *Optical Glass*, American Institute of Physics Translation Series (American Institute of Physics, New York, 1986), p. 197.
17. M. Schinhaerl *et al.*, in *Current Developments in Lens Design and Optical Engineering V*, edited by P. Z. Mouroulis, W. J. Smith, and R. B. Johnson (SPIE, Bellingham, WA, 2004), Vol. 5523, pp. 273–280.
18. P. Schinhaerl *et al.*, in *Detectors and Associated Signal Processing II*, edited by J.-P. Chatard and N. J. Peter (SPIE, Bellingham, WA, 2005), Vol. 5965, pp. 659–670.
19. P. A. Barata and M. L. Serrano, Fluid Phase Equilib. **141**, 247 (1997).
20. S. R. Arrasmith, S. D. Jacobs, I. A. Kozhinova, L. L. Gregg, A. B. Shorey, H. J. Romanofsky, D. Golini, W. I. Kordonski, S. Hogan, and P. Dumas, in *Finishing of Advanced Ceramics and Glasses*, edited by R. Sabia, V. A. Greenhut, and C. G. Pantano, Ceramic Transactions, Vol. 102 (The American Ceramic Society, Westerville, OH, 1999), pp. 201–210.
21. J. E. DeGroote, H. J. Romanofsky, I. A. Kozhinova, J. M. Schoen, and S. D. Jacobs, in *Manufacturing and Testing V*, edited by H. P. Stahl (SPIE, Bellingham, WA, 2004), Vol. 5180, pp. 123–134.
22. I. A. Kozhinova, H. J. Romanofsky, A. Maltsev, S. D. Jacobs, W. I. Kordonski, and S. R. Gorodkin, Appl. Opt. **44**, 4671 (2005).
23. B. M. Kavlicoglu *et al.*, in *Smart Structures and Materials 2002: Damping and Isolation*, edited by S. A. Gregory (SPIE, Bellingham, WA, 2002), Vol. 4697, pp. 393–400.
24. W. Zhou, C.-M. Chew, and G.-S. Hong, in *Proceedings of the 2005 IEEE/ASME International Conference on Advanced Intelligent Mechatronics* (IEEE, New York, 2005), pp. 473–478.
25. I. B. Jang *et al.*, J. Appl. Phys. **97**, 10Q912 (2005).
26. F. F. Fang and H. J. Choi, Phys. Status Solidi A **204**, 4190 (2007).
27. T. J. Swihart, U.S. Patent No. 4,731,191 (15 March 1988).
28. H. Rutz and F. G. Hanejko, U.S. Patent No. 5,063,011 (5 November 1991).
29. T. Atarashi and K. Nakatsuka, U.S. Patent No. 6,280,658 (28 August 2001).
30. J. C. Ulicny and Y. T. Chang, U.S. Patent No. 6,929,757 (16 August 2003).
31. K. D. Weiss, D. J. Carlson, and D. A. Nixon, U.S. Patent No. 5,578,238 (26 November 1996).
32. H. Pu, F. Jiang, and Z. Yang, Mater. Lett. **60**, 94 (2006).
33. J. C. Ulicny *et al.*, U.S. Patent Appl. No. 11/971,298; Pub. No. US 2008/0185554 A1 (7 August 2008).
34. Carbonyl Iron (CI) HQ, BASF Aktiengesellschaft Inorganic Specialties, Ludwigshafen, Germany.
35. R. Shen, S. N. Shafrir, C. Miao, M. Wang, J. C. Lambropoulos, S. D. Jacobs, and H. Yang, "Synthesis and Corrosion Study of Zirconia Coated Carbonyl Iron Particles," to be published in the Journal of Colloid and Interface Science.
36. SUPRA 40VP Scanning Electron Microscope (SEM), Zeiss-Leica, Germany.
37. L. Kumari, W. Li, and D. Wang, Nanotechnology **19**, 195602 (2008).

38. Zirconium Oxide Material Safety Data Sheet, Zircar Zirconia, Inc., Florida, NY 10921-0287.

39. S. Koynov, M. S. Brandt, and M. Stutzmann, Appl. Phys. Lett. **88**, 203107 (2006).

40. VCA 2500xe Video Contact Angle System, AST Products, Inc., Billerica, MA 01821.

41. AccuPyc II 1340 Gas Pycnometer, Micromeritics Instrument Corporation, Norcross, GA 30093-2901.

42. D. R. Lide, *CRC Handbook of Chemistry and Physics: A Ready-Reference Book of Chemical and Physical Data: 2008–2009*, 89th ed. (CRC Press, Boca Raton, FL, 2008), p. 4-101.

43. R. M. Cornell and U. Schwertmann, *The Iron Oxides: Structures, Properties, Reactions, Occurrences, and Uses*, 2nd ed. (Wiley-VCH, Weinheim, 2003), p. XVIII.

44. Brookfield Cone and Plate Viscometer Model DV-III CP, Brookfield Engineering Laboratories, Inc., Middleboro, MA 02346.

45. J. C. Lambropoulos and R. Varshneya, in *Frontiers in Optics 2004*, OSA Technical Digest (Optical Society of America, Rochester, NY, 2004), Paper OTuA1.

46. Talysurf CCI 3000 Noncontact 3-D Surface Profiler (Taylor Hobson, Inc., Rolling Meadows, IL 60008-4231). The 50× objective (0.37 × 0.37 mm^2) and four phase averages were used for each measurement, unfiltered. The Talysurf CCI has a maximum resolution of 0.1 Å in the z-axis and 0.47 mm in the x–y axis (maximum optical resolution).

47. S. N. Shafrir, J. C. Lambropoulos, and S. D. Jacobs, Appl. Opt. **46**, 5500 (2007).

48. D. C. Harris, in *Materials for Infrared Windows and Domes: Properties and Performance*, Tutorial Texts in Optical Engineering (SPIE Optical Engineering Press, Bellingham, WA, 1999), Vol. PM70, p. 145.

49. Microgrit Micro Abrasives Corporation, Westfield, MA 01086-0669.

50. Hastilite Precision Polishes for Advanced Optics (PO), J. H. Rhodes, a Division of Universal Photonics, Inc., Franklin Springs, NY

51. 915 Pitch, Universal Photonics, Inc., Hicksville, NY 11801-1014.

52. Buehler METADI Diamond Suspension (water based), Buehler Ltd., Lake Bluff, IL 60044-1699.

53. Kay Diamond Products, LLC, Boca Raton, FL 33487.

54. Zygo Mark IVxp Interferometer (Zygo Mark IVxp™, Zygo Corporation, Middlefield, CT 06455). This instrument is a 4-in. HeNe Fizeau interferometer with a wavelength of 632.8 nm. Peak-to-valley (p–v) for surface flatness and depth of deepest penetration (ddp) of the spot was measured in microns.

55. NewView 5000 Noncontact Profilometer (Zygo Corporation, Middlefield, CT 06455).

56. Beckman 210 pH Meter, Beckman Instruments Inc., Fullerton, CA 92643.

57. D. Golini and S. D. Jacobs, in *Advanced Optical Manufacturing and Testing*, edited by L. R. Baker, R. B. Reid, and G. M. Sanger (SPIE, Bellingham, WA, 1990), Vol. 1333, pp. 80–91.

58. The moisture content is measured using an Arizona Instrument Computrac Max-1000 moisture analyzer, Arizona Instrument, LLC, Tempe, AZ 85281.

59. Probemet Conductive Molding Compound, Buehler Ltd., Lake Bluff, IL 60044-1699.

60. Specimen Mounting Press, Buehler Ltd., Lake Bluff, IL 60044-1699.

All-Fiber Optical Magnetic Field Sensor Based on Faraday Rotation in Highly Terbium Doped Fiber

Magnetic field sensors have been widely used for navigation, vehicle detection, current sensing, and spatial and geophysical research. Many techniques developed for magnetic field sensors are based on electronics, including superconducting quantum interference devices (SQUID's), search coils, fluxgates, Hall-effect sensors, anisotropic magnetoresistive devices, and giant magnetoresistive devices.[1] All-fiber optical magnetic field sensors are desirable because of their immunity to electromagnetic interference, low weight, small size, and long-distance signal transmission for remote operation.

Many all-fiber magnetic field sensors use material coatings. For example, if a magnetostrictive or metal jacket is deposited on the fiber, the optical phase can be changed by strain or Lorentzian force, respectively, when immersed in a magnetic field.[2,3] In another method, a fiber end is coated with a composite material and butt coupled to another fiber. The optical coupling between the fibers changes with the transverse displacement of the coated fiber in the magnetic field.[4] In yet another method, iron film is deposited on a side-polished fiber Bragg grating. The reflective wavelength of the fiber grating shifts with the strain induced by a magnetic field.[5]

Faraday rotation can also be used for magnet sensors. Because the Verdet constant of silica fiber is small [~1.1 rad/(Tm) at 1064 nm], the fiber is usually coiled multiturn to increase the polarization rotation angle. This kind of magnet sensor is often used for current sensing.[6,7] However, bend-induced linear birefringence affects the state of polarization and quenches the desired Faraday effect. In this article, an all-fiber optical magnet sensor based on Faraday rotation is demonstrated. The device is made of a fiber Faraday rotator spliced to a fiber polarizer. The fiber Faraday rotator is a 2-cm-long terbium-doped (Tb) fiber, which is sufficiently short to avoid bending. The fiber polarizer is Corning SP1060 single-polarization fiber (PZ).

The magnetic sensing principle is shown in Fig. 120.44. Linear-polarized input light from the laser source is transmitted to the Tb fiber via polarization-maintaining (PM) fiber. The polarization of the light rotates when the Tb fiber experiences a magnetic field along the axis of light propagation. The light then goes through the fiber polarizer, which extinguishes light whose polarization is not aligned to its principle axis. PM fiber transmits the remaining light to a detector. Because of the polarizer, the power received at the detector is a function of the polarization rotation angle given by Malus' Law.[8] Since the polarization rotation angle in the Tb fiber is related to the magnetic field strength by the Faraday effect, the magnetic field can be measured by monitoring the output power of the sensor.

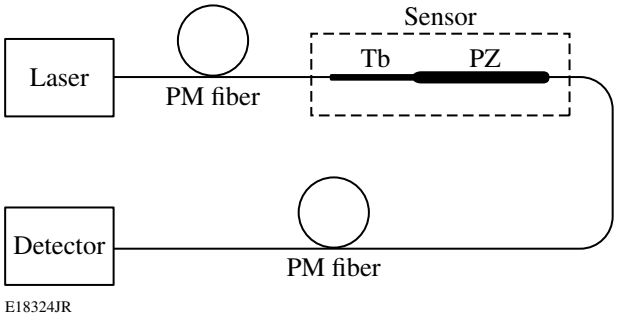

Figure 120.44
Sensing principle of an all-fiber Faraday magnet sensor. PZ: single-polarization fiber; PM: polarization-maintaining fiber.

Terbium doping is an effective way to increase the Verdet constant in the fiber to reduce the fiber length and avoid coiling. Highly terbium doped silicate glasses were designed and fabricated. Boron oxide and aluminum oxide were added into the glass composition to improve the solubility of terbium oxide. Fifty-six-wt% terbium-oxide–doped glass is used as the core glass. The rod-in-tube technique was used for single-mode fiber fabrication. The fiber pulling temperature is around 1000°C. The N.A. and diameter of the core are 0.14 and 4 μm, and cladding diameter of the fiber is 130 μm. The propagation loss of the fiber is measured to be 0.11 dB/cm at 1310 nm using the cutback technique. The effective Verdet constant was measured to be -24.5 ± 1.0 rad/(Tm), using the measurement technique described in Refs. 9 and 10.

Single-polarization fiber is a type of fiber in which only one polarization mode can propagate. This kind of fiber has large birefringence to separate the two orthogonal polarization modes so that each has a different cutoff wavelength. Therefore, within a certain wavelength region, one polarization mode propagates while the other is eliminated because of high loss. In this way, the fiber functions as a polarizer. Such large birefringence can be introduced via stress from boron-doped rods, elliptical core/cladding, or air holes.

In this experiment, Corning SP1060 fiber was used as the polarizing element.[11] With two air holes on either side of an elliptical core, large birefringence and therefore spectrally separated fundamental-mode cutoff were achieved. The core diameter along the major axis was 8 μm, and the clad diameter was 125 μm, with a core N.A. of 0.14. The propagation loss of the surviving mode was 0.1 dB/m at 1060 nm. The center wavelength was 1065 nm and the bandwidth was 25 nm. The polarization extinction ratio was dependent on the length of the fiber. A 1-m PZ fiber was used in the experiment and was coiled with a 15-cm diameter to shift the PZ bandwidth toward the shorter wavelength, resulting in an extinction ratio >16 dB at a 1053-nm working wavelength.

The experimental configuration used to test the sensor is shown in Fig. 120.45. A 2-cm section of Tb-doped fiber, spliced between the PM fiber and 1-m section of PZ fiber, went through a magnet tube. Linearly polarized 1053-nm light was launched into the PM fiber. The polarization directions of the PM and PZ fibers were aligned with a rotational difference of θ_0, which should have been set between 20° to 70° to obtain a nearly linear response curve of magnetic field strength as a function of measured power. The N48 NdFeB magnet tube was 4 cm long with inner and outer diameters of 5 mm and 6 cm, respectively. As the magnet was translated along the fiber, the magnetic field imposed on the Tb fiber changed.

Magnetic fields can be readily calculated by using the geometrical shape of the magnet.[12] The axial component of the magnetic field distribution along the central axis of the magnet tube was derived to be

$$B_z(z) = \frac{B_r}{2}\left\{\frac{z + l/2}{\left[a_1^2 + (z + l/2)^2\right]^{1/2}} - \frac{z + l/2}{\left[a_2^2 + (z + l/2)^2\right]^{1/2}} - \frac{z - l/2}{\left[a_1^2 + (z - l/2)^2\right]^{1/2}} + \frac{z - l/2}{\left[a_2^2 + (z - l/2)^2\right]^{1/2}}\right\}, \quad (1)$$

where a_1 and a_2 are the inner and outer radii, respectively, l is the length of the magnet, and B_r is the residual magnetic flux density. Figure 120.46 shows the calculated $B_z(z)$ for the N48 magnet used in the experiment (B_r = 1.35 T) along with the measured magnetic field outside the magnet. The physical ends of the magnet are also shown for reference. The magnetic field, measured only outside the magnet because the probe size is larger than a_1, agreed very well with the theoretical curve calculated from Eq. (1). The averaged magnetic density flux B_{av} experienced by the 2-cm length of Tb fiber (calculated in the center of Tb fiber) is also shown in the figure. This curve is nearly linear from −3 to −1 cm along the z axis. This region will be used in the measurement.

After considering the extinction ratio of the polarizing fiber, Ex, the relative transmission through the PZ fiber is derived as[13]

$$I/I_0 = \cos^2(\theta_0 + \theta) + \sin^2(\theta_0 + \theta)\,10^{(-\mathrm{Ex}/10)}, \quad (2)$$

where I/I_0 is the measured output power normalized to its maximum I_0, $\theta = VB_{av}L$ is the Faraday rotation angle in the Tb fiber, and V and L are the effective Verdet constant and the length of the Tb fiber, respectively. In the experiment, Ex = 18 dB and $\theta_0 = 50°$. The experimental and theoretical curves of the relative transmission are shown in Fig. 120.47. The error is determined to be 0.01 by a polarization-stability measurement. The experimental data agree well with the theoretical curve, both of which show a nearly linear response. The nominal

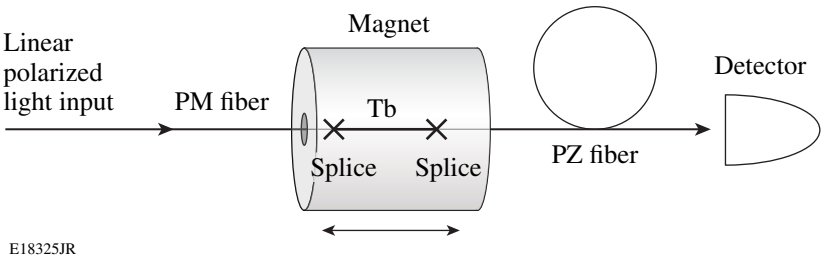

Figure 120.45
Experimental configuration of an all-fiber magnet sensor.

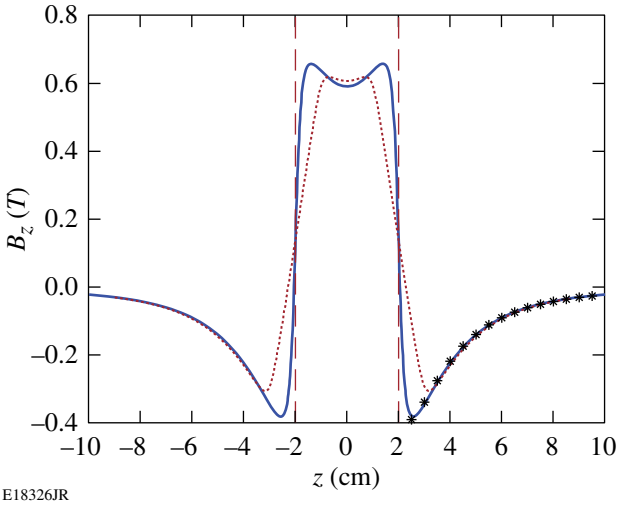

Figure 120.46
Theoretical (solid) and measured (star) magnetic density flux distribution B_z along the center axis z. The dashed lines represent the magnet ends and the dotted line represents B_{av}, the magnetic density flux averaged over a 2-cm length along the axis z.

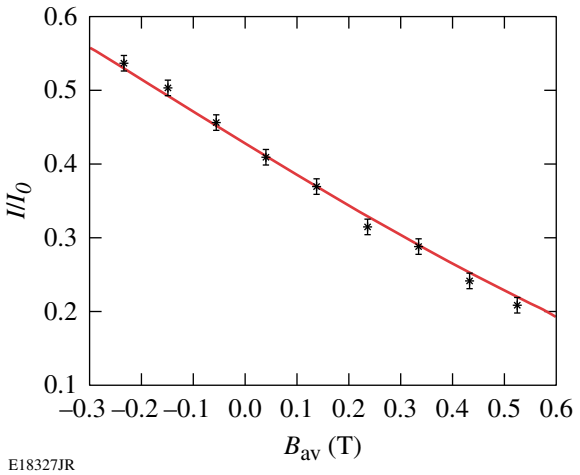

Figure 120.47
Measured (star) and calculated (solid) relative transmission of an all-fiber magnet sensor.

transmission loss through the device is 10 dB, mainly induced by the mode mismatch between the PZ and Tb fibers and the splicing loss between the Tb and silica fibers.

The sensitivity of the all-fiber sensor is given by $d\theta/dB_{av} = VL = 0.49$ rad/T. This can be increased by increasing the effective Verdet constant and/or length of the Tb fiber. Since the polarization rotation may go beyond 90°, a maximum detected magnetic field $B_{max} = (\pi/2)/VL$ of 3.2 T can be measured in this configuration without ambiguity. A larger magnetic field could be measured by decreasing the effective Verdet constant or the length of the Tb fiber.

The resolution of the magnetic sensor is obtained by taking the derivative and absolute value of both sides of Eq. (2):

$$\Delta B = \frac{\Delta I}{I_0 VL \sin\left[2\left(\theta_0 + \theta\right)\right]} = \frac{\Delta I}{I_0} \frac{2B_{max}}{\pi \sin\left[2\left(\theta_0 + \theta\right)\right]}. \quad (3)$$

In this equation, the effect of the extinction ratio was neglected, which is appropriate for Ex > 20. Increasing the effective Verdet constant and the length of the Tb fiber could also help to increase the resolution, at the expense of reducing B_{max}. The most effective way is to decrease the ratio $\Delta I/I_0$. For example, if the detector resolution is at the nW level, increasing I_0 to the mW level yields a sensor resolution of 2.0×10^{-6} T, with B_{max} still at 3.2 T. In the experiment, $\Delta I/I_0$ is around 10^{-2}, making the minimum measurable magnetic field 0.02 T. If higher resolution and higher B_{max} are both required, two all-fiber magnetic field sensors could be co-located. In this scenario, one sensor has a large VL product to obtain the desired resolution; the other one has a small VL product to obtain the desired maximum detected magnetic field by removing the ambiguity of the other sensor.

The Verdet constant of the Tb fiber is dependent on the temperature; for example, $1/V\, dV/dT$ is around 10^{-4}/K for silica.[14] To mitigate the impact of temperature on the measurement results, a fiber-grating temperature sensor could be cascaded or co-located with the magnetic field sensor to monitor the temperature near the magnetic field sensor. In this way, the sensor can give accurate results, providing the device has been calibrated as a function of temperature.

Since the all-fiber magnetic field sensor can measure only magnetic fields parallel to its axis, three orthogonally oriented sensors can be combined to provide a complete three-dimensional magnetic field sensor.

In conclusion, an all-fiber optical magnetic field sensor has been demonstrated. It consists of a fiber Faraday rotator and a fiber polarizer. The fiber Faraday rotator uses a 2-cm-long section of 56-wt%-terbium–doped silicate fiber, and the fiber polarizer is Corning SP1060 single-polarization fiber. The all-fiber optical magnetic field sensor has a sensitivity of 0.49 rad/T and can measure magnetic fields from 0.02 T to 3.2 T.

ACKNOWLEDGMENT

This work was supported by the U.S. Department of Energy Office of Inertial Confinement Fusion under Cooperative Agreement No. DE-FC52-08NA28302, the University of Rochester, and the New York State Energy Research and Development Authority. The support of DOE does not constitute an endorsement by DOE of the views expressed in this article. This work is also supported in part by Wright-Patterson Air Force Research Laboratory under contract FA8650-09-C-5433. The authors would like to acknowledge the technical support of Dr. R. L. Nelson and W. D. Mitchell from AFRL.

REFERENCES

1. J. E. Lenz, Proc. IEEE **78**, 973 (1990).
2. A. Yariv and H. V. Winsor, Opt. Lett. **5**, 87 (1980).
3. H. Okamura, J. Lightwave Technol. **8**, 1558 (1990).
4. V. Radojevic *et al.*, J. Magn. Magn. Mater. **272–276**, e1755 (2004).
5. C.-L. Tien *et al.*, IEEE Trans. Magn. **42**, 3285 (2006).
6. G. W. Day *et al.*, Opt. Lett. **7**, 238 (1982).
7. V. Annovazzi-Lodi, S. Merlo, and A. Leona, J. Lightwave Technol. **13**, 2349 (1995).
8. W. E. Gettys, F. J. Keller, and M. J. Skove, *Physics, Classical and Modern* (McGraw-Hill, New York, 1989).
9. L. Sun, S. Jiang, J. D. Zuegel, and J. R. Marciante, Opt. Lett. **34**, 1699 (2009).
10. L. Sun, S. Jiang, and J. R. Marciante, "All-Fiber Optical Isolator Based on Faraday Rotation in Highly Terbium-Doped Fiber," submitted to Optics Letters.
11. D. A. Nolan *et al.*, Opt. Lett. **29**, 1855 (2004).
12. M. McCaig and A. G. Clegg, *Permanent Magnets in Theory and Practice*, 2nd ed. (Wiley, New York, 1987).
13. J. R. Marciante, N. O. Farmiga, J. P. Kondis, and J. R. Frederick, Opt. Express **11**, 1096 (2003).
14. P. A. Williams *et al.*, Appl. Opt. **30**, 1176 (1991).

Femtosecond Optical Pump–Probe Characterization of High-Pressure–Grown $Al_{0.86}Ga_{0.14}N$ Single Crystals

The group-three–nitride (III-N) semiconducting system, in general, and (Al,Ga)N compounds, in particular, have attracted a very strong interest in recent years for the development of optoelectronic devices from the green to deep-ultraviolet wavelength range.[1] Moreover, III-N materials have also well-documented advantages in high-temperature and high-power electronics, as well as in acoustic-wave applications.[2–4] A considerable amount of research has been devoted to the epitaxial growth of (Al,Ga)N films, using MOCVD and/or MBE methods.[5,6] The growth of bulk, dislocation-free (Al,Ga)N crystals is also critical not only for getting much-needed single-crystal substrates for homoepitaxy, but also for applications where the devices operate based on the volume-absorption principle, e.g., x-ray and other radiation detectors. Unfortunately, the growth of even small, high-quality (Al,Ga)N single crystals, especially those with the high Al content, is very challenging, and only very recently, the synthesis of $Al_xGa_{1-x}N$ crystals with the Al content x between 0.5 and 1 has been reported by Belousov *et al.*[7]

In this article, we report our femtosecond, time-resolved pump–probe spectroscopy studies in $Al_{0.86}Ga_{0.14}N$ (AlGaN) single crystals and demonstrate that the observed transient transmissivity signal is a superposition of the femtosecond correlation signal caused by a coherent process of simultaneous absorption of both the pump and probe photons and a conventional, picosecond-in-duration hot-electron cooling. The pump–probe correlation studies, typically called a two-photon absorption (TPA) process, are important in nonlinear optics and have been investigated in many semiconducting materials, such as GaAs, GaN, and (In,Ga)N;[8] the large magnitude of the TPA coefficients β are reported in Ref. 9. Moreover, the TPA measurement is a useful tool for characterizing optical pulse widths and determining the optical energy gap in wide-bandgap semiconductor materials. At the same time, the photoresponse relaxation transient, which in our case follows the initial correlation spike, provides information about the electron–phonon decay time and the across-bandgap carrier recombination.

Our single AlGaN crystals used in this study were synthesized from solution at high temperatures using a high-pressure gas system, which consists of a compressor, pressure intensifier, and a high-pressure chamber of 40-mm internal diameter with an internal, three-zone furnace. First, a polycrystalline (Al,Ga)N precursor pellet was synthesized by a solid-phase reaction in a cubic anvil at 30 kbar and 1800°C from a mixture of high-purity GaN and AlN powders (Alfa Ceasar). The prereacted pellet acted as an Al source and was placed in the Ga melt in the upper part of a graphite crucible. The graphite crucible had an internal diameter of 14 mm and a length of 70 mm. For the AlGaN crystal growth, we applied a nitrogen pressure of up to 7.5 kbar and a temperature of up to 1760°C, following our earlier, experimentally derived pressure-versus-temperature diagram.[7] The synthesis process was conducted under the constant thermal gradient of about 20 K/cm for 6 to 7 days. The crystals grown in the colder part of the graphite crucible were colorless, up to $0.8 \times 0.8 \times 0.8$ mm^3 in size, and exhibited the hexagonal form and wurtzite structure. After processing, the samples were etched from the remaining unreacted Ga/Al melt using hydrochloric acid and *aqua regia*. The structural composition was determined by a laser-ablation, inductively coupled plasma mass spectrometry technique.

Our time-resolved photoresponse studies were performed in a transmission configuration, using a two-color, femtosecond pump–probe technique. We used a passively mode-locked Ti:sapphire laser as a source of 100-fs-wide, 76-MHz-repetition-rate optical pulses, tunable in the 720- to 860-nm range. The Ti:sapphire output was split into two beams by a 60/40 beam splitter. The pump beam, frequency doubled by using a BaB_2O_4 crystal, was focused onto the surface of the AlGaN crystal with a spot diameter of ~100 μm at an incident angle of ~20°. The probe pulses, directly generated by the Ti:sapphire laser, were delayed with respect to the pump by passing through a computer-controlled delay stage and were near normally aimed at the sample on the same area as the pump beam with a spot diameter of ~10 μm. The small spot size of the probe

beam ensured that it probed a region with uniform pump photoexcitation and somewhat relaxed the stringent requirement for the delay-stage alignment. The probe light transmitted through the sample was filtered from any scattered pump photons by a near-infrared filter and collected by a photodetector. The photodetector signal was measured by a lock-in amplifier, synchronized with an acousto-optical modulator operating at frequency of 99.8 KHz. We stress that in our experiments both the pump and probe beams had an average power incident on a sample of a same order (with a typically used ratio $P_{\text{pump}}/P_{\text{probe}}$ of 1:2) and their photon energies were much smaller than the expected ~6-eV bandgap of our AlGaN sample. All experiments were performed at room temperature.

Figure 120.48 presents a typical time-resolved normalized differential transmissivity ($\Delta T/T$) transient, obtained by exciting our AlGaN crystal with a 380-nm pump and probed with a 760-nm probe. Figure 120.48(a) depicts the full transient in a long-time window, and the dashed line is a numerical fit, which will be described later. We observe an initial (near-zero delay), subpicosecond-in-duration negative spike, followed by a much-slower exponential decay. In Fig. 120.48(b), we show the same waveform (solid squares), but on a much-shorter (<3 ps) time scale, and note that the experimental $\Delta T/T$ transient can be very accurately decomposed into a Gaussian-shaped pulse (open triangles) of a full width at half maximum (FWHM) of 310 fs and a second transient (open circles) with an approximately 1-ps-wide rise time, modeled as the error function, and a slow [on the scale of Fig. 120.48(b)] exponential decay. The superposition of the above two transients (open squares) fits our experimental data extremely well [see also dashed line in Fig. 120.48(a)].

Based on our decomposition procedure, we can interpret the ultrafast Gaussian pulse as a TPA-type correlation signal since the 310-fs FWHM coincides well with the overlap of our ~150-fs-wide pump and probe pulses. The TPA signal can be observed only when both the pump and probe photons are simultaneously incident on the sample and their total energy is greater than the material's bandgap E_g. Therefore, we must conclude that in our case, the correlation effect actually involves three photons (one pump photon and two probe photons) since any other combination would give a total photon energy that would be either much too large or too low. The second, slow component of the experimental transient is a typical $\Delta T/T$ pump–probe photoresponse signal, associated in direct-bandgap semiconductors (i.e., in III-N materials) with across-the-bandgap electron-hole excitation, followed by a subsequent cooling of photo-induced electrons. On a long time scale, the relaxation component of the $\Delta T/T$ transient can be fitted [Fig. 120.48(a) (dashed line)] as a bi-exponential decay with an initial 12-ps time constant, followed by a slow, ~130-ps-

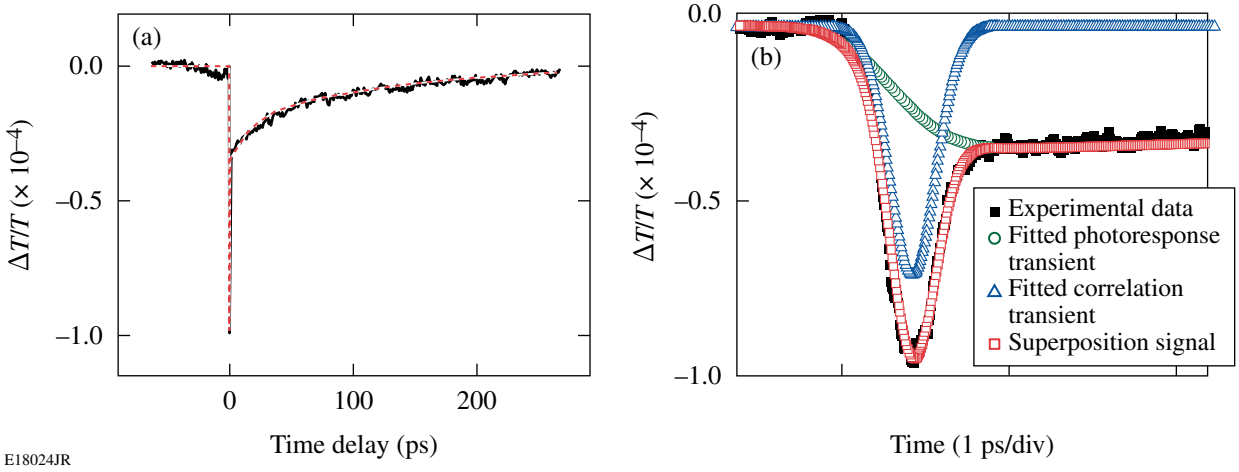

Figure 120.48
(a) Time-resolved $\Delta T/T$ transient measured for the pump λ = 380 nm and the probe λ = 760 nm. The red dashed line represents a theoretical fit. (b) The same $\Delta T/T$ transient (black squares), but on a much-shorter time scale. The blue triangles are the best fit corresponding to a Gaussian-shaped correlation signal of the pump and probe photons. The green circles fit the photoresponse component of the transient, with the rising part represented by the error function and the decay modeled as a double-exponent relaxation. The red squares correspond to the superposition of the correlation and photoresponse components and overlay the experimental data. The fit of the red squares in (b) is identical to the red dashed line in (a).

long relaxation. The fast decay time constant represents the electron–phonon relaxation process toward a quasi-equilibrium condition at the bottom of the conduction band, while the slow time constant is the carrier lifetime, which includes both the radiative (across the bandgap) and nonradiative (trapping) recombination.

We have also studied the amplitude dependence of the photon-correlation signal deconvoluted from the experimental $\Delta T/T$ transient on the pump power's density (see Fig. 120.49) and have found that, in the regime of low attenuation of the incident pump and probe beams, it followed a linear behavior, well-established for the TPA process:[10]

$$\Delta T/T = -\beta d P_{\text{eff}}, \tag{1}$$

where d is the sample thickness and P_{eff} is the effective, absorbed pump-beam power per pulse. The data presented in Fig. 120.49 were collected for the pump-beam wavelength λ = 380 nm and d = 1 mm. Using Eq. (2) and taking into account that in our experiment the pump spot diameter is 100 μm and its absorption coefficient is ~80%, the linear fit (solid line) in Fig. 120.49 allowed us to calculate β = 0.42±0.02 cm/GW. We note that our β value is significantly smaller than the ones observed in other III-N materials [e.g., for GaN, β = 12 cm/GW at 377 nm (Ref. 8)], apparently due to a much larger E_g value for (Al,Ga)N.

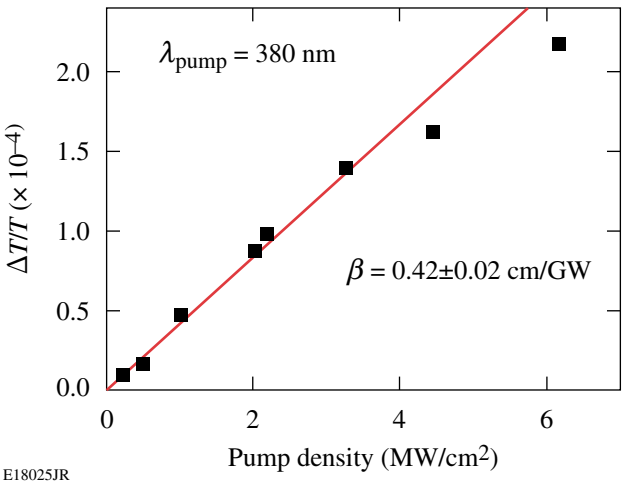

Figure 120.49
Dependence of the correlation signal amplitude (squares) on the pump power's intensity, measured for a 380-nm pump wavelength. The solid red line is the linear best fit and its slope corresponds to the β coefficient.

Following the procedure discussed in connection with Fig. 120.49, we obtained β coefficients for the pump λ's ranging from 360 nm to 430 nm. The results (solid circles) are summarized in Fig. 120.50 and compared directly with the theoretical model of Sheik–Bahae *et al.*,[11] derived for wide, direct-bandgap semiconductors:

$$\beta(\omega) = K\frac{\sqrt{E_p}}{n_0^2 E_g^3} F_2\left(\frac{\hbar\omega}{E_g}\right), \tag{2}$$

where K is a material-independent constant, E_p is the matrix element related to the interband momentum and is ~21 eV for most semiconductors, n_0 is the refractive index, and the $F_2\left(\hbar\omega/E_g\right)$ function is given as $F_2 = (2x-1)^{3/2}/(2x)^5$.

In our case, K = 3100, E_g = 5.81 eV (from our bandgap measurement presented below), and n_0 is a function of λ and for our AlGaN sample is given by $n_0(\lambda) = 2.02 + 4.7e^{-\lambda/93.86}$ (Ref. 5). We observe a very good agreement of our experimental β values with the Sheik–Bahae model, within the pump light λ's achievable by our experimental setup. The inset in Fig. 120.50 presents a subset of the same data (β values very close to zero) as the main panel, but plotted as a function of total energy of photons incident on our sample and participating in the pump–probe correlation process (one pump photon and two probe photons). In this way, we can observe the optical

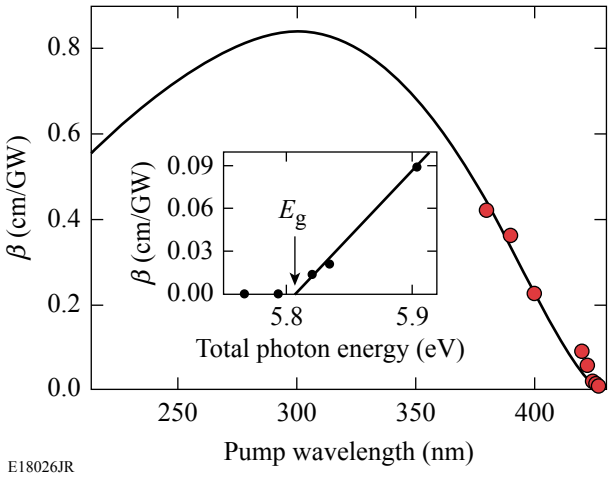

Figure 120.50
The correlation coefficient β as a function of the pump beam's wavelength. The red circles are our experimental data points, while the solid line corresponds to the Sheik–Bahae theory [Eq. (3)]. The inset shows β dependence on the total energy of absorbed photons with the optical bandgap absorption edge indicated.

transition edge in detail, and a simple linear fit allows us to very accurately determine the optical E_g of our AlGaN crystal to be equal to 5.81±0.01 eV.

We have performed time-resolved characterization of AlGaN single crystals using femtosecond pump–probe spectroscopy with both the pump and probe beams having wavelengths much longer than the wavelength corresponding to the AlGaN bandgap. Examination of our experimental data showed that two different processes contributed simultaneously to the $\Delta T/T$ transients observed on our experiments. The first was the ~300-fs-wide correlation signal, observed near the zero-delay point and corresponding to the photon correlation process involving a coherent (simultaneous) absorption of one pump and two probe photons. It was followed by a second, much slower (tens of picosecond in duration) relaxation transient representing photoresponse and cooling of photo-excited carriers. Analysis of the correlation signal amplitude on both the pump photon power and wavelength allowed us to obtain the correlation β coefficient for our AlGaN crystal and its spectral dependence. We demonstrated that, within our laser-tuning range, $\beta(\lambda)$ agreed very well with the Sheik–Bahae theory. We also determined that the optical E_g of AlGaN was 5.81±0.01 eV. The dynamics of the photoresponse decay component demonstrated that the carrier relaxation in AlGaN was dominated by trapping since the measured 130-ps time constant was relatively short.

ACKNOWLEDGMENT

The authors would like to thank Prof. D. Günther from the Laboratory for Inorganic Chemistry, ETH Zurich, for his assistance in (Al,Ga)N mass spectrometry characterization. J. Z. acknowledges support from the Frank Horton Graduate Fellowship Program at the University of Rochester Laboratory for Laser Energetics, funded by the U.S. Department of Energy Office of Inertial Confinement Fusion under Cooperative Agreement No. DE-FC52-08NA28302 and the New York State Energy Research and Development Authority. The support of DOE does not constitute an endorsement by DOE of the views expressed in this article.

REFERENCES

1. S. N. Mohammad, A. A. Salvador, and H. Morkoc, Proc. IEEE **83**, 1306 (1995).
2. Q. Chen *et al.*, Appl. Phys. Lett. **70**, 2277 (1997).
3. U. K. Mishra *et al.*, Proc. IEEE **96**, 287 (2008).
4. S. Wu, P. Geiser, J. Jun, J. Karpinski, J.-R. Park, and R. Sobolewski, Appl. Phys. Lett. **88**, 041917 (2006).
5. M. Stutzmann *et al.*, Mater. Sci. Eng. B **B50**, 212 (1997).
6. Y. Koide *et al.*, J. Appl. Phys. **61**, 4540 (1987).
7. A. Belousov, S. Katrych, J. Jun, J. Zhang, D. Günther, R. Sobolewski, and J. Karpinski, J. Cryst. Growth **311**, 3971 (2009).
8. C.-K. Sun *et al.*, Appl. Phys. Lett. **76**, 439 (2000).
9. S. Krishnamurthy, K. Nashold, and A. Sher, Appl. Phys. Lett. **77**, 355 (2000).
10. C. Rauscher and R. Laenen, J. Appl. Phys. **81**, 2818 (1997).
11. M. Sheik-Bahae *et al.*, IEEE J. Quantum Electron. **27**, 1296 (1991).

LLE's Summer High School Research Program

During the summer of 2009, 16 students from Rochester-area high schools participated in the Laboratory for Laser Energetics' Summer High School Research Program. The goal of this program is to excite a group of high school students about careers in the areas of science and technology by exposing them to research in a state-of-the-art environment. Too often, students are exposed to "research" only through classroom laboratories, which have prescribed procedures and predictable results. In LLE's summer program, the students experience many of the trials, tribulations, and rewards of scientific research. By participating in research in a real environment, the students often become more excited about careers in science and technology. In addition, LLE gains from the contributions of the many highly talented students who are attracted to the program.

The students spent most of their time working on their individual research projects with members of LLE's technical staff. The projects were related to current research activities at LLE and covered a broad range of areas of interest including experimental diagnostic development, computational modeling of implosion physics, laser physics, experimental and theoretical chemistry, materials science, cryogenic target characterization, target vibration analysis, and computer control systems (see Table 120.VII).

The students attended weekly seminars on technical topics associated with LLE's research. Topics this year included laser physics, fusion, holography, glass fracture, nonlinear optics, electrostatics, and electronic paper. The students also received safety training, learned how to give scientific presentations, and were introduced to LLE's resources, especially the computational facilities.

The program culminated on 26 August with the "High School Student Summer Research Symposium," at which the students presented the results of their research to an audience including parents, teachers, and LLE staff. The students' written reports will be made available on the LLE Web site and bound into a permanent record of their work that can be cited in scientific publications.

Two hundred and forty-nine high school students have now participated in the program since it began in 1989. This year's students were selected from a record 80 applicants.

At the symposium LLE presented its 13th annual William D. Ryan Inspirational Teacher Award to Mr. Jeffrey Klus, a mathematics teacher at Fairport High School. This award is presented to a teacher who motivated one of the participants in LLE's Summer High School Research Program to study science, mathematics, or technology and includes a $1000 cash prize. Teachers are nominated by alumni of the summer program. Mr. Klus was nominated by Nicholas Hensel and Angela Ryck, participants in the 2008 Summer Program. Nick describes Mr. Klus as "a great teacher" with an "obvious enjoyment of teaching and the material he teaches. Sarcastic quips and quirky comments were always close at hand in class, bringing humor to the otherwise droll, factual world of mathematics…I will always remember Mr. Klus's love for teaching, his continually enjoyable humor, and the way he treated all of his students as equals…He inspired in me a fresh love for math." Angela agreed about the humor Mr. Klus brought to class. She wrote, "Mr. Klus is a legend in my school…His entertaining stories kept us laughing at our seats, and the kids who rarely smiled in math class beamed in his presence…My favorite thing about Mr. Klus is that he encourages students to try new things… Mr. Klus has had an enormous effect on my education, and he is truly an inspiration to me." Ms. Pam Ciranni, Assistant Principal of Fairport High School, added, "Jeff is the driving force behind the AP computer classes. He is an advisor to the masterminds and chess clubs. He is a mentor to the other teachers. He is a consummate professional, understands the students' needs, and acts with the students as a peer."

Table 120.VII: High School Students and Projects—Summer 2009.

Name	High School	Supervisor	Project Title
Dustin Axman	Irondequoit	R. Rombaut, R. Russo	A Graphical Network Interface to Oscilloscopes
Leela Chocklingham	Brighton	K. L. Marshall	Abrasion-Resistant Anti-Reflective Silane Sol-Gel Coatings
Ted Conley	McQuaid	J. Bromage	Automated Injection for High-Power Fiber Amplifiers
Cheryl Liu	Pittsford Sutherland	J. P. Knauer	Neutron Detection with High Bandwidth and High Dynamic Range
Trevor Lu	Webster Thomas	D. H. Edgell	X-Ray Phase-Contrast Characterization of Cryogenic Targets
Evan Miller	Pittsford Mendon	J. A. Delettrez	Electron Reflection in Monte Carlo Simulations with the Code GEANT
Lindsay Mitchel	Spencerport	R. S. Craxton	Exploration of the Feasibility of Polar Drive on the LMJ
Justin Owen	Irondequoit	R. Kidder, C. Kingsley, M. Spilatro	Using Networked Data Services for System Analysis and Monitoring
Ben Petroski	Livonia	W. T. Shmayda	Water Desorption from Copper at Room Temperature
Aaron Van Dyne	Brighton	J. A. Marozas	Optimization of 1-D Multiple-FM SSD Designs for OMEGA EP and the NIF
Marisa Vargas	Webster Thomas	C. Dorrer, K. L. Marshall	Laser Beam Shaping with Optically Patterned Liquid Crystals
Kate Walden	Wayne	T. C. Sangster, M. Burke	The Effect of Alcohol Hydroxide Solutions on the Bulk Etch Rate of CR-39
Victor Wang	Webster Thomas	K. L. Marshall	Computational Modeling of Optically Switchable Azobenzenes
Paul Watrobski	Penfield	W. Theobald	UV Probe Beam for Plasma Characterization and Channeling Experiments
Mia Young	Penfield	R. Epstein	Analysis of Implosion Radiographs
Harvest Zhang	Brighton	L. Lund	Resonance and Damping Characterization in Cryogenic Fusion Targets

FY09 Laser Facility Report

During FY09 the Omega Laser Facility conducted 1153 target shots on OMEGA and 349 target shots on OMEGA EP for a total of 1502 combined target shots (see Table 120.VIII). OMEGA conducted 24 DT and 24 D_2 low-adiabat spherical cryogenic target implosions. Triple-picket pulse-shaping developments highlighted the ongoing development of direct-drive cryogenic implosion capability. A planar cryogenic platform to measure spherical shock timing was validated and used extensively to support spherical cryogenic experiments. A total of 31 planar cryo target shots were taken. The OMEGA Availability and Experimental Effectiveness averages for FY09 were 93% and 96%, respectively.

Table 120.VIII: OMEGA Facility target shot summary for FY09.

OMEGA Target Shot Summary					
Laboratory	Planned Number of Target Shots	Actual Number of Target Shots	NIC	Shots in Support of NIC	Non-NIC
LLE	476	488	68	420	0
LLNL	200	230	125	0	105
NLUF	145	165	0	0	165
LANL	85	93	3	0	90
LBS	70	73	0	0	73
CEA	45	51	0	0	51
AWE	30	35	0	0	35
U. Mich.	10	11	0	0	11
SNL	5	7	7	0	0
Total	1066	1153	203	420	530
OMEGA EP Target Shot Summary					
Laboratory	Planned Number of Target Shots	Actual Number of Target Shots	NIC	Shots in Support of NIC	Non-NIC
LLE	215	212	0	212	0
LLNL	40	42	16	0	26
NLUF	40	43	0	0	43
LBS	45	36	0	0	36
LANL	10	11	0	0	11
CEA/AWE	5	5	0	0	5
Total	355	349	16	212	121

OMEGA EP was operated extensively in FY09 for a variety of internal and external users. A total of 298 short-pulse IR target shots were conducted. Of these, 212 target shots were taken on the OMEGA EP target chamber and 86 joint target shots were taken on the OMEGA target chamber. Beams 1 and 2 were activated to target in the UV, and the first four-beam UV target shots were conducted. A total of 76 OMEGA EP target shots included UV beams. OMEGA EP averaged 4.7 target shots per day with Availability and Experimental Effectiveness averages for FY09 of 90% and 97%, respectively. Highlights of other achievements for FY09 are shown in Table 120.VIII.

OMEGA pulse-shaping capability continues to evolve to meet the demands of producing triple-picket–shaped pulses for cryogenic experiments (see Fig. 120.51). New environmental hardware and controls upgrades to the Driver Electronics Room have improved temperature and humidity stability. The thermal stability improvements resulted in better stability for the temporal pulse shape. As a result, triple-picket pulse shapes that meet increasingly demanding specifications are now routinely achieved. Pulse-shape measurement diagnostics and analysis software continue to become more sophisticated to accurately predict picket energies and UV pulse shapes.

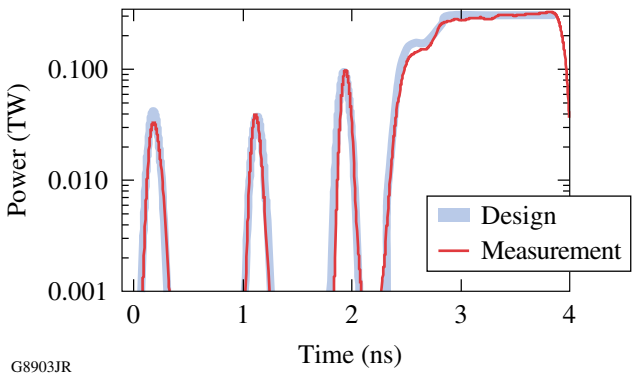

Figure 120.51
OMEGA average pulse shape from a cryogenic target implosion (shot 55723) using pulse shape HE330201T. This shot produced 300-mg/cm^2 ρR, the highest-recorded ρR to date.

The Omega Laser Facility added a planar Moving Cryogenic Transfer Cart (MCTC) to the existing inventory of five MCTC's, bringing the active total to two planar target MCTC's and four spherical target MCTC's. It is an important addition since the planar MCTC's can be interleaved to increase the number of planar experiments that can be carried out in a single shot day. Up to five planar target shots were taken in a single shot day in FY09, and with some minor adjustments to MCTC operations in FY10, the total will be increased further. Planar cryogenic target shots have been particularly instrumental in combination with shock-timing diagnostics to optimize the performance of cryogenic implosions.

A significant change was made in FY09 to the mounting system used for cryogenic implosions. The previous "C-mount" that used four spider-silk supports to suspend the target was replaced by a single-stalk-mount design that has proven to be an operationally robust component. The high-pressure fill, transfer to MCTC, and deployment attrition rates were reduced to negligible levels while maintaining and improving target performance metrics. Operationally, the key metrics are laser pulse shape, layer quality, and target offset (displacement from target chamber center at shot time). The fraction of targets with high-quality layers has increased to ~85%, and the target offset performance has improved to ~50%. Offset remains a difficult challenge and is being addressed through improved use of the tools built into the Target Viewing System and a re-engineered MCTC for spherical targets.

The Target Viewing System (TVS) upgrade in FY08 resulted in new tools becoming available for cryogenic target operations. The primary tool that has been used to make significant improvements in the cryogenic target offset is a pair of 2000-frame-per-second fast cameras. These cameras were used in FY09 to characterize the dynamic performance of the four spherical target MCTC's. There are sources of mechanical instability that occur as a result of the rapid removal of the cryogenic shroud system that occasionally perturb the target beyond acceptable levels; however, a significant fraction of targets are now within the desired 20 μm or less of displacement from target chamber center. This was achieved by three main improvements: use of the fast cameras for characterizing the target alignment carefully with shrouds in place and removed, optimizing the retraction trajectories, and cold-head-pump–induced vibration management.

A Grating Inspection System (GIS) was installed and activated on both OMEGA EP compressors. The GIS is an illumination and imaging scanning system that measures scattered light from the fourth grating of the compressor to detect optical damage. The system can identify grating damage site growth that is 500 μm or larger. The GIS is a key facility diagnostic that is routinely operated after each laser shot to ensure that maximum energy is available to short-pulse users, without risking damage to the gratings.

OMEGA EP was routinely operated at ≥1 kJ in a 10-ps pulse. An exploratory energy-ramp campaign was conducted with energies up to 2.1 kJ on target at ~10 ps to characterize short-pulse optic damage growth rates.

Determining the fraction of laser energy transferred into energetic electrons in intense laser–matter interactions is a vital parameter in high-fluence backlighter development and advanced ignition experiments, including fast ignition. Foil targets were irradiated in OMEGA EP experiments at laser intensities of $I > 10 \times 10^{18}$ W/cm^2 with up to 2.1 kJ of laser energy and pulse durations between 10 to 12 ps. These are the highest-energy, short-pulse laser–matter interaction experiments ever conducted. These experiments demonstrate that powerful electron sources can be generated with high-power, short-pulse lasers in the multikilojoule regime.

The temporal contrast of the two short-pulse OMEGA EP beamlines has been measured up to 0.5 ns before the main pulse. The diagnostic operated for more than 60 high-energy shots, demonstrating very good reliability and reproducibility. No evidence of short prepulse was found prior to main pulse, and an incoherent pedestal generated by the optical parametric chirped-pulse–amplifier's front-end was precisely characterized. The pedestal extends a few nanoseconds before the main pulse and has an intensity of less than 10^{-6} of the peak intensity for a 10-ps pulse. Approximately 10^{-4} of the laser energy is contained in this. Since the pedestal's energy contrast ratio is independent of the compressed pulse width, the intensity contrast would be an order of magnitude larger for a 1-ps pulse (i.e., $>10^7$). Contrast improvements based on LLE-demonstrated technologies are planned for the future to increase the intensity contrast.

There is considerable demand for high-pressure experiments on OMEGA EP. The velocity interferometry system for any reflector (VISAR) is the primary instrument for these experiments. A VISAR diagnostic based on the OMEGA system was installed in June 2009. This system worked as designed on the first shot and is now available for the high-pressure experiments scheduled on OMEGA EP in FY10.

National Laser Users' Facility and External Users' Programs

Under the governance plan implemented in FY08 to formalize the scheduling of the Omega Laser Facility as an NNSA facility, OMEGA shots are allocated by campaign. The majority of the FY09 target shots (56.6%) were allocated to the National Ignition Campaign (NIC), and integrated experimental teams from LLNL, LANL, SNL, and LLE conducted a variety of NIC-related experiments on both the OMEGA and OMEGA EP Laser Systems. Twenty percent (20%) of the FY09 shots were allocated to high-energy-density stewardship experiments (HEDSE) from LLNL and LANL. Under this governance plan, 25% of the facility shots were allocated to basic science experiments. Roughly half of these were dedicated to university basic science, i.e., the National Laser Users' Facility (NLUF) Program, and the remaining shots were allotted to the Laboratory Basic Science (LBS) Program, comprising peer-reviewed basic science experiments conducted by the national laboratories and LLE/FSC.

The Omega Facility is also being used for many experiments by teams from the Commissariat à l'Énergie Atomique (CEA) of France and the Atomic Weapons Establishment (AWE) of the United Kingdom. These programs are conducted on the basis of special agreements put in place by DOE/NNSA and the participating institutions.

The external users during this year included a record 11 collaborative teams that participated in the NLUF Program as shown in Table 120.IX. Ten teams from LLNL, LANL, and LLE were allotted shots under the LBS Program (Table 120.X). Integrated experimental teams from the national laboratories and LLE conducted 851 shots for the NIC, and investigators from LLNL, LANL, and LLE conducted over 232 shots for the HEDSE programs. A total of 56 shots were conducted by scientists from CEA and 35 shots were carried out by scientists from AWE.

Table 120.IX: FY09–FY10 NLUF Projects.

Principal Investigator	Affiliation	Proposal Title
F. Beg	University of California, San Diego	Systematic Study of Fast-Electron Transport and Magnetic Collimation in Hot Plasmas
R. P. Drake	University of Michigan	Experimental Astrophysics on the OMEGA Laser
R. Falcone	University of California, Berkeley	Detailed *In-Situ* Diagnostics of Multiple Shocks
U. Feldman	ARTEP, Inc.	OMEGA EP–Generated X-Ray Source for High-Resolution 100- to 200-keV Point-Projection Radiography
Y. Gupta	Washington State University	Ramp Compression Experiments for Measuring Structural Phase Transformation Kinetics on OMEGA
P. Hartigan	Rice University	Dynamics of Shock Waves in Clumpy Media
R. Jeanloz	University of California, Berkeley	Recreating Planetary Core Conditions on OMEGA, Techniques to Produce Dense States of Matter
K. Krushelnick	University of Michigan	Intense Laser Interactions with Low-Density Plasmas Using OMEGA EP
R. Mancini	University of Nevada, Reno	Three-Dimensional Studies of Low-Adiabat Direct-Drive Implosions on OMEGA
M. Meyers	University of California, San Diego	Response of BCC Metals to Ultrahigh Strain Rate Compression
R. D. Petrasso	Massachusetts Institute of Technology	Monoenergetic Proton and Alpha Radiography of Laser-Plasma-Generated Fields and of ICF Implosions

Table 120.X: Approved FY09 LBS Experiments.

Principal Investigator	Affiliation	Proposal Title	Facility Required
R. Betti	LLE/FSC	Ultra-Strong Shock and Shock-Ignition Experiments on OMEGA EP	OMEGA EP long pulse/short pulse
H. Chen	LLNL	Electron–Positron Jets	OMEGA EP short pulse/2 beams
J. H. Eggert	LLNL	Powder X-Ray Diffraction on OMEGA: Phase Transitions in Tin	OMEGA
M. B. Hegelich	LANL	Proton and Light Ion Production for Fast Ignition and Warm Dense Matter Applications	OMEGA EP short pulse
D. G. Hicks	LLNL	A New Technique for Efficient Shockless Compression to Several Mbar: Studies Using X-Ray Absorption Spectroscopy	OMEGA 40 beams
A. J. MacKinnon	LLNL	Fast Electron Transport in Hot Dense Matter	OMEGA EP long pulse
H.-S. Park	LLNL	Study of High-Z Material Properties Under Compression Using High Energy Backlighter Diffraction	OMEGA EP long pulse/short pulse
P. K. Patel	LLNL	Fundamental Benchmarking of Relativistic Laser–Matter Interaction Physics	OMEGA EP short pulse
S. P. Regan	LLE	Probing Hydrogen–Helium Warm Dense Matter (WDM) with Inelastic X-Ray Scattering: Toward the Equation of State of Jupiter's Core	OMEGA
W. Theobald	LLE	Integrated Core Heating for Fast Ignition	OMEGA and OMEGA EP

In this section, we briefly review all the basic science activity on OMEGA during FY09, including NLUF and LBS Programs, briefly summarize the FY09 NIC and high-energy-density experiments, and conclude with a summary of CEA and AWE activities.

FY09 NLUF Programs

FY09 was the first of a two-year period of performance for the NLUF projects approved for the FY09–FY10 funding and OMEGA shots. Eleven NLUF projects were allotted OMEGA and OMEGA EP shot time and received a total of 165 shots on OMEGA and 43 shots on OMEGA EP in FY09. Some of this work is summarized in this section. A new solicitation will be issued by the DOE in FY10 for NLUF grants for the period FY11–FY12.

Systematic Study of Fast-Electron Generation and Transport

Principal Investigators: T. Yabuuchi and F. N. Beg (University of California, San Diego)

Co-investigators: H. Sawada (University of California, San Diego); R. B. Stephens (General Atomics); M. H. Key and P. Patel (LLNL); D. Batani (University of Milano, Bicocca); and L. A. Gizzi (IPCF-CNR)

Understanding fast-electron generation and transport in the cone and hot, dense plasma is crucial to the success of the cone-guided fast-ignition scheme. The goal of the University of California at San Diego's NLUF project is to investigate the fast-electron transport in hot plasmas and to demonstrate collimation of fast electrons by an external magnetic field. The project consists of three steps: (1) characterization of fast-electron source and transport through the cone tip; (2) study of fast-electron transport in hot, dense plasmas; and (3) demonstration of fast-electron collimation with an external magnetic field. The first step of the project is described here: a copper wire is attached to the tip of a hollow gold cone to investigate the characteristics of the fast electrons through the tip of the cone after they are generated by the OMEGA EP 10-ps pulse.

Figure 120.52 shows the schematic of the experimental setup of cone/wire shots on the OMEGA EP laser. The one short pulse (interaction pulse) was focused into the cone/wire target. Here, the wire (40-μm diam, 1 mm long) was made of copper and attached to the tip of a gold cone with a 20-μm-thick sidewall capped with 6-μm-thick, 30-μm-inner-diam foil. The detailed target information is shown in the inset of Fig. 120.52. The Cu K_α x-ray emission from the wire was diagnosed with a highly oriented pyrolytic graphite (HOPG) spectrometer at

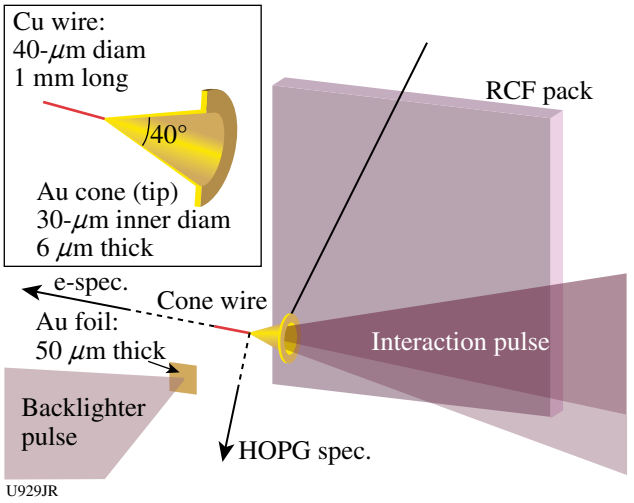

Figure 120.52
Experimental setup for cone/wire shots with proton deflectometry. The directions of the x-ray and electron spectrometers are indicated in the figure. The detailed cone/wire information is shown in the inset.

the normal direction to the wire axis. The energy spectra of the fast electrons were measured along the wire direction, i.e., on the interaction laser axis. In addition, the second short pulse (backlighter pulse) was used to generate a high-energy proton beam to measure the electrostatic field around the cone/wire target using a proton deflectometry technique. The backlighter pulse axis was perpendicular to the axis of the interaction pulse. A stack of radiochromic films (RCF's) was positioned on the axis of the backlighter pulse to detect protons at various energies, which can provide the electric field information at various timings, depending on the proton energies with a magnification of 9. The detectable proton energy range was 5 MeV to 60 MeV. The temporal resolution of the proton deflectometry was 10 ps to 50 ps. In the experiment, the interaction pulse energy was varied from 260 J to 820 J at a 10-ps pulse duration. At the best-focus position, 80% of the laser energy was contained within a 45-μm-diam spot. The beam-pointing stability was monitored with an x-ray pinhole camera that can also monitor the plasma inside the cone. A 0.7-ps pulse duration was used as the backlighter pulse to minimize the proton-generation time window. The energy of the backlighter pulse was up to 300 J.

The Cu K_α signal was observed on the HOPG spectrometer with a signal-to-background contrast of up to 1.4. The Cu K_α x-ray signal was observed to be linearly dependent on the interaction pulse energy as shown in Fig. 120.53(a). The results indicate that the coupling efficiency from the laser to the K_α photons is quasi-constant in the energy range of 260 J to 814 J; therefore, more electrons pass through the tip of the cone at the higher laser energy. The energy spectra of the vacuum electrons observed at 260-J and 814-J shots are shown in Fig. 120.53(b). Preliminary data analysis of the spectra shows that the slope temperature varies from 1.7 MeV to 2.5 MeV.

Figure 120.54 shows the proton radiographs observed on a shot with 260 J in the interaction pulse. Figure 120.54(a) shows a radiograph taken before the interaction pulse is incident on

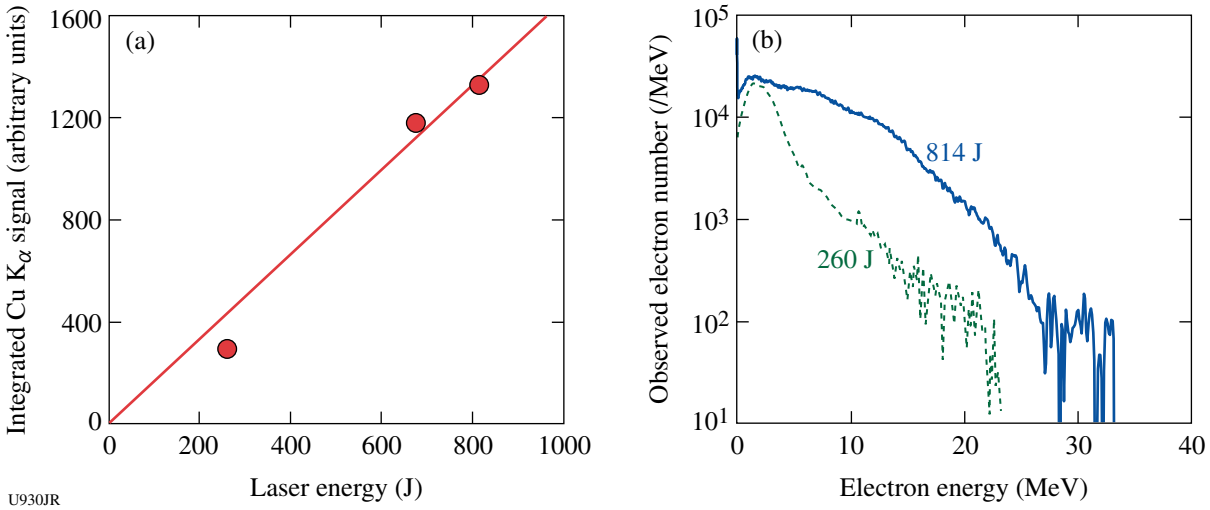

Figure 120.53
(a) Dependence of integrated Cu K_α signal on laser energy. The straight line is a linear fit to the data. (b) Energy spectra of vacuum fast electrons measured on the wire axis.

the cone/wire target by protons with an energy of ~18 MeV. The proton beam deflected by the electrostatic field around the target was observed with low-energy protons (5 MeV) as shown in Fig. 120.54(b). Protons were deflected by the electrostatic field only in the vertical direction in the figure because the magnetic field was in the azimuthal direction around the wire and canceled out any deflection. The electrostatic field strength observed in Fig. 120.54(b) was estimated at approximately tens of kV/μm using a simple calculation of proton ray tracing. Note that the maximum field strength could be higher than this estimate because the field strength can vary within a much shorter time scale than the temporal resolution of the diagnostic setup. Hybrid/PIC (particle-in-cell) modeling has been performed to investigate the fast electrons propagating through the cone tip. The transport study with such fast electrons in hot, dense plasmas and in an external magnetic field will be performed in the coming year.

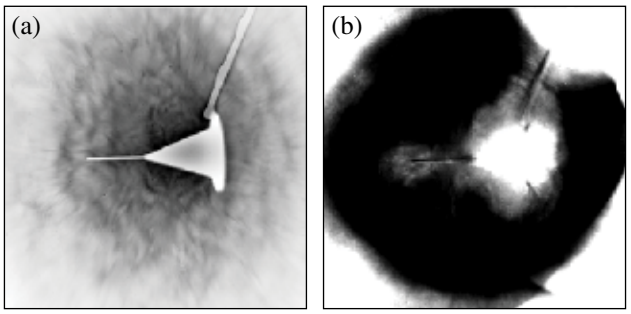

U931JR

Figure 120.54
Cone/wire target proton backlight images observed with (a) ~18-MeV and (b) 5-MeV protons at an interaction pulse energy of 260 J. The 5-MeV protons passed through the cone/wire target at about 200 ps after the interaction pulse hits the target.

Experimental Astrophysics on the OMEGA Laser

Principal Investigator: R. P. Drake (University of Michigan)
Co-investigators: D. Arnett (University of Arizona); T. Plewa (Florida State University); J. Glimm, D. Swesty, X. Li, and A. C. Calder (State University of New York–Stony Brook); I. Sokolov, J. Holloway, and K. Powell (University of Michigan); J. P. Knauer and T. R. Boehly (LLE); and B. A. Remington, H. F. Robey, J. F. Hansen, A. R. Miles, S. H. Glenzer, and D. H. Froula (LLNL)

The OMEGA laser can create conditions of very high energy density that are relevant to astrophysical phenomena. This is feasible because OMEGA can produce pressures greater than 10 Mbar on areas of square millimeters. This project explores the contribution of hydrodynamic instabilities to structure in supernovae and the dynamics of radiative shock waves. Radiative shock waves produce shocked matter so hot that it radiates away most of its thermal energy. This causes a complex, three-dimensional internal structure to develop, perhaps made even more complex by an instability. This three-dimensional structure is studied using x-ray radiography and other diagnostics. To better diagnose it, a stereoscopic imaging experiment was recently performed.

In the experiment, ten OMEGA laser beams irradiated a beryllium drive disk with UV light for 1 ns. The beams deposited a total energy of ~3.8 KJ, giving an average irradiance of $\sim 7 \times 10^{14}$ W/cm^2, generating an ablation pressure of ~46 Mbar in the beryllium drive disk. The ablation pressure first shocked and then accelerated the Be material, which then acted as a piston to drive a shock down a cylindrical shock tube filled with xenon gas. The shock moved through the xenon with an average velocity of the order of 150 km/s, which was fast enough to cause radiative effects to play a dramatic role in the shock dynamics. An additional ten OMEGA laser beams irradiated two vanadium foils on the stereoscopic backlighting target for 200 ps, creating the x rays used to image the shock tube through pinholes. To investigate the radiative shock at different velocities, we varied the drive-disk thicknesses and backlighting times. The two detectors were spaced at 37.4° and collected the x rays onto film backed by image plates. Figure 120.55 shows the images from a single target, taken 1 ns apart.

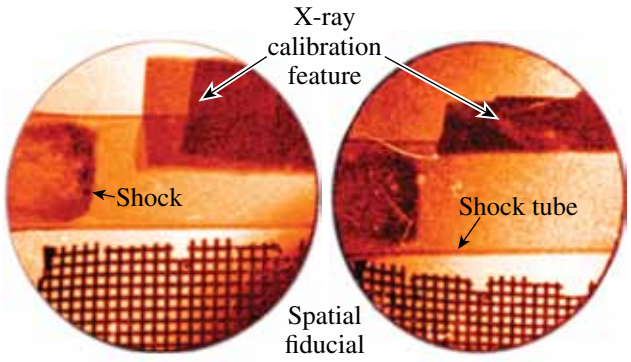

U932JR

Figure 120.55
Stereoscopic radiographs of a radiative shock in xenon gas. One can see the radiating shock, shock tube, the spatial fiducial, and the x-ray calibration feature used in the experiment. The shock, which moved from left to right within the shock tube, produced dense xenon that absorbed the diagnostic x rays, revealing its structure.

Detailed In-Situ *Diagnostics of Multiple Shocks*

Principal Investigators: R. W. Falcone (University of California, Berkeley); H. J. Lee (SLAC); and T. Döppner, O. L. Landen, and S. H. Glenzer (LLNL)

X-ray Thomson-scattering diagnostics were employed to measure the electron density and temperature of shock-compressed matter in the Fermi-degenerate state, which is of great interest to test dense-plasma modeling and to address fundamental physics questions such as the equation of state and the structure of dense matter. Powerful laser-produced x-ray sources of 6 keV have been used to probe the dense state, making possible a quantitative *in-situ* diagnostic.[1] A 250-μm-thick beryllium (Be) foil [Figs 120.56(a) and 120.56(b)] was driven by 12 beams smoothed with distributed phase plates (SG-4) in a counter-propagating geometry of heater beams. Laser intensities of 2×10^{14} W/cm^2 in 3-ns-long flat pulses were applied onto each side of the Be.

The Compton-scattering spectrum measured at a scattering angle of $\theta = 140°$ accessing the noncollective scattering regime with $\alpha = 0.4$ and $k = 5.88$ Å^{-1} shows a parabolic spectrum downshifted in energy from the incident radiation by the Compton effect;[2] the shift is determined by the Compton energy $E_C = h^2k^2/2m_e = 130$ eV. The theoretical fits to the measured spectra in Figs. 120.56(c) and 120.56(d) show that the electron density (n_e) changes with delay time. Radiation–hydrodynamic calculations using Hyades estimate the collision of two shocks around 4.3 ns. Calculated spectra using the theoretical form factor indicate compression by a factor of 5 with $n_e \sim 1.4 \times 10^{24}$ cm^{-3} by a collision of counter-propagating shocks. Further analysis will address the density and temperature evolution according to the shock propagation.

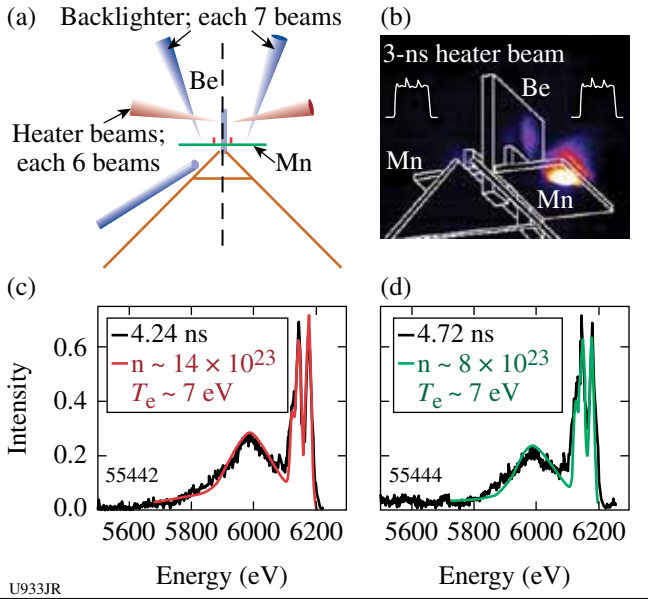

Figure 120.56

(a) Target configuration and (b) time-integrated image for $E > 2$ keV showing the emission produced by heater and probe beams. Scattering data and fit at (c) 4.24 ns and (d) at 4.72 ns.

OMEGA EP–Generated X-Ray Source for High-Resolution 100- to 200-keV Point-Projection Radiography

Principal Investigator: U. Feldman (Artep Inc.)

During the first three months of this NLUF project (which began 15 December 2008) the OMEGA EP transmission crystal spectrometer (ECS) was designed and underwent the required design reviews that assured compliance with the Omega EP Facility requirements. The small standoff distance (25.4 cm) between the target chamber center (TCC) and the ECS crystal made it necessary, on one hand, to place massive shielding fairly close to the TCC as protection from the harsh OMEGA EP hard x-ray radiation environment and, on the other hand, to ensure that the total instrument weight would not exceed the 100-lb limit and that the instrumental center of gravity would be within the TIM's (ten-inch manipulator's) allocated position. The competing requirements forced a totally new spectrometer design.

During May and June the spectrometer parts were machined and assembled and the crystal was cut and polished. In mid-July the crystal was installed and the spectrometer was aligned using the NIST 400-keV industrial tungsten x-ray source. Figure 120.57 shows the spectrometer at the NIST facility and the tungsten spectra recorded on the Rowland circle and at 20 in. and 40 in. from it. On 17 July 2009 the ECS was shipped to LLE for final checks.

On 26–27 August, the ECS was placed in TIM-13 and recorded data from 14 shots. The first shot of each day was at an energy of 35 J to 40 J and a duration of 9 ps to 10 ps; the remainder of the shots were at ~1000 J and 9 ps to 10 ps. Additional information on the shots is provided in Table 120.XI. The low-energy shots, which were focused on a thin foil of Gd, produced clean spectra; on the high-energy shots, however, the spectra were obscured by high background emission. The bright background emission was eventually identified as fairly soft x-ray radiation that was scattered from the general direction of the center of the target chamber. The scattered soft x-ray radiation was eventually removed from the spectra by a 1.2-mm-thick aluminum strip that was placed in front of the image plate and acted as a soft x-ray filter. Spectra from a Gd foil target are shown in Fig. 120.58.

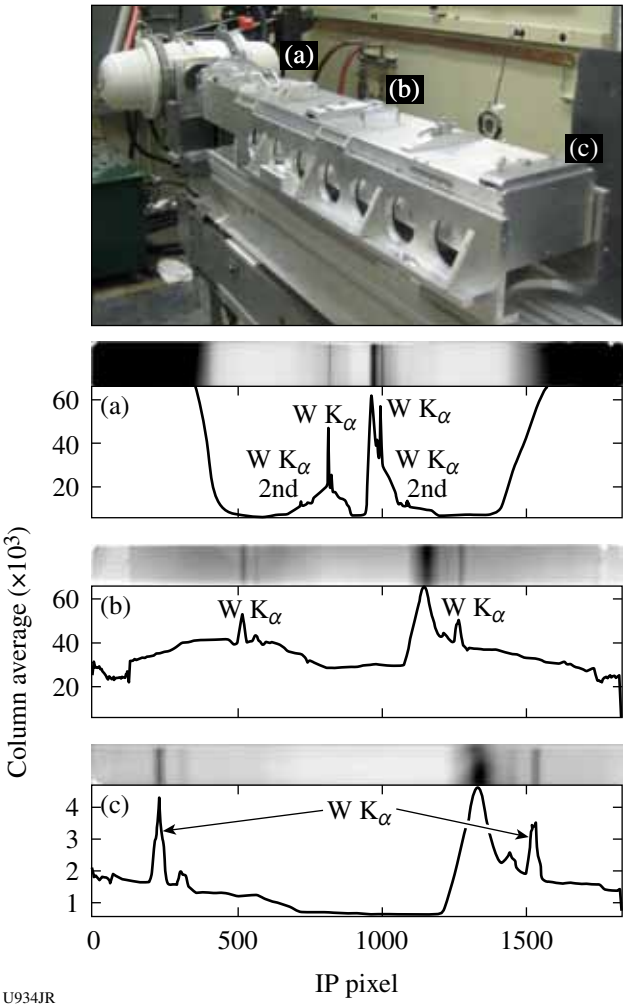

Figure 120.57
The ECS spectrometer at the NIST x-ray facility and sample x-ray spectra at IP positions (a), (b), and (c), on the Rowland circle and at 20 and 40 in. from it, respectively.

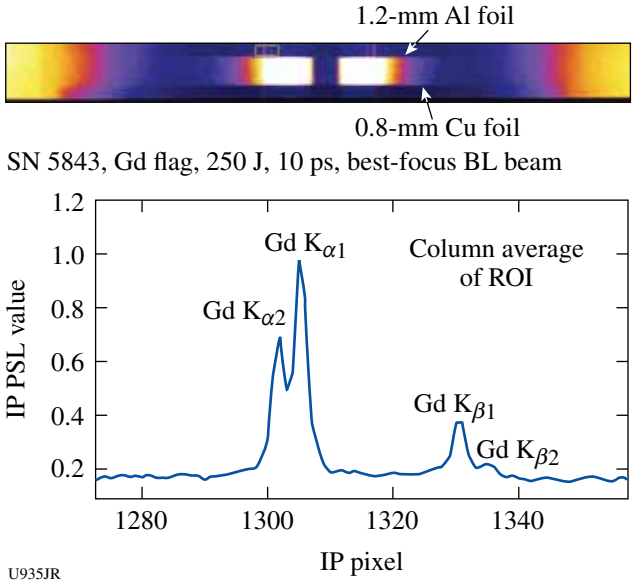

Figure 120.58
X-ray spectra on the ECS from a Gd foil target.

Table 120.XI: Shots on OMEGA EP within PPRad-EP-09, 26–27 August 2009.

Shot numbers	Beam energy (J)	Pulse	Target	Target description	RID	Results
5827	36	9 to 10 ps	FEP-8	Dy foil	29390	Data on ECS, TCS
5828	984	9 to 10 ps	Al-7	Hf foil	28653	No lines
5829	986	9 to 10 ps	Al-1	Ho Dy Tb	29384	No lines
5831	980	10 ps	FEP-2	Ho Dy Tb	29385	No lines
5833	987	10 ps	FEP-9	Dy foil	29386	Lines on TCS
5834	488	9 ps	Al-2	Ho Dy Tb	29388	No lines
5835	486	9 ps	FEP-1	Ho Dy Tb	29389	No lines
5839	35	10 ps	Gd flag	1 × 1 × 0.127 mm	29404	Lines
5840	982	10	Gd flag	1 × 1 × 0.127 mm	29405	Lines on all
5841	998	10	Au flag	2 × 2 × 0.05 mm	29410	No lines on ECS
5842	990	9	Gd flag	1 × 1 × 0.127 mm	29411	Lines maybe on ECS
5843	249	10	Gd flag	1 × 1 × 0.127 mm	29412	Nice lines on ECS
5844	975	9	Au flag	2 × 2 × 0.05 mm	29413	TCS in TIM 13
5845	1053	9	Au flag	2 × 2 × 0.05 mm	29414	Au lines on ECS

Preliminary results indicate that although the laser was focused to about 50 μm, the size of the emitting source was significantly larger (~400 μm).

During September the front end of the three image plate holders was modified by adding a layer of 0.5- to 1.0-mm aluminum. Additional shielding will be provided between the crystal and the TCC. It is expected that these additions will greatly reduce or completely eliminate the scattered radiation problem.

Second-Year Plans

The plan for the second year is to replace the image plate at the 60-in. location, which has pixel sizes of 100 μm or larger, with a pair of electronic detectors that will have a pixel size of the order of ~25 μm. The design of the electronic system is in progress. The design change will be implemented on the ECS before the next scheduled run on the OMEGA EP laser in July 2010.

Artep Inc., as part of an earlier project that was associated with measurements of hard x-ray sources on the sun, developed a Soller collimator that consisted of tens to hundreds of foils stacked together. The collimator's pitch (foil thickness and space) is as small as 50 μm. Attempts will be made to manufacture and install such a collimator in the optical pass. It is expected that the collimator will not only prevent scattered radiation from reaching the detector but more importantly will provide spectra with spatial resolution of the order of 30 μm at the source.

Ramp Compression Experiments for Measuring Structural Phase Transformation Kinetics on OMEGA

Principal Investigators: T. S. Duffy, J. Wang, and G. Finkelstein (Princeton University); R. F. Smith, J. H. Eggert, P. M. Celliers, D. Braun, and M. Bastea (LLNL); T. R. Boehly (LLE); and Y. M. Gupta (Washington State University)

This proposal was awarded 1.5 shot days on OMEGA in FY09 to explore phase transformations and their associated kinetics in new high-pressure regimes (200 to 500 GPa). These initial shots were focused on two materials that are very important in the study of planetary science: quartz and Fe. To keep these samples in the solid phase (i.e., avoid melt), it is important to minimize the temperature rise during compression. To achieve this, the target package was designed to launch a ramp compression wave into the sample of interest. Here, the compression is quasi-isentropic and the temperature is much smaller than for comparable pressures achieved through shock compression. As shown in Fig. 120.59(a), a composite pulse shape of ~10-ns duration (18 beams) from the OMEGA laser was used as input into a gas-filled halfraum. This generated a time-dependent x-ray drive, which, via a 20-μm diamond abla-

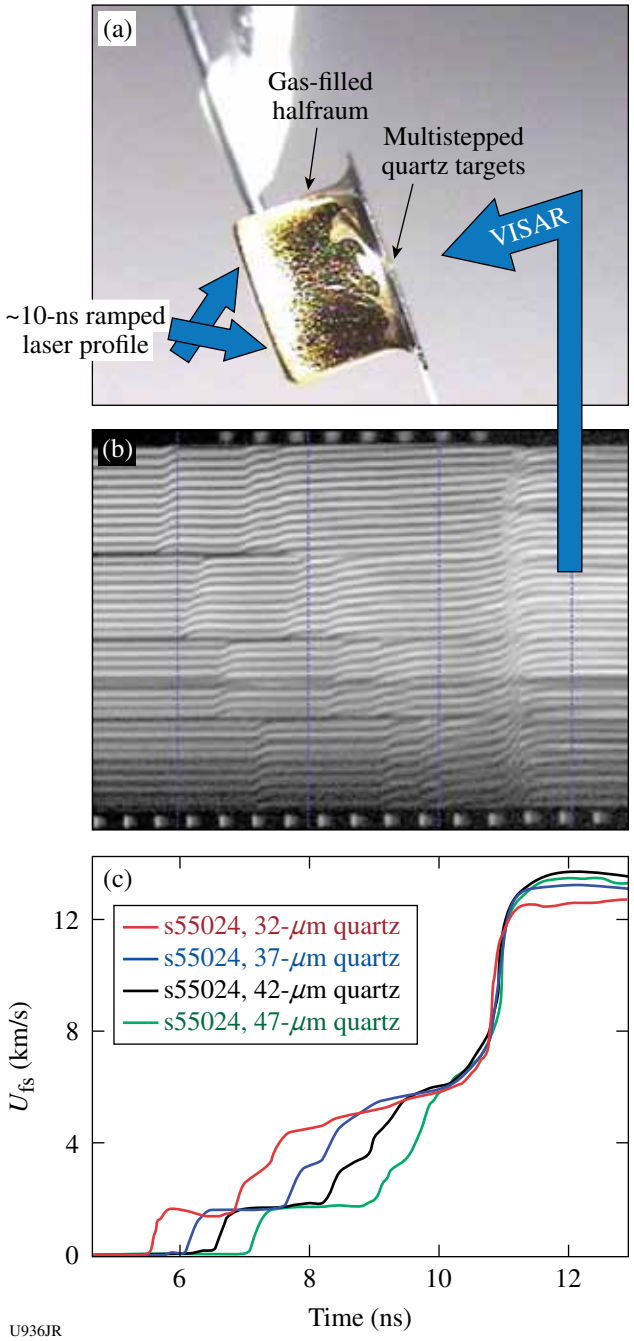

Figure 120.59
(a) A 10-ns ramped laser drive (18 beams) was used to compress a multistepped quartz target without shock. (b) The free-surface velocity was recorded using a velocity interferometer (VISAR). (c) The structured free-surface velocity profiles contain information with respect to phase transformations.

tor, launched a ramp compression wave into a multistepped quartz sample. The transmitted compression wave was recorded with a line-imaging velocity interferometer [i.e., velocity interferometer system for any reflector (VISAR), a.k.a. active shock breakout diagnostic] for each step [Fig. 120.59(b)]. These free-surface velocity profiles (U_{fs}) are shown in Fig. 120.59(c). Here the peak velocity of ~14 km/s was equivalent to a peak pressure of ~260 GPa. The structured nature of these profiles was consistent with the material undergoing one or more structural phase transformations as the pressure within the sample was steadily increased.

In addition to quartz, multistepped Fe samples (Fig. 120.60) were also shot. The target design is described in Fig. 120.59(a). The main difference between the quartz and Fe designs was that each had a unique composite laser-pulse profile, which was optimized from the material's equation of state. The composite pulse shape for Fe is shown in Fig. 120.60(a). This pulse shape resulted in the velocity profiles in a 40-/47-/54-/61-μm multistepped Fe sample shown in Fig. 120.60(b). Here, the peak velocity of 7.1 km/s corresponds to a peak pressure of ~250 GPa.

In FY09 a total of 16 shots were taken for this experiment. Analysis is ongoing for both the quartz and Fe data sets to extract equation-of-state (stress-density) and phase-transformation information. Future campaigns will focus on optimizing the design to ramp compress to peak pressures exceeding 5 Mbar (500 GPa). For reference the peak pressure at the center of the Earth is ~360 GPa.

Laboratory Experiments of Supersonic Astrophysical Flows Interacting with Clumpy Environments

Principal Investigator: P. Hartigan (Rice University)
Co-investigators: R. Carver and J. Palmer (Rice University); J. M. Foster, P. A. Rosen, and R. Williams (AWE); B. H. Wilde and M. Douglas (LANL); A. Frank (University of Rochester); and B. E. Blue (General Atomics)

Strong shock waves occur in many astrophysical systems, and the morphology of the emission lines that occur from the hot gas behind these shocks is often highly clumpy. The objective of this sequence of NLUF experiments is to develop scaled laboratory experiments to study the hydrodynamics of clumpy supersonic flows. The laboratory work complements new astrophysical images from the Hubble Space Telescope that were motivated by the results of a previous NLUF program.

In the past year, a new target concept was designed and tested in which several dozen 130-μm-diam sapphire spheres were embedded within a cylindrical foam target and a strong shock was propagated through this composite. We also compared how the shock propagation differs between a highly clumped target and a uniform one with the same overall density. The shots were successful, and we were able to observe the small clumps as they were entrained within the passing shock. This situation has a close astrophysical analog in many outflows from young stars (see Fig. 120.61).

In the last year the Astrophysical Journal accepted a paper by this collaboration that describes the results from the previous set of experiments examining the shock waves that occur when a collimated jet deflects from a single large obstacle.

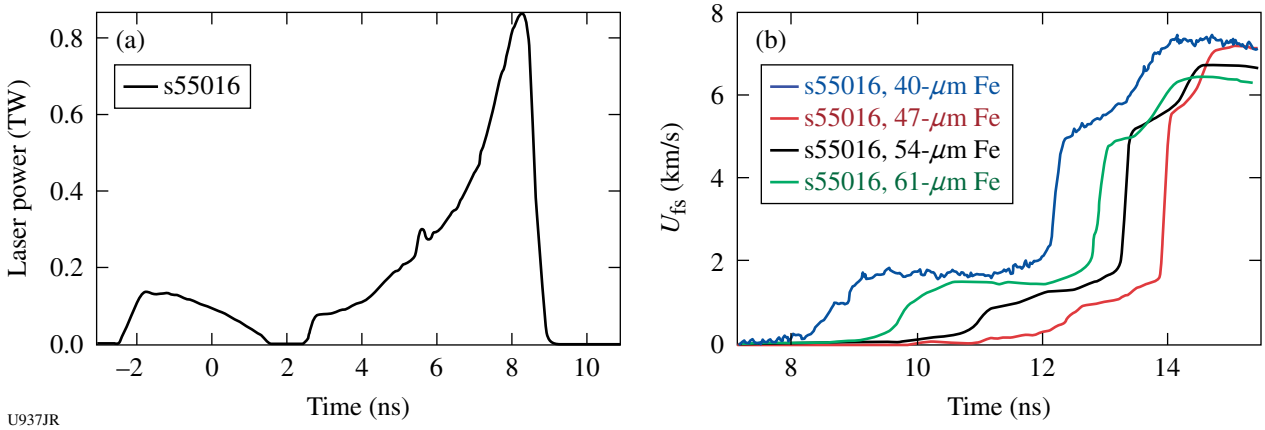

Figure 120.60
(a) Composite laser pulse shape (18 beams) was used to compress a multistepped Fe target without shock. (b) The free-surface velocity was recorded using a velocity interferometer (VISAR). Peak pressures of 3 Mbar were achieved in the Fe sample.

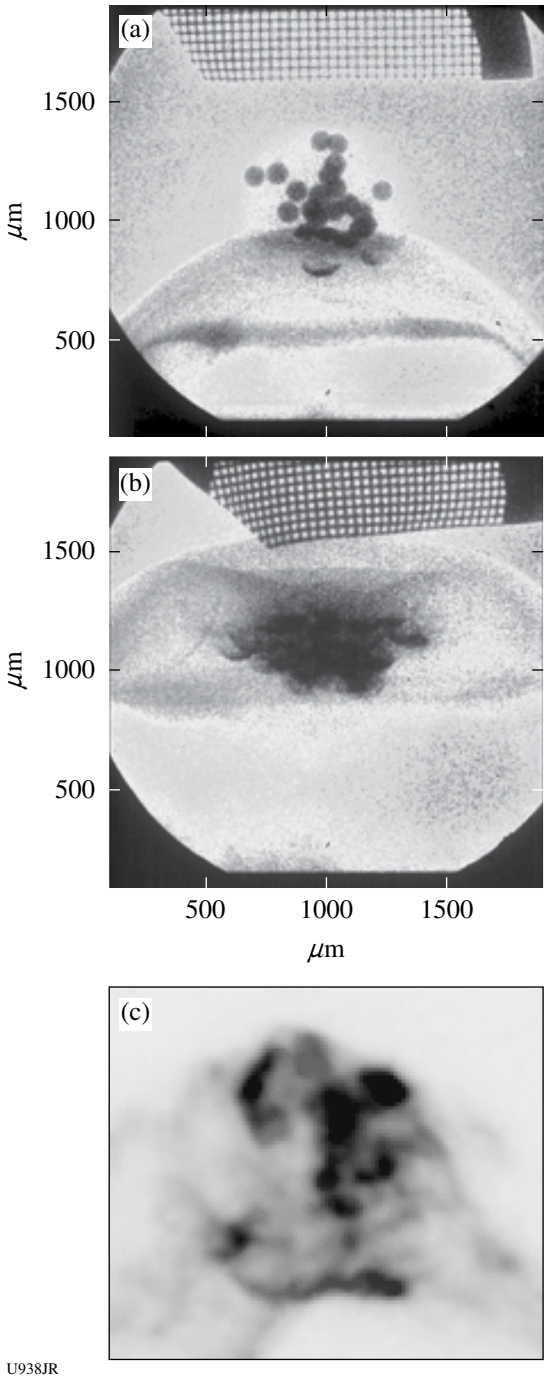

Figure 120.61
[(a),(b)] A strong bow shock propagates through a foam within which are embedded numerous sapphire spheres. Small bow shocks form around each of the spheres as they are overrun and entrained by the main shock wave. The scales are in microns, and the herringbone pattern at the top is a grid used to verify the scale of the images. (c) The astrophysical analog, HH 47, as observed with the Hubble Space Telescope. In all cases the clumps are embedded in a flow that moves from the bottom to the top in the figures.

FY09 Low-Density Plasma Interactions

Principal Investigators: L. Willingale, K. Krushelnick, and A. Maksimchuk (University of Michigan); P. M. Nilson, C. Stoeckl, and T. C. Sangster (LLE); and W. Nazarov (University of St. Andrews)

The propagation of relativistically intense laser pulses into near-critical-density plasma has been shown to be influential on the rear-side proton acceleration,[3] and it is of interest for fast-ignition scenarios to determine laser penetration.[4,5] Investigations of proton acceleration and laser propagation using the OMEGA EP laser (1000 J, 10 ps, 2×10^{19} W/cm^2) interacting with low-density targets have been performed. Very low density, submicron-pore-size CHO foam targets (3 to 100 mg/cm^3) produce plasmas of between 0.9 n_c and 30 n_c, where n_c is the nonrelativistic critical density. Proton beams are observed from the rear side to have maximum energies of up to 51 MeV.

Also, proton radiography, which can image quasi-static electromagnetic fields and density perturbations, is used to investigate the interaction of the 1000-J, 10-ps laser pulse interaction with a 1.5-n_c plasma. A schematic of this experiment is shown in Fig. 120.62. Using the second OMEGA EP short-pulse beam (700 fs, 250 J) to create the proton beam (proton energy of up to 60 MeV) and detecting the different proton energy images using a radiochromic film stack make it possible to obtain a picosecond resolution "movie" of the 10-ps laser interacting

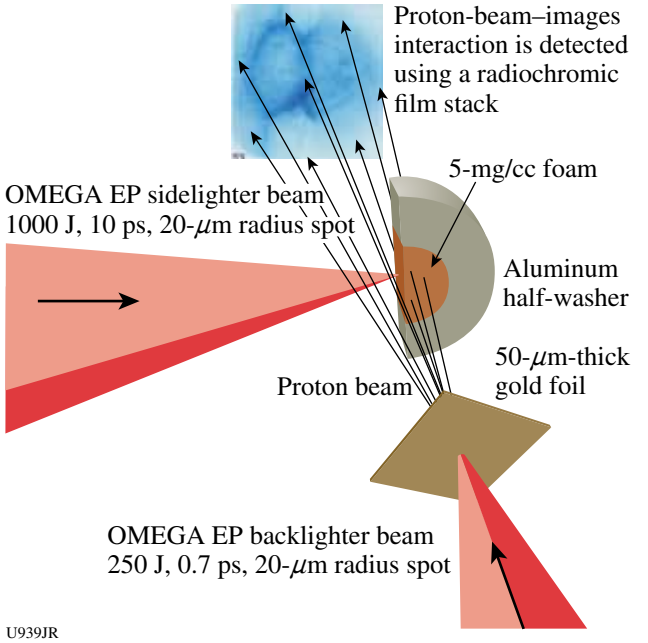

Figure 120.62
Experimental setup for the proton radiography.

with the foam target. The transit time from the proton source foil to the interaction means the different energy protons pass the main interaction at different times. The technique also requires that the interpulse timing be known accurately, which was verified using the ultrafast x-ray streak camera. Examples of the proton radiographs are shown in Fig. 120.63. The most-striking feature is the rapidly expanding front, back toward the laser from the target surface. It is traveling at a velocity of up to 1×10^8 ms^{-1}, which corresponds to proton energies of about 50 MeV. Filamentary structures are observed where the laser has passed through the pre-plasma.

Three-Dimensional Studies of Low-Adiabat Direct-Drive Implosions on OMEGA

Principal Investigator: R. Mancini (University of Nevada, Reno)

Determining the spatial structure of implosion core temperature conditions is of current interest in inertial confinement fusion experiments. Three methods have been developed and tested in OMEGA direct-drive implosions to extract temperature spatial profiles from the analysis of narrowband x-ray images recorded with a DDMMI instrument. The targets consisted of plastic shells filled with deuterium gas and a trace amount of argon for diagnostic purposes and driven with a low-adiabat $\alpha \sim 2$ pulse shape. The analysis methods treat space integration and radiation transport effects with different levels of approximation.

The emissivity ratio of $\mathrm{Ly}_\beta/\mathrm{He}_\beta$ argon lines is strongly dependent on electron temperature T_e but only weakly dependent on electron density N_e; therefore, it can be used as a temperature diagnostic. The first method considers the ratio of $\mathrm{Ly}_\beta/\mathrm{He}_\beta$ image intensities. If we neglect the radiation transport effect, each intensity point on the image plane can be interpreted as the line integral of the emissivity along a given chord in the plasma source. Therefore, the ratio of $\mathrm{Ly}_\beta/\mathrm{He}_\beta$ intensities on the image plane corresponds to the ratio of average emissivities along chords in the core, and this ratio can be converted into an average or effective electron temperature T_e integrated along the chord. The result of this analysis is displayed in Fig. 120.64. The x and y coordinates in the surface plot correspond to the coordinates on the image plane. The

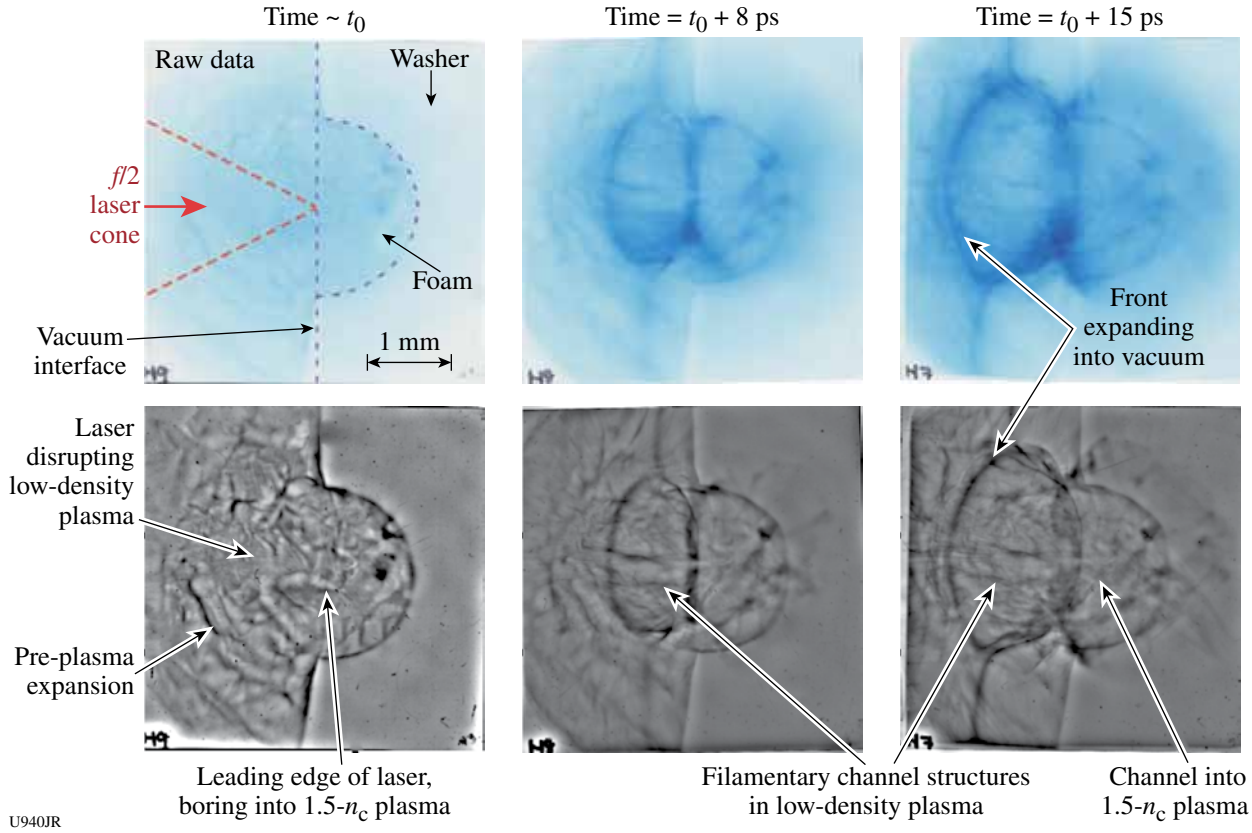

Figure 120.63

Proton images from a single shot of the 1000-J, 10-ps laser (coming in from the left) interacting with the 5-mg/cm^3 foam target. The top row shows the raw data; the bottom row shows the same images enhanced to bring out the features.

electron temperature T_e varies in the range from 900 eV near the core edge to 1400 eV in a region off core center. We note that no symmetry assumptions or geometry inversions are required to perform this analysis.

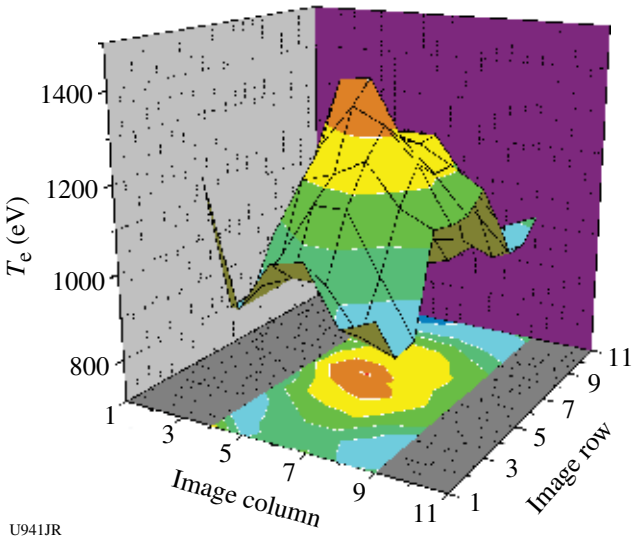

Figure 120.64
Electron-temperature T_e spatial distribution obtained from the ratio of Ly_β/He_β image intensities.

The second method splits the core into a collection of core slices and uses an Abel inversion procedure for each core slice to go from intensity distribution on the image plane to emissivity profile in the plasma source. The Abel inversion unfolds the line integration corresponding to chords in each core slice to yield local emissivity in the core slice, but it still assumes negligible radiation-transport effects. Also, the application of the Abel inversion procedure requires local axial symmetry in each core slice. To satisfy this condition, intensity profiles associated to a given core slice must be made symmetric about a suitable center point. This operation partially removes some of the asymmetries observed on the image, thereby yielding Abel-inverted emissivities as a function of radial coordinate r in the core slice. As a result, the ratio of Abel-inverted Ly_β/He_β emissivities can be converted into a spatial profile of T_e as a function of the radial coordinate in the core slice, i.e., $T_e(r)$. The collection of $T_e(r)$ profiles from all core slices represents a quasi-three-dimensional map of the electron-temperature spatial distribution. The result of this analysis is shown in Fig. 120.65. The x and y coordinates in the surface plot now correspond to core slice label and a projection of the radial coordinate in the core slice on the image plane. While this analysis still neglects the radiation-transport effect, the unfolding of the chord line integration via the Abel inversion results in an electron temperature that ranges from about 900 eV near core edge to 1900 eV inside the core but off the core center. This temperature distribution is axially symmetric in each core slice but it still has some of the asymmetry present in the image data.

Finally, the third method is an attempt to unfold both the chord line integration and the radiation-transport effect. As in the second method, the core is split into slices and each core slice is assumed to be axially symmetric. Then, a multi-objective Pareto genetic algorithm is used to drive a search in parameter space with the goal of finding the temperature and density profiles that yield the best simultaneous and self-consistent fits (i.e., approximations) to three objectives: the He_β image intensity distribution, the Ly_β image intensity distribution, and the space-integrated line spectrum. Alternatively, the Ly_β/He_β image intensity ratio can also be used as an objective instead of one of the image intensities. Optimal fits are obtained by following up the genetic algorithm search with a "fine-tuner" step driven by a nonlinear least-squares minimization algorithm. The image intensity distribution on the image plane is approximated by transporting the line radiation, one photon energy at a time, inside the core slice via an integration of the radiation transport equation. The result of this analysis is shown in Fig. 120.66. Accounting for both space integration and radiation transport effects yields a temperature spatial distribution in the core that spans the range from 900 eV near core edge to 2250 eV inside the core, resulting in a temperature spatial structure with the steepest gradients. Therefore, neglecting space integration and radiation transport effects leads to a

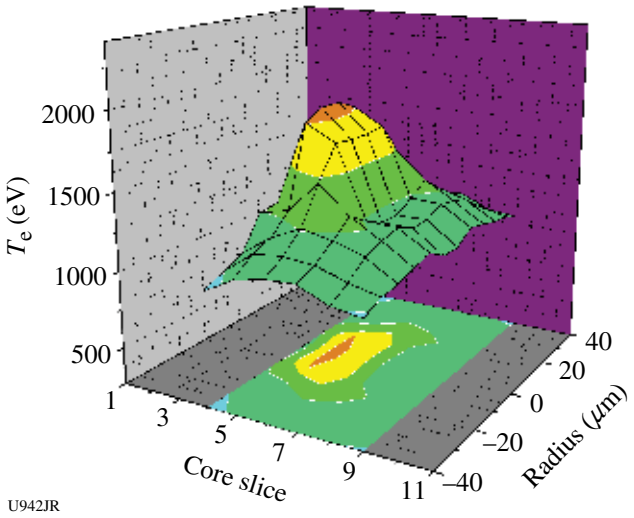

Figure 120.65
Electron-temperature T_e spatial distribution obtained from the ratio of Ly_β/He_β Abel-inverted emissivities.

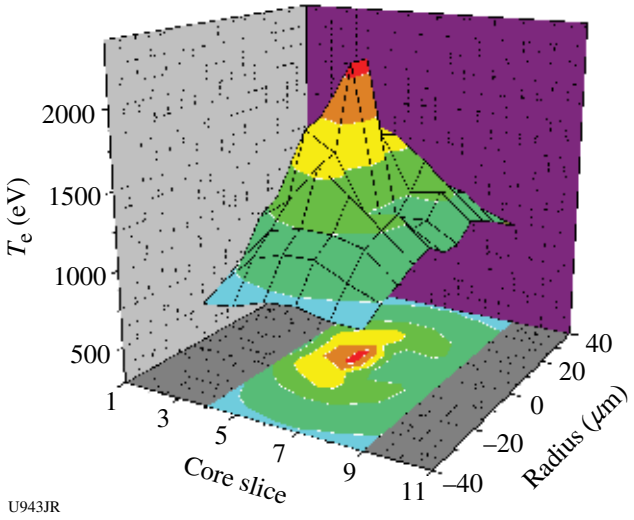

Figure 120.66
Electron-temperature T_e spatial distribution obtained from a search and reconstruction method driven by a Pareto genetic algorithm.

temperature spatial structure characteristic of the shallowest spatial gradients, while taking both effects into account yields a spatial structure with the steepest spatial gradients. Work is in progress to extend these methods to account for image data recorded simultaneously along three lines of sight with three DDMMI identical instruments.

Proton Radiography of Direct- and Indirect-Drive ICF Experiments and HEDP Plasmas

Principal Investigators: R. D. Petrasso and C. K. Li (Massachusetts Institute of Technology)
Co-investigators: F. H. Séguin and J. A. Frenje (MIT); J. P. Knauer and V. A. Smalyuk (LLE); J. R. Rygg and R. P. J. Town (LLNL).

MIT's NLUF Program has continued an ongoing series of experiments utilizing charged-particle radiography in the study of plasmas and transient electromagnetic fields generated by the interactions of OMEGA laser beams with plastic foils, direct-drive inertial confinement fusion (ICF) target capsules, hohlraums, indirectly driven ICF targets, and plastic or metal foils combined with foam cylinders (for laboratory-scaled astrophysical jets). This work, involving novel studies of field instabilities, magnetic reconnection, ICF implosion dynamics, and self-generated electromagnetic fields in ICF implosions and hohlraums, has already resulted in many publications, including six in Physical Review Letters[6–11] and one in Science,[12] as well as several invited talks[13–21] and many contributed talks at conferences. While most of the experiments have used exploding-pusher backlighters on OMEGA to produce monoenergetic protons and alpha particles,[22] work this year used protons from backlighter foils driven by OMEGA EP short-pulse beams. One experiment involved the simultaneous use of both types of backlighter.

Illustrating one of these important series of experiments, Fig. 120.67 shows the basic setup that was used for the first observations of self-generated fields associated with laser-irradiated hohlraums.[10] An exploding-pusher backlighter was driven by 21 OMEGA beams, while two hohlraums to be studied were driven by ten beams each (the isotropic emission of the backlighter makes it possible to image multiple objects simultaneously in different directions), as shown in Fig. 120.67(a). The backlighter produced short bursts (~130 ps) of monoenergetic protons at two different energies (3.3 MeV and 15 MeV), as shown in Fig. 120.67(b), and the special detector pack based on CR-39 nuclear track detectors made it possible for separate images to be recorded at each energy. As indicated in the left part of Fig. 120.67(a), a metal mesh was placed on the end of each holhraum nearest the backlighter; this divided the incident particles into beamlets whose deflec-

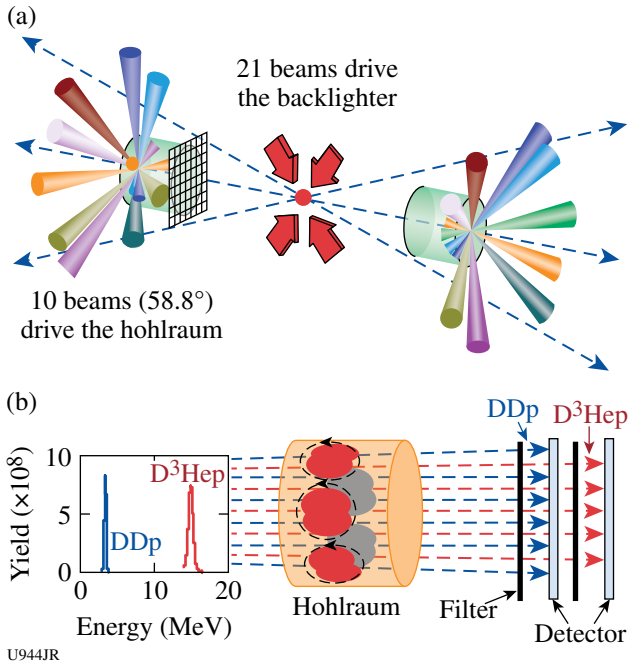

Figure 120.67
(a) Experimental setup, with proton backlighter, subject hohlraums, and laser beams. (b) Typical energy spectrum and CR-39 detector pack. The distance between the backlighter and the mesh (detector) was 0.7 (27) cm. Filters in the detector pack were carefully chosen so that 3.3-MeV and 15-MeV protons were recorded on the front and back detectors, respectively.

tions in the image plane could be measured for quantification of particle trajectory bending within the hohlraum caused by electric and/or magnetic fields.

Figure 120.68 shows sequences of proton images covering a time period from the beginning of the laser pulse (t = 0 ns) to 0.8 ns after it was turned off ($t \approx 1.8$ ns). At earlier times ($t \geq 0.9$ ns) the beamlet arrays in the 15-MeV images [Fig. 120.68(a)] show minimal displacement by fields or plasma, but beamlets have different sizes at different times, reflecting the presence of an E field of $\sim 2 \times 10^9$ V m^{-1} at ~0.37 ns that then decays away. At later times the 15-MeV beamlets show some chaotic spatial structure, indicating that their trajectories have been affected by large-field and plasma effects. In the 3.3-MeV images, beamlet arrays are coherently distorted by t = 0.52 ns and disappear altogether (due to stronger deflections) at later times. Quantitative analysis of the beamlet displacements indicates the presence of B fields with peak values of ~10^6 Gauss. The five-prong asterisk-like fluence pattern in the 3.3-MeV proton images at $t \geq 1.01$ ns was shown to be a consequence of the staggered distribution of laser beams on each hohlraum wall. The ten beams were grouped into five pairs that produced five plasma bubbles; the asterisk pattern was caused by scattering of the protons in Au-plasma jets between the bubbles shooting inward from the hohlraum wall at about ~Mach 4 (~1000 μm ns^{-1}). The Au density was inferred to be ~10 mg cm^{-3} (note that this should not occur in an ignition hohlraum, where a gas fill would impede the jets). These experimental results have important implications for understanding the precise conditions and plasma dynamics inside vacuum hohlraums and provide an impetus for the further development of 3-D multifluid codes with self-consistent field generation.

FY09 Laboratory Basic Science Programs

Ten proposals were approved and allocated 25 shot days on the Omega Facility in FY09 (Table 120.X). Unfortunately, because of the DOE funding shortfall in FY09, only 17 days (109 shots) of LBS experiments were actually funded and carried out during this fiscal year. The FY10 solicitation for the LBS Program resulted in 25 proposals with shot requests totaling 63.5 shot days. After peer review by an independent committee, 13 LBS proposals have been recommended for 29 shot days in FY10. Three additional shot days were recommended and approved for FY09 make-up shots. The approved FY10 LBS proposals are listed in Table 120.XII. This section includes brief summaries of LBS experiments carried out in FY09.

Electron–Positron Jets

Principal Investigators: H. Chen and S. C. Wilks (LLNL)
Co-investigators: J. F. Myatt and C. Stoeckl (LLE);
and E. Lang (Rice University)

On 16 April 2009, an LLNL/LLE team performed a Laboratory Basic Science experiment on the OMEGA EP Laser System to study positron production in high-intensity laser interactions with high-Z targets. The OMEGA EP backlighter produced ~1 kJ in a 10-ps laser pulse that interacted with a 1-mm-thick Au target. The positrons that were emitted from the rear side of the target were measured with a magnetic positron spectrometer. A quasi-monoenergetic positron beam was observed with a maximum energy of ~20 MeV as shown in Fig. 120.69. It is estimated that 10^{12} positrons were produced. This is a factor of ~10 more than were produced with a 260-J, 10-ps laser in LLNL experiments.[23] It was anticipated that the number of positrons produced would scale approximately with the laser energy.[24] The quasi-monoenergetic positron

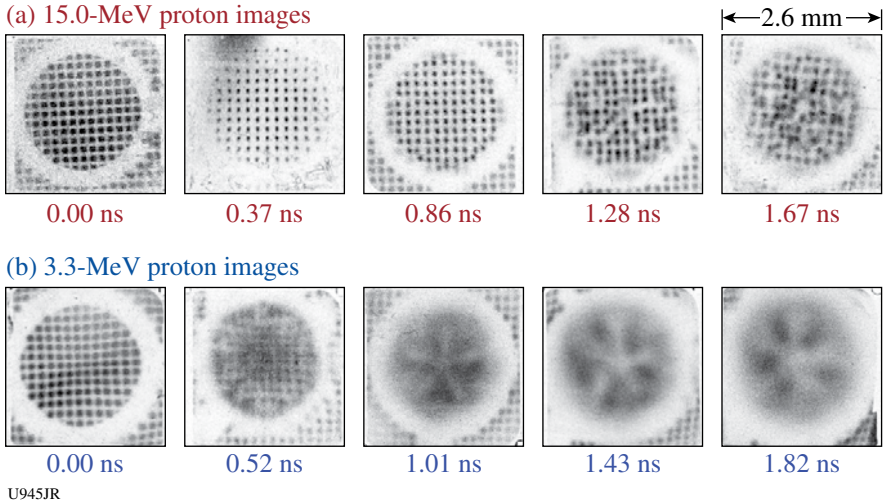

Figure 120.68
Radiographs of a laser-driven, vacuum Au hohlraum at different times, taken with (a) 15.0-MeV and (b) 3.3-MeV protons, illustrating spatial structure and time evolution of proton deflection and beamlet size. Pairs of images in (a) and (b) were taken in the same shot, but they represent different sample times because of different proton velocities. In each image, darker means higher fluence; the gray-scale mapping is different in each image to account for the different backlighter yields.

Table 120.XII: Approved FY10 LBS Experiments.

Principal Investigator	Affiliation	Proposal Title	Facility Required
R. Betti	LLE/FSC	Integrated Shock-Ignition Experiments on OMEGA	OMEGA
P. M. Celliers	LLNL	Measurement of the Viscosity of Shock-Compressed Fluids: Studies of Water and Silica	OMEGA
H. Chen	LLNL	Producing Pair Plasma and Gamma-Ray Burst Using OMEGA EP	OMEGA EP
D. E. Fratanduono	LLE	Optical Properties of Compressed LiF	OMEGA and OMEGA EP
D. H. Froula/J. S. Ross	LLNL	First Observations of Relativistic Plasma Effects on Collective Thomson Scattering	OMEGA
S. H. Glenzer	LLNL	Capsules Adiabat Measurements with X-Ray Thomson Scattering	OMEGA
D. G. Hicks	LLNL	Ramp and Multi-Shock Compression of Iron to Several Megabars: Studies Using Extended and Near Edge X-Ray Absorption Spectroscopy	OMEGA
H.-S. Park	LLNL	Study of High-Z Material Properties under Compression Using High-Energy Backlighter Diffraction	OMEGA EP
P. K. Patel	LLNL	Benchmarking Laser-Electron Coupling at Fast Ignition–Relevant Conditions	OMEGA EP
S. P. Regan	LLE	Validating Inelastic X-Ray Scattering from H and H/He Warm Dense Matter with Shock Velocity Measurements: Toward the Equation of State of Jupiter's Core	OMEGA
R. Smith/J. H. Eggert/ S. M. Pollaine	LLNL	Phase Transformation Kinetics	OMEGA
C. Stoeckl/ W. Theobald/W. Seka	LLE	Channeling in Long-Scale-Length Plasmas	OMEGA EP
W. Theobald	LLE	Integrated Core Heating for Fast Ignition	OMEGA and OMEGA EP

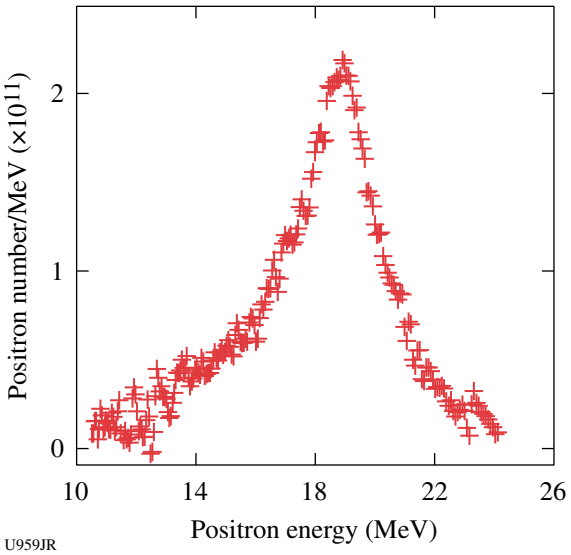

Figure 120.69
Positron spectrum measured on the OMEGA EP laser.

spectrum is likely a cause of positron acceleration from the sheath formed by escaping electrons on the rear surface of the target. The differences between the two experiments will be studied to understand the consequences of these results. The positron-production rate during the laser shot appears to be the highest ever observed in the laboratory.

Positron research has extended over diverse fields from particle physics and astrophysics to medical application. This often requires the production of large numbers of positrons on a short time scale, which has been difficult to supply. The new OMEGA EP results could profoundly alter the direction of the quest of establishing a laser-produced positron source for research in these fields.

X-Ray Absorption Fine Structure Measurements of Iron Compressed to a Few Megabars

Principal Investigators: Y. Ping and D. G. Hicks (LLNL)
Co-investigators: J. H. Eggert (LLNL); B. Yaakobi and T. R. Boehly (LLE); and R. Hemley (Carnegie)

X-ray absorption fine structure (XAFS) measurements were performed on iron that was ramp and multishock compressed to a pressure of a few megabars. By dynamically compressing a few-micron-thick iron sample sandwiched between thin diamond anvils, near-constant pressure conditions were produced inside the iron with the bulk of the pressure evolution taking place in the adjacent, x-ray-transparent diamond anvils. A spherical, imploding backlighter source was used to produce a smooth broadband source of x rays for the absorption measurement. Several different target configurations were studied in the single day of shots performed in FY09 to establish the optimum configuration of target versus backlighter drive and how best to achieve simultaneous measurements of the pressure using a velocity interferometer system for any reflector (VISAR). Success was achieved by maximizing the number of beams used on the backlighter and driving the target package with a stacked, multishock pulse. The resulting XAFS spectra (Fig. 120.70, compared to an undriven target) were analyzed using the FEFF code and found to give a compression of 1.55 and a temperature of 6000 K, with a pressure of 2.5 Mbar obtained from the VISAR. A modified analysis is being developed to determine the radial distribution function $g(r)$ from these data. Future work will scan through different regions of pressure, density, and temperature space to map out the iron phase diagram.

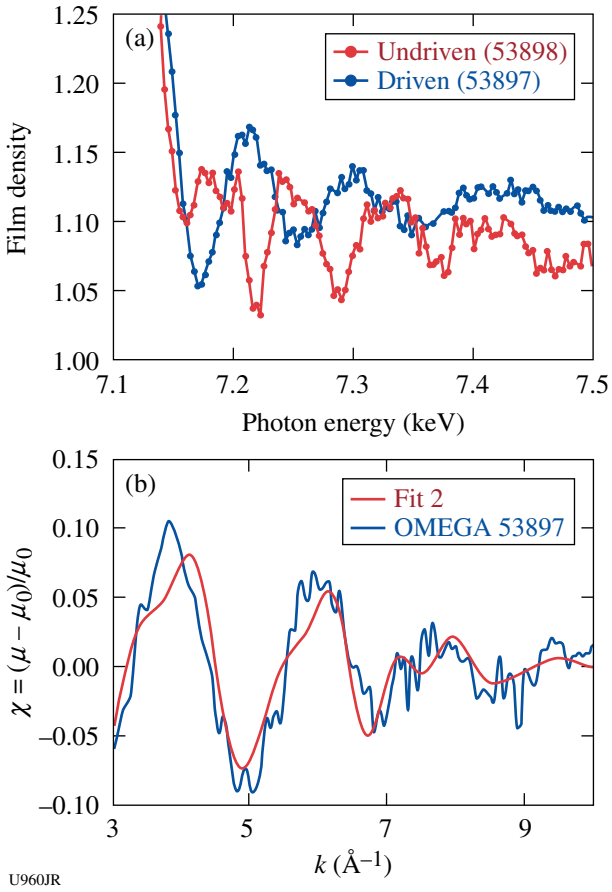

Figure 120.70
(a) Comparison of raw x-ray absorption spectra for undriven iron and multishocked iron compressed to ~2.5 Mbar. (b) A best fit to the x-ray absorption coefficient as a function of wave number gives a compression of 1.55 and a temperature of 6000 K.

Probing H/He Warm Dense Matter with Inelastic X-Ray Scattering: Toward the Equation of State of Jupiter's Core

Principal Investigator: S. P. Regan (LLE)
Co-investigator: G. Gregori (LLNL)

The objective of this research is to measure the equation of state (n_e, T_e, Z) of direct-drive, shock-heated, planar cryogenic H/He targets using spectrally resolved x-ray scattering (i.e., inelastic x-ray scattering) in the 1- to 100-Mbar range. The H/He warm dense matter is relevant to planetary interiors. The largest planet in our solar system, Jupiter, is composed primarily of H and He, having a predicted pressure in the tens-of-megabars range. The research has a synergistic relationship with the programmatic direct-drive inertial confinement fusion (ICF) research being conducted at the Omega Facility. It works in parallel with the ICF research, which uses inelastic x-ray scattering to study the equation of state (EOS) of direct-drive, shock-heated, planar cryogenic deuterium targets. In the truncated LBS shot schedule, one day on OMEGA was dedicated to demonstrating this experimental platform. A planar liquid deuterium target was chosen to maximize the likelihood of success. The polyimide ablator was irradiated with a 6-ns constant-intensity (~10^{14} W/cm^2) laser drive forming an ~100-μm-thick layer of shocked deuterium, which is uniform in the transverse dimension over a 0.5-mm diameter. The 1-D predictions for the laser-ablation–driven shock wave are P = 12 Mbar, T_e = 22 eV, $n_e = 2 \times 10^{23}$ cm^{-3}, ρ = 0.8 g/cm^2, and Z = 1. A collimated beam of Cl Ly$_\alpha$ emission (2.96 keV) was scattered from the shocked deuterium and detected with a gated x-ray spectrometer at a scattering angle of 90°. The measured spectrum of Cl Ly$_\alpha$ emission (2.96 keV) and He-like satellites transmitted through the shocked liquid deuterium is shown in Fig. 120.71(a). The measured spectrum of noncollective x-ray scattering for Cl Ly$_\alpha$ emission at 90° (diamonds) is compared

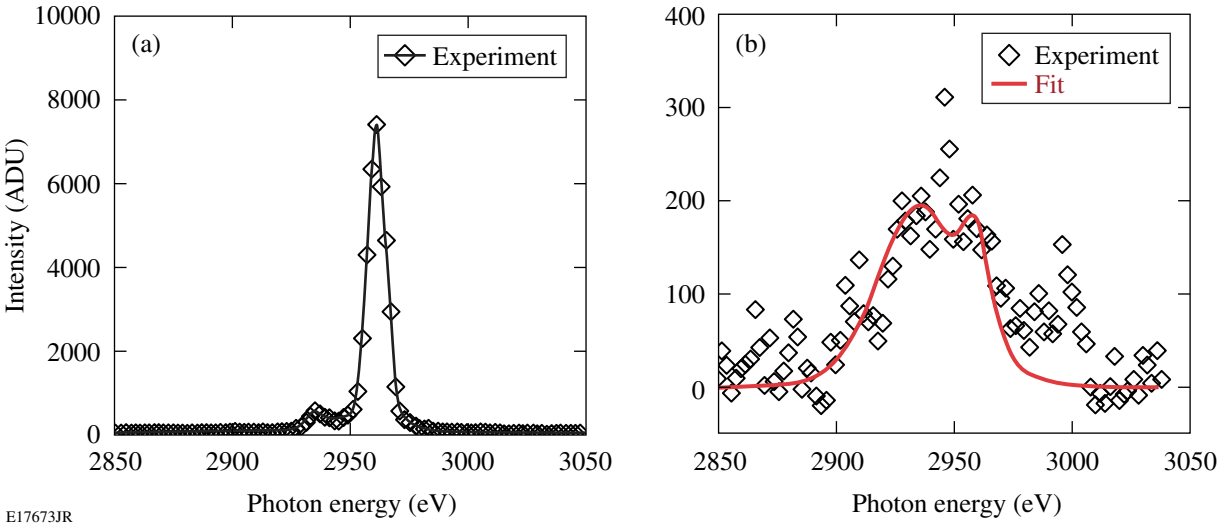

Figure 120.71
(a) Measured spectrum of Cl Ly$_\alpha$ emission (2.96 keV) and He-like satellites transmitted through the shocked liquid deuterium; (b) measured spectrum of noncollective x-ray scattering for Cl Ly$_\alpha$ emission at 90° (diamonds) compared with spectrum predicted for $T_e = 20$ eV, assuming $n_e = 1 \times 10^{23}$ cm^{-3} and $Z \sim 1$.

with spectrum predicted (red curve) for $T_e = 20$ eV, assuming $n_e = 1 \times 10^{23}$ cm^{-3} and $Z \sim 1$ in Fig. 120.71(b). The initial results are promising; however, further optimization in the experiment is needed to improve the noisy, scattered x-ray signal.

Integrated Shock-Ignition Experiments on OMEGA

Principal Investigators: W. Theobald and R. Betti (LLE)

Parametric plasma instabilities are of concern in an ignition target design with spike-pulse intensities in the range of 10^{15} to 10^{16} W/cm^2 and pulse durations of approximately several hundred picoseconds. The instabilities degrade the laser energy coupling to the capsule and increase the fraction of the laser energy transferred to hot electrons, which is a potential source of preheat that can reduce the final core compression in functional ICF implosions.

To test the effect of laser–plasma instabilities and hot electrons, shock-ignition laser–plasma experiments have been performed on the OMEGA laser with shock-generating laser intensities of up to ~8×10^{15} W/cm^2 (Ref. 25). Figure 120.72 shows a schematic of the experiments. The compression pulse

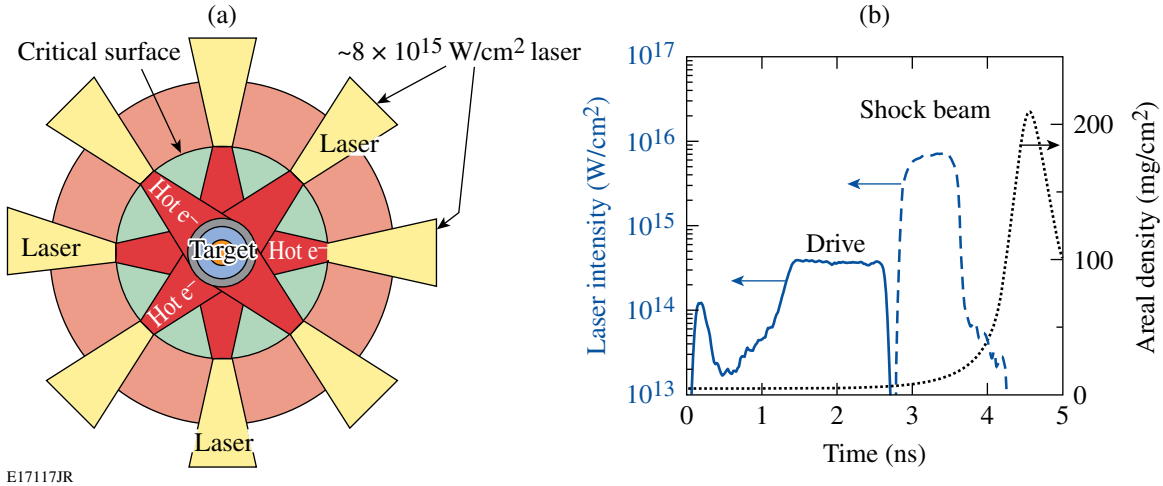

Figure 120.72
(a) Schematic of the setup for studying laser–plasma interactions and preheating at high laser intensities relevant to shock ignition. Forty of the OMEGA laser beams implode the capsule at low intensities. Twenty delayed beams are tightly focused onto the critical-density surface, where plasma instabilities lead to the generation of energetic electrons heating the dense core. (b) Pulse shapes of the 40 drive beams (solid), 20 shock beams (dashed), and areal-density evolution (dotted).

consists of a shaped low-adiabat pulse (solid) using 40 OMEGA beams with ~13.6 kJ of UV laser energy. The targets were 36-μm-thick, 430-μm-outer-radius, deuterated plastic shells coated outside with a 0.1-μm layer of aluminum and filled with D_2 gas with a pressure of ~30 atm. A late shock was driven by the remaining 20 UV beams that were delayed and tightly focused on the compressed core to achieve intensities at the critical-density surface ranging from $\sim 2 \times 10^{15}$ to $\sim 8 \times 10^{15}$ W/cm^2.

The effect of high-intensity shock beams on neutron and hard x-ray yields was studied as a function of the delay between the 40 and 20 beams [Figs. 120.73(a) and 120.73(b)]. The delay time defined by the onset of the high-intensity beam with respect to the start of the drive pulse was varied from 2.3 ns to 2.9 ns. The neutron yield increased by a factor of ~7 from 5×10^8 to $\sim 3.5 \times 10^9$ for the shortest time delay. Two reference implosions with only 40 drive beams produced neutron yields of 1.4×10^8 and 3.7×10^8; the solid line in Fig. 120.73(a) represents the average of these yields. Figure 120.73(b) shows the hard x-ray signal, which is indicative of hot-electron production. A similar trend is observed for the hard x-ray yield, showing a larger amount of hot electrons generated at shorter time delays. The measured neutron yields of the 40-beam implosion show that, despite large target-illumination nonuniformity, a significant amount of the high-intensity-pulse energy is coupled into the capsule, producing up to ~20× more neutrons and a strong hard x-ray signal.

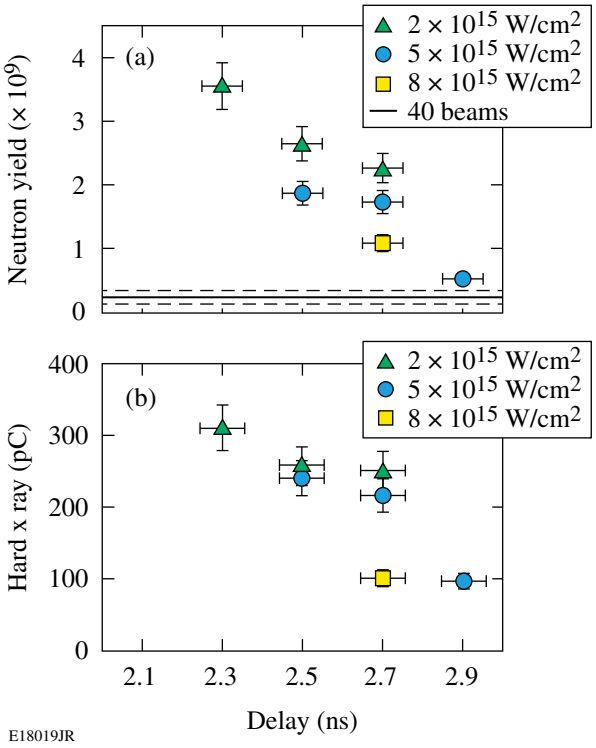

Figure 120.73
(a) Measured neutron yield and (b) hard x-ray yield versus the delay time of the high-intensity beam. The different symbols represent different focus positions with respect to the critical-density surface. The solid line in (a) is the average yield for 40-beam implosions; the dashed lines represent the error range. The 40-beam implosions produced no measurable hard x-ray signal.

Integrated Fast-Ignition Experiments

Principal Investigators: W. Theobald and C. Stoeckl (LLE)
Co-investigators: R. Betti and J. A. Delettrez (LLE); R. S. Stephen (General Atomics); and A. J. MacKinnon (LLNL)

Integrated fast-ignition (FI) experiments[26] began in FY09 at the Omega/Omega EP Laser Facility. The targets were 40-μm-thick empty CD shells of ~870-μm outer diameter, where a hollow gold cone with a full opening angle of 34° was inserted through a hole in the shell (see Fig. 120.74). The cone had a sidewall thickness of 10 μm with 10- and 15-μm-thick tips. A low-adiabat laser pulse comprised of a short picket pulse and a shaped ~2.7-ns drive pulse with 351-nm wavelength and ~18 kJ of energy imploded the capsule. The 1053-nm-wavelength short pulse was injected through the hollow cone, had an energy of 1 kJ and a duration of 10 ps, and was focused to a spot of ~40-μm diameter containing 80% of the laser energy. The corresponding peak laser intensity at the center of the tip of the cone was estimated to be $\sim 6 \times 10^{18}$ W/cm^2.

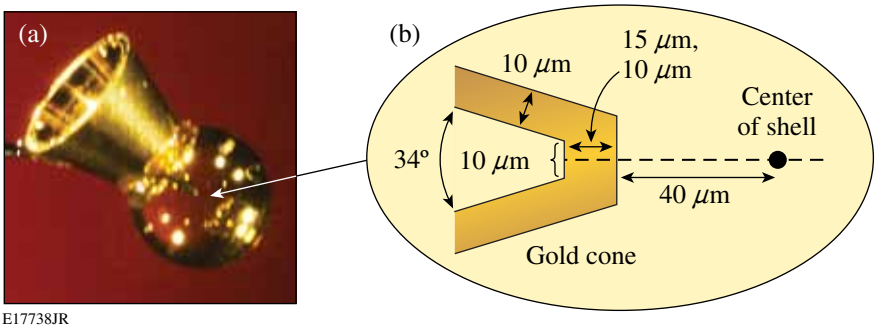

Figure 120.74
(a) Photograph of a gold re-entrant cone target; (b) schematic showing the cone-tip dimensions.

X-ray images show a threefold increase in x-ray emission with short-pulse energy of up to 1 kJ compared with similar implosions without a short-pulse beam. The pinhole images provide only qualitative information. Yield measurements of the 2.45-MeV neutrons from D–D fusion reactions are required to obtain quantitative information on the coupling efficiency. Neutron-yield measurements were challenging because of the emission of an intense γ-ray pulse. The strong background consisted of bremsstrahlung emission generated by MeV electrons streaming through the gold cone target. The γ-ray pulse induced a fluorescence background in the neutron detectors that persisted for several hundred nanoseconds and masked the much weaker neutron signal. A new neutron detector that was developed to overcome this problem now reliably measures neutron yields in integrated FI experiments. The detector uses an organic liquid scintillator that is saturated with molecular oxygen.

Figure 120.75 shows the measured neutron yield from integrated shots obtained at various arrival times of the short-pulse laser. The solid line represents the measured yield without the short-pulse laser. The neutron yield increased more than a factor of 2 with an appropriately timed OMEGA EP beam producing up to $1.5\pm0.6 \times 10^7$ additional neutrons. Initial *DRACO/LSP* simulations were performed to study core heating in the integrated fast-ignition (FI) experiments. The calculated neutron-yield increase caused by fast-electron heating is $\sim 2 \times 10^7$ if it is assumed that ~10% of the short-pulse energy is converted into fast electrons. The simulations did not take radiation transport and power balance into account, which leads to an over-prediction of density and temperature of the imploding shell. The calculated neutron-yield increase caused by the short-pulse laser is probably optimistic because the predicted higher density leads to a larger fraction of stopped fast electrons and because the gold cone material was not included in the electron-transport calculation. Fast-electron transport through the tip of the gold cone is significantly affected by the material properties and will affect the neutron yield.

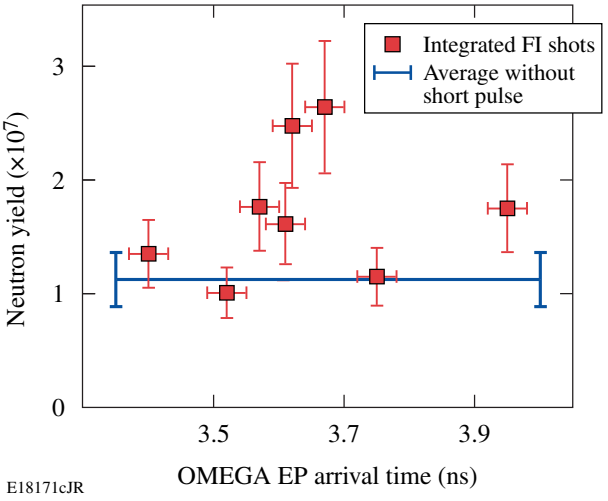

Figure 120.75
Measured D–D neutron yield from integrated fast-ignition shots (squares) versus timing of the short-pulse laser. The solid line represents the measured yield without the short-pulse laser.

FY09 LLNL OMEGA Experimental Programs

In FY09, LLNL led 238 target shots on the OMEGA Laser System. Approximately half of these shots supported the National Ignition Campaign (NIC). The remainder were dedicated to experiments for the high-energy-density stewardship experiments (HEDSE).

Objectives of the LLNL-led NIC campaigns on OMEGA included

- *Laser–plasma interaction studies in physical conditions relevant for the National Ignition Facility (NIF) ignition targets*
- *Demonstration of* T_r *= 100-eV foot-symmetry tuning using a re-emission sphere*
- *X-ray scattering in support of conductivity measurements of solid-density Be plasmas*
- *Experiments to study the physical properties (thermal conductivity) of shocked-fusion fuels*
- *High-resolution measurements of velocity nonuniformities created by microscopic perturbations in NIF ablator materials*
- *Development of a novel Compton radiography diagnostic platform for inertial confinement fusion (ICF) experiments*
- *Precision validation of the equation of state for quartz*

The LLNL HEDSE campaigns included the following:

- *Quasi-isentropic (ICE) drive used to study material properties such as strength, equation of state, phase, and phase-transition kinetics under high pressure*
- *Development of a high-energy backlighter for radiography in support of material strength experiments using OMEGA EP and the joint OMEGA/OMEGA EP configuration*
- *Debris characterization from long-duration, point-apertured, point-projection x-ray backlighters for NIF radiation transport experiments*

- *Demonstration of ultrafast temperature and density measurements with x-ray Thomson scattering from short-pulse-laser–heated matter.*
- *The development of an experimental platform to study nonlocal thermodynamic equilibrium (NLTE) physics using direct-drive implosions*
- *Opacity studies of high-temperature plasmas under LTE conditions*
- *Characterization of copper (Cu) foams for HEDSE experiments*

1. National Ignition Campaign

Laser–Plasma Interactions: The FY09 laser–plasma interaction experiments continued to emulate the plasma conditions expected along the laser-beam path in inertial confinement fusion designs. An interaction beam (Beam 30) aligned along the axis of a gas-filled hohlraum is used to study laser-beam propagation. This year, the effect of polarization smoothing was shown to increase laser-stimulated Brillouin scattering backscatter thresholds by about the 1.6× factor expected analytically and from simulations.[27] Second, the sensitivity of stimulated Raman scattering to density was checked in NIC-relevant plasmas.[28] The results will be presented as an invited talk at the APS DPP 2009 meeting.

Symmetry Diagnosis by Re-emission Sphere: The indirect-drive NIC proposes to set the first 2 ns of hohlraum radiation symmetry by observing the instantaneous soft x-ray re-emission pattern from a high-Z sphere in place of the ignition capsule. The soft x-ray measurements require low-Z windows over diagnostic holes and the laser beams that otherwise would interact with these windows have to be turned off. To assess this technique under NIC conditions, we used the Omega Laser Facility to image the re-emission of Bi-coated spheres placed inside a vacuum hohlraum with 200-ps temporal, 50- to 100-μm spatial, and 30% spectral resolution. The experiment is shown schematically in Fig. 120.76. Different from the previous experiments performed in scale-0.6 NIF hohlraums,[29] the new experiments were performed in larger scale-0.93 NIF hohlraums, making it possible to achieve a hohlraum laser-entrance-hole (LEH) size and inner laser-beam illumination, similar to upcoming NIF experiments, by azimuthally steering four inner beams away from the diagnostic window. Furthermore, compared to the experiments of Ref. 29, these experiments use a less-perturbing off-axis stalk rather than a thin CH tent to hold the capsule.

As shown in Fig. 120.77, by using 1-ns square laser pulses, we achieved hohlraum radiation temperatures measured with Dante that are similar to those calculated for future NIF experiments. The laser beams smoothed with SG4 phase plates generated intensities at the hohlraum wall that are similar to the foot of the NIF ignition design.

We acquired good re-emission images in the 0.4- to 1.3-ns time interval corresponding to 85- to 115-eV NIF foot hohlraum temperatures for both 900- and 1200-eV energy bands at several inner-to-outer beam power balances; the images are shown in Fig. 120.78. The x-ray background from the sphere stalk was negligible, validating the target design for upcoming NIF re-emit experiments. The data confirm the required measurement accuracies of <3% P_2/P_0 and P_4/P_0 Legendre mode flux asymmetry demonstrated in Ref. 29. Furthermore, the image signal-to-noise ratio is in agreement with a Planckian model for sphere re-emission, similar to Ref. 29.

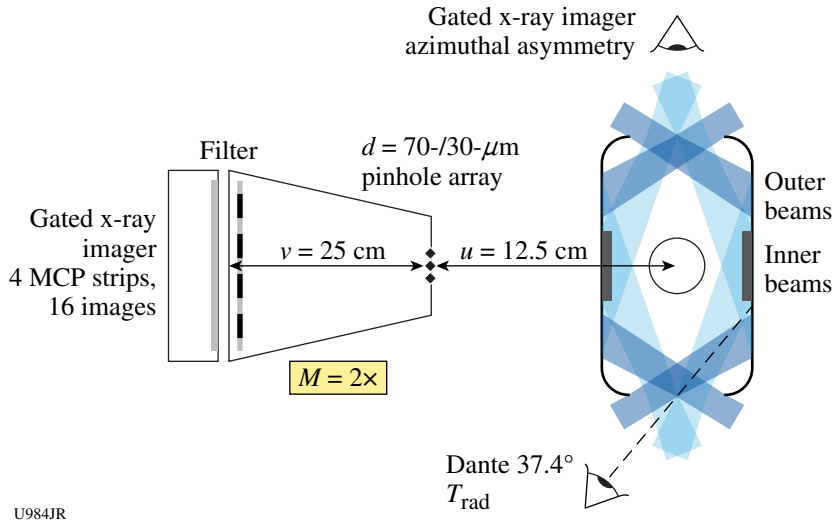

Figure 120.76
Re-emission experimental setup for the NIF and OMEGA.

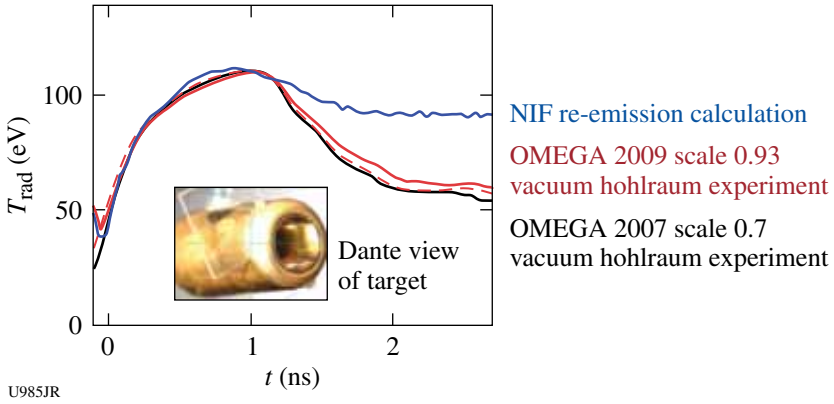

Figure 120.77
Hohlraum radiation temperatures measured with Dante in the OMEGA experiments and calculated for the NIF.

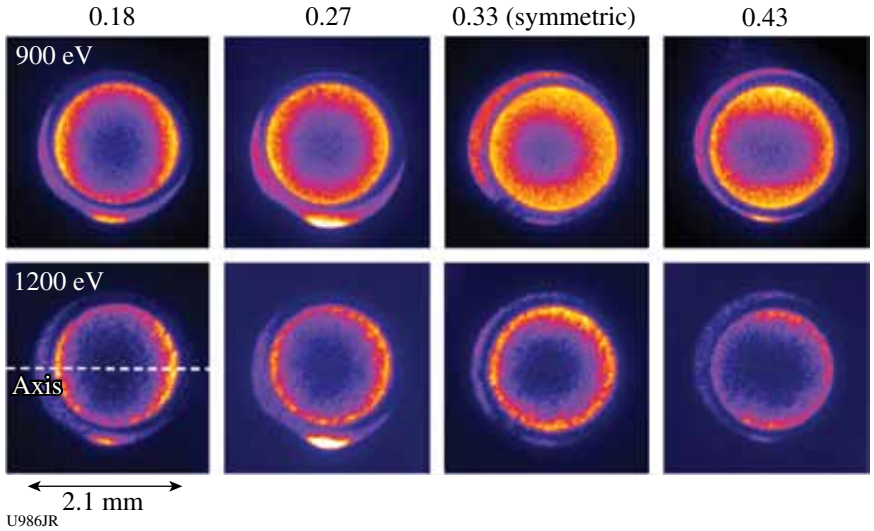

Figure 120.78
Re-emission images acquired at t = 0.8 ns at 900-eV and 1200-eV energy bands versus inner-to-outer beam power balance (in units of inner/total laser power).

As shown in Fig. 120.78, by changing the inner-to-outer beam power balance that will be used to tune early time P_2/P_0 in NIF ignition targets, we were able to change the radiation symmetry at the capsule from pole hot to equator hot. Figure 120.79 shows the measured average P_2/P_0 as a function of power balance.

The measured P_2/P_0 sensitivity to power balance per beam is consistent with Ref. 29, where smaller hohlraums, larger LEH (75% versus 60% of the hohlraum diameter), and fewer inner beams (4 versus 8) were used. In both experiments the measured 1200-eV to 900-eV P_2/P_0 relative sensitivity of 2 is larger than the $h\nu$ ratio (1.33), which is given by an ideal Planckian model for the sphere re-emission. This difference is under investigation.

X-Ray Thomson Scattering—Conductivity of Warm, Dense Matter: The goal of these FY09 experiments was to isochorically heat a 250-μm Be foil to sufficiently high temperatures in order to observe upshifted plasmon signals with collective x-ray Thomson scattering (XRTS). Quantitatively measuring the ratio of upshifted over downshifted plasmon strength enables one to infer the electron-plasma temperature based on first principles from the detailed balance relation, i.e., it is proportional to the Boltzmann factor $\exp\left(-h\nu_{res}/k_B T_e\right)$, with $h\nu_{res}$ the plasmon shift.

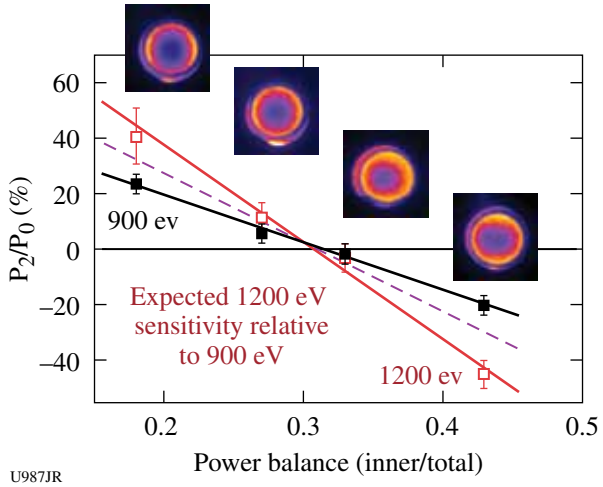

Figure 120.79
Re-emission images measured at 0.8 ns at 900 eV for constant and the corresponding P_2/P_0 versus inner-to-outer beam power balance

We utilized the XRTS target platform, which had been proven very successful in experiments on shock-compressed Be. For isochoric heating we employed L-shell x rays[30,31] that were created in thin Ag, Au, or Rh foils that were directly mounted to the Be, cf. Fig. 120.80(a) for a schematic experimental setup. Time delayed to the 10 heater beams, 16 probe beams created the Cl Ly$_\alpha$ x-ray probe at 2.96 keV. The source spectrum is plotted in Fig. 120.80(b). The x rays scattered off the rear Be surface under a 40° scattering angle were recorded by the gated Thomson spectrometer, which is based on high-opacity pyrolitic graphite as the Bragg crystal.

We obtained the best results with a silver x-ray converter foil. The scattering spectrum (black solid line), plotted in Fig. 120.80(b), shows inelastically scattered contributions that are up- and downshifted in energy compared to the Cl Ly$_\alpha$ source line. The plasmon features are rather broad since the collectivity parameter $\alpha = 1.22$, putting the experiment just into the collective scattering regime. The best fit (red line) to the data is achieved for T_e = 18 eV and $n_e = 1.8 \times 10^{23}$ cm^{-3}. The temperature is determined from detailed balance with an accuracy of 20%.

D_2 Thermal Conductivity: Reflectance and thermal conductivity of deuterium increase dramatically during compression above 1 Mbar. Simultaneous measurements of velocity, reflectance, and emissivity are being used to investigate the transport properties of cryogenic D_2 compressed by multiple shocks up to 6 Mbar at 7000 K (see Fig. 120.81). In FY10 reliability improvements to the experimental platform will enable one to measure D_2 transport properties across a wide region of phase space.

Capsule Instability Seeding by Shock Nonuniformity: Two consecutive shot days were devoted to CAPSEED campaigns in FY09. The primary focus of these campaigns was to study Be ablator samples of varying quality in order to compare them with results from detailed metrology such as grazing-angle x-ray scattering, electron microscopy, and surface profile measurements. The OMEGA high-resolution velocimeter (OHRV) diagnostic was configured with higher sensitivity than previ-

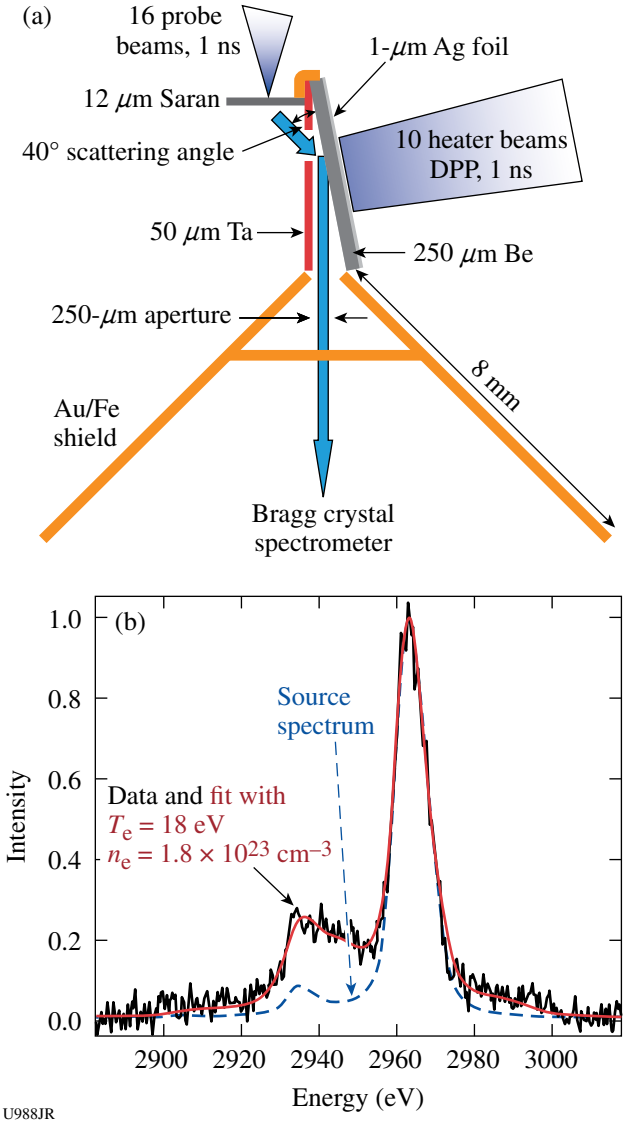

Figure 120.80
(a) Experimental setup to isochorically heat a 250-μm Be foil that is characterized with a Cl Ly$_\alpha$ x-ray probe at 2.96 keV. Shields block the direct line of sight to the spectrometer (toward the bottom). (b) X-ray Thomson scattering data show up- and downshifted plasmon signals that make it possible to infer temperature from a detailed balance relation.

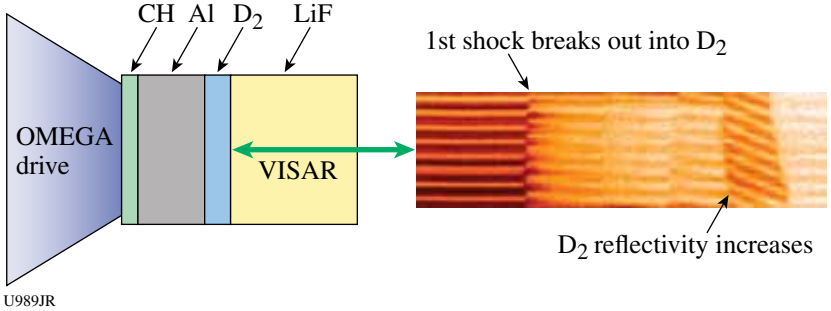

Figure 120.81
Experimental setup and VISAR record of multi-shock compressed D_2 to 6 Mbar. A dramatic increase in the D_2 reflectance can be seen in the streak record at the arrival of the final shock.

ous experiments to reduce the noise floor as low as possible. Analysis of the data led to several conclusions: (1) the velocity nonuniformities in high-quality Be samples are effectively at the noise floor of the OHRV, which meets the NIF requirement for ablator performance; and (2) poor-quality sample batches produced a higher level of nonuniformities than better-quality sample batches. The velocity nonuniformities observed in the poor-quality batches (Fig. 120.82) were attributed to the presence of a significant fraction of voids in the samples. The sample quality is batch dependent, so it is possible to identify high- and low-quality batches after fabrication. This will help to eliminate low-performing batches from the NIF experiments using electron microscopy and x-ray scattering. Future developments will focus on improving the noise floor of the instrument and continuing with high-sensitivity measurements on CH(Ge) and diamond samples.

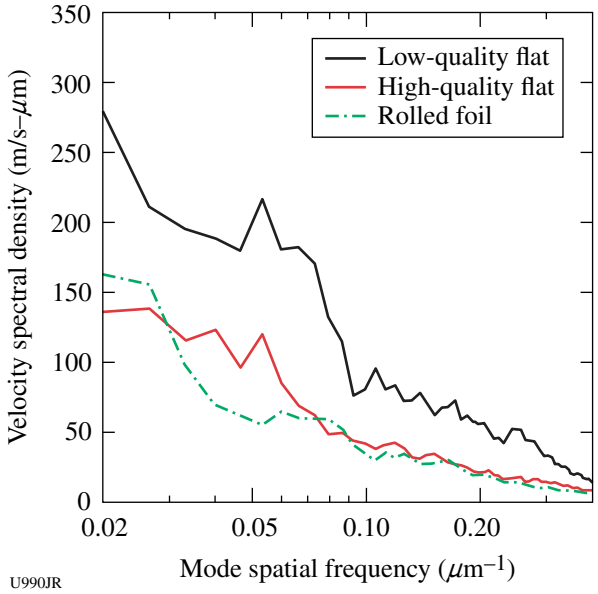

Figure 120.82
Velocity amplitude spectra recorded for three different Be sample types. The flats were Cu-doped sputtered Be foils, and the rolled foil was a polished sample of commercially available Be foil.

Compton Radiography: The goal of the Compton radiography campaign is to build a novel diagnostic platform for ICF. In FY09 we successfully obtained the first-ever radiographs of implosions, at photon energies around and above 60 keV, where Compton scattering largely dominated the opacity of the plastic shell. In our experiments we used 60 beams of the OMEGA laser for direct-drive implosions of 40-μm-thick, 870-μm-diam CH capsules filled with 3 atm of DD gas, located at OMEGA's target chamber center. As a backlighter we used a 10-μm-diam Au wire, 300 μm long, in a point-projection, end-on geometry 10 mm from the CH shell. The backlighter was driven by the OMEGA EP short-pulse beam, delivering ~1 kJ at 10 ps in a 100-μm-square spot size. The time delay between the OMEGA EP short pulse and the OMEGA laser pulses was chosen to match the time of peak compression predicted by *LILAC* 1-D simulations. To record the radiographs, we designed and built a dedicated Compton radiography snout (CRS) consisting of a three-stage collimator, a layered structure of Al–Pb to shield against neutrons and high-energy x and γ rays, and a permanent magnetic field to deflect electrons away from the radiography line of sight. CRS allows for the insertion of filters at different locations and hosts a Fujifilm BAS imaging plate detector at about 400 mm from target chamber center. By progressively increasing filtration in the CRS, we obtained good-quality radiographs (with a signal-to-noise ratio of a few at 2% contrast) at (average) photon energies of approximately 60 keV, 80 keV, and 100 keV. As an example, Fig. 120.83 shows a radiograph of the imploding CH shell, near peak compression, at t = 4 ns, obtained at a photon energy of ~60 keV. The

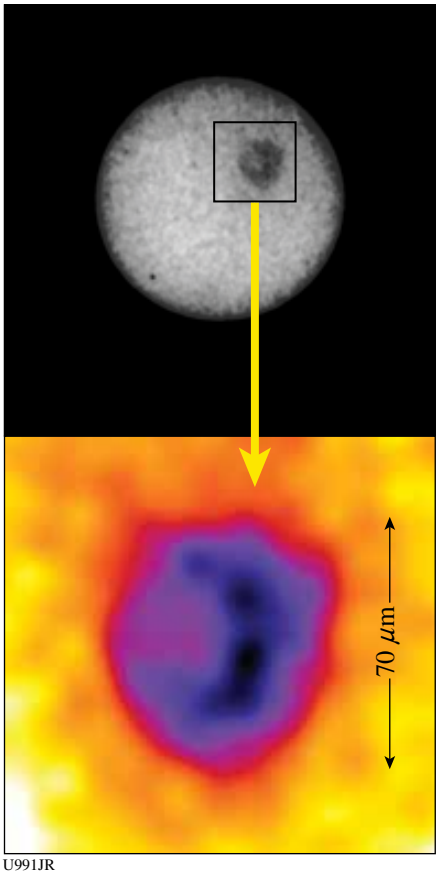

Figure 120.83
Compton radiograph of CH shell near peak compression: $\langle h\nu \rangle \sim 60$ keV. (a) CH shell radiograph inside the shadow of a CRS collimator; (b) blowup of radiograph.

diameter measured from the radiograph was 70 μm: very close to the value of 60 μm predicted by *LILAC* 1-D simulations. The CRS features a built-in step wedge filter that allows one to reconstruct the backlighting Bremsstrahlung spectrum and therefore measure the density from the radiograph.

Precision Validation of Quartz Equation of State (EOS): CH_n EOS measurements performed earlier in the year relied on quartz as the impedance-matching standard. The quartz (SiO_2) Hugoniot, measured several years ago on OMEGA, was found to be in good agreement with a linear shock velocity to particle velocity relation [see Fig. 120.84(a)]. This fit was also in agreement with earlier Russian measurements up to 6 Mbar and a single 20-Mbar point. However, given the sensitivity of impedance-matching measurements to uncertainties in the impedance-matching standard, it was necessary to further increase our confidence in the quartz Hugoniot. This was done by using a new "bootstrap" impedance-matching method, whereby quartz (ρ_0 = 2.65 g/cc) is impedance matched to another polymorph of SiO_2 fused silica (ρ_0 = 2.2 g/cc) [see Fig. 120.84(b)]. Since each Hugoniot probes a slightly different region of the SiO_2 high-pressure phase diagram, the results are highly sensitive to derivative quantities, in particular the slope of the U_s–U_p relation and the Gruneisen parameter.

2. High-Energy-Density Stewardship Experiments

Material Properties: In FY09 five experiment campaigns on OMEGA and OMEGA EP were performed in support of the material dynamics effort: thin-walled hohlraum drive development (1/2 day each, two campaigns); low-density foam reservoir tests (1/2 day); tantalum Rayleigh–Taylor experiment using OMEGA plus OMEGA EP in a joint experiment day; and high-energy backlighter characterization (one OMEGA EP day).

Quasi-Isentropic Compression Hohlraum Drive Development: The main goal of the first half-day of OMEGA shots was to test the thin-walled hohlraum's performance to decrease the late-time radiation temperature (Tr) to delay and reduce the strength of the late-time shock in the quasi-isentropic pressure drive platform. The thin-walled hohlraums had a 1-μm Au wall with 100-μm-thick epoxy backing. In this experiment the ablator was 75 μm of CH, to make a direct comparison with thick-walled hohlraum data from previous shots in March 2008. Our data suggest that the thin-walled hohlraums do delay the arrival of the late-time shock, so we will be able to utilize this platform for our strength experiment. The other goal for this campaign was to test low-density foams as the final layer in our reservoir. We tested 50-mg/cc SiO_2 aerogel (100 and 200 μm thick) and 100-mg/cc carbonized resorcinol formaldehyde (CRF) (50-μm-thick) foams. The ablator was 25 μm of Be. Comparison between the data and the simulations showed that these low-density foams worked well and showed no hydro-instabilities. The simulations of the velocity interferometry system for any reflector (VISAR) data show abrupt velocity steps for each reservoir layer, corresponding to the foam followed by the CH (12.5% Br) layer. The data also showed distinct velocity steps for each reservoir layer, but the transition between layers was smoother than the simulated results, likely because of hydrodynamic mixing at the interface. Both simulations and data showed a late-time stagnation shock.

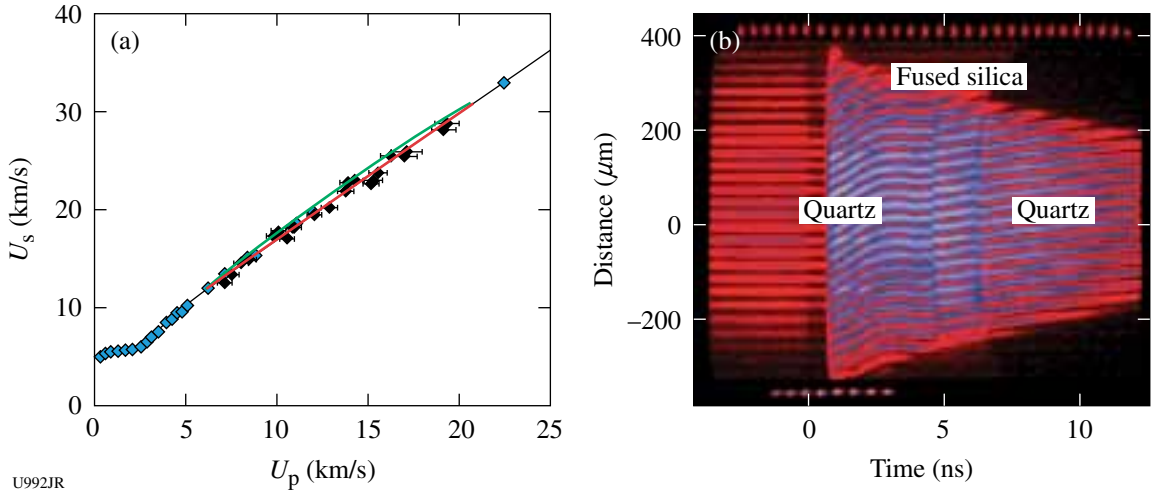

Figure 120.84
(a) Previously measured quartz Hugoniot. The red line provides the best linear fit to data; the green line provides a possible outlier fit to the data. New measurements were designed to determine possible deviations from the original linear fit. (b) Impedance matching of a quartz/fused silica/quartz target.

The goal of the second half-day of OMEGA shots was to test the thin-walled hohlraum drive using both Al and Ta witness samples to verify that they give consistent drive measurements. These two witness plate samples gave consistent results. The second goal of this half-day was to test the stacked CRF foam reservoir properties: 50 μm of 500-mg/cc CRF followed by 100 μm of 50-mg/cc CRF. We used 25-μm Be ablators for all shots during this half-day. This reservoir scales to a NIF design that reaches 5 Mb in a Ta-strength experiment. Post-shot simulations match well with the measured drive using the stacked foam reservoir. The simulated VISAR results predicted abrupt velocity steps, corresponding to each layer in the reservoir. The data, however, showed much smoother transitions between the different layers in the reservoir, likely because of hydrodynamic mixing between the layers. Provided this mixing is reproducible, this added smoothing improves the drive by minimizing shock heating.

ICE Gradient-Density Reservoir Development: The goal of this half-day of OMEGA shots was to test the foam reservoir performance for the material strength experiment. Therefore we used thick-walled hohlraums for this experiment (since the foam in the reservoir modifies only the early-time drive). We tested the low-density, 50-mg/cc SiO_2 foams by measuring the shock-breakout (SBO) times from 75/100/125 μm of SiO_2 foam thicknesses. The data matched the predictions. The second part of the experiment was to test stacked foam layers in the reservoir of 500-mg/cc CRF (50 μm thick) and 50-mg/cc SiO_2 (100 μm thick). The release profile and the SBO's on various material layers were compared to simulations, with poor agreement between the detailed interface arrival times and shape. This could be due to uncertainties in the EOS of the SiO_2 foam.

ICE Tantalum Rayleigh–Taylor Experiments: We have successfully performed the first OMEGA and OMEGA EP joint shots (60-beam long-pulse laser plus OMEGA EP short-pulse laser combined) to measure Ta Rayleigh–Taylor (RT) ripple growth to test models of Ta material strength at ~1-Mbar pressures and high strain rates of $\sim 10^7$ s^{-1}. The OMEGA EP laser was used to generate a high-energy backlighter (>20 keV) with high spatial resolution (<10 μm) to probe a 50-μm-thick Ta sample with 3-μm peak-to-valley sinusoidal ripples. We had four joint shots to measure the Ta RT growth, interleaved with six OMEGA-only (long-pulse) shots to measure the hohlraum drive. The joint-shot radiography technique worked well. For a few of the joints shots, the OMEGA EP beam slightly missed the 100-μm-diam micro-flat backlighter target, producing low-signal images. The growth-factor measurements require a good understanding of the backlight spectrum. Figure 120.85 shows the experimental configuration, Fig. 120.86 shows the target details, and Fig. 120.87 shows a resulting Ta RT radiography image using the high-energy Ag backlighter. Future

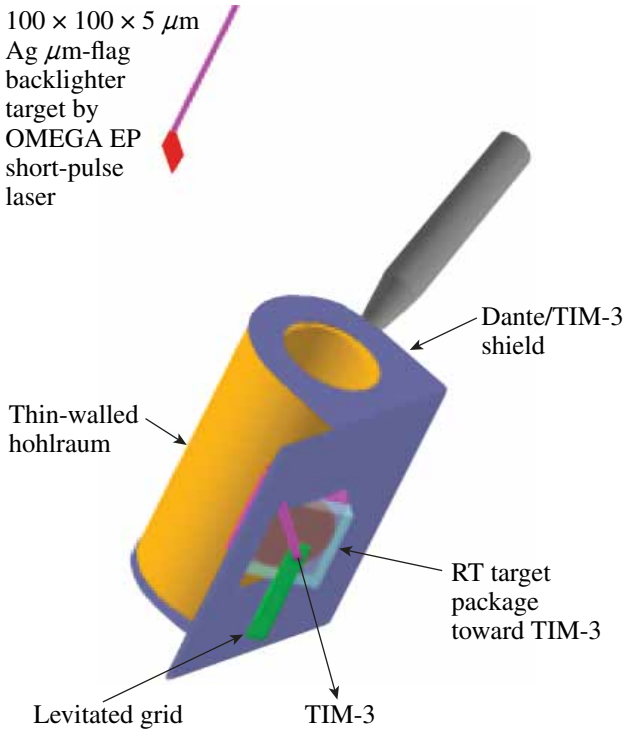

Figure 120.85
ICE tantalum Rayleigh–Taylor (ICE Ta RT)-09A experimental setup.

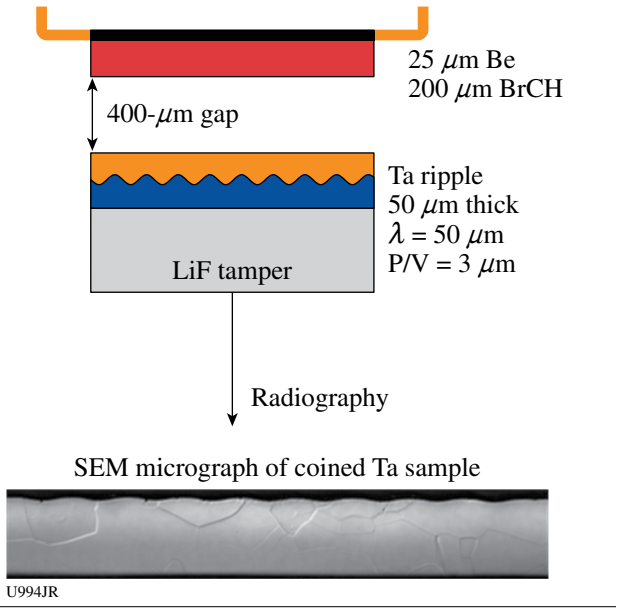

Figure 120.86
ICE tantalum Rayleigh–Taylor (ICE Ta RT) target details.

experiments will acquire data that will allow us to compare predictions of Ta strength using standard material models (PTW, Steinberg–Guinan) at ~Mbar pressure. In conclusion, we have demonstrated that Rayleigh–Taylor experiments for Ta (and other high-Z) samples are possible, and this type of experiment opens up a new capability for high-photon-energy radiography on OMEGA experiments. This experiment also led to three invited talks: IFSA 09 (The Sixth International Conference on Inertial Fusion Science and Applications, San Francisco, CA, September 2009); APS/DPP (American Physical Society, Atlanta, GA, November 2009); and JOWG-37 (Livermore, CA, October 2009).

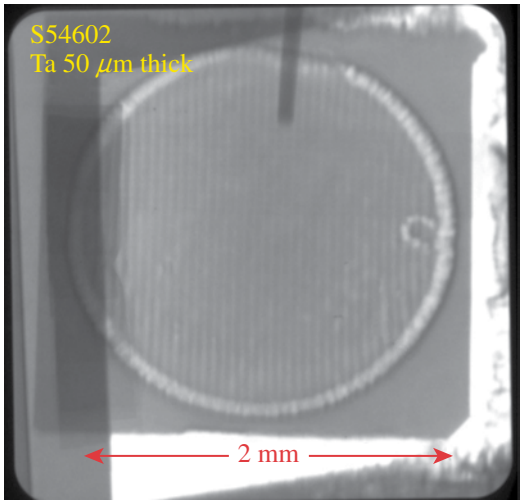

Figure 120.87
ICE Ta RT radiography using OMEGA + OMEGA EP joint shot.

High-Energy Backlighter (HEBL) Development: The goal of the HEBL OMEGA EP campaign was to measure the high-energy backlighter spectrum that would be utilized for the Ta Rayleigh–Taylor strength experiment on the NIF. The high-energy backlighter is created by the OMEGA EP short-pulse beam illuminating a micro-flag target. The absolute spectrum will be crucial to the quantitative analysis of results from the radio-graphy data. We utilized a transmission crystal spectrometer (TCS) that covers a 15- to 70-keV range; a Bremsstrahlung x-ray spectrometer that covers 70 keV to 1 MeV; and Ross-pair filters to get an absolute yield in the 20- to 70-keV range. We had six shots total and our settings were changed to test backlighter repeatability, laser spot-size dependency, and radiography object dependency. By combining detectors that span different energy ranges we were be able to produce a composite spectrum from 15 keV to 1 MeV, as shown in Fig. 120.88.

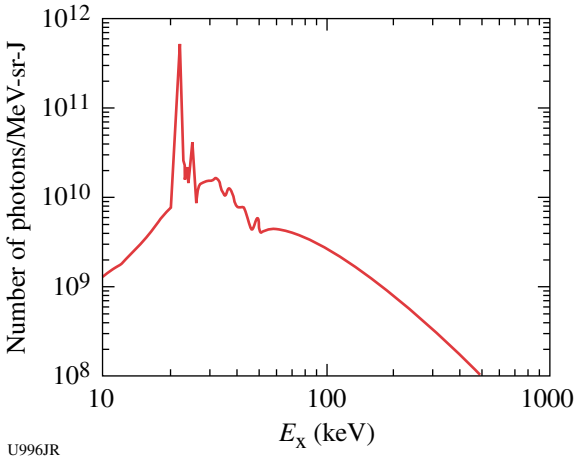

Figure 120.88
High-energy backlighter spectrum using the OMEGA EP short-pulse laser. Measurements were made using many different detectors.

Debris Characterization from Long-Duration Point-Source Backlighters: An 8-ns point-source backlighter developed on OMEGA was demonstrated on the NIF for streaked radiography. This configuration provided sufficient photons, high spatial resolution (~20 μm), and instrument protection from debris. To extend this to multiframe 2-D radiography, experiments were performed on OMEGA to characterize the debris and signal level. Pinhole-apertured point-projection backlighters generally produce either solid or liquid ballistic spall from the pinhole substrate, which generally is accelerated normal to the pinhole surface. On experiments where using a tilted pinhole substrate is undesirable, diagnostics must be protected from spall launched directly at the x-ray detector. This is traditionally done with thick pieces of beryllium that can offer protection without sacrificing x-ray transmission.

Alternate materials are being developed for debris mitigation for pinhole-apertured point-projection backlighters that are pointed directly at imaging diagnostics. We tested several thicknesses of aluminum and boron carbide (B_4C) for debris mitigation. Twenty OMEGA beams (10-kJ laser energy) drove a Ni pinhole-apertured point-projection backlighter (75-μm-thick Ta pinhole substrate) from P6 toward up to six 75-μm-thick or up to three 150-μm-thick filters. These filters were spaced at least 15 mm apart in the MSpec snout in TIM-6, with an image plate in the static pinhole camera array detector. We found (see Fig. 120.89) that three 150-μm-thick B_4C filters encapsulated in 8-μm Kapton let debris penetrate the rear-most filter once or twice, whereas three 75-μm-thick Al filters or two

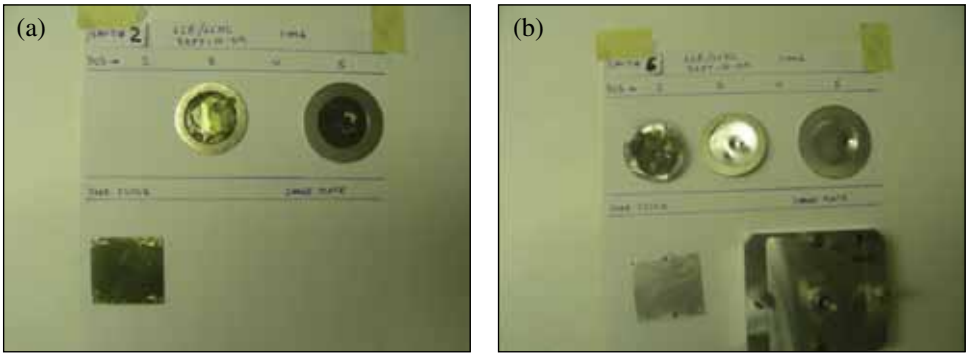

Figure 120.89
Damaged filters from debris testing. (a) Three 150-μm-thick B_4C-Kapton filters, showing one pinhole in the rear filter; (b) four 75-μm-thick Al filters, with the first three showing some ballistic damage, and a clean rear filter.

150-μm-thick Al filters stopped all the ballistic debris, leaving at least one clean rear filter. This suggests that the debris can be mitigated while allowing sufficient x-ray transmission.

X-Ray Thomson Scattering: The objective of this campaign was to demonstrate ultrafast temperature and density measurements with x-ray Thomson scattering from short-pulse-laser–heated matter. In March 2009, we used OMEGA EP to heat a 200-μm beryllium cube with a 1-kJ, 10-ps short-pulse laser beam and performed the first noncollective x-ray scattering measurements using a Zn K_α x-ray probe at 8.62 keV (see Fig. 120.90). The probing x rays were produced by the second OMEGA EP 10-ps short-pulse laser beam. On the first day of shots, we performed a total of four shots including the very first shots with two short-pulse beams fired simultaneously for target physics experiments. In addition, we successfully fielded the new Zink von Hamos high-efficiency x-ray spectrometer, a dedicated diagnostic developed for the K_α x-ray Thomson-scattering project. This instrument has shown elastic and inelastic scattering signals of beryllium with only 180 J in the probe beam.

Since these experiments were the first to use both OMEGA EP short-pulse laser beams simultaneously on target, we had to field

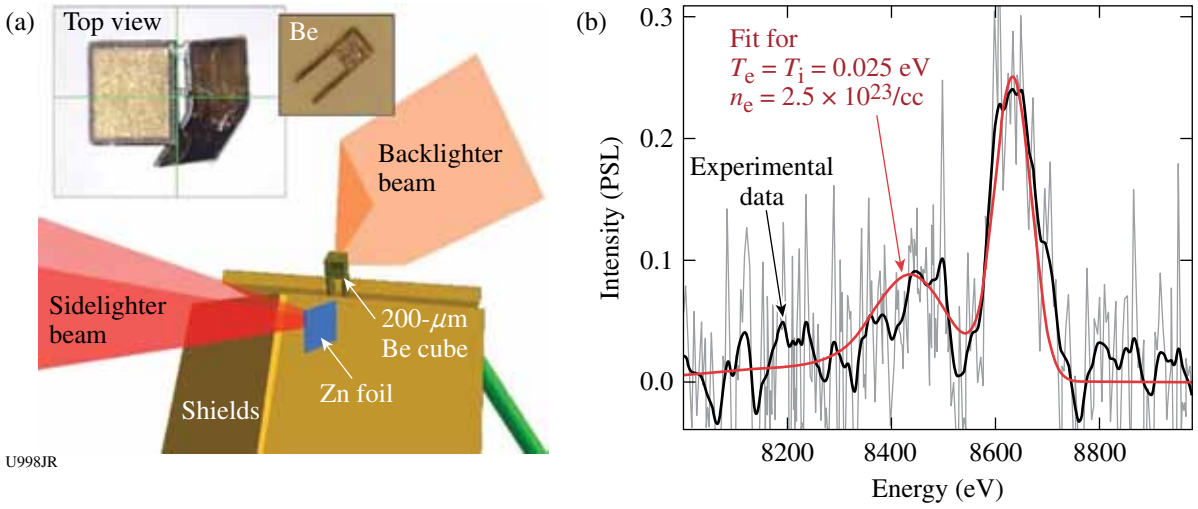

Figure 120.90
(a) Experimental setup showing the OMEGA EP backlighter beam heating a 200-μm Be cube. The OMEGA EP sidelighter beam creates a Zn K_α x-ray probe at 8.62 keV. Shields block the direct line of sight to the spectrometer (toward the bottom). (b) X-ray Thomson-scattering spectrum from cold beryllium, measured with only 180 J in OMEGA EP sidelighter beam. The downshifted inelastically scattered Compton feature is fitted with the parameters for cold, solid beryllium.

dedicated diagnostics to measure beam synchronization. We achieved synchronization to an accuracy of only 250±200 ps, which must be improved in the future to reach ~100 ps for this experiment. We also employed low-energy activation shots (50 J) to successfully record the x-ray source spectrum and to determine the spectrometer dispersion. The third shot of the day delivered ~1 kJ within a 10-ps pulse in the *backlighter* beam to heat the Be and ~1.3 kJ in the *sidelighter* beam to create the x-ray probe. Since the sidelighter shot was higher in energy than originally anticipated, we reduced the energy to 180 J on the last shot of the day. Nevertheless, we were able to record elastic- and inelastic-scattering signals of cold beryllium. This is a very promising result. We also assessed the bremsstrahlung level and background levels. These measurements will enable us to improve the experimental design to measure plasma temperatures of short-pulse-laser–heated beryllium with high temporal resolution using K_α x-ray Thomson scattering on future shots.

Non-LTE Implosions: The goal of the non-LTE campaign is to build a platform to study the energy balance in implosions by measuring ion, electron, and radiation temperatures as a function of high-Z dopant concentration. In our FY09 experiments, we used 60 beams of the OMEGA laser for direct-drive implosions of thin (4-μm) glass capsules filled with 10 atm of D^3He gas and Kr gas as a spectroscopic tracer. The relative concentration of DD and ^3He was varied during the shots, the Kr concentrations were 0.001 and 0.005 atm, and some capsules also contained as much as ~0.1 atm of Xe. As a time-resolved electron temperature (T_e) diagnostic, we fielded a mica conical crystal spectrometer that was coupled to a streak camera and viewed K-shell emission lines from the Kr dopant. Time-integrated spectra were also recorded with the HENEX spectrometer. We also fielded a high-resolution spectrometer to use the Doppler broadening of x-ray lines for measuring the ion temperature T_i.

We observed a decrease in the DD/DT yield ratio with increasing Xe concentration. This trend is well reproduced by LASNEX/DCA:T simulations. We observed an increase in the DD/DT yield ratio with increasing DD concentration as well as an increase in the ion temperature, inferred from proton and neutron emission time histories and spectra. Increasing Xe dopant concentration appears to reduce compression-phase T_i by coupling to radiative cooling.

We inferred the time-integrated electron temperature T_e from a Bremsstrahlung functional form fit to the continuum part of the spectra recorded by HENEX. As reported in Fig. 120.91, T_e shows a linear decrease with an increase in Xe dopant concentration: a behavior reproduced by simulations, although experimental measurements give values higher by a factor of about 30%.

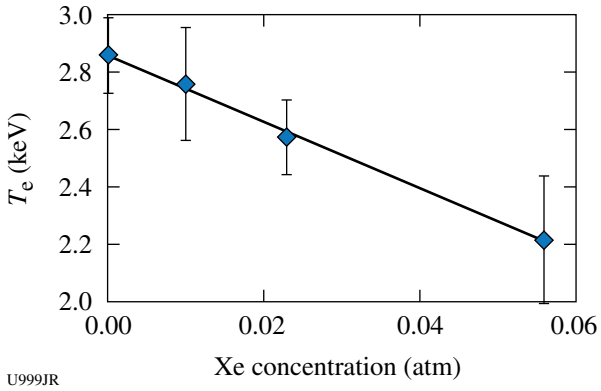

Figure 120.91
Time-integrated T_e, inferred from HENEX spectra, shows a linear decrease with an increase in Xe-dopant concentration.

We used the time-resolved spectra from the conical crystal spectrometer to study the temporal evolution of the Kr He$_\beta$ lines. The $He_{\beta 2}/He_{\beta 1}$ line ratio shows a peak in the central 50 ps of the Kr emission as well as a decrease with increasing Xe concentration, as shown in Fig. 120.92.

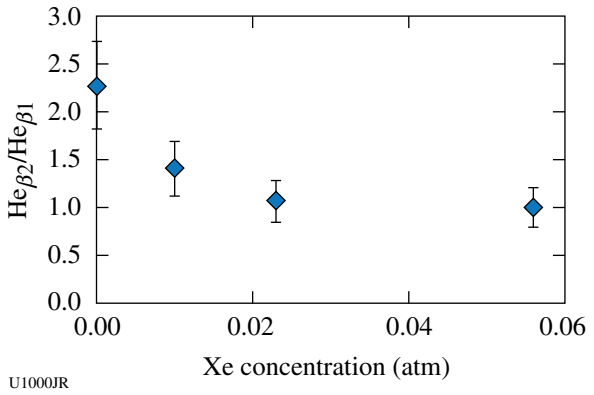

Figure 120.92
The $He_{\beta 2}/He_{\beta 1}$ line ratio, measured from conical crystal spectra, shows a decrease with increasing Xe concentration.

High-Temperature Plasma Opacity: In FY08 LLNL completed the development of a high-temperature laser opacity platform. In FY09, detailed x-ray transmission spectra from fully characterized, high-temperature plasmas were produced using the OMEGA laser to provide validation benchmarks for the x-ray opacity codes (and associated data tables) underlying

simulations of radiation transport experiments. Shots in FY09 produced detailed benchmark data on tantalum–titanium and sodium chloride–titanium plasmas. In these experiments, 24 beams heated a 1.6-mm-diam hohlraum, which in turn radiatively heated and expanded a tamped Ti foil. Additional beams drove two broadband backlighters: a rear-wall burnthrough halfraum (14 beams) and a Kr-filled "dynamic hohlraum" capsule implosion (10 beams). Looking through the sample to these backlighters, two broadband spectrometers characterized the sample transmission from 250 eV to 1600 eV and 3000 eV to 5500 eV, respectively; the lower energy band encompassed the bulk of the Rosseland mean opacity. The plasma density of 0.05±0.01 g/cc, measured by expansion radiography, agreed well with pre-shot calculations. The plasma temperature implied by the titanium ionization features in the 3000- to 5500-eV spectra was 110±5 eV (Fig. 120.93). Rosseland mean opacity data from 250 to 1600 eV is now being analyzed. Discrepancies with theory have been observed and are undergoing detailed investigation. For the future, an extension of these techniques to the NIF would enable us to investigate much hotter plasmas at conditions relevant to stellar core modeling, where recent observational data (helioseismology) contradict standard solar models. A small change in the technique will also enable us to perform a scaled experiment to study photoionized plasmas relevant to black hole accretion disk physics.

Characterization of Cu Foams: Two half-days of OMEGA shots (a total of eight) were used in support of characterization of Cu foams for HEDSE experiments. Material characteristics of interest included both the internal energy (EOS) and the opacity of the foams, at several Mbar of pressure. Pure metal foams are of use as backlighter sources, as low-density materials for radiation–hydrodynamic experiments and opacity experiments. The first set of shots used a hohlraum to drive a CH ablator paired with a Cu foam (density about 0.89 g/cm^3) and a SiO_2 payload (density 0.05 g/cc). The purpose of this experiment was to measure, on the same shot, shock breakout from the Cu into the (transparent) SiO_2, shock velocity in the SiO_2, and the position of the Cu/SiO_2 interface by point-projection radiography. The results are sensitive to the EOS of the Cu foam but not to the opacity. Post-shot simulations agreed with the experimental results. A typical radiograph from this series is shown in Fig. 120.94(a).

The second round of shots continued characterization of Cu foam by using the Cu as an ablator in a hohlraum-driven experiment. The Cu ablator for a typical target is shown during the machining process [Fig. 120.94(b)]; the Cu foam density was about 0.89 g/cm^3. The shock-breakout time and the foil burnthrough time are sensitive to the opacity as well as the internal energy of the foam. The post-shot simulations were again consistent with the experimental results. These results

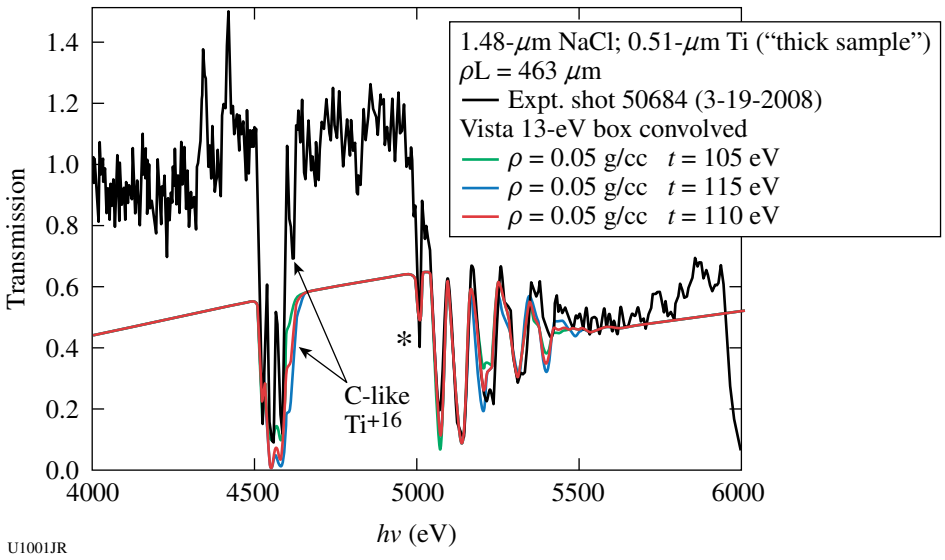

Figure 120.93
X-ray transmission opacity data from gated space-resolved titanium absorption spectra for photon energies from 4 keV to 5.9 keV. To the left are $n = 1$ to 2 absorption lines of F-like to C-like Ti, with the C-like feature being strongly temperature dependent. To the right are $n = 1$ to 3 lines of the same ions, plus a narrow feature from the Ne-like ion (*). Analysis using the VISTA opacity model indicates a temperature of 110±5 eV for densities in measured range, 0.050±0.010 g/cc.

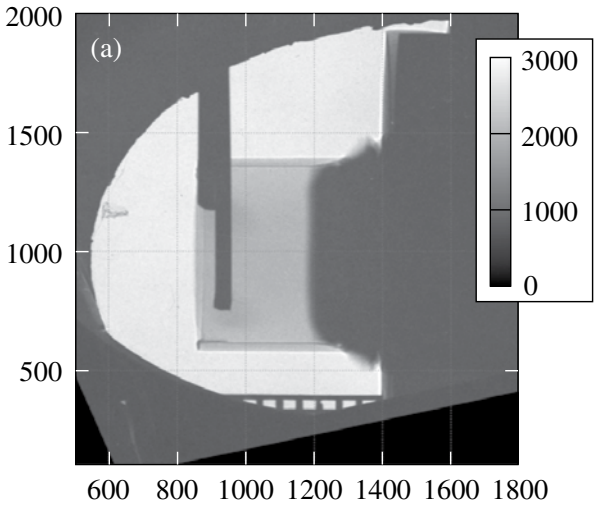

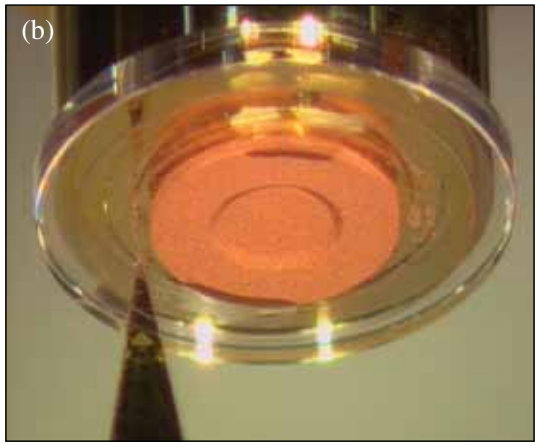

U1002JR

Figure 120.94
(a) A typical radiograph taken during a shock-breakout experiment; (b) a picture of one of the copper foam ablator targets.

will allow us to proceed in FY10 with designing experiments using this Cu foam.

This work performed under the auspices of the U.S. Department of Energy by Lawrence Livermore National Laboratory under Contract DE-AC52-07NA27344.

FY09 LANL OMEGA Experimental Programs

Los Alamos National Laboratory (LANL) successfully fielded a range of experiments on the OMEGA laser during FY09 in support of the national program. LANL conducted a total of 104 target shots: 93 on OMEGA and 11 on OMEGA EP. Collaborations with LLNL, LLE, LULI, NRL, MIT, NSTec, UCSD, and AWE remain an important component of LANL's program on OMEGA.

NIF-5: The NIF-5 campaign had many successes during the course of FY09. The NIF-5 spectrometer, a high-resolution x-ray spectrometer, was qualified for use on OMEGA. Preliminary analysis of the spectra indicates the spectrometer is performing as expected.

In June 2009, the NIF-5 campaign conducted experiments to study hydrodynamic features caused by a radiation drive. The target (Fig. 120.95) consisted of a gold hohlraum. Connected to the hohlraum was a gold tube and a Be tube. A plastic (CH) foam filled the Be tube and the Au tube and extended into the hohlraum. The hohlraum (1200-μm outer diameter) was heated on each end by 15 lasers beams using a 1-ns square pulse. The x rays created by this interaction then heated the CH foam. A Sc backlighter [Fig. 120.95(b)] was illuminated with laser beams to create x rays to diagnose the foam in the Be tube.

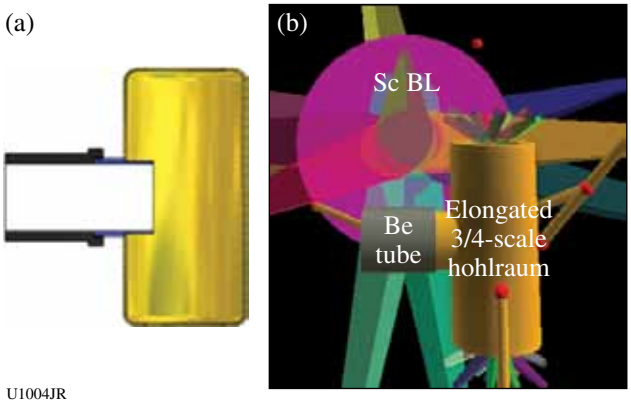

U1004JR

Figure 120.95
(a) A schematic of the target showing the placement of the foam in the Be tube, the Au tube, and the hohlraum; (b) a Visrad model showing the backlighter and the target.

Two of the radiographic images obtained are shown in Fig. 120.96. The top half of the figure shows a radiograph of a radiatively induced shock in a 120-mg/cm^3 foam, 5.9 ns after the hohlraum drive lasers were fired. The bottom half shows a radiograph of a radiatively induced shock in 104-mg/cm^3 foam, 4.7 ns after the hohlraum drive beams were fired. The results of these experiments are being analyzed and will be used to help improve our future simulations.

High-Z: The purpose of the high-Z project is to investigate the effect of high-Z dopants on D_2 fusion burn. This is an ongoing project in which we have obtained a large data set showing that dopant gases such as ^{3}He, Ar, Kr, and Xe degrade the yield in an inertial confinement fusion (ICF) implosion. This

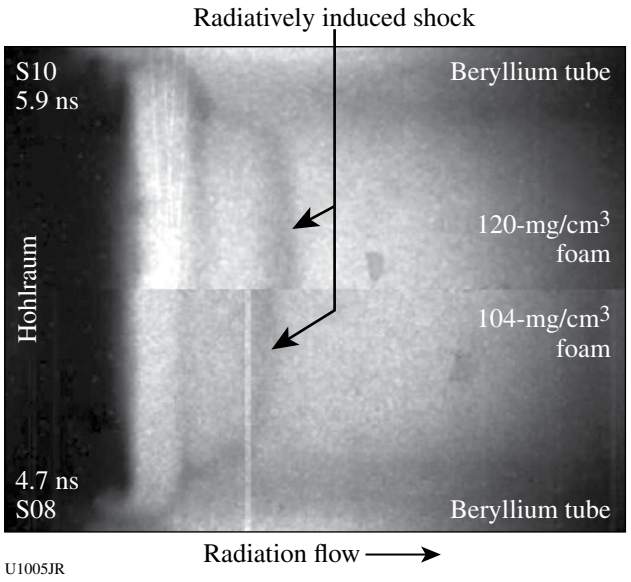

Figure 120.96
The top half of the figure shows a radiograph of a radiatively induced shock in a 120-mg/cm^3 foam, 5.9 ns after the hohlraum drive beams were fired. The bottom half shows a radiograph of a radiatively induced shock in 104-mg/cm^3 foam, 4.7 ns after the hohlraum drive beams.

degradation is more than calculated by our codes and occurs mostly during the latter compression stages of the implosion, after the initial shock reflects off the axis and hits the capsule shell. The reason for the degradation is unknown but understanding this degradation was the focus of FY09 activities.

The high-*Z* project successfully completed two full days of experiments on OMEGA in FY09. The first day of experiments focused on testing whether the OMEGA EP laser could be used as an x-ray backlighter for obtaining radiographs of imploded glass capsules. The capsule, a 4.3-mm-thick, 925-μm-diam SiO_2 capsule filled with 8.75 atm of deuterium and 0.1 atm of argon, was driven by a 0.6-ns-long pulse with a maximum energy of 239 J/beam and also by a distributed polarization rotator, an SG-4 phase plate, and full smoothing by spectral dispersion. The reason for radiographing the shell at late times is to determine if our simulation codes are correctly predicting the amount of ablation from the shell and the properties of the glass during the implosion. The backlighter was a 15-μm-thick iron foil illuminated by an OMEGA EP beam with a pulse length of about 10 ps and an irradiance of less than 5×10^{15} W/cm^2. We obtained nine shots on this shot day, five of which included the OMEGA EP laser. We were able to obtain good data on nearly every shot, although we determined that the x-ray intensity of the 6.7-keV Fe backlighter was not as bright as the implosion at the times of interest, as demonstrated in the results shown in Fig. 120.97. The spectral radiance of the backlighter, with a measured energy conversion efficiency of about 3×10^{-5}, was found to be weaker than the emission from the implosion by a factor of 8 (Fig. 120.98). The second day focused on testing a new experimental platform using Fe-doped glass shells. The doped shells were used to provide a source of Fe ions in the gas, which could then emit x rays that can be measured by an MMI (multiframe monochromatic imager) diagnostic. The MMI is useful in obtaining spatial profiles of temperature and density in the gas (something we do not presently measure) and would provide important information for understanding the yield degradation. On this day we were again quite successful in obtaining good data for a total of 12 shots. We used glass capsules that had 0%, 0.3%, or 0.9% Fe in the glass. We were able to measure the emission of the Fe lines but determined that the emission levels were too weak at these dopant levels to ensure successful application of the MMI diagnostic. We are pursuing plans to develop glass shells that have a higher concentration of Fe, but there are important target fabrication issues that remain to be addressed.

OMEGA EP Ions Campaign: LANL led a series of ion-generation experiments (26 March and 17 August) on OMEGA EP performed by experimental Principal Investigator (PI) K. Flippo with diagnostic PI's J. Cobble (TPIE) and D. Offermann (LANL PFPII-mod and THVL). These experiments were carried out in collaboration with UCSD, LLNL, and LLE/UR under the project leadership of LANL's M. Schmitt.

In the first series of shots (26 March), we had a total of seven shots on target that provided good data on the performance of OMEGA EP in terms of ion energies from dielectric targets [chemical vapor deposition (CVD) diamond] and conductors (Cu) using the PFPII loaded with Radiochromic film as the primary diagnostic. Figure 120.99 compares the beam quality and spectrum from (a) copper and (b) CVD diamond targets at 15-μm thicknesses. The beam profile from the 15-μm target had a well-defined outer edge of the proton beam and a higher temperature to the beam, 5.58 keV versus the beam from the copper target, which had a large defuse beam, and an inner darker beam, with a characteristic temperature of 3.79 keV. Overall the beam from the copper target contained more protons in the 4- to 36-MeV range, but fewer total ions in the higher end of the spectrum, 15 MeV to 36 MeV. Approximately 2.04% and 1.81% of the laser energy was converted into protons for CVD and copper, respectively.

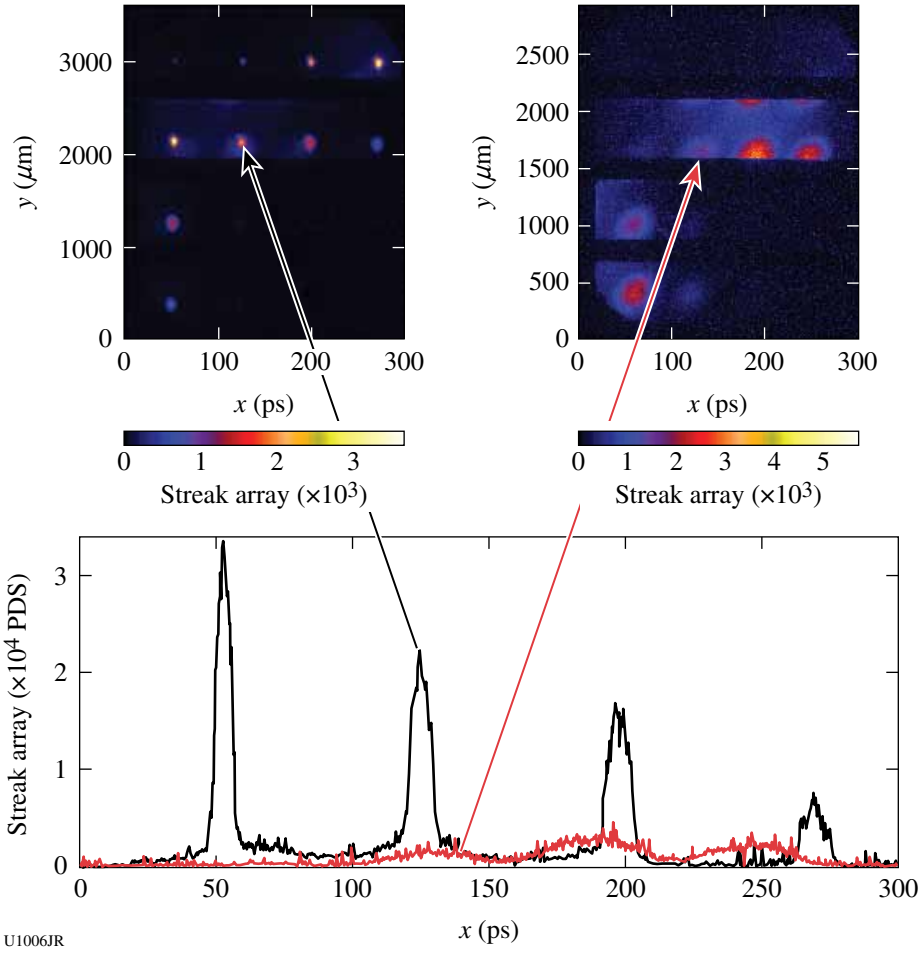

Figure 120.97
X-ray framing-camera images and lineouts from the OMEGA EP joint shots 53548 and 53549. Shot 53548 shows an image that includes the backlighter and the capsule, while shot 53549 shows the intensity of the backlighter only. The lineouts were taken from the second horizontal frame and show the relative intensity of the emission from the imploding capsule and the x-ray backlighter.

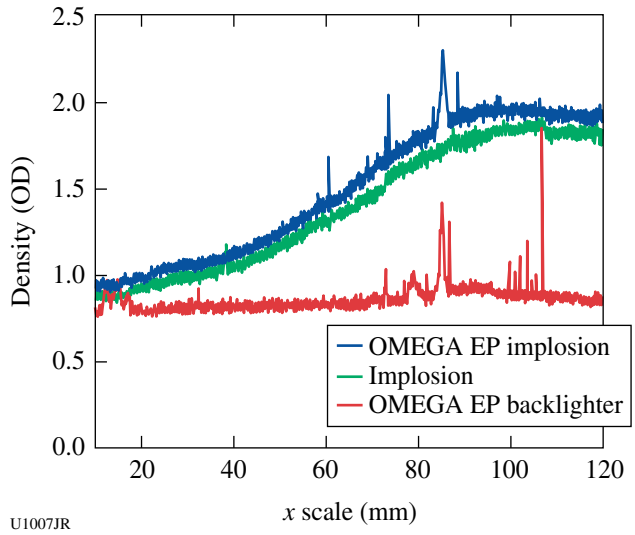

Figure 120.98
Spectral radiance measured by an XRS spectrometer showing the relative emissions of the implosion, backlighter, and the combined spectrum.

The second series of shots (18 August) yielded six shots, the first two on planar diamond foil targets, completing the data set begun in March. The completed data set (see Fig. 120.100) shows that proton beam energy from planar targets peaks around 45 MeV for a target thickness of about 24 μm for an OMEGA EP pulse length of 10 ps and a pulse energy of ~1000 J. These results are currently being prepared for a publication documenting the first ions generated at OMEGA EP; they were also presented at the IFSA 2009 conference in September.

The next four shots were used to perform focusing experiments on OMEGA EP using hemi-shell targets. The third shot of the day (the first hemi) was the first shot to give good data from LANL's new TPIE diagnostic (a ion energy and species analyzer). Preliminary analysis of the PFPII data indicates that the beam quality from the hemis is good and laminar.

The last shot explored the generation of ions over a large area of the hemi-shell (need for higher flux ion beam generation)

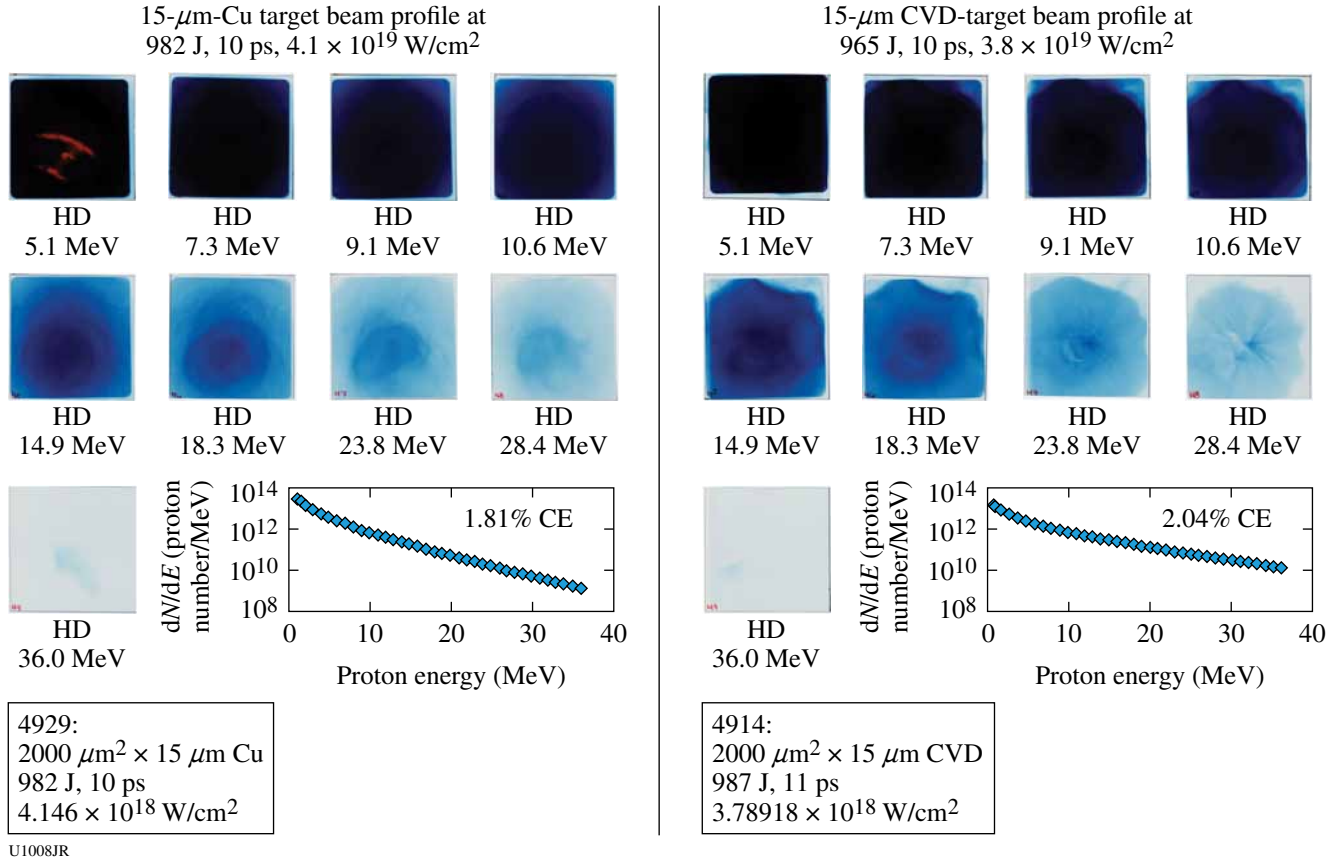

Figure 120.99
Comparison of 15-μm CVD diamond target (right panel) with 15-μm-copper target (left panel). The panels show PFPII data from the RCF film stack with energies associated for each layer, and a calculated proton spectrum fitting the data in the lower right of each panel.

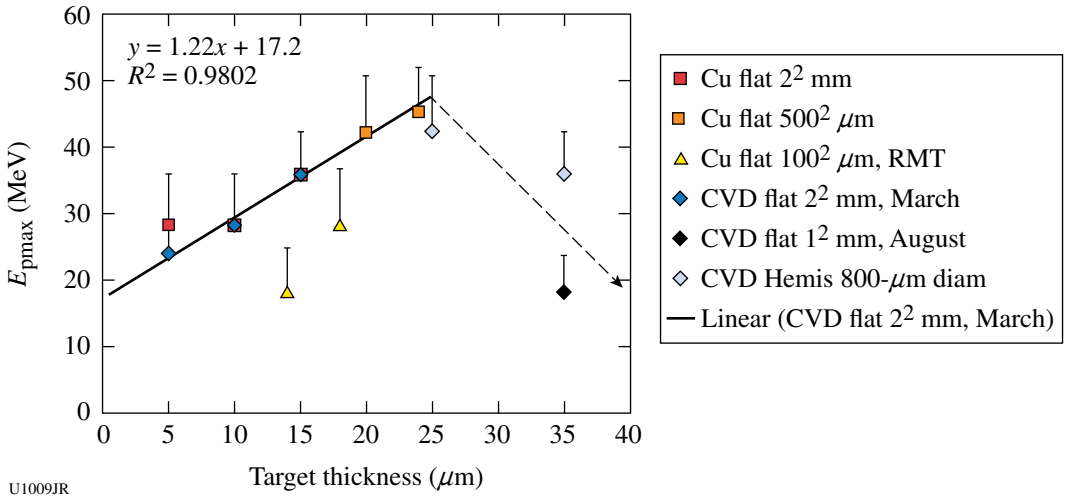

Figure 120.100
OMEGA EP proton scaling with target thickness and an area showing a linearly increasing trend toward 25-μm thickness for CVD (diamond) and Cu targets with areas greater than 100^2 μm^2, with a drop after 25 μm and lower performance in general for targets with areas smaller than 500^2 μm^2.

by using a large laser focus at the target. Data were generated using a copper grid behind the hemi that provided information on the focal quality of the ion beam. The TPIE diagnostic performed well in the completely retracted TIM position using a 250-μm pinhole aperture but with low flux. On a later shot, the TPIE was run in 30 in. and the CR39 moved to the 10-cm position to increase the flux and reduce noise. This provided us with information on the dynamic range of the TPIE instrument. Preliminary analysis of this data indicates that improved performance will be achieved if we add shielding to reduce the noise on the CR39.

Gamma Reaction History Diagnostics: A gamma reaction history (GRH) diagnostic has been developed for the National Ignition Campaign and thoroughly tested on OMEGA this year. The GRH is a follow-on design to the Gas Cherenkov Detector (GCD-1), which has been productive on OMEGA for the past ten years.[32] Figure 120.101 depicts the GRH currently installed on OMEGA. It is designed to detect the 16.7-MeV gamma rays that are emitted in approximately one of every 10,000 DT fusion reactions. These gammas are converted, primarily through Compton scattering, to relativistic electrons inside the domed port cover. The electrons traveling faster than the speed of light in a pressurized gas generate UV/visable Cherenkov radiation, which is collected with off-axis parabolic reflectors into an ultrafast photomultiplier tube (PMT).[33,34] Varying the pressure of the gas (typically CO_2 or SF_6) varies the index of refraction and hence the Cherenkov threshold (requires $v_e > c/n$, where v_e is the electron velocity, c is the speed of light, and n is the index of refraction of the gas). The electrical PMT signal is sent to a Mach–Zehnder modulator in the electronics enclosure for optical transmission to digitizers without loss of bandwidth.[35] A complete system impulse response has been measured to be ~95 ps—fast enough to measure the expected burn widths of 80 ps to 150 ps from the THD campaign planned for the spring of 2010 at the National Ignition Facility (NIF). Fiber-optic connectors make it possible for timing fiducials and calibration signals to be injected directly into the optical path and provide a dry-run capability for verifiable reliability.

The higher laser energies and neutron yields expected at the NIF dictate larger standoff distances for diagnostics. The advantage of gamma rays over neutrons is that they do not suffer velocity Doppler spreading with increasing distance, so gamma-ray detectors can be placed a significant distance from the imploding capsule without loss of signal bandwidth. Increasing standoff distance, however, also reduces the subtended solid angle and therefore measurement sensitivity, so the instrument must be designed to maximize sensitivity. The GCD-1 routinely operates at 20 cm from target chamber center (TCC) by insertion into a ten-inch manipulator (TIM). This necessitated a compact, coaxial design utilizing Cassegrain optics. By mounting the GRH outside the chamber, we were able to take advantage of off-axis light collection utilizing off-axis parabolic mirrors for increased Cherenkov light collection. The GRH-6m at the NIF will be only two orders of magnitude less sensitive than GCD-1 at 20 cm, even though it will be located 30× farther away from TCC. For the NIF, the GRH-6m will consist of four gas cell channels run in parallel for increased redundancy and reliability plus the ability to run at several gamma-ray threshold energies to diagnose various gamma rays of interest [e.g., $t(d,\gamma)$ at 16.7 MeV, $t(h,\gamma)$

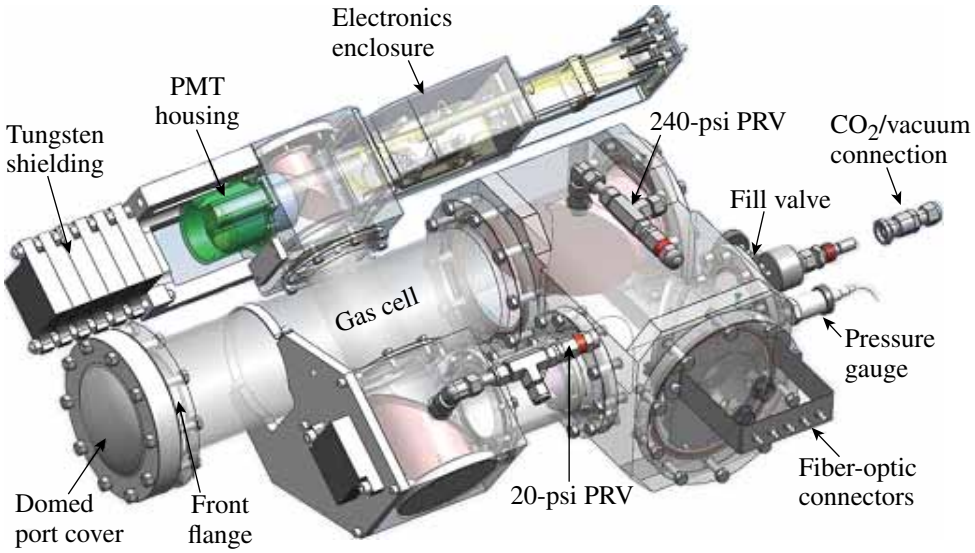

Figure 120.101
First GRH-6m channel, currently installed on OMEGA.

at 19.8 MeV, $^{12}C(n,n')\,\gamma$ at 4.4 MeV]. These detectors will be capable of measuring fusion bang times relative to the t_0 of the composite laser pulse to within 50 ps and burn widths to within 5 ps to 10 ps at yields $>1 \times 10^{13}$ at the NIF. These parameters will be key in diagnosing shell velocity and the various possible failure modes in attempts at ICF ignition on the NIF. The GRH may also prove useful as a means of providing a time-resolved measure of ablator ρR, indicative of ablator mass remaining and ablator/fuel mix.

Figure 120.102 shows a gamma-ray measurement from an imploded DT-filled plastic capsule with the GRH pressure with 100 psia of CO_2 (~6-MeV Cherenkov threshold). Also shown is a background measurement from a previous shot with the CO_2 removed, resulting in no Chernkov production, but still exhibiting direct gamma interaction with the PMT (this background is also present when the PMT input window is blocked with black tape). DT fusion gammas and n–γ from DT fusion neutrons passing through the imploding capsule [primarily $^{12}C(n,n')\,\gamma$ from CH capsules] interact directly with the PMT, causing the "precursor" peak approximately 4.1 ns before bang time. The speed-of-light transit time from TCC through the optical delay of the Cherenkov cell is calculated to be 4.26 ns longer than the direct line-of-sight (LOS) transit time from TCC to the microchannel plate (MCP) in the PMT (i.e., directly through the tungsten shielding). Other experiments have shown that 6 in. of tungsten shielding is adequate to eliminate direct LOS gammas (and x rays), so the precursor from these shots with 9 in. of shielding must be from gammas originating at TCC reaching the MCP on scattering paths delayed approximately 160 ps relative to a direct LOS path, or an extra 4.8 cm. Additional small peaks after the precursor are n–γ generated by interaction of DT neutrons with mass near TCC. Similar peaks have been correlated with various TIM-based diagnostics as they are moved near TCC. These masses must be closer than 22 cm from TCC to generate a signal before or at bang time because of the slower transit time of the neutrons. Although the current background levels are adequate for bang-time and burn-width measurements, the shielding being designed for the NIF will do a much better job of further reducing the background.

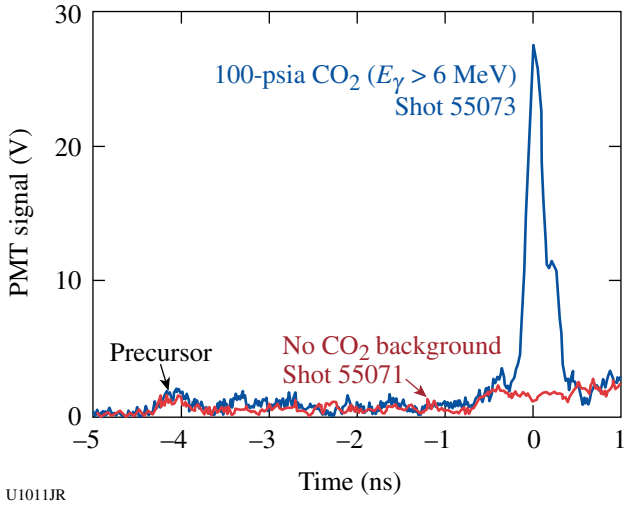

Figure 120.102
GRH data from high-yield shots with (blue) and without (red) pressurized CO_2.

In July the GRH was absolutely timed using x rays generated with 100-ps laser pulses directed onto gold ball targets. The γ-to-e^- converter in the GRH was replaced with a BC-422 x-ray sensitive scintillator for these shots. The x rays/scintillator photons have essentially the same transit time through the system as the γ rays/relativistic electrons/Cherenkov photons. As a result the x-ray pulse can be used to generate a t_0 time stamp on the scope from which the optical fiducial is calibrated. Figure 120.103 shows an x-ray shot and a high-yield shot overlaid by lining up the fiducials. The difference between the rising edge of the x-ray pulse and the peak of the fusion signal is representative of the absolute bang time.

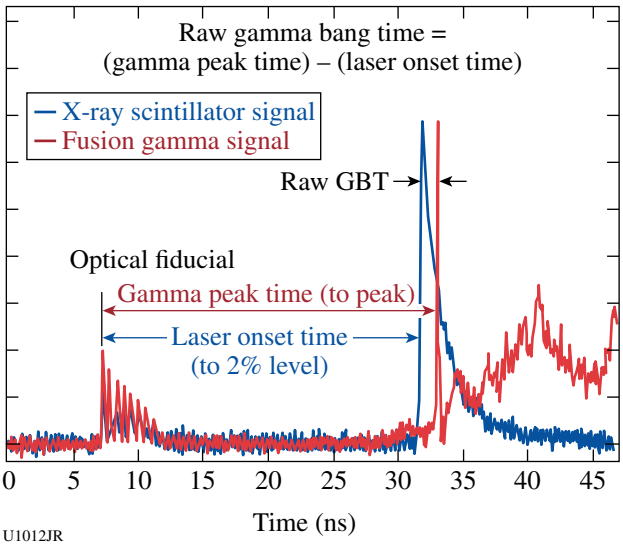

Figure 120.103
X-ray pulse from a gold ball target (blue) used to calibrate an optical timing fiducial overlaid with a Chernkov signal from a high-yield DT shot.

In addition to the GRH development, the Gas Cherenkov Detector also continued to provide valuable insight into gamma-ray physics. In particular, a secondary gamma experiment (a.k.a., "hockey puck" experiment) was carried out using GCD-1. The primary experimental objective was to simulate the neutron-induced secondary gamma (n–γ) production

from a NIF hohlraum, thermomechanical package (TMP), and implosion capsule. During four shot days within FY09 (November, April, May, and July), three group of pucks were placed between TCC and GCD: (1) Au and Cu pucks for the hohlraum, (2) Al and Si pucks for the TMP, and (3) SiO_2, Al_2O_3, and BeO pucks for an implosion glass capsule n–γ study. Three key experimental results were obtained in support of the NIF–GRH (gamma-ray reaction history) diagnostic development program:

1. Proximity n–γ sources were experimentally characterized. The GCD detected time-delayed and Doppler-broadened n–γ signals from all seven pucks. The high-bandwidth GCD can temporally distinguish DT–γ and n–γ signals as long as the proximity source is located at least 2 cm from TCC. The n–γ sensitivity's dependence on seven materials was found and used to validate the MCNP code. Silicon produced the strongest n–γ signal as expected by MCNP simulations.

2. It was experimentally confirmed that the GCD can cut off n–γ signals effectively by adjusting energy threshold, which will allow one to measure clean DT–γ without interference of n–γ at the NIF. At 9-MeV threshold, it is expected that DT–γ will be at least 10× higher than n–γ signals.

3. n–γ signals from the hockey puck experiment were used for MCNP/ACCEPT code validation. Also, puck signals served as an *in-situ* GCD calibration source; as a result they provided one method to determine the $D(T,\gamma)/D(T,n)$ branching ratio. Preliminary calculations carried out using four puck materials indicate $D(T,\gamma)/D(T,n)$ ranges from 1×10^{-5} to 4×10^{-5}.

Defect Implosion Experiment (DIME): The Los Alamos DIME campaign involves perturbed spherical implosions, driven by 60 OMEGA beams with uniform, symmetrical illumination (~24 kJ). DT-filled CH-shell targets with equatorial-plane defects are designed to produce a nonspherical neutron burn region. The objectives of the DIME series are to observe the nonspherical burn with the neutron imaging system (NIS) and to successfully simulate the physics of the neutron production. For the first shot day on OMEGA (shots 54135 to 54145), we demonstrated adequate yield for NIS imaging and monitored yield degradation for the presence of defects. The targets had a diameter of 860 μm. All were filled with 5 atm of DT. We used two separate shell thicknesses: 8 μm and 15 μm, thereby testing both exploding pusher and ablative designs. Perfect targets have no defects. Target defect details are shown in Fig. 120.104. For all shots, the groove depth was 2 μm.

The yield compared to perfect capsules was reduced by ~50% for both thick- and thin-walled targets with defects (see Fig. 120.105), although the exploding pusher capsules (thin walls) performed better for total yield. Both the NIS and a gated, x-ray framing camera diagnosed target emission edge-on—in the plane of the defect. In all cases, the NIS obtained neutron images but was not optimal for resolving the defect. This is encouraging because the perturbation was minimal, and additional degradation for larger defects should be less disruptive of yield. Numerical simulations predicted enhanced x-ray emission, as suggested in Fig. 120.106. During the next campaign, experiments will feature larger, deeper channel defects, and the NIS will be more mature.

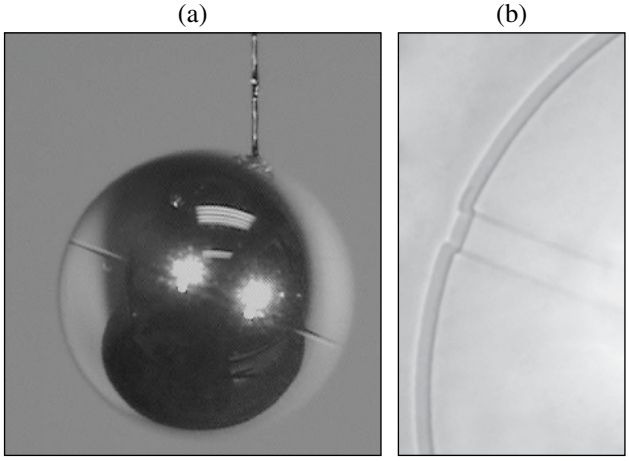

Figure 120.104
(a) LLE photograph of a target with a 20-μm-wide groove defect. (b) A General Atomics radiograph of a 30-μm wide defect with high magnification.

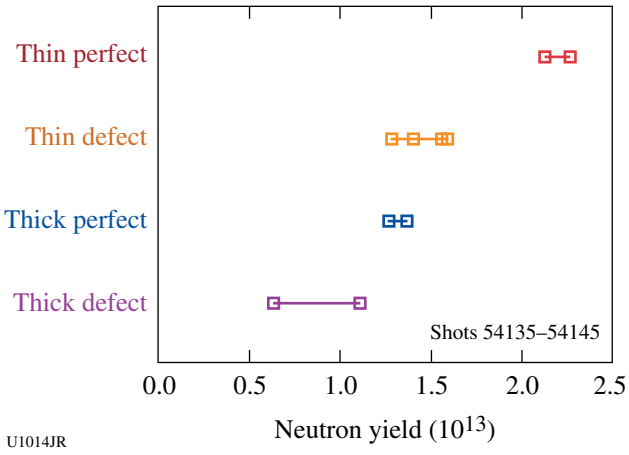

Figure 120.105
Yield for 20-μm-wide, 2-μm-deep groove defects.

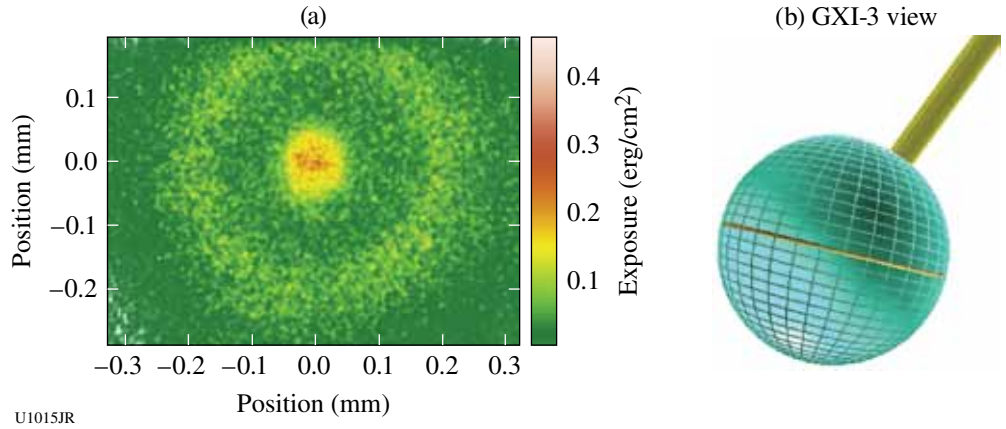

Figure 120.106
(a) A gated, x-ray image (3 to 5 keV) of a defect target implosion suggests enhanced x-ray emission (higher density) in the plane of the defect. (b) The VISRAD view of the GXI-3 x-ray framing camera.

High-Energy Backlighting on OMEGA EP: At the end of January 2009 Los Alamos participated in the first international collaboration on OMEGA EP along with LLE, LLNL, LULI, and NRL. These experiments produced high-quality x-ray images of static gold grids using silver K_α emission produced from 100-ps, 1-kJ laser pulses (Fig. 120.107).

Los Alamos experiments in March 2009 were in collaboration with NRL and were limited to the spectroscopic evaluation of high-energy x-ray backlighters (imaging diagnostics were not available because of requalification). A scan of x-ray yield as a function of pulse duration of silver K_α emission was performed and measured with the NRL diagnostic dual-crystal spectrometer (DCS), which is a high-energy Laue configuration spectrometer. Excellent data were obtained with the spectrometer showing very little change in conversion efficiency with pulse durations ranging from 10 ps to 100 ps.

Neutron Imaging: The Neutron Imaging Campaign made great advances with the NIS to be fielded on the NIF during FY09. Using a staggered approach, different components of the NIF Ia neutron imaging system were tested to ensure that each component functioned properly. The spatial resolution and the DQE of the NIF Ia detector were determined from these experiments. The response and time delay of new paddle detectors were also measured.

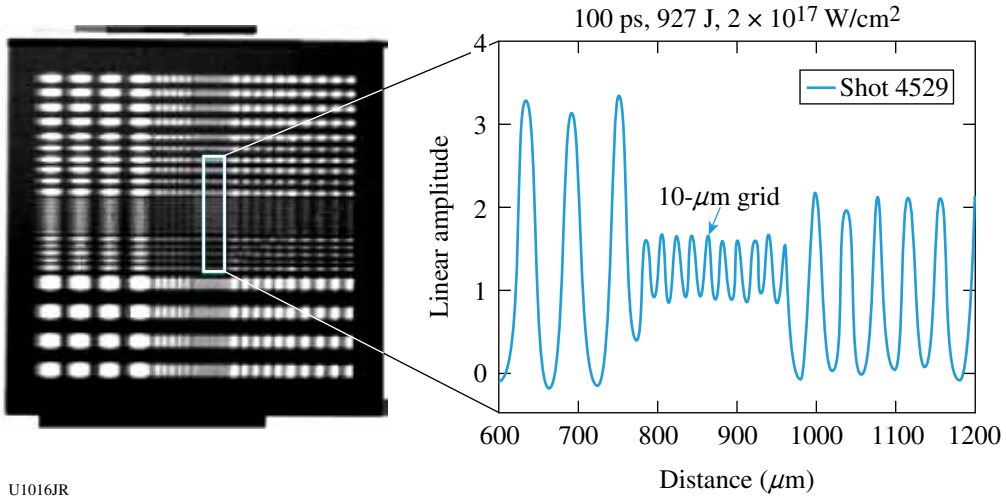

Figure 120.107
(a) A radiographic image of a resolution grid using a silver backlighter. (b) A lineout from the radiograph demonstrating high spatial resolution.

FY09 AWE OMEGA Experimental Programs

AWE-led experiments on OMEGA in FY09 continued to test radiation–hydrodynamic simulations of hohlraum drive and capsule implosion under conditions where a hohlraum target was driven in a deliberately asymmetric manner.

Techniques to achieve uniform, near-spherical symmetry of radiation drive on a capsule in a laser-heated hohlraum have received detailed attention in the context of inertial confinement fusion. Much less attention, however, has been paid to understanding the hohlraum physics and hydrodynamics in cases where the radiation drive departs significantly from spherical symmetry. In work on the OMEGA laser, AWE has carried out a series of experiments to study the implosion dynamics of a capsule irradiated by a deliberately asymmetric x-ray drive. The experimental data provide a sensitive test of radiation transport within the hohlraum enclosure in which drive symmetry was modulated by using variable albedo layers (low-Z coatings on the high-Z hohlraum wall), asymmetric laser-beam timing, and other techniques. In cases where the radiation drive was highly asymmetric, the imploding capsule developed a well-defined polar jet that interacted with the opposite capsule wall. The hydrodynamics of jet formation and interaction were investigated using x-ray backlighting radiography, providing a sensitive test of hydrodynamic modeling in this strongly converging geometry.

A 1.6-mm-diam, 2.7-mm-overall-length hohlraum was used (Fig. 120.108) and driven with up to 30 beams (1.6-ns pulse duration) from the OMEGA laser. Asymmetry was introduced by means of an imbalance of laser energy or timing between the two ends of the hohlraum, or by asymmetry of wall material. In some cases the wall material of one half of the hohlraum cavity was aluminum (low albedo, in comparison with the gold wall material of the other half of the hohlraum); in other cases a thin aluminum coating on the gold hohlraum wall was used to introduce a time-varying albedo (low albedo at early time, followed by increased drive after the laser beams burned through the aluminum layer).

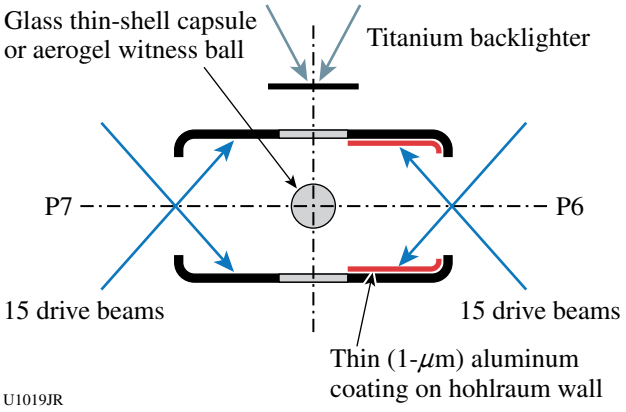

Figure 120.108
Experiment to investigate asymmetric hohlraum drive. The hohlraum was aligned on the P6–P7 axis of the OMEGA target chamber, and asymmetry was introduced by imbalance of laser beam energy and timing from the P6 and P7 directions, and by the use of a low-Z coating on the hohlraum wall.

Both silica aerogel spheres (600-μm diameter, 325-mg cm^{-3} density) and thin-walled glass capsules (600-μm diameter, 3.5-μm wall thickness, 30-μm-thick CH ablator coating) were used as diagnostics of the angular distribution of radiation drive. The position of the ablation front in the aerogel witness spheres[36,37] was used to characterize the angular distribution of the drive, whereas the integral effect of asymmetric drive on the implosion hydrodynamics[38] was observed in the late-time evolution and jet formation of the thin-shell capsules. Both were diagnosed by x-ray backlighting, using a 4.75-keV titanium area backlighter and x-ray framing camera. Hohlraum wall emission was also characterized using the Dante diagnostic, viewing through the laser entry hole of the hohlraum. The experiments were modeled using the AWE Lagrangian radiation–hydrodynamics code NYM, followed by the Eulerian code PETRA to which the simulation was linked after the mesh in the Lagrangian phase of the simulation became sufficiently distorted to limit further progress. The hydrodynamics simulation was post-processed to generate synthetic radiographs for comparison with the experimental data.

The position of the ablation front in the aerogel witness-sphere experiments was characterized by its decomposition into Legendre polynomials. Figure 120.109 shows a comparison between the amplitudes of Legendre moments from both the experimental data and simulation. The simulation was shown to reproduce the experiment rather closely.

The hydrodynamics of the thin-shelled capsules was significantly more sensitive than that of the foam witness balls to the angular distribution of drive. Figure 120.110 compares experimental data with post-processed images for a NYM–PETRA simulation at different times after the onset of the radiation drive. The hydrodynamics is seen to progress somewhat slower in experiment than simulation (as quantified by the equatorial diameter), and although both experiment and simulation show a well-defined polar jet at late time (Fig. 120.111), the density distribution at the hot pole of the capsule was different in the two cases. It seems likely that these differences arose from

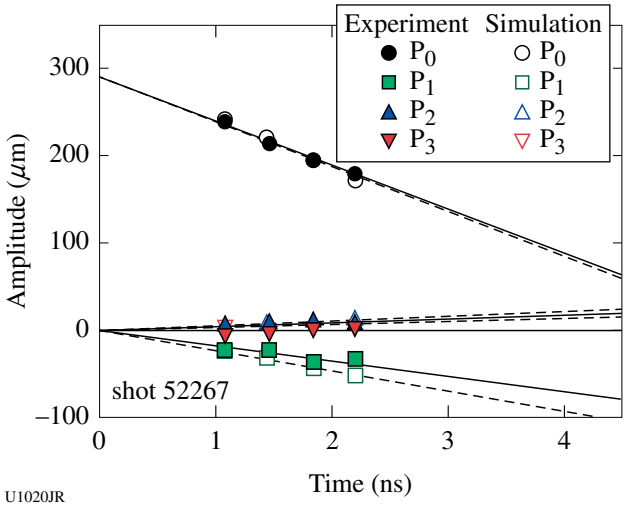

Figure 120.109
Legendre polynomial decomposition of the position of the ablation front in an asymmetrically driven foam witness-ball experiment. The amplitudes of the first four Legendre polynomials (P_0, P_1, P_2, P_3) are shown for both experiment (filled symbols) and simulation (open symbols).

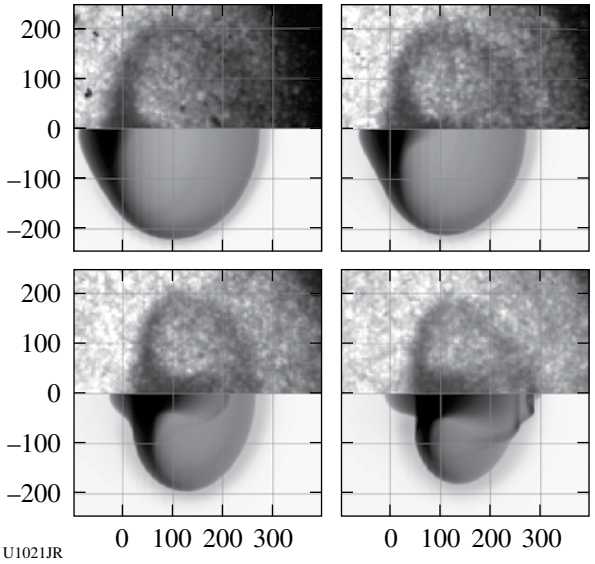

Figure 120.110
Sequence of frames showing experimental data (top) and simulation (bottom) of the implosion of an asymmetrically driven, thin-shell glass capsule. The sequence of times is 2.8, 3.2, 3.6, and 4.0 ns in the experimental data and 2.6, 2.8, 3.0, and 3.4 ns in the simulation. In the simulation, times were chosen to match approximately the experimentally observed equatorial diameter of the capsule. The formation and propagation of the polar jet were reproduced in the simulation, although there are some differences of density distribution at the pole of the capsule. (Units shown are microns.)

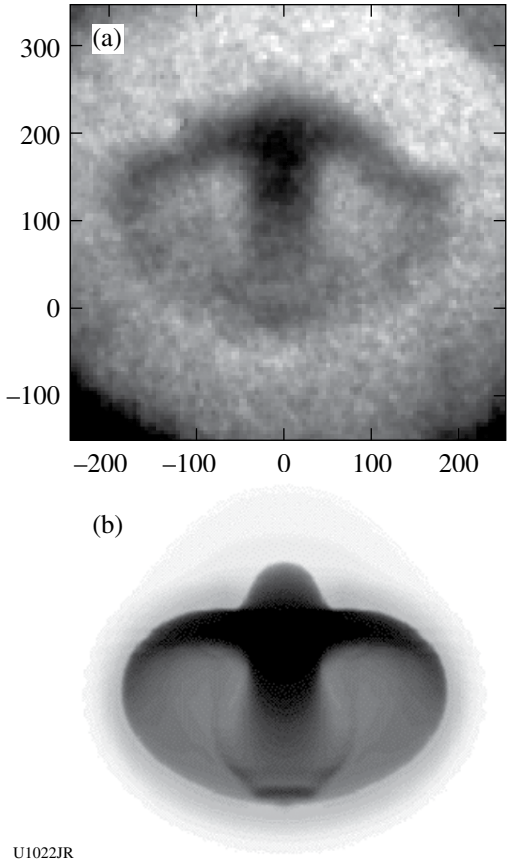

Figure 120.111
The bow shock produced on interaction of the polar jet with the opposite wall of the capsule is clearly seen in (a) experiment (top) and evident also in (b) simulation (bottom).

subtle differences in the laser hot-spot position, or the albedo of the indirectly heated hohlraum wall, and resolving these differences will form the focus for further work during FY10.

FY09 CEA OMEGA Experimental Programs

CEA conducted 56 shots on the Omega Laser Facility in FY09. The CEA efforts included the following:

CEA Copper Activation Diagnostic for Primary DT Neutron-Yield Measurement: The neutron yield is one of the most important parameters used to characterize the performance of inertial confinement fusion experiments. For the Laser Megajoule (LMJ) and National Ignition Facility (NIF), neutron-yield measurements will be performed by an array of neutron time-of-flight (nTOF) detectors composed of scintillation counters and chemical vapor deposition (CVD) diamond detectors. An accuracy of 4% is required to measure neutron yield. All these detectors are calibrated against the nuclear activation diagnostic, which is a valuable measurement technique because of its reaction threshold and its absolute calibration. The copper activation method is used for the 14.1-MeV primary DT neutron-yield measurement. This diagnostic has been used as a reference on many laser facilities (PHEBUS, NOVA, OMEGA) and will now be used on future megajoule-scale lasers. Copper activation will be the first nuclear diagnostic installed on LMJ.

The copper disk to be used for this diagnostic is pure copper (99.99%) and is composed of 69.2% of ^{63}Cu and 30.8% of ^{65}Cu. The ^{63}Cu(n,2n)^{62}Cu reaction has a Q value of 11 MeV. ^{62}Cu decays with a half-life of 9.73 min and emits a positron, resulting in the production of two back-to-back 511-keV gamma rays on annihilation. On the other hand, the ^{65}Cu(n,2n)^{64}Cu reaction produces ^{64}Cu that decays with a half-life of 12.7 h and emits a positron. The CEA activation acquisition system consists of two 7.62-mm-diam, 7.62-mm-thick NaI(Tl) scintillation detectors. Associated electronics allow us to detect 511-keV gammas in coincidence between two detectors. In 2002 the activation diagnostic was calibrated on a Van De Graaff accelerator at CEA Bruyères le Châtel with an accuracy of 4.5%. The main error contribution comes from the reference detector, which measures the neutron yield delivered by the accelerator. The optimum sensitivity is obtained by using a 10-mm-thick copper disk because it is the best compromise between copper activation and 511-keV gamma detection. We use a 7.62-mm-diam copper disk that is similar in dimension to the NaI(Tl) detectors.

To compare CEA and LLE primary DT neutron calibration, a CEA copper activation diagnostic was implemented on OMEGA during direct-drive implosions of DT capsules yielding 10^{13} primary DT neutrons. The tertiary activation diagnostic (TAD) inserter was used to place copper disks at 40 cm and 100 cm from target chamber center (TCC). Immediately after the shot, the TAD inserter was retracted and the activated copper disk was extracted from the target chamber. The disk was then dropped into a plastic container by the Target Bay operators and carried to the acquisition systems to be measured. Data acquisition began about 10 min after the shot, and measurements were made every minute for at least 2 h to properly describe the ^{62}Cu and ^{64}Cu decays (see Fig. 120.112). This acquisition technique allows us to remove the ^{64}Cu decay contribution to evaluate the neutron yield with the ^{62}Cu decay only. Since OMEGA shots are at about 1-h intervals, we used two acquisition systems.

A 10-mm-thick, 7.62-mm-diam copper disk was used during the three first shots performed in February 2009 to test our operating procedure (shots 53590 to 53592). We decided to use this sample geometry because its calibration is well known with an accuracy of 4.5%. However, the high copper activation level produced by a 10^{13} neutron yield results in an acquisition system saturation with a dead time of 40% about 30 min after the shots. Therefore, neutron yield was determined using data below a coincidence count rate of 300 c/s. Counting-station saturation is a crucial problem because it prevents us from determining the primary DT neutron yield from ^{62}Cu decay when the ^{64}Cu contribution is minimum, even if it was previously calibrated. To reduce acquisition system saturation in the later shots taken in May, we used 3-mm-thick copper disks placed at 1 m from TCC.

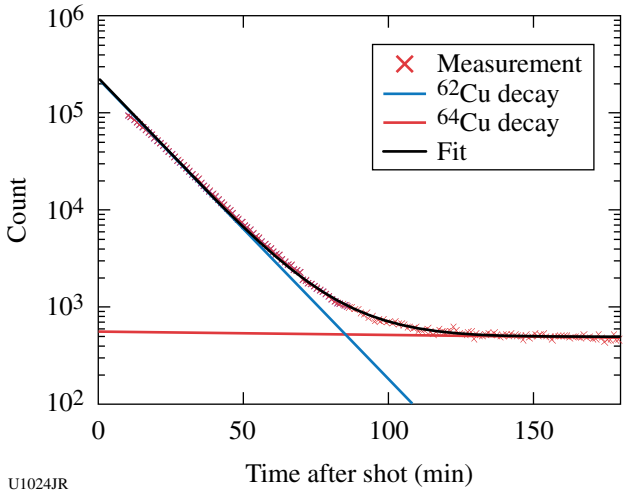

Figure 120.112
^{62}Cu and ^{64}Cu decays measured at 1 m from TCC with a 3-mm-thick disk during shot 54460 yielding 2×10^{13} neutrons.

The primary DT neutron yield was compared to the LLE time-of-flight scintillation counter located at 12 m from the target (12mnTOFh). The CEA copper activation diagnostic was used on 19 DT shots. The neutron yields in these experiments ranged from 8.9×10^{12} to 3×10^{13}. The neutron-yield measurement accuracy was 4.6%. Except for one shot (54471), nTOF measurements were consistent with the CEA copper activation. If we compare shot-to-shot CEA copper activation and LLE nTOF measurements, the dispersion is about 3.6% (rms) and the average difference between primary DT neutron-yield calibrations is only 1.8% (see Fig. 120.113).

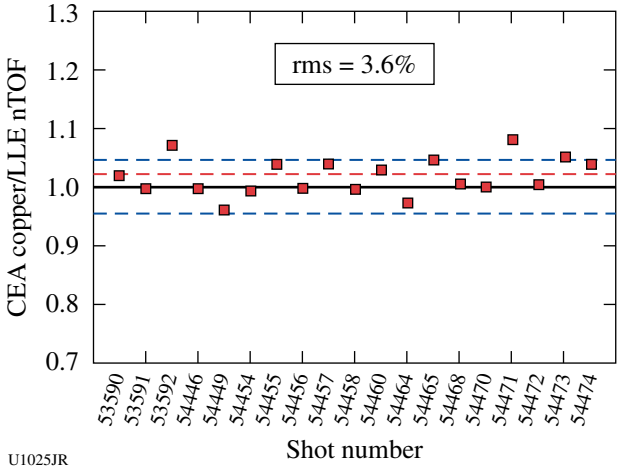

Figure 120.113
Shot-to-shot comparison between CEA copper activation and nTOF neutron-yield measurement. The two independently calibrated neutron-yield diagnostics show a dispersion of 3.6% (dashed blue line) with an average difference of 1.8% (dashed red line).

The 2009 copper-activation measurement campaign confirmed that the CEA and LLE independent neutron-yield calibrations are very close.

It is worth noting that, compared to a 10-mm-thick geometry, the sensitivity of the 3-mm-thick sample was determined with only one calibration measurement at 14.1 MeV. The best way to reduce statistical effects is to perform several measurements with exactly the same sample geometry at the same energy. For this reason, two calibration weeks have been scheduled between 16 and 27 November 2009 on the 4-MV Van de Graaff accelerator at CEA (Bruyères le Châtel). All data acquired on OMEGA will be processed again with this new calibration to determine final results.

MeV Photon X-Ray Sources Produced on OMEGA EP: High-power laser–plasma experiments have been used for several years to study the generation of energetic particles. With chirped-pulse–amplification laser systems, the interaction of a high-intensity laser pulse ($I\lambda^2 > 10^{19}$ W/cm^2 μm^2) with a gas-jet or thin-foil target leads to the generation of relativistic, multi-MeV electrons, accelerated from many physical processes, such as the Brunel effect, ponderomotive or $j \times B$ acceleration, and Wakefield acceleration. If they propagate in a high-Z solid target located behind the interaction area, these relativistic electrons will generate copious high-energy Bremsstrahlung emission. These x-ray photons can be an interesting bright high-energy (>1 MeV) source for radiography, nuclear activation, radiation effects, and radiation safety studies.

Two experiments were carried out using the "backlighter" of the OMEGA EP laser. For the first experiment performed in a high-power regime (CEA/LLE collaboration), the short pulse delivered up to 300 J in τ = 0.6 ps at a wavelength of λ = 1.053 μm. The short pulse was focused at the center of the vacuum chamber, at 45° of the normal to the target. Peak laser intensity was estimated to be $\sim 4 \times 10^{19}$ W/cm^2. Two types of targets were irradiated: 20-μm-thick (500×500 μm^2) and 100-μm-thick (200×200 μm^2) square gold foils.

For the second experiment performed in a high-energy regime (CEA/AWE collaboration), the short pulse delivered up to 1 kJ in τ = 10 ps and was focused at the center of the vacuum chamber, at 18° off the normal to the target. The peak laser intensity was estimated to be $\sim 8 \times 10^{18}$ W/cm^2 and the target was a 2-mm-thick, 2-mm-diam Ta cylinder coated with 10-μm-thick plastic. For some of the shots, a nanosecond heating beam (1 kJ, 1 ns, ϕ = 800 μm) was used to produce a preformed plastic plasma that was intended to increase the short-pulse energy absorption. Since no phase plate was available for the heating beam, a large focal spot was obtained by defocusing the beam.

In these experiments, the ratio $d/(c\tau/2)$, where c is the speed of light in vacuum and roughly corresponds to the speed of the fastest electrons and d is the target thickness, is close to 1 for thin targets (<1 for a 20-μm target and >1 for a 100-μm target) and is well above 1 for a 1-mm-thick target. Electron recirculation in the target is therefore expected to result in greater bremsstrahlung emission and a larger source size in thinner targets.

The high-energy part (>10 MeV) of the x-ray spectrum was studied from ^{63}Cu(γ,n)^{62}Cu and ^{12}C(γ,n)^{11}C photonuclear reaction measurements. Assuming a Maxwellian distribution for the spectrum $S(E) \sim K_h \exp(-E/T_h)$, where K_h is the amplitude

of the spectrum, T_h can be deduced from an activity ratio measurement. The x-ray dose is inferred using x-ray dosimeters and from the radiography of a tower of Hanoi-shaped structure composed of W (tungsten). The x-ray source size is estimated using a penumbral imaging diagnostic (cylindrical 80-mm-thick W pinhole) and also from the radiography of an image quality indicator (IQI). This IQI is made of two 20-mm-diam W hemispheres with internal sinusoidal modulations. The signal is recorded using image plates combined with Ta reinforcement screens that increase the plate sensitivity for high-energy photons.

Figures 120.114(a) and 120.114(b) show spatial profiles of penumbral images obtained during the high-power-regime experiment with 20-μm-thick and 100-μm-thick gold targets, respectively. These profiles can be estimated with an edge response function associated to an x-ray source with either a Bennett or a Gaussian radial profile. The Bennett fit gives a source size of FWHM = 160 μm (resolution ~40 μm) for the 20-μm-thick foil and FWHM = 90 μm (resolution ~30 μm) for the 100-μm-thick foil. Surprisingly, a larger x-ray source size was obtained with the thinnest foil. This may be explained by the electron recirculation in targets of different sizes. Activation measurements show a quite high temperature T_h ~ 10±4 MeV for 100-μm-thick foils and a significantly lower temperature T_h ~ 5±1 MeV for 20-μm-thick foils. The effects of electron circulation on bremsstrahlung emission and x-ray source dimensions will be studied using the PIC numerical code Calder coupled to the Monte Carlo code MCNP.

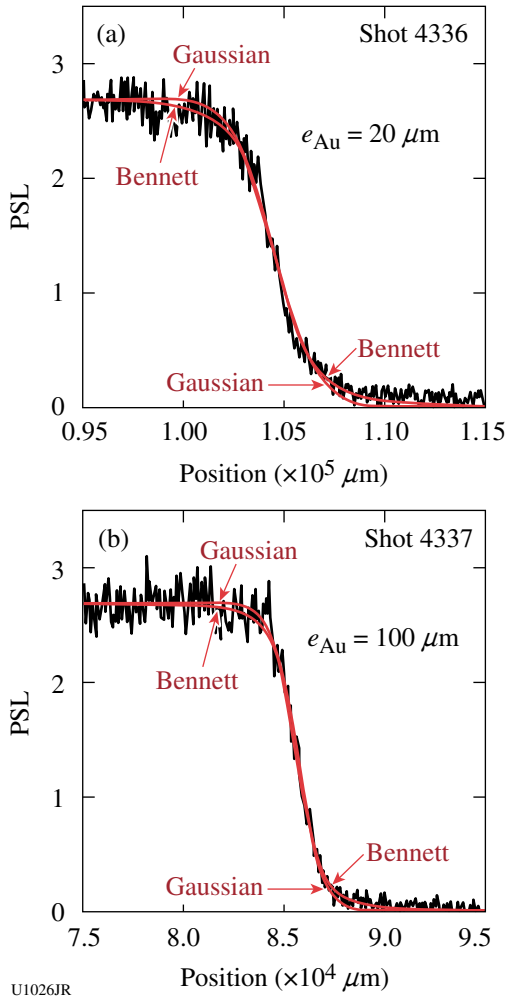

Figure 120.114
Spatial profiles of penumbral images obtained from laser shots on (a) 20-μm-thick and (b) 100-μm-thick gold foils.

Results from the second experiment using a thick Ta target (2 mm) in a high-energy laser regime show a relatively large x-ray source, FWHM = 400 μm (resolution ~130 μm), when the heating beam was combined with the short pulse [Fig. 120.115(a)]. Analysis of the radiographic image of the IQI [Fig. 120.115(b)] indicates that a smaller x-ray source (below 200 μm) was obtained when only the short pulse was focused on target, which is in agreement with past results obtained on other laser facilities. The results also show that the x-ray dose produced with only the short pulse was almost one order of magnitude larger than when the heating beam was combined. Since this long pulse had to be defocused here to produce large preformed plasma, the short pulse probably encountered inhomogeneous plasma with transverse density gradients that can lead to laser refraction. Phase plates should be available in FY2010 for long pulse and will be used for the next experiment.

CEA γ-Background Measurements after High-Neutron-Yield Shots on OMEGA: Knowledge of γ doses produced after high-neutron-yield shots is very important for the nuclear safety of megajoule-class laser facilities (NIF and LMJ). Indeed, neutrons produced during fusion reactions can activate the structural materials in the experimental hall, and γ background levels should be monitored after high-neutron-yield shots (DT implosions). Experiments dedicated to these measurements on OMEGA were initiated in 2005 and were continued in 2008 and 2009. These results will allow us to validate Monte Carlo activation calculations and therefore better predict γ background levels after high-gain shots on LMJ.

<u>γ-Dose-Rate Measurements with a FH40 Dosimeter.</u> During the two first campaigns (2005 and 2008), a FH40 dosimeter (based on a plastic scintillator) was used to perform the measurements [see Fig. 120.116(a)]. This dosimeter can measure the γ-dose rate per second (in μSv/h) in the range of 40 keV to

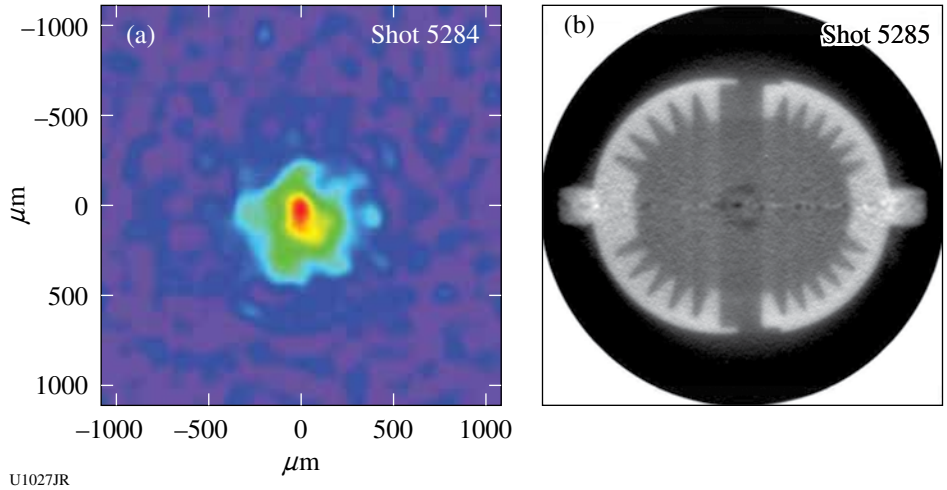

Figure 120.115
Reconstructed image of (a) the x-ray source and (b) radiography of the IQI after tomography obtained during the high-energy laser regime experiment.

1.3 MeV. The dynamic range covers 10 nSv/h up to 100 mSv/h with a 5% uncertainty.

In May 2008, we performed γ-dose-rate measurements at three positions [see Fig. 120.116(b)]:

- at ~8 m from TCC in the Target Bay [near the CEA-neutron imaging system's (NIS) alignment station]
- at ~3 m from TCC in the Target Bay (in the P9 port), and
- in La Cave, just below the target chamber, under the 70-cm concrete slab

Figure 120.117 shows the γ-dose rate measured by the FH40 dosimeter in La Cave before the high-neutron-yield shot campaign. The mean residual background was 0.07±0.02 μSv/h.

Similar results were obtained in the Target Bay. During this high-yield shot campaign (21–22 May 2009), 23 shots were recorded (ten at the NIS position, eight in the P9 port, and five in La Cave), for neutron yields ranging from 2.46×10^{12} to 4.3×10^{13}. A typical signal obtained with the FH40 dosimeter is shown in Fig. 120.118, for the "NIS" position (at ~8 m from TCC).

Similar temporal behavior was observed in all three positions. At least three materials with a high half-life (>1 min) were activated (red lines on the curve of Fig. 120.118). These results have to be compared with calculations and predictions of Monte Carlo simulations.

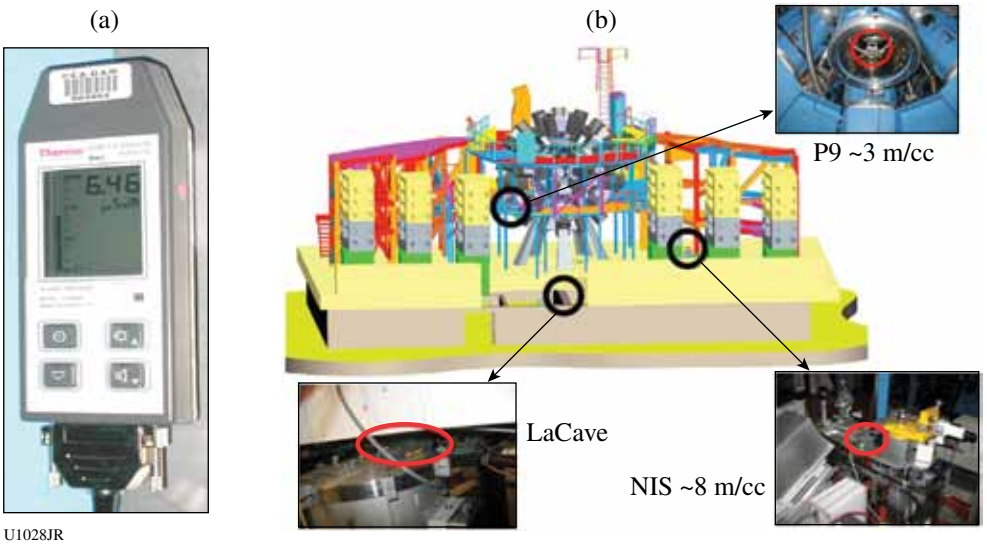

Figure 120.116
(a) The FH40 dosimeter; (b) the three positions for the FH40 dosimeter.

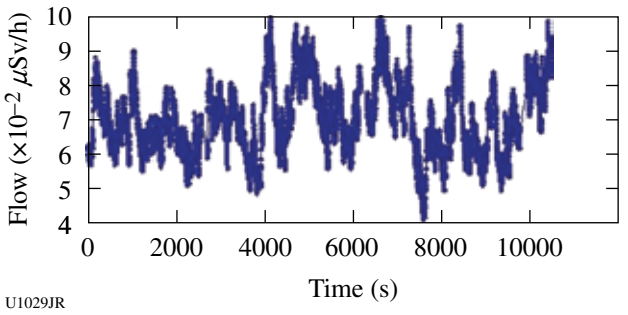

Figure 120.117
Residual γ-dose rate recorded in La Cave before a high-neutron-yield shot with the FH40 dosimeter.

Figure 120.119
Germanium detector with its electronic cryogenic module.

γ Spectroscopy with a Germanium Detector. To obtain more-detailed results on this γ background after high-neutron-yield shots, γ spectroscopy was performed with a germanium detector in May 2009. This detector was an N-type germanium coaxial diode with 85% relative efficiency (see Fig. 120.119). The dimensions of the germanium crystal were 79 mm in diameter and 62 mm in length. The resolution was 2 keV for a 1-MeV γ, and the detectable energy range was 100 keV to 3 MeV. To avoid the use of liquid nitrogen, the crystal was cooled with an electronic cryogenic module.

Monte Carlo activation calculations were performed at CEA for a 5×10^{13} neutron yield on the OMEGA facility. Table 120.XIII shows expected γ rates, 4 m from TCC.

As in the 2008 campaign, the detector was located in three different positions:

- at ~8 m from TCC in the Target Bay (near the CEA-NIS alignment station)
- at ~4 m from TCC in the Target Bay (near the chamber)
- in La Cave, protected by the 70-cm concrete slab

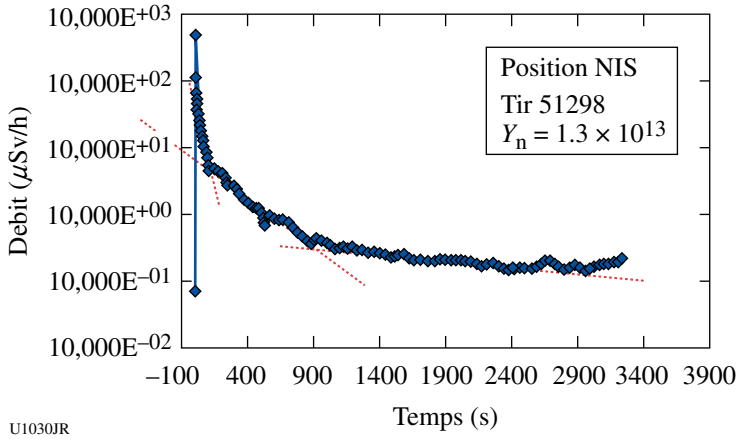

Figure 120.118
γ-dose rates recorded on OMEGA for shot 51298 ("NIS" position) with the FH40 dosimeter.

Table 120.XIII: Gamma-ray rates predicted using a Monte Carlo activation calculation for a 5×10^{13}-neutron-yield OMEGA shot at 4 m from TCC.

Time after shot	Rate (γ/cm^2)	Main radionuclide	Reaction channel	$T_{1/2}$
10 s	5.2×10^2	^{27}Mg	^{27}Al(n,p)^{27}Mg	9.46 min
100 s	2.3×10^2	^{24}Na	^{27}Al(n,α)^{24}Na	14.66 h
1000 s	4.7×10^1	^{24}Na	^{27}Al(n,α)^{24}Na	14.66 h

To protect the electronic device, the detector was inactive during the shot. The high voltage was turned on 2 to 3 min after the shot. To observe the decay time of γ rays, γ spectra were recorded each minute. Figure 120.120 presents a background γ spectrum recorded before the high-neutron-yield shots campaign during a 10-h period. For example, one can clearly see the 1460.8-keV γ ray coming from the ^{40}K nucleus. Other radioactive nuclei present in the environment (concrete, etc.), derived from uranium or thorium, may be identified in the spectrum.

For this campaign (13–14 May 2009), 15 shots were recorded (nine shots in NIS position, four near the aluminum chamber, and two in La Cave). The γ spectrum of Fig. 120.121 was obtained for shot 54446 ($Y_n = 2.58 \times 10^{13}$). The germanium detector was located in the NIS position, at ~8 m from TCC. The spectrum shows all γ rays recorded by the germanium detector during the 64-min period after the shot.

Some reaction channels are clearly identified:

- ^{27}Al (n,p) ^{27}Mg
- ^{27}Al (n,α) ^{24}Na

We also identified neutron activation of iron present in the OMEGA Target Bay structure and also neutron capture on ^{27}Al (because of slow neutrons diffused by the environment).

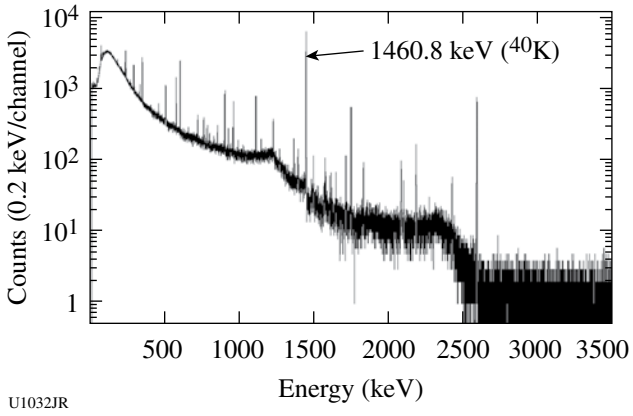

Figure 120.120
γ-background spectrum recorded by the germanium detector during a 10-h period before high-yield shots.

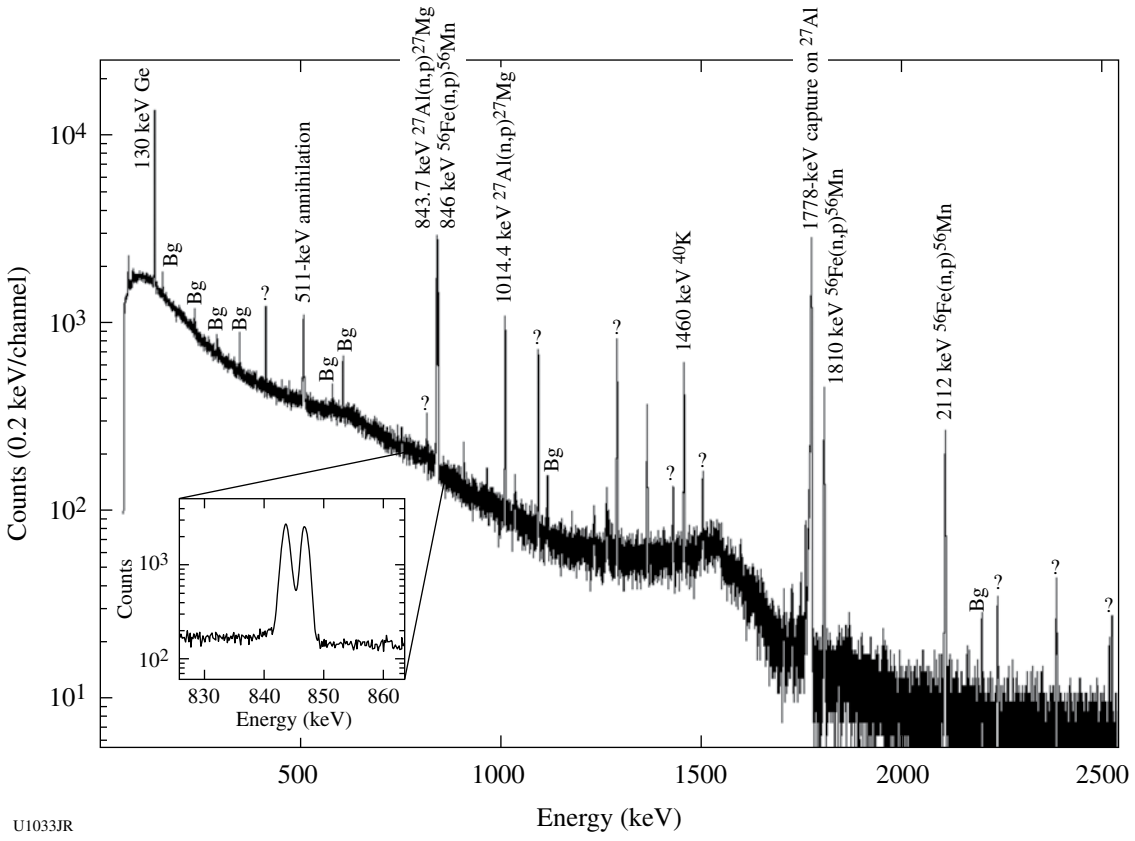

Figure 120.121
γ spectrum recorded by the germanium detector during a 64-min period after shot 54446 (see text for details).

Some γ rays present in the background spectrum were found and labeled "Bg." They were caused only by natural radioactivity and not related to the DT shot. Unknown γ rays were present in the spectrum and have to be identified. Data analysis is still in progress in France. The zoom in Fig. 120.121 shows that we can separate closely spaced γ rays thanks to the high resolution of the germanium detector.

As for the γ-dose-rate measurements, these results will be useful in constraining our simulations. Indeed, not all materials of the environment are well known (exact concrete composition, for example), and data from γ spectroscopy will give us some idea of the main radionuclei responsible of γ background after high-neutron-yield shots.

Two New Neutron-Imaging Systems on OMEGA: Neutron imaging system experiments by CEA have been conducted on OMEGA for many years. For the LMJ nuclear diagnostics development, we have tested several imaging techniques based on the use of thick penumbral apertures. It was shown[39] that design and alignment are essential for measurement quality. We also experimented with several detector designs and configurations using segmented scintillators,[40] or capillary arrays filled with a high-refractive-index liquid scintillator.[41,42] The latter was found to be very efficient and gave a high spatial resolution.

We designed and assembled a large (150-mm entrance diameter) neutron imaging system (LNIS) based on the capillary-filled technique. A large capillary array had to be composed by assembling four arrays of 5-cm length. A large optical-fiber taper reducer (150/75 mm) collected light generated in the scintillator sealed in the capillaries to a fast and large light amplifier (75-mm diameter). This amplifier allows for time gating down to 12 ns with accurate timing precision and therefore makes it possible to select light generated by 14-MeV neutrons interacting with the scintillator material. A second optical fiber taper (75/50 mm) matched the amplifier diameter to a cooled charge-coupled device (CCD) 2084 $\times$ 2084 pixels of 24 μm^2 (see Fig. 120.122). Two rotations were added to the system to allow for detector autocollimation on the neutron line-of-sight (LOS) path.

Our aim was to test this detector on OMEGA during National Ignition Campaign (NIC) shots. Following the OMEGA qualification procedure (starting in February 2008 with a Preliminary Design Review), we were able to implement this camera using a 13-m LOS on the May 2009 NIC campaign. This detector was placed in the La Cave area. Using this LOS, we obtained a good shielding from scattered neutrons and γ rays generated in the Target Bay; also, by using our usual penumbral aperture[43] at this distance, we were able to obtain a larger magnification ratio and, therefore, a smaller resolution (down to 15 μm) with this capillary technique detector. Alignment was performed by using our laser technique (for details see Ref. 44) with the alignment station placed on the Target Bay floor at 8 m.

The detector was characterized on an accelerator-generated 14-MeV neutron source and on a Co^{60} gamma-ray source. The images obtained are shown in Fig. 120.123. We note that the capillary assembly is clearly visible. We also distinguish four black spots that correspond to capillaries destroyed during manufacturing. The top-left part of the image is more intense than the rest of the image by a factor of 2 due to light amplifier

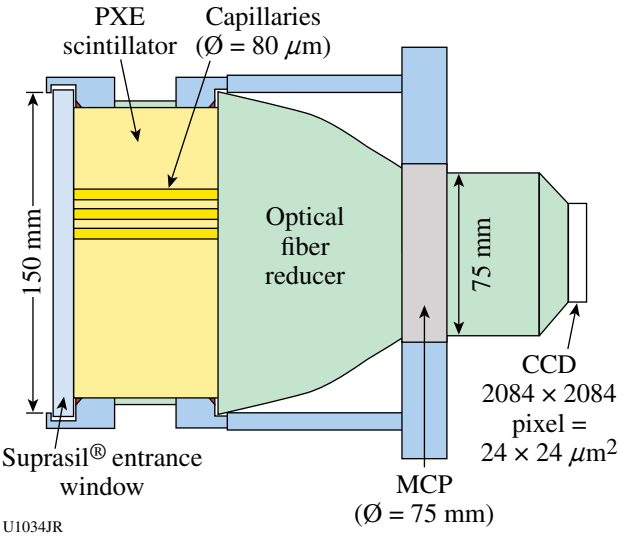

Figure 120.122
LNIS neutron detector scheme.

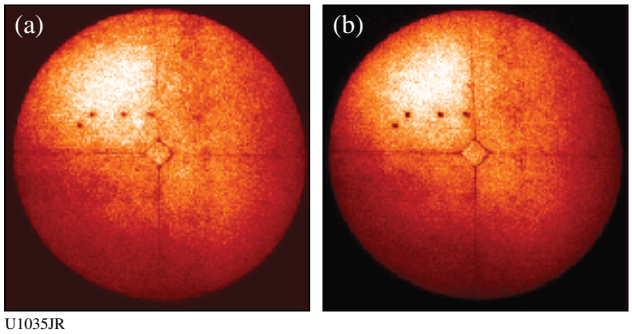

Figure 120.123
(a) Neutron flat-field image yield 8.5 $\times$ 10^3 n/cm^{-2}; (b) Co^{60} γ-rays flat-field image.

inhomogeneity. There is a good agreement between these images, showing that detector response is similar in neutron and γ rays. At low neutron yield (see Fig. 120.124), we were able to register individual proton recoil tracks with a range of about 625 μm, consistent with detector resolution for 14-MeV neutrons.[43]

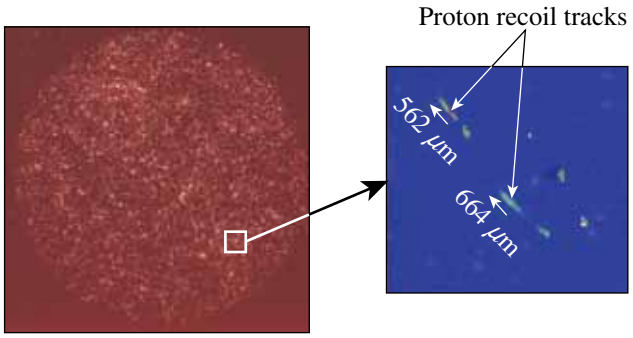

Figure 120.124
14-MeV neutrons image obtained on an accelerator (yield = 53 n/cm^2).

We were able to register ten penumbral images and three flat-field images on the CCD during the two days of target shots. Some shots were dedicated to amplifier time-gating adjustment on DT neutron time of flight. A sample raw penumbral image obtained for shot 54466 at 1.15×10^{13} neutrons is shown in Fig. 120.125(a). In Fig. 120.125(b), one can see that the black spots do not alter image quality since they are not in a region that contains image information. The spots are not visible after flat-fielding the image. The image was then unfolded using our autocorrelation method[45] [see Fig. 120.126(a)]. In that case, the unfolded image was not corrected from optical transport image distortions. In Fig. 120.126(b) we plotted the vertical and horizontal lineout showing that the source diameter was about 50-μm FWHM. Figure 120.127(a) shows an image resulting from the superposition of a 2- to 10-keV x-ray image with a neutron image contour obtained for shot 54466. Figure 120.127(b) is also a superposition of an x-ray image from 7 keV to 9 keV with the same neutron image contour. We see that both images are consistent in shape and size.

A small neutron imaging system (SNIS) was also developed this past year. This system is based on a detector that was specifically designed for low-neutron-yield shots (10^9 to 10^{10} neutrons/4π). This detector was implemented at the rear port of the TIM-6 at 4 m from TCC. As for the previous one, this detector is based on a scintillator-filled capillary array. High sensitivity is obtained primarily by the fact that this camera does not contain any optical-fiber reducer between the capillaries and the light amplifier (see Fig. 120.128). The entrance diameter is 40 mm. This detector was also characterized on an a Co^{60} γ-ray source and measurements showed that efficiency is 4× lower than for the traditional NIS. At this distance, the

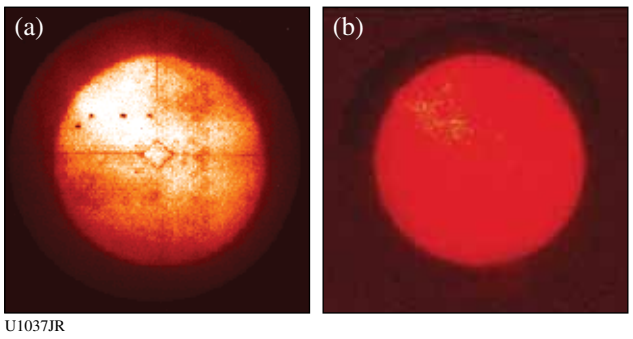

Figure 120.125
(a) Raw image of a DT implosion (shot 54466) yielding 1.15×10^{13} neutrons; (b) flat-fielded image.

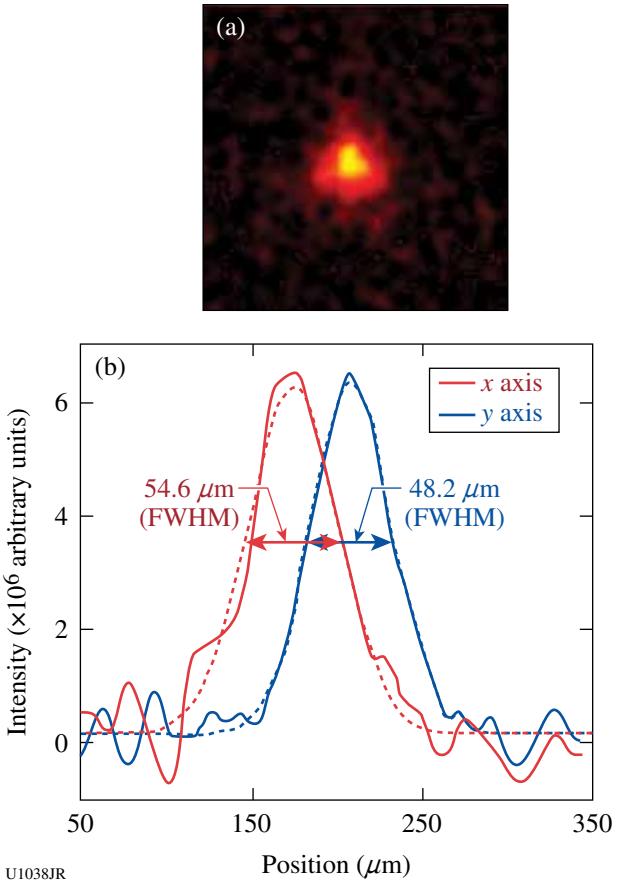

Figure 120.126
(a) Unfolded image using autocorrelation method[42] (SNR = 16); (b) vertical and horizontal lineouts.

magnification ratio is smaller; therefore achievable resolution is larger (43 μm). At 4 m from TCC, the neutron fluence is 4× higher than at 8 m. The aperture type and alignment technique are the same as used for the larger NIS.

This detector was activated on 16 June shots for indirect-drive, deuterium-filled targets. We were able to register an image on shot 54747 with a neutron yield of 1.37×10^{10} neutrons/4π [Fig. 120.129(a)]. In this image, one can see that the statistics are quite low compared to the LNIS image. To reach a reasonable signal-to-noise ratio (SNR) with the autocorrelation technique, the resolution had to be degraded to 54 μm in the unfolded image [Fig. 120.129(b)]. This last image reveals a noncircular shape. This observation is contrary to the circular source (caused by the implosion symmetry) that would be expected along the hohlraum axis. This result could be due to source misalignment in the aperture field of view, or aperture misalignment itself, or

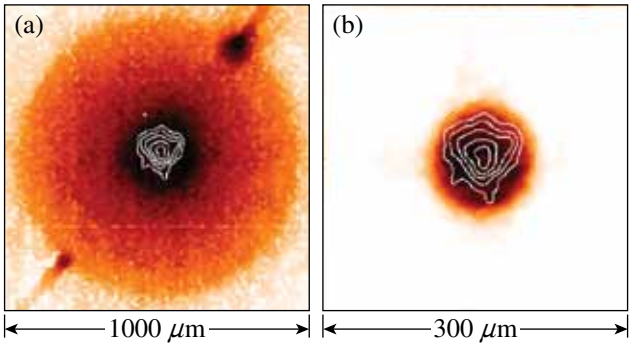

Figure 120.127
(a) Neutron (contours) and x-ray (2- to 10-keV) image superposition; (b) neutron (contours) and x-ray (7- to 9-keV) image superposition.

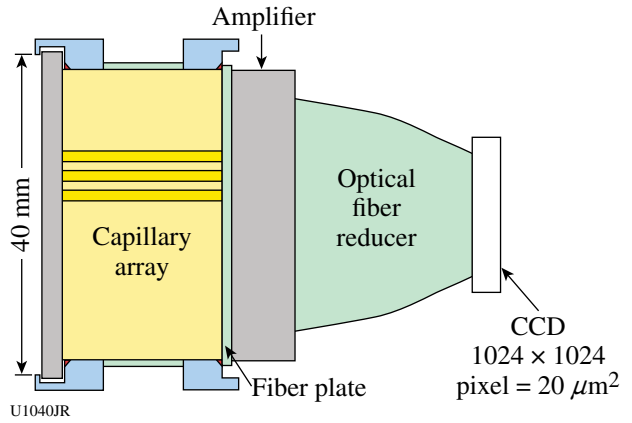

Figure 120.128
SNIS neutron detector scheme.

due to optical coupling between the light amplifier and the fiber plate, which was found imperfect after detector tests. Nevertheless, this camera had demonstrated its particular high sensitivity to low-neutron-yield shots.

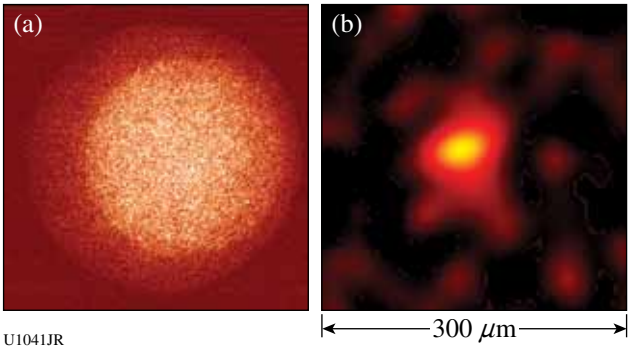

Figure 120.129
(a) Raw image of DD implosion (shot 54747) yielding 1.37×10^{10} neutrons; (b) unfolded image (SNR = 10, resolution = 54 μm).

Neutron-imaging measurements were obtained for the first time with 15-μm resolution on OMEGA during the May 2009 NIC campaign. We successfully tested the first part of the LMJ-NIS detector design. This detector resolution may now help us to discriminate the anisotropy in the neutron source linked to the driver energy balance, but this will require specific dedicated experiments.

The first neutron image on an indirect-drive shot was registered with 54-μm resolution. This last image was a milestone for CEA-NIS, which is now able to register images with resolution from 43 μm to 15 μm and detection threshold from a few 10^9 until the maximum accessible yields on OMEGA.

Next year's experiments will be dedicated to indirect-drive shots and, more particularly, to improving optical coupling between a fiber plate and a light amplifier. This will probably improve light collection and detector sensitivity. Concerning LNIS, a new light amplifier and a new one-block capillary array will be implemented.

Ablative Rayleigh–Taylor Stabilization Mechanisms Experiment: Ablative Rayleigh–Taylor growth measurements in laminated samples were obtained on OMEGA on 17 June 2009. The experimental platform consisted of a gas-filled, 1.2-mm-diam halfraum along with side-on and face-on radiography x-ray sources (Fig. 120.130).

Rayleigh–Taylor growth measurements were obtained using face-on radiography and are in good agreement with 2-D hydrodynamic simulations based on published theoretical and numerical predictions.[46] Different behavior was found for homogeneous and laminated samples (Fig. 120.131), the latter showing a strong reduction of the initial perturbation mode.

Side-on radiography shows the absence of Rayleigh–Taylor spikes in the case of laminated samples (Fig. 120.132), while the acceleration was found to be identical for both kinds of samples.

These first experimental measurements strongly motivate new designs using laminated structures for ignition capsules.

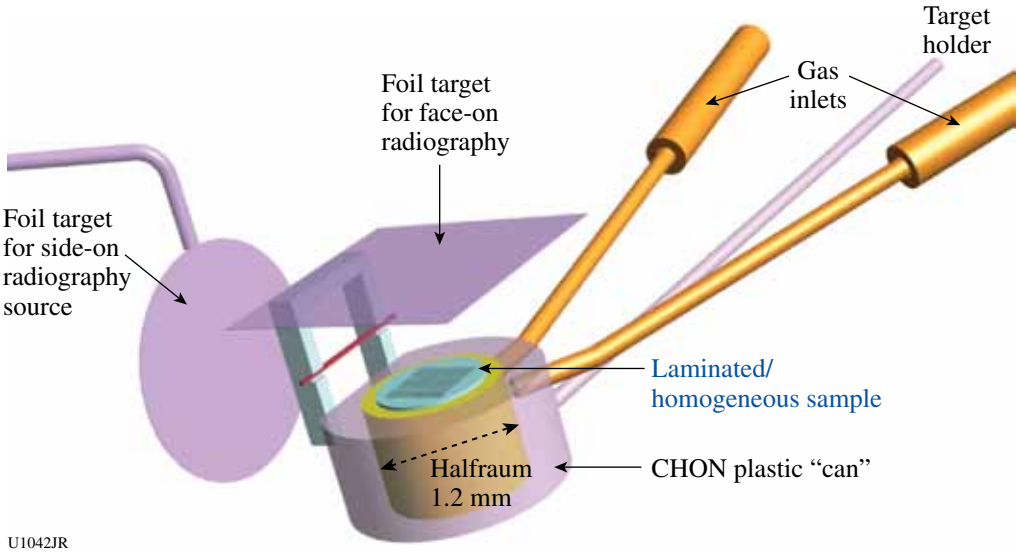

Figure 120.130
Experimental setup.

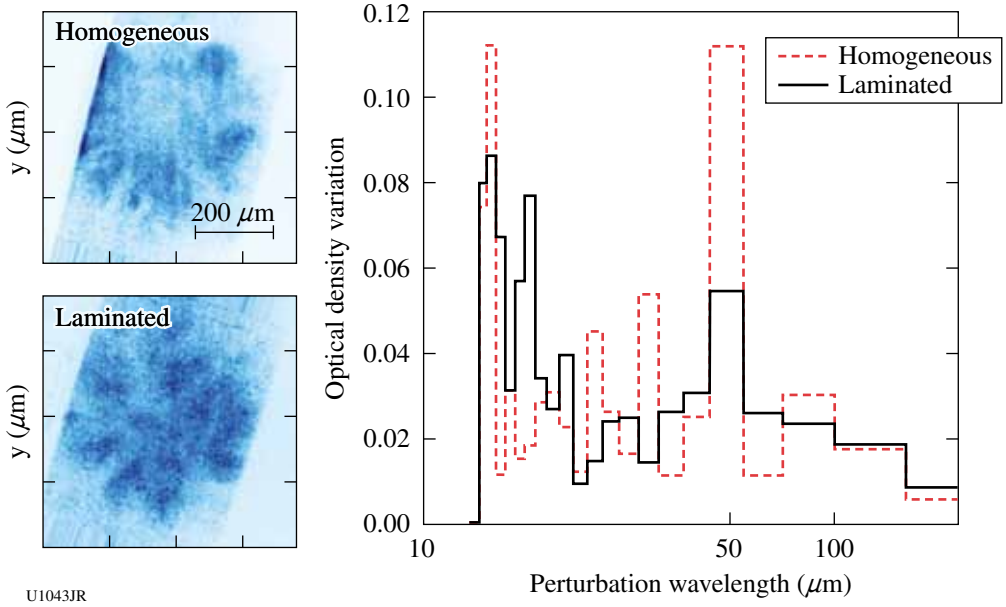

Figure 120.131
Face-on snapshots for homogeneous and laminated samples and corresponding perturbation spectra.

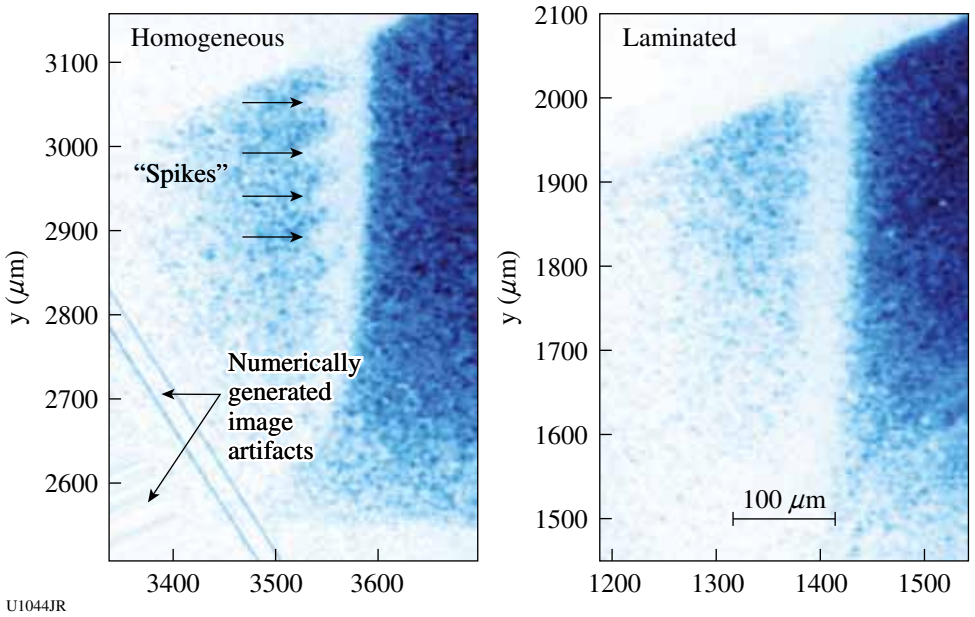

Figure 120.132
Side-on radiographies of (a) homogeneous and (b) laminated samples.

REFERENCES

1. S. H. Glenzer *et al*., Phys. Rev. Lett. **90**, 175002 (2003).
2. H. J. Lee, P. Neumayer, J. Castor, T. Döppner, R. W. Falcone, C. Fortmann, B. A. Hammel, A. L. Kritcher, O. L. Landen, R. W. Lee, D. D. Meyerhofer, D. H. Munro, R. Redmer, S. P. Regan, S. Weber, and S. H. Glenzer, Phys. Rev. Lett. **102** 115001 (2009).
3. L. Willingale *et al*., Phys. Rev. Lett. **96**, 245002 (2006); L. Willingale *et al*., Phys. Rev. Lett. **102**, 125002 (2009).
4. A. L. Lei *et al*., Phys. Plasmas **16**, 056307 (2009).
5. G. Li *et al*., Phys. Rev. Lett. **100**, 125002 (2008).
6. C. K. Li, F. H. Séguin, J. A. Frenje, J. R. Rygg, R. D. Petrasso, R. P. J. Town, P. A. Amendt, S. P. Hatchett, O. L. Landen, A. J. Mackinnon, P. K. Patel, V. A. Smalyuk, T. C. Sangster, and J. P. Knauer, Phys. Rev. Lett. **97**, 135003 (2006).
7. C. K. Li, F. H. Séguin, J. A. Frenje, J. R. Rygg, R. D. Petrasso, R. P. J. Town, P. A. Amendt, S. P. Hatchett, O. L. Landen, A. J. Mackinnon, P. K. Patel, M. Tabak, J. P. Knauer, T. C. Sangster, and V. A. Smalyuk, Phys. Rev. Lett. **99**, 015001 (2007).
8. C. K. Li, F. H. Séguin, J. A. Frenje, J. R. Rygg, R. D. Petrasso, R. P. J. Town, O. L. Landen, J. P. Knauer, and V. A. Smalyuk, Phys. Rev. Lett. **99**, 055001 (2007).
9. C. K. Li, F. H. Séguin, J. R. Rygg, J. A. Frenje, M. Manuel, R. D. Petrasso, R. Betti, J. Delettrez, J. P. Knauer, F. Marshall, D. D. Meyerhofer, D. Shvarts, V. A. Smalyuk, C. Stoeckl, O. L. Landen, R. P. J. Town, C. A. Back, and J. D. Kilkenny, Phys. Rev. Lett. **100**, 225001 (2008).
10. C. K. Li, F. H. Séguin, J. A. Frenje, R. D. Petrasso, P. A. Amendt, R. P. J. Town, O. L. Landen, J. R. Rygg, R. Betti, J. P. Knauer, D. D. Meyerhofer, J. M. Soures, C. A. Back, J. D. Kilkenny, and A. Nikroo, Phys. Rev. Lett. **102**, 205001 (2009).
11. R. D. Petrasso, C. K. Li, F. H. Séguin, J. R. Rygg, J. A. Frenje, R. Betti, J. P. Knauer, D. D. Meyerhofer, P. A. Amendt, D. H. Froula, O. L. Landen, P. K. Patel, J. S. Ross, and R. P. J. Town, Phys. Rev. Lett. **103**, 085001 (2009).
12. J. R. Rygg, F. H. Séguin, C. K. Li, J. A. Frenje, M. J.-E. Manuel, R. D. Petrasso, R. Betti, J. A. Delettrez, O. V. Gotchev, J. P. Knauer, D. D. Meyerhofer, F. J. Marshall, C. Stoeckl, and W. Theobald, Science **319**, 1223 (2008).
13. C. K. Li, F. H. Séguin, J. A. Frenje, J. R. Rygg, R. D. Petrasso, R. P. J. Town, P. A. Amendt, S. P. Hatchett, O. L. Landen, A. J. Mackinnon, P. K. Patel, V. Smalyuk, J. P. Knauer, T. C. Sangster, and C. Stoeckl, presented at the 16th Topical Conference on High-Temperature Plasma Diagnostics, Williamsburg, VA, 7–11 May 2006 (invited).
14. C. K. Li, presented at the Fifth International Conference on Inertial Fusion Sciences and Applications, Kobe, Japan, 9–14 September 2007, Paper ThO4.1 (invited).
15. R. Petrasso, presented at the Program of the 49th Annual Meeting of the Division of Plasma Physics, Orlando, FL, 12–16 November 2007, Paper GI1 4 (invited).
16. C. K. Li, presented at the 50th Annual Meeting of the APS Division of Plasma Physics, Dallas, TX, 17–21 November 2008, Paper BI1 5 (invited).
17. R. D. Petrasso, presented at the 2008 APS April Meeting and HEDP/HEDLA Meeting, St. Louis, MO, 11–15 April 2008, Paper 14HE.00002 (invited).
18. R. D. Petrasso, C. K. Li, F. H. Séguin, J. A. Frenje, M. Manuel, D. Casey, N. Sinenian, M. Rosenberg, H. Rir. Landen, J. R. Rygg, R. P. J. Town, R. Betti, J. Delettrez, J. P. Knauer, F. J. Marshall, D. D. Meyerhofer, V. A. Smalyuk, J. M. Soures, C. A. Back, J. D. Kilkenny, and A. Nikroo,

presented at the Second International Conference on High Energy Density Physics, Austin, TX, 19–22 May 2009 (invited).

19. C. K. Li, presented at The 8th Pacific Rim Conference on Lasers and Electro-Optics (CLEO/Pacific Rim 2009), Shanghai, China, 30 August–3 September 2009 (invited).

20. C. K. Li, presented at The Sixth International Conference on Inertial Fusion Sciences and Applications (IFSA 2009), San Francisco, CA, 6–11 September 2009, Paper 5.2.3 (invited).

21. J. A. Frenje, D. T. Casey, F. H. Séguin, C. K. Li, N. Sinenian, R. D. Petrasso, V. Yu. Glebov, T. C. Sangster, D. D. Meyerhofer, S. Hatchett, S. Haan, C. Cerjan, D. Eder, O. Landen, M. Moran, K. Fletcher, and R. Leeper, presented at the Sixth International Conference on Inertial Fusion Sciences and Applications (IFSA 2009), San Francisco, CA, 6–11 September 2009, Paper 3.6.3 (invited).

22. C. K. Li, F. H. Séguin, J. A. Frenje, J. R. Rygg, R. D. Petrasso, R. P. J. Town, P. A. Amendt, S. P. Hatchett, O. L. Landen, A. J. Mackinnon, P. K. Patel, V. Smalyuk, J. P. Knauer, T. C. Sangster, and C. Stoeckl, Rev. Sci. Instrum. **77**, 10E725 (2006).

23. H. Chen, S. C. Wilks, J. D. Bonlie, E. P. Liang, J. Myatt, D. F. Price, D. D. Meyerhofer, and P. Beiersdorfer, Phys. Rev. Lett. **102**, 105001 (2009).

24. J. Myatt, A. V. Maximov, R. W. Short, and D. D. Meyerhofer, presented at the 49th Annual Meeting of the APS Division of Plasma Physics, Orlando, FL, 12–16 November 2007, Paper CO6 1.

25. W. Theobald, R. Betti, V. A. Smalyuk, K. S. Anderson, J. A. Delettrez, J. A. Frenje, V. Yu. Glebov, F. J. Marshall, D. D. Meyerhofer, J. F. Myatt, R. D. Petrasso, C. Ren, T. C. Sangster, W. Seka, A. A. Solodov, C. Stoeckl, and B. Yaakobi, "Shock-Ignition Experiments on OMEGA and NIF-Relevant Intensities," submitted to Physical Review Letters.

26. W. Theobald, K. S. Anderson, R. Betti, R. S. Craxton, J. A. Delettrez, J. A. Frenje, V. Yu. Glebov, O. V. Gotchev, J. H. Kelly, C. K. Li, A. J. Mackinnon, F. J. Marshall, R. L. McCrory, D. D. Meyerhofer, J. F. Myatt, P. A. Norreys, P. M. Nilson, P. K. Patel, R. D. Petrasso, P. B. Radha, C. Ren, T. C. Sangster, W. Seka, V. A. Smalyuk, A. A. Solodov, R. B. Stephens, C. Stoeckl, and B. Yaakobi, "Advanced-Ignition-Concept Exploration on OMEGA," Plasma Phys. Control. Fusion **51**, 124052 (2009).

27. D. H. Froula, L. Divol, R. L. Berger, R. A. London, N. B. Meezan, D. J. Strozzi, P. Neumayer, J. S. Ross, S. Stagnitto, L. J. Suter, and S. H. Glenzer, Phys. Rev. Lett. **101**, 115002 (2008).

28. D. H. Froula, Phys. Rev. Lett. **103**, 045006 (2009).

29. E. L. Dewald *et al*., Rev. Sci. Instrum. **79**, 10E903 (2008).

30. T. Döppner, O. L. Landen, H. J. Lee, P. Neumayer, S. P. Regan, and S. H. Glenzer, High Energy Density Phys. **5**, 182 (2009).

31. T. Döppner, P. F. Davis, A. L. Kritcher, O. L. Landen, H. J. Lee, S. P. Regan, and S. H. Glenzer, in *Soft X-Ray Lasers and Applications VII*, edited by J. Dunn and G. J. Tallents (SPIE, Bellingham, WA, 2009), Vol. 7451, p. 74510H.

32. *LLE Review Quarterly Report* **116**, 249, Laboratory for Laser Energetics, University of Rochester, Rochester, NY, LLE Document No. DOE/NA/28302-866 (2008).

33. H. W. Herrmann, R. M. Malone, W. Stoeffl, S. E. Caldwell, S. C. Evans, J. M. Mack, P. Sanchez, T. Sedillo, C. S. Young, C. J. Horsfield, D. Drew, E. K. Miller, and V. Yu. Glebov, presented at the 17th Topical Conference on High-Temperature Plasmas Diagnostics, Albuquerque, NM, 11–15 May 2008, Paper D35.

34. H. W. Herrmann, S. C. Evans, J. M. Mack, C. S. Young, C. J. Horsfield, R. M. Malone, E. K. Miller, V. Yu. Glebov, and W. Stoeffl, presented at the 17th Topical Conference on High-Temperature Plasma Diagnostics, Albuquerque, NM, 11–15 May 2008, Paper D34.

35. E. Miller, presented at The Sixth International Conference on Inertial Fusion Sciences and Applications (IFSA 2009), San Francisco, CA, 6–11 September 2009, Poster 3.10.110.

36. P. Amendt *et al*., Rev. Sci. Instrum. **66**, 785 (1995).

37. P. Amendt *et al*., Phys. Rev. Lett. **77**, 3815 (1996).

38. A. A. Hauer *et al*., Phys. Plasmas **2**, 2488 (1995).

39. *LLE Review Quarterly Report* **112**, 270, Laboratory for Laser Energetics, University of Rochester, Rochester, NY, LLE Document No. DOE/SF/19460-790 (2007).

40. L. Disdier, A. Rouyer, D. C. Wilson, A. Fedotoff, C. Stoeckl, J. L. Bourgade, V. Yu. Glebov, J.-P. Garçonnet, and W. Seka, Nucl. Instrum. Methods Phys. Res. A **489**, 496 (2002).

41. L. Disdier, A. Rouyer, A. Fedotoff, J.-L. Bourgade, F. J. Marshall, V. Yu. Glebov, and C. Stoeckl, Rev. Sci. Instrum. **74**, 1832 (2003).

42. L. Disdier, R. A. Lerche, J. L. Bourgade, and V. Yu. Glebov, Rev. Sci. Instrum. **75**, 2134 (2004).

43. L. Disdier, A. Rouyer, I. Lantuéjoul, O. Landoas, J. L. Bourgade, T. C. Sangster, V. Yu. Glebov, and R. A. Lerche, Phys. Plasmas **13**, 056317 (2006).

44. *LLE Review Quarterly Report* **116**, 258, Laboratory for Laser Energetics, University of Rochester, Rochester, NY, LLE Document No. DOE/NA/28302-866 (2008).

45. A. Rouyer, Rev. Sci. Instrum. **74**, 1234 (2003).

46. L. Masse, Phys. Rev. Lett. **98**, 245001 (2007).

Publications and Conference Presentations

Publications

A. Belousov, S. Katrych, J. Jun, J. Zhang, D. Günther, R. Sobolewski, J. Karpinski, and B. Batlogg, "Bulk Single-Crystal Growth of the Ternary $Al_xGa_{1-x}N$ from Solution in Gallium Under High Pressure," J. Cryst. Growth **311**, 3971 (2009).

B. Ciftcioglu, L. Zhang, J. Zhang, J. R. Marciante, J. Zuegel, R. Sobolewski, and H. Wu, "Integrated Silicon PIN Photodiodes Using Deep N-Well in a Standard 0.18-μm CMOS Technology," J. Lightwave Technol. **27**, 3303 (2009).

C. Dorrer, "High-Damage-Threshold Beam Shaping Using Binary Phase Plates," Opt. Lett. **34**, 2330 (2009).

G. Guarino, W. R. Donaldson, M. Mikulics, M. Marso, P. Kordoš, and R. Sobolewski, "Finite Element Simulation of Metal–Semiconductor–Metal Photodetector," Solid-State Electron. **53**, 1144 (2009).

S. X. Hu, L. A. Collins, and B. I. Schneider, "Attosecond Photoelectron Microscopy of H_2^+," Phys. Rev. A **80**, 023426 (2009).

I. V. Igumenshchev, "Magnetic Inversion as a Mechanism for the Spectral Transition of Black Hole Binaries," Astrophys. J. **702**, L72 (2009).

I. V. Igumenshchev, F. J. Marshall, J. A. Marozas, V. A. Smalyuk, R. Epstein, V. N. Goncharov, T. J. B. Collins, T. C. Sangster, and S. Skupsky, "The Effects of Target Mounts in Direct-Drive Implosions on OMEGA," Phys. Plasmas **16**, 082701 (2009).

A. V. Okishev, D. Westerfeld, L. Shterengas, and G. Belenky, "A Stable Mid-IR, GaSb-Based Diode Laser Source for the Cryogenic Target Layering at the Omega Laser Facility," Opt. Express **17**, 15,760 (2009).

B. Punsly, I. V. Igumenshchev, and S. Hirose, "Three-Dimensional Simulations of Vertical Magnetic Flux in the Immediate Vicinity of Black Holes," Astrophys. J. **704**, 1065 (2009).

J. Sanz, R. Betti, V. A. Smalyuk, M. Olazabal-Loume, V. Drean, V. Tikhonchuk, X. Ribeyre, and J. Feugeas, "Radiation Hydrodynamic Theory of Double Ablation Fronts in Direct-Drive Inertial Confinement Fusion," Phys. Plasmas **16**, 082704 (2009).

V. A. Smalyuk, S. X. Hu, J. D. Hager, J. A. Delettrez, D. D. Meyerhofer, T. C. Sangster, and D. Shvarts, "Rayleigh-Taylor Growth Measurements in the Acceleration Phase of Spherical Implosions on OMEGA," Phys. Rev. Lett. **103**, 105001 (2009).

W. Theobald, C. Stoeckl, P. A. Jaanimagi, P. M. Nilson, M. Storm, D. D. Meyerhofer, T. C. Sangster, D. Hey, A. J. MacKinnon, H.-S. Park, P. K. Patel, R. Shepherd, R. A. Snavely, M. H. Key, J. A. King, B. Zhang, R. B. Stephens, K. U. Akli, K. Highbarger, R. L. Daskalova, L. Van Woerkom, R. R. Freeman, J. S. Green, G. Gregori, K. Lancaster, and P. A. Norreys, "A Dual-Channel, Curved-Crystal Spectrograph for Petawatt Laser, X-Ray Backlighter Source Studies," Rev. Sci. Instrum. **80**, 083501 (2009).

Forthcoming Publications

J. Bromage, C. Dorrer, J. R. Marciante, M. J. Shoup III, and J. D. Zuegel, "Modal Measurement of a Large-Mode-Area Photonic-Crystal Fiber Amplifier Using Spatially Resolved Spectral Interferometry," to be published in Solid State Diode Laser Technology Review.

W. R. Donaldson, J. R. Marciante, and R. G. Roides, "An Optical Replicator for Single-Shot Measurements at 10 GHz with a Dynamic Range of 1800:1," to be published in the IEEE Journal of Quantum Electronics.

D. French, C. Dorrer, and I. Jovanovic, "Two-Beam SPIDER for Dual-Pulse Single-Shot Characterization," to be published in Optics Letters.

W. Guan and J. R. Marciante, "A 1-W Single-Frequency Hybrid Brillouin/Ytterbium Fiber Laser," to be published in Optics Letters.

J. Kitaygorsky, R. Shouten, S. Dorenbos, E. Reiger, V. Zwiller, and R. Sobolewski, "Resolving Dark Pulses from Photon Pulses in NbN Superconducting Single-Photon Detectors," to be published in the Journal of Modern Optics.

G. P. Pepe, L. Parlato, N. Marrocco, V. Pagliarulo, G. Peluso, A. Barone, F. Tafuri, U. Scotti di Uccio, F. Miletto, M. Radovic, D. Pan, and R. Sobolewski, "Novel Superconducting Proximized Heterostructures for Ultrafast Photodetection," to be published in Cryogenics.

S. P. Regan, "Applied Plasma Spectroscopy I: Laser-Fusion Experiments," to be published in High Energy Density Physics.

S. N. Shafrir, H. J. Romanofsky, M. Skarlinski, M. Wang, C. Miao, S. Salzman, T. Chartier, J. Mici, J. C. Lambropoulos, R. Shen, H. Yang, and S. D. Jacobs, "Zirconia Coated Carbonyl Iron Particle-Based Magnetorheological Fluid for Polishing Optical Glasses and Ceramics," to be published in Applied Optics.

R. Shen, S. N. Shafrir, C. Miao, M. Wang, J. C. Lambropoulos, S. D. Jacobs, and H. Yang, "Synthesis and Corrosion Study of Zirconia Coated Carbonyl Iron Particles," to be published in the Journal of Colloid and Interface Science.

W. Theobald, K. S. Anderson, R. Betti, R. S. Craxton, J. A. Delettrez, J. A. Frenje, V. Yu. Glebov, O. V. Gotchev, J. H. Kelly, C. K. Li, A. J. Mackinnon, F. J. Marshall, R. L. McCrory, D. D. Meyerhofer, J. F. Myatt, P. A. Norreys, P. M. Nilson, P. K. Patel, R. D. Petrasso, P. B. Radha, C. Ren, T. C. Sangster, W. Seka, V. A. Smalyuk, A. A. Solodov, R. B. Stephens, C. Stoeckl, and B. Yaakobi, "Advanced-Ignition-Concept Exploration on OMEGA," to be published in Plasma Physics and Controlled Fusion.

B. Yaakobi, O. V. Gotchev, R. Betti, and C. Stoeckl, "Study of Fast-Electron Transport in Laser-Illuminated Spherical Targets," to be published in Physics of Plasmas.

L. Zeng, T. Y.-H. Lee, P. B. Merkel, and S. H. Chen, "A New Class of Non-Conjugated Bipolar Hybrid Hosts for Phosphorescent Organic Light-Emitting Diodes," to be published in the Journal of Materials Chemistry.

Conference Presentations

L. Ji, W. R. Donaldson, and T. Y. Hsiang, "Electro-Optic Sampling Using Two/Multiple Optical Pulses," 14th Opto-Electronics and Communications Conference, Hong Kong, 13–17 July 2009.

The following presentations were made at Optical Manufacturing and Testing VIII, San Diego, CA, 2–6 August 2009:

C. Miao, J. C. Lambropoulos, S. N. Shafrir, H. Romanofsky, and S. D. Jacobs, "Contributions of Nanodiamond Abrasives and Deionized Water in Magnetorheological Finishing of Aluminum Oxynitride."

C. Miao, S. N. Shafrir, J. C. Lambropoulos, and S. D. Jacobs, "Normal Force and Drag Force in Magnetorheological Finishing."

S. N. Shafrir, R. Shen, C. Miao, H. Romanofsky, M. Wang, J. Mici, J. Yang, J. C. Lambropoulos, and S. D. Jacobs, "Zirconia Coated Carbonyl Iron Particle-Based Magnetorheological Fluid for Polishing."

E. Glowacki, C. W. Ching, and K. L. Marshall, "Photoswitchable Gas Permeation Membranes Based on Azobenzene-Doped Liquid Crystals," Optics and Photonics, San Diego, CA, 2–6 August 2009 (invited).

The following presentations were made at the Ultrafast Optics and High Field Short Wavelength Meeting, Arcachon, France, 31 August–4 September 2009:

C. Dorrer, "High-Damage-Threshold Beam Shapers for High-Energy Laser Systems."

C. Dorrer and J. Bromage, "Simple High-Sensitivity, Electro-Optic Sagnac Spectral Shearing Interferometry for Optical Pulse Characterization."

C. Dorrer, J. Bromage, and J. D. Zuegel, "Single-Shot High-Dynamic-Range Cross-Correlator for High-Energy Laser Systems."

The following presentations were made at the Sixth International Conference on Inertial Fusion Sciences and Applications, San Francisco, CA, 6–11 September 2009:

R. Betti, K. S. Anderson, P. Y. Chang, R. Nora, and C. D. Zhou, "A Measurable Lawson Criterion for Inertial Confinement Fusion."

T. R. Boehly, V. N. Goncharov, D. E. Fratanduono, M. A. Barrios, S. X. Hu, T. C. Sangster, D. D. Meyerhofer, D. Munro, P. M. Celliers, D. G. Hicks, H. F. Robey, G. W. Collins, N. Landen, R. E. Olson, and A. Nikroo, "Demonstration of the Shock-Timing Technique for Ignition Targets at the National Ignition Facility."

V. N. Goncharov, T. C. Sangster, T. R. Boehly, R. L. McCrory, D. D. Meyerhofer, P. B. Radha, V. A. Smalyuk, S. Skupsky, J. A. Frenje, and R. D. Petrasso, "Multiple-Picket, Cryogenic Target Designs and Performance for OMEGA and the NIF."

R. L. McCrory, R. Betti, R. S. Craxton, J. A. Delettrez, D. H. Edgell, V. Yu. Glebov, V. N. Goncharov, D. R. Harding, S. X. Hu, J. P. Knauer, F. J. Marshall, P. W. McKenty, D. D. Meyerhofer, P. B. Radha, S. P. Regan, T. C. Sangster, W. Seka, R. W. Short, D. Shvarts, S. Skupsky, V. A. Smalyuk, J. M. Soures, C. Stoeckl, W. Theobald, B. Yaakobi, J. A. Frenje, C. K. Li, R. D. Petrasso, F. H. Séguin, and D. T. Casey, "Progress in Cryogenic Target Implosions on OMEGA."

P. W. McKenty, R. S. Craxton, J. A. Marozas, A. M. Cok, M. J. Bonino, D. R. Harding, D. D. Meyerhofer, R. L. McCrory, J. D. Kilkenny, A. Nikroo, J. Fooks, M. Hoppe, J. M. Edwards, A. J. MacKinnon, D. H. Munro, and R. J. Wallace, "Design of High-Neutron-Yield Polar-Drive Targets for Diagnostic Activation Experiments on the NIF."

D. D. Meyerhofer, R. Betti, T. R. Boehly, J. Bromage, C. Dorrer, V. Yu. Glebov, J. H. Kelly, B. E. Kruschwitz, S. J. Loucks, R. L. McCrory, S. F. B. Morse, J. F. Myatt, P. M. Nilson, J. Qiao, T. C. Sangster, A. A. Solodov, C. Stoeckl, W. Theobald, J. D. Zuegel, H. S. Park, B. Maddox, A. MacPhee, J. Workman, M. Koenig, E. Brimbrank, C. Szabo, and G. Holland "Performance of and Initial Experimental Results from the Omega EP Laser System."

S. P. Regan, P. B. Radha, T. R. Boehly, T. Doeppner, K. Falk, V. N. Goncharov, S. H. Glenzer, G. Gregori, O. L. Landen, D. D. Meyerhofer, P. Neumayer, T. C. Sangster, and V. A. Smalyuk, "Inferring the Electron Temperature and Density of Shocked Liquid Deuterium Using Inelastic X-Ray Scattering."

T. C. Sangster, L. Ahle, D. Bleuel, D. T. Casey, M. J. Eckart, M. J. Edwards, R. J. Fortner, J. A. Frenje, V. Yu. Glebov, G. P. Grim, H. W. Herrmann, C. J. Horsfield, J. D. Kilkenny, O. Landoas, R. A. Lerche, K. J. Moody, M. J. Moran, R. D. Petrasso, M. Schmitt, D. Schneider, D. A. Shaughnessy, C. Stoeckl, W. Stoeffl, and M. D. Wilke, "The Nuclear Diagnostics Suite for the NIF."

A. A. Solodov, M. Storm, J. F. Myatt, R. Betti, D. D. Meyerhofer, P. M. Nilson, W. Theobald, and C. Stoeckl, "The Role of Resistive Filamentation and Self-Generated Magnetic Fields in Hot-Electron-Beam Transport Through Solid Targets."

A. L. Rigatti, J. B. Oliver, A. Kozlov, and A. W. Schmid, "Comparison of 10-ps In-Air and In-Vacuum Damage Thresholds," Laser Damage 2009, Boulder, CO, 21–23 September 2009.


1850
MELIORA
UNIVERSITY of
ROCHESTER